# Studies on Experiments and Free-Electron laser concepts with a Transverse Gradient Undulator

Dissertation
zur Erlangung des Doktorgrades
an der Fakultät für Mathematik, Informatik und Naturwissenschaften
Fachbereich Physik
der Universität Hamburg

vorgelegt von

## Farzad Jafarinia

Gutachter der Dissertation:             Prof. Dr. Wolfgang Hillert
                                        Dr. Ralph W. Aßmann

Hamburg
2021

Gutachter/innen der Dissertation:        Prof. Dr. Wolfgang Hillert

Dr. Ralph W. Aßmann

Zusammensetzung der Prüfungskommission:    Prof. Dr. Wolfgang Hillert

Dr. Ralph W. Aßmann

Prof. Dr. Daniela Pfannkuche

Prof. Dr. Markus Drescher

Dr. Axel Bernhard

Vorsitzende der Prüfungskommission:    Prof. Dr. Daniela Pfannkuche

Datum der Disputation:    30.07.2021

Vorsitzender Fach-Promotionsausschusses PHYSIK:    Prof. Dr. Wolfgang Hansen

Leiter des Fachbereichs PHYSIK:    Prof. Dr. Gunter Hans Walter Sigl

Dekan der Fakultät MIN:    Prof. Dr. Heinrich Graener

# Abstract

Free-electron lasers (FELs) are the fourth generation of synchrotron light sources operating in the ultraviolet and X-ray wavelength range. The large size and the high costs of such sources limit the handiness of them. Emerging new acceleration techniques in the recent years, opened the way to design more compact accelerators. Due to generation of high energy electron beams in a very short distance with a high peak current, laser-plasma accelerators (LPAs) are regarded as capable candidates for deriving FELs. The major problem with these types of accelerators is the relatively large energy distribution of the electrons within the beam. Such a large energy spread will hinder the FEL performance resulting in a reduction of the gain and the power. In this purpose, modified undulator schemes, so-called transverse gradient undulators (TGUs), were proposed. In this dissertation, the concept of a transverse gradient undulator is studied in detail. The concept relies on fulfilling the resonance condition for different particles' energy within the beam. The resonance condition can be satisfied for all particles with different energies if the positions and the energies of the particles are related to the magnetic field gradient of the TGU. This can be done by introducing dispersion, which is matched to the TGU gradient. The first superconducting cylindrical TGU with 40 periods (TGU40) was built at Karlsruhe Institute of Technology (KIT) and it was originally planned to perform an experiment with the ARES linac at SINBAD facility at DESY in order to test its capability in compensation of the energy spread. The detailed setup of the experiment with the simulation results are presented. Moreover, the TGU scheme is investigated from an FEL point of view. After a successful test of the prototype TGU40, the first demonstration of an FEL lasing experiment with a TGU and a laser-plasma accelerator as the beam generator should be performed. In this regard, a scaling study is presented in order to determine the minimum beam requirement for achieving FEL power. The scaling is done over a possible range of the LPA parameters which can be reached by the current technology and an optimized LPA setup. In addition to the mentioned above studies, a compact beam line transport to deliver LPA beam to the TGU is designed and the effect of the beam line and the collective effects like space-charge and coherent synchrotron radiation on the beam properties are investigated. This comprehensive study opens the way of demonstrating the possible lab-scale free-electron laser experiment with a laser-plasma accelerator.

# Zusammenfassung

Freie Elektronenlaser (FELs) sind die vierte Generation von Synchrotron Lichtquellen, die im ultravioletten und Röntgenwellenlängenbereich arbeiten. Die Größe und die hohen Kosten solcher Quellen begrenzen deren Handlichkeit. Die in den letzten Jahren aufkommenden neuen Beschleunigungstechniken haben den Weg für die Entwicklung kompakterer Beschleuniger geebnet. Aufgrund der Erzeugung energiereicher Elektronenstrahlen in sehr kurzer Entfernung mit hohem Spitzenstrom gelten Laser-Plasma-Beschleuniger (LPAs) als geeignete Kandidaten für die Konstruktion neuer FELs. Das Hauptproblem bei diesen Arten von Beschleunigern ist die relativ große Energiebreite der Elektronen innerhalb des Strahls. Eine solche große Energieverteilung verhindert den FEL-Prozess, was zu einer Verringerung der Verstärkung und der Leistung führt. Zu diesem Zweck wurden modifizierte Undulatorschemata, sogenannte Transversalgradienten-Undulatoren (TGUs), vorgeschlagen. In dieser Dissertation wird das Konzept eines Transversalgradienten-Undulators eingehend untersucht. Das Konzept basiert auf der Erfüllung der Resonanzbedingung für die Energien verschiedener Partikel im Strahl. Die Resonanzbedingung kann für alle Teilchen mit unterschiedlichen Energien erfüllt sein, wenn die Positionen und Energien der Teilchen mit dem Magnetfeldgradienten der TGU Korreliert sind. Dies kann durch Einführen einer Dispersion erfolgen, die an den TGU-Gradienten angepasst ist. Das erste supraleitende zylindrische TGU mit 40 Perioden (TGU40) wurde am Karlsruher Institut für Technologie (KIT) gebaut. Es war ursprünglich geplant, ein Experiment mit dem ARES linac in der SINBAD-Anlage in DESY durchzuführen, um seine Fähigkeit zur Kompensation der Energieverteilung zu testen. Die Details eines möglichen Experiments mit den Simulationsergebnissen werden vorgestellt. Darüber hinaus wird das TGU-Schema unter FEL-Gesichtspunkten untersucht. Nach einem erfolgreichen Test des Prototyps TGU40 sollte die erste Demonstration des FEL-Laserexperiments mit einer TGU und einem Laser-Plasma-Beschleuniger als Strahlgenerator durchgeführt werden. In diesem Zusammenhang wird eine Skalierungsstudie vorgestellt, um die minimale Strahlanforderung zum Erreichen der FEL-Leistung zu bestimmen. Die Skalierung erfolgt über einen möglichen Bereich der LPA-Parameter, der mit der aktuellen Technologie und einem optimierten LPA-Setup erreicht werden kann. Zusätzlich zu den oben genannten Studien wird ein kompakter Strahllinientransport eines LPA-Strahls zur TGU entworfen und der Einfluss der Strahllinie und kollektive Effekten wie Raumladung und kohärente Synchrotron Strahlung auf die Strahleigenschaften untersucht. Diese umfassende Studie legt die Grundlagen für ein mögliches Freie-Elektronen-Laserexperiment im Labormaßstab mit einem Laser-Plasma-Beschleuniger und einen TGU.

# Contents

# Chapter 1

# Introduction

The application range of particle accelerators has been growing, especially for the past few decades, when they have become indispensable instruments for scientific research in many science fields. Their capability of generating synchrotron radiation even more extended their applications, ranging from solid-state physics to the medical fields [1]. Nowadays modern synchrotron facilities can provide high spectral brightness photon beams as the premier light sources in the UV to X-ray region. While the bending magnet radiation was the main source in the early synchrotron radiation facilities, inclusion of many long straight sections for dedicated insertion devices, undulators and wigglers (in addition to bending magnets), in modern storage rings result in synchrotron radiation at specific wavelengths with higher flux and spectral brightness [2, 3].

The synchrotron radiation in an undulator is produced when electrons perform a harmonic oscillation with respect to the straight path along the undulator due to the periodic magnetic field. For certain beam parameters and long enough interaction distances the radiated field can interact with the electrons that leads to an amplification of radiation. This forms the basis of the free electron laser (FEL) interaction. The energy exchange between electrons and former emitted radiation leads to a density modulation of electrons in the bunch on the scale of the radiation wavelength. The intensity of the radiation field grows exponentially as the electron density modulation, so-called microbunching, increases along the undulator resulting in a growing radiation field amplitude [4]. Free Electron Lasers are the world's brightest light sources, capable of generating high intensity coherent photon pulses ranging from ultraviolet to X-ray range.

The core limitation of such photon sources is the large size of the facility operating in high beam energy [5]. Due to the maximum achievable gradient by the current radio frequency (RF) technology, which is on the order of 100 MV/m, an accelerator length of 10-100 m is required for operating of the X-ray FEL in the nanometer to angstrom range, which needs beam energies on

the order of 1-10 GeV. With the purpose of reaching high accelerating gradients above GeV/m to reduce the size of the accelerator, different advanced acceleration approaches have been proposed. Among the new acceleration techniques, the combination of having an ultra-short acceleration distance with achievable high peak current of multiple kA and small transverse emittance makes laser plasma accelerator as a favorable accelerator for the next generation compact FEL light sources [6]. The major drawback of laser plasma-based accelerators compared to conventional accelerators is the high energy spread of the electrons within the generated beams, which is typically in the order of some percent. Such a large energy spread prevents FEL lasing by disrupting the microbunching and FEL gain processes [7].

Furthermore, the broad energy spread of the LPA beam has an indirect effect on the FEL performance, since it causes chromatic emittance growth in the transport line. The large energy spread in combination with a relatively large divergence of the LPA beam poses serious challenges for capturing and transporting the beam while preserving the beam quality [8].

In order to compensate the effect of the energy spread on the FEL performance, modified undulator schemes, so-called transverse gradient undulators (TGUs), were proposed [9]. Although the idea at the beginning was proposed for low-gain FELs to reduce the sensitivity to the electron energy jitter for FEL oscillators, it has been reconsidered in high-gain FELs concepts due to its ability to increase the FEL gain in the case of beams with large energy spread such as the beam from a laser-plasma accelerator [10]. The scheme is based on mitigating the energy spread problem by fulfilling the resonance condition for different particles' energy in the electron beam. This can be done with properly dispersing the electron beam and matching the energy of the particles to the transverse field of the undulator by introducing a linear transverse field dependence in the undulator. The result matching leads to a narrow radiation bandwidth, an increase in the saturation power and shortening the gain length.

It was originally planned to test the prototype 40 period superconducting TGU (TGU40) built at Karlsruhe Institute of Technology (KIT) with the ARES linac at SINBAD facility at DESY. SINBAD is an accelerator research and development (R&D) facility, which hosts multiple independent experiments [11]. The TGU experiment was discussed in collaboration with KIT and the University of Jena. The TGU40 has been developed and built at KIT and was planned to be transported to DESY after finishing the magnetic field measurement. The diagnostics for the radiation detection was planned to be provided by the University of Jena. The main objective of the experiment is the validation of the TGU concept by demonstrating the TGU capability in producing monochromatic radiation from a beam with a relatively large energy spread.

In this thesis the TGU concept is studied in detail including the possibility of demonstration of FEL lasing by using a TGU attached to a laser plasma accelerator. Following the introduction chapter, an overview of the linear beam dynamics and radiation generation with a short description of FEL physics and laser plasma acceleration concept are presented in chapter 2. Chapter 3 provides a detail study of the TGU concept including the design of an experiment to test the prototype TGU40 with the ARES linac at SINBAD facility at DESY. In chapter 4 the TGU concept is investigated

from an FEL point of view. A nominal LPA beam parameter set is chosen based on the current achievable parameters from the laser plasma accelerators. In order to find the minimum beam requirement for an FEL demonstration experiment a scaling study in terms of the energy, charge, energy spread, normalized emittance and the bunch length is done over a possible range of parameters which can be reached by an optimized LPA setup. Finally, the major points in designing a beam line for a TGU are addressed and an optimized compact beam line is proposed in chapter 5. At the end of the chapter 5, a start-to-end (S2E) simulation is performed including collective effects in the beam line.

*Chapter 2*

# *Theory of Beam Acceleration and Radiation generation*

## 2.1 Beam Optics

In this section the basics of beam optics theory are presented. The goal of this chapter is to provide an introduction to the basic principles of the linear beam dynamics which are the basics for the later considerations. The content is based on references [12, 13].

### 2.1.1 Coordinate System and Magnets

Particle motion in an arbitrary beam transport system can be described by a coordinate system co-moving with the reference particle. In this coordinate system the direction of flight of the reference particle is pointed by $s$, while $x$ and $y$ show the transverse offset with respect to the reference particle. The trajectory of an individual particle can be described with respect to the ideal trajectory, which the reference particle takes, and is called the orbit. The Fig. 2.1 shows a sketch of this coordinate system.

Generally, the steering and deflecting of the particles is done by using magnetic fields. The magnetic field can be expanded in the vicinity of the orbit using the Taylor series:

$$B(x) = B_0 + B'x + B''x^2 + B'''x^3 + ... \tag{2.1}$$

The three lowest orders of this expansion are the dipole, the quadrupole and the sextupole. The dipole magnet is used to steer and deflect the reference orbit. It consists of two parallel poles, such that for an idealized dipole the magnetic field between these poles is constant. The
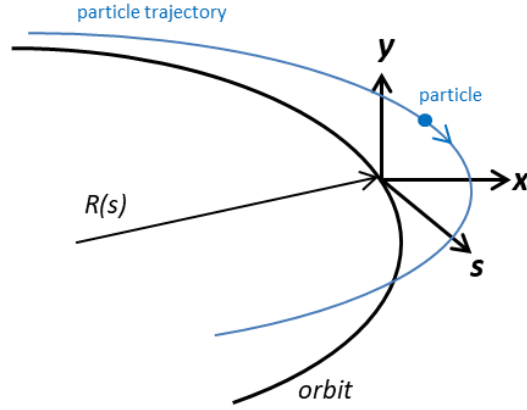
Figure 2.1: Sketch of the definition of the coordinate system and the reference path.

radius of the curvature of a particle with momentum $p$ moving in this field is:

$$R = \frac{P}{eB_y} \tag{2.2}$$

where $e$ is the charge of an electron. The bending radius also can be expressed in terms of dipole length $L$ and deflection angle $\theta$:

$$R = \frac{L}{\theta} \tag{2.3}$$

A quadrupole magnet has four poles with hyperbolic surfaces and is used to focus the particle by introducing a force which is proportional to the distance from the center. Due to the shape of the field lines between the poles a quadrupole which focuses in the horizontal plane, defocuses in the vertical plane. The focusing strength of a quadrupole $k$, determined by the particle momentum $p$, and the field gradient $g$:

$$k = \frac{eg}{p} \tag{2.4}$$

The next higher order multipole is the sextupole which consists of six poles arranged with alternating polarity at an angle of 60° to the next. It is used to compensate the chromatic effects in dispersive parts in the beam line. The strength of the sextupole $m$, for a given energy is determined by [12]:

$$m = \frac{eg'}{p} \tag{2.5}$$

The basic structure of dipole, quadrupole and sextupole are depicted in Fig. 2.2.
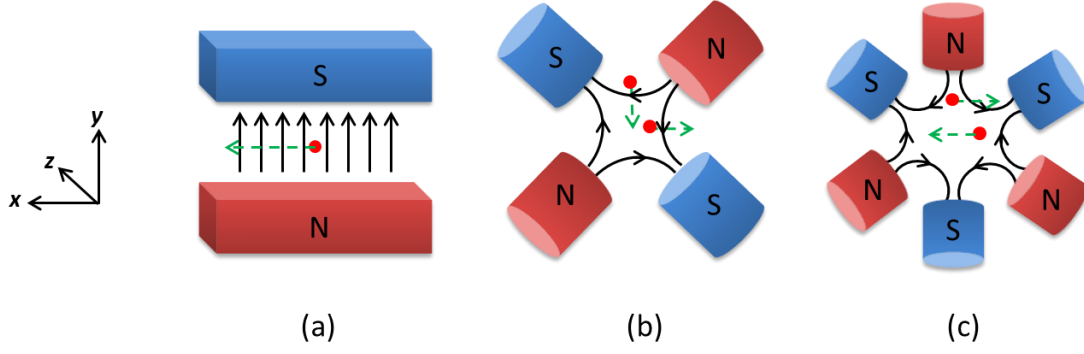
Figure 2.2: Schematic view of a dipole (a), quadrupole (b) and sextupole (c). Black arrows show the direction of magnetic field and the green arrows show the force on the electron (red dots) that goes in the *z* direction.

## 2.1.2 Particle Trajectories and Transfer Matrices

The linear equations of motion for a particle traveling through the magnetic structure of an accelerator with respect to the orbit are given by [12]:

$$x''(s) + \left( \frac{1}{R^2(s)} - k(s) \right) x(s) = \frac{1}{R(s)} \frac{\Delta p}{p} \tag{2.6}$$

$$y''(s) + k(s) y(s) = 0 \tag{2.7}$$

By solving these equations, we can express the effect of each section (drift, dipole, quadrupole and …) of the beam line on the particle trajectory by a transfer matrix. The general transformation including transverse components $(x, y)$, longitudinal offset $(z)$ and momentum deviation $(\delta)$ is a 6-D matrix. So, for a particle which is described in 6-D coordinate system $(x, x', y, y', z, \delta)$, the transformation between the initial $X_i$, and the final $X_f$ coordinates is given by

$$X_f = M \, X_i \tag{2.8}$$

Here $M$ is the first order transfer matrix and in its general form is determined by

$$M = \begin{pmatrix} M_{11} & M_{12} & M_{13} & M_{14} & M_{15} & M_{16} \\ M_{21} & M_{22} & M_{23} & M_{24} & M_{25} & M_{26} \\ M_{31} & M_{32} & M_{33} & M_{34} & M_{35} & M_{36} \\ M_{41} & M_{42} & M_{43} & M_{44} & M_{45} & M_{46} \\ M_{51} & M_{52} & M_{53} & M_{54} & M_{55} & M_{56} \\ M_{61} & M_{62} & M_{63} & M_{64} & M_{65} & M_{66} \end{pmatrix} \tag{2.9}$$

The transfer matrices for a drift, dipole and quadrupole (focusing) are listed below [13]:

$$
M_{drift} = \begin{pmatrix}
1 & L & 0 & 0 & 0 & 0 \\
0 & 1 & 0 & 0 & 0 & 0 \\
0 & 0 & 1 & L & 0 & 0 \\
0 & 0 & 0 & 1 & 0 & 0 \\
0 & 0 & 0 & 0 & 1 & L/\gamma^2 \\
0 & 0 & 0 & 0 & 0 & 1
\end{pmatrix} \tag{2.10}
$$

$$
M_{dipole} = \begin{pmatrix}
\cos\theta & R\sin\theta & 0 & 0 & 0 & R(1-\cos\theta) \\
-(1/R)\sin\theta & \cos\theta & 0 & 0 & 0 & \sin\theta \\
0 & 0 & 1 & R\theta & 0 & 0 \\
0 & 0 & 0 & 1 & 0 & 0 \\
-\sin\theta & -R(1-\cos\theta) & 0 & 0 & 1 & (R\theta/\gamma^2) - R(\theta - \sin\theta) \\
0 & 0 & 0 & 0 & 0 & 1
\end{pmatrix} \tag{2.11}
$$

$$
M_{quad/focusing} = \begin{pmatrix}
\cos(\sqrt{k}L) & \frac{1}{\sqrt{k}}\sin(\sqrt{k}L) & 0 & 0 & 0 & 0 \\
-\sqrt{k}\sin(\sqrt{k}L) & \cos(\sqrt{k}L) & 0 & 0 & 0 & 0 \\
0 & 0 & \cosh(\sqrt{k}L) & \frac{1}{\sqrt{k}}\sinh(\sqrt{k}L) & 0 & 0 \\
0 & 0 & \sqrt{k}\sin(\sqrt{k}L) & \cosh(\sqrt{k}L) & 0 & 0 \\
0 & 0 & 0 & 0 & 1 & L/\gamma^2 \\
0 & 0 & 0 & 0 & 0 & 1
\end{pmatrix}
$$

(2.12)

Here $k$ is the absolute value of the quadrupole strength, $\gamma$ is the Lorentz factor, and $L$ is the length of each element. The transport matrix of the whole transport system can be determined by successive multiplication of the transfer matrices of each element in the beam line. It should be noted that the transformation matrix can be extended to include second and third order effects.

## 2.1.3 Twiss Parameters and Emittance

The matrix formalism up to here allows us to describe the trajectory of single particle through the elements in a beam line. By assuming $1/R = 0$ and $\delta = 0$ (just drift and quadrupole) in

equation (2.6) the behavior of many particles as a beam can be determined by solving the Hill's differential equation [12, 13]

$$x''(s) + k(s)x(s) = 0 \qquad (2.13)$$

The general solution of Hill's equation has the form

$$x(s) = \sqrt{\varepsilon}\sqrt{\beta(s)}\cos\left(\psi(s) + \phi\right) \qquad (2.14)$$

$$x'(s) = -\frac{\sqrt{\varepsilon}}{\sqrt{\beta(s)}}\left[\alpha(s)\cos\left(\psi(s) + \phi\right) + \sin\left(\psi(s) + \phi\right)\right] \qquad (2.15)$$

Here β(s) is the beta function; also known as the amplitude function, α(s) is given by

$$\alpha(s) = -\frac{\beta'(s)}{2} \qquad (2.16)$$

$\varepsilon$ is defined as the beam emittance, $\psi(s)$ is the electron phase and $\phi$ is the initial phase offset. By eliminating the terms which depend on the phase $\psi(s)$ in equations (2.14) and (2.15) and introducing the parameter

$$\gamma(s) = \frac{1 + \alpha^2(s)}{\beta(s)} \qquad (2.17)$$

we can get the equation of the emittance ellipse which describes the particle motion in x-x' plane as

$$\gamma(s)x^2(s) + 2\alpha(s)x(s)x'(s) + \beta(s)x'^2(s) = \varepsilon \qquad (2.18)$$

The Twiss parameters $\alpha$, $\beta$ and $\gamma$ determine the shape and orientation of the ellipse. The phase space ellipse and related Twiss parameters are plotted in Fig. 3.2.

According to Liouville's Theorem the density in phase space of a system of non-interacting particles subject to a Hamiltonian (such as that of an electromagnetic field) is constant in time. This means that the area of the phase space ellipse and hence the beam emittance $\varepsilon$, which is area/$\pi$, are invariants of the particle motion. Using equations (2.14) and (2.15) and considering only the part of the beam which is within one standard deviation of the distribution we get [14]:

$$\sigma_x^2 = \left\langle x^2 \right\rangle = \varepsilon_{rms}\beta$$

$$\sigma_{x'}^2 = \left\langle x'^2 \right\rangle = \varepsilon_{rms}\gamma \qquad (2.19)$$

$$\sigma_{xx'} = \left\langle xx' \right\rangle = -\varepsilon_{rms}\alpha$$
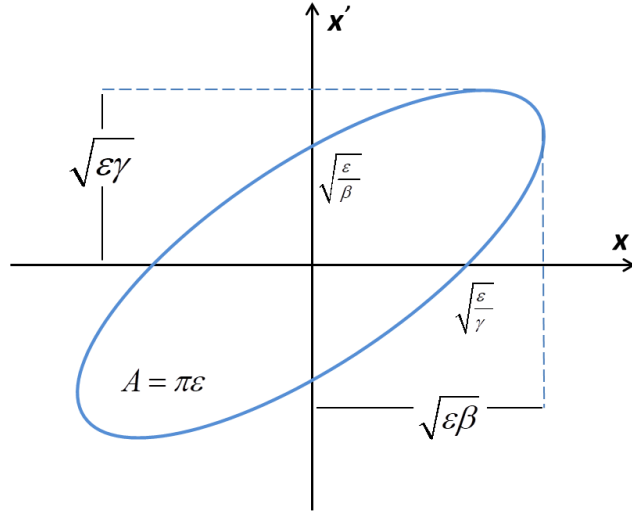
Figure 3.2: The phase space ellipse in x-x' plane and the related Twiss parameters.

And the rms beam emittance can be expressed by

$$\varepsilon_{rms} = \sqrt{\left\langle x^2 \right\rangle \left\langle x'^2 \right\rangle - \left\langle xx' \right\rangle^2} \tag{2.20}$$

From the above equations it is clear that the beam can be described by calculating the evolution of Twiss parameters through the beam line. For this purpose, the transport matrix used for single particle tracking can be adapted to propagation of the Twiss parameters. Using the fact that emittance is invariant between two points in the beam line one can get the transport matrix linking the initial and the final Twiss parameters along the beam line [12]

$$\begin{pmatrix} \beta \\ \alpha \\ \gamma \end{pmatrix} = \begin{pmatrix} M_{11}^2 & -2M_{11}M_{12} & M_{12}^2 \\ -M_{11}M_{21} & M_{11}M_{22} + M_{12}M_{21} & -M_{22}M_{12} \\ M_{21}^2 & -2M_{22}M_{21} & M_{22}^2 \end{pmatrix} \begin{pmatrix} \beta_0 \\ \alpha_0 \\ \gamma_0 \end{pmatrix} \tag{2.21}$$

In here the elements $M_{ij}$ are the corresponded elements of the transport matrix used for calculating the trajectory of a single particle.

## 2.1.4 Dispersion

The dispersion function $D(x,s)$ is defined as the change in particle position with fractional momentum offset $\delta$ :

$$x = D(x,s)\delta \tag{2.22}$$

It can be derived as a special solution to a first-order chromatic perturbation term in Hill's differential equation

$$D(s) = \int_0^s \frac{1}{R(\overline{s})} [S(s)C(\overline{s}) - C(s)S(\overline{s})] d\overline{s} \tag{2.23}$$

where $C(s)$ and $S(s)$ are the cosine- and sine-like solutions of the homogeneous Hill's equation (2.13) (with $\delta$ = 0) [13]. Regarding this fact that the particle deviation from the reference path can be expressed by betatron motion $x_\beta$, and a displacement due to the momentum difference $x_\delta = D\delta$

$$x = x_\beta + x_\delta \tag{2.24}$$

one can get a transformation matrix for the dispersion function

$$\begin{pmatrix} D(s) \\ D'(s) \\ 1 \end{pmatrix} = M \begin{pmatrix} D(s_0) \\ D'(s_0) \\ 1 \end{pmatrix} \tag{2.25}$$

Here $M$ is a $3 \times 3$ transformation matrix in the dispersive plane. Due to the electron beam finite momentum spread the beam size increases by the dispersion. For a Gaussian beam the transverse beam size including the dispersion effect is determined by

$$\sigma_x = \sqrt{\varepsilon_x \beta_x(s) + D^2(s)\sigma_\delta^2} \tag{2.26}$$

In analogy to the beam size, we can determine the beam divergence due to the dispersion as:

$$\sigma_{x'} = \sqrt{\varepsilon_x \gamma_x(s) + D'^2(s)\sigma_\delta^2} \tag{2.27}$$

# 2.2 Synchrotron Radiation

A charged particle moving at relativistic speed in a curved path will emit electromagnetic radiation. The emitted radiation has a sharp forward peak distribution. This phenomenon is known as synchrotron radiation since it was first observed experimentally in high energy circular electron accelerators, namely the synchrotrons. Nowadays modern synchrotron facilities can provide high spectral brightness photon beams as the premier light source in the UV to X-ray region. Three main types of synchrotron radiation sources are: bending magnets, undulators, and wigglers. Bending magnets were the first magnetic structures that have been

used to produce synchrotron radiation. The radiation spectrum from a bending magnet is very broad and is emitted into a cone of angle typically $1/\gamma$, where $\gamma$ is the Lorentz relativistic factor. An undulator is a periodic magnet structure which can be regarded as a series of bending magnets of periodic polarities that make the electron to perform a harmonic oscillation with respect to the straight path along the undulator. Due to the relatively weak magnetic field the amplitude of each undulation is small which results in a narrow cone radiation. The radiation cone is narrowed by a factor of $1/\sqrt{N}$ comparing to a bending magnet where $N$ is the number of the undulator periods. The radiation generated in different parts of the trajectory can overlap and interfere with each other which results in a discrete spectrum. Wigglers have the same magnetic structure as the undulators but with a strong magnetic field which results in a higher photon flux and more power. Due to the large angular excursion, the produced radiation cone is broader with respect to undulators and the radiation generated in different segments of the trajectory do not overlap. That results in no interference [15].

## 2.2.1 Electron Trajectory in an Undulator

The magnetic field inside an undulator can be calculated by solving the Maxwell's equations for a static magnetic field $\nabla \times B = 0$ and $\nabla \cdot B = 0$. Using this fact that the field can be written as the gradient of a scalar magnetic potential which satisfies Laplace's equation and assuming the undulator pole is much larger than the undulator period length $\lambda_u$, the magnetic field can be expressed by [16]:

$$
\begin{aligned}
B_x &= 0, \\
B_y &= -B_0 \cosh\left(k_u y\right) \sin\left(k_u z\right), \\
B_z &= -B_0 \sinh\left(k_u y\right) \cos\left(k_u z\right)
\end{aligned}
\tag{2.28}
$$

Here $B_0$ is the peak field on axis and $k_u = 2\pi / \lambda_u$ is the wavenumber of the undulator. The equation of motion of an electron in the electric and magnetic field is given by Lorentz force:

$$
\frac{dp}{dt} = -e(E + v \times B)
\tag{2.29}
$$

where $p = \gamma m v$ is the momentum, $e$ is the electron charge, $m$ is the electron mass, $v$ is the electron velocity, and $E$ and $B$ are the electric and magnetic fields, respectively. In the undulator the electron is deflected in the horizontal plane and the trajectory can be calculated by using the on-axis magnetic field on the symmetry plane $y = 0$

$$
B = -B_0 \sin\left(k_u z\right) \hat{y}
\tag{2.30}
$$

By solving the Lorentz force equation for the magnetic field above and assuming $E = 0$ and $v = v_z = c = Const.$, the electron's transverse velocity, to the first order, can be written as

$$v_x(z) = \frac{Kc}{\gamma} \cos(k_u z) \tag{2.31}$$

Here $K$ is known as undulator parameter which shows the magnetic strength of such a periodic structure and defined as

$$K = \frac{eB_0}{mck_u} \tag{2.32}$$

using the speed of light in vacuum $c$. As the electron moves on a sinusoidal orbit along the undulator the angle that it makes with longitudinal axis $z$, is given by

$$\theta_d \simeq \frac{K}{\gamma} \cos(\frac{2\pi z}{\lambda_u}) \tag{2.33}$$

and the maximum angle of such an excursion is

$$\theta_{d,\max} \simeq \frac{K}{\gamma} \tag{2.34}$$

Regarding this point that the radiation is emitted into a cone of angle of about $1/\gamma$, it is clear that for an undulator with $K \leq 1$ the electron angular excursions stay within the radiation cone and radiations from various parts of the trajectories can overlap in space and interfere after propagation. For the case that $K \gg 1$ the maximum angle will go beyond the radiation cone angle and there is no interference effect. This case is referred to as wiggler radiation.

Since the electron takes a sinusoidal trajectory along the undulator the longitudinal component of velocity is not constant. The average axial (longitudinal) velocity is given by [15, 16]

$$\overline{v}_z = (1 - \frac{1}{2\gamma^2}(1 + \frac{K^2}{2}))c \tag{2.35}$$

So, the second-order particle trajectory is expressed by

$$x(t) = \frac{K}{\gamma k_u} \sin(\overline{v}_z k_u t),$$

$$z(t) = \overline{v}_z t - \frac{K^2}{8\gamma^2 k_u} \sin(2\overline{v}_z k_u t) \tag{2.36}$$

## 2.2.2 Undulator equation

Considering the frame that moves with electron in the undulator, the electron experiences an oscillation with contracted period

$$\lambda' = \lambda_u / \gamma \tag{2.37}$$

and starts radiation. The frequency of this radiation in the co-moving frame is

$$f' = \frac{c}{\lambda'} = \frac{c\gamma}{\lambda_u} \tag{2.38}$$

In the laboratory frame of reference due to the Doppler shift the radiation frequency at small observation angles off- axis ($\theta \neq 0$) changes by

$$f = \frac{2c\gamma^2}{\lambda_u(1+\gamma^2\theta^2)} \tag{2.39}$$

Translating the frequency to the observation wavelength $\lambda = f / c$, to the first order yields

$$\lambda = \frac{\lambda_u}{2\gamma^2}(1+\gamma^2\theta^2) \tag{2.40}$$

By taking into account the second order correction for the longitudinal velocity, equation (2.35), an effective relativistic factor can be introduced as

$$\gamma_m = \frac{\gamma}{\sqrt{1+K^2/2}} \tag{2.41}$$

and we can get the modified form of equation (2.40) by substituting the effective relativistic factor $\gamma_m$ instead of $\gamma$ which leads to the undulator equation

$$\lambda = \frac{\lambda_u}{2\gamma^2}(1+\frac{K^2}{2}+\gamma^2\theta^2) \tag{2.42}$$

From this equation we can see that the undulator radiation wavelength can be tuned through variation of undulator period $\lambda_u$, the beam energy $\gamma$, and the undulator parameter $K$. Also, there is a red-shift due to the off-axis radiation with increasing observation angle $\theta$. It should be noted that regarding wavelength tuning, changing the magnetic field amplitude (i.e. undulator parameter) is the most convenient way and it can be done either by changing the magnet gap (in case of permanent magnet setup) or changing the applied current (in case of electromagnets). Due to the longitudinal velocity oscillation, higher harmonics are present. The harmonics wavelengths scale as $\lambda_1 / n$ where $\lambda_1$ is the fundamental radiation wavelength

and $n$ is the harmonic number. The importance of using higher harmonics is more evident specially in free-electron lasers (FELs) developing towards the shorter wavelength ranges [17].

## 2.2.3 Properties of the Undulator Radiation

The bandwidth of the undulator radiation can be calculated by considering that an electron which goes through an undulator with $N_u$ periods makes $N_u$ oscillations and the resulting wave train has $N_u$ cycles in time domain. The frequency spectrum of this wave train (natural bandwidth) can be obtained by Fourier transformation [16, 19, 24, 25]

$$\frac{\Delta\omega}{\omega} = \frac{\Delta\lambda}{\lambda} \approx \frac{2.8}{\pi N_u} \approx \frac{1}{N_u} \tag{2.43}$$

Confining the undulator radiation in the natural bandwidth we can estimate the natural angular width of a Gaussian beam for the first harmonic as

$$\sigma_\theta = \frac{1}{\gamma}\sqrt{\frac{1+K^2/2}{2N_u}} = \sqrt{\frac{\lambda}{L_u}} \tag{2.44}$$

where $L_u$ is the length of the undulator. The above equation shows a reduction in the first harmonic of the undulator radiation by a factor of $\sqrt{N_u}$ respect to the opening angle of synchrotron radiation typically $\sim 1/\gamma$. The photon beam emittance $\varepsilon_l$ emitted by a single electron is given by [22]

$$\varepsilon_l = \sigma_r\sigma_\theta = \frac{\lambda}{4\pi} \tag{2.45}$$

Natural radiation beam size can be calculated by using the natural radiation beam divergence, equation (2.44) and equation (2.45)

$$\sigma_r = \frac{\sqrt{\lambda L_u}}{4\pi} \tag{2.46}$$

Besides the natural broadening of the radiation, there are some other effects like emittance, energy spread of the electron beam and the undulator magnetic field errors that widen the undulator bandwidth and reduce the radiation intensity. The total radiation bandwidth including these effects is given by[1] [25]

$$\frac{\Delta\lambda}{\lambda} \approx 2\frac{\Delta\gamma}{\gamma} + \frac{\gamma^2\sigma_{x,y}'^2}{1+K^2/2} + \frac{2K^2}{1+K^2}\frac{\Delta K}{K} \tag{2.47}$$

---

[1] Assuming that the wavelength variation be smaller than the natural bandwidth of the undulator radiation

where $\sigma'_{x,y}$ is the electron beam divergence. The first term in equation (2.47) shows the energy spread effect on broadening of the spectrum. The second term represents the effect of angular divergence of the electron beam and the third term is related to the undulator magnetic field or undulator period errors that also can be regarded as bandwidth broadening due to the vertical beam size (for short period undulator with small gaps).

## 2.2.3.1 Undulator Angular flux Distribution

The spectral angular flux distribution is defined as the energy radiated by the electron per solid angle $\Omega$ into a particular frequency band $d\omega$, and is expressed as

$$\frac{d^2W}{d\Omega d\omega} = 2\varepsilon_0 cR^2 \left| E(\omega) \right|^2 \tag{2.48}$$

Here $W$ is the radiated energy, $\varepsilon_0$ is the permittivity in vacuum, $R$ is the distance from radiation source, and $E(\omega)$ is the electric field of the radiation. In the far-field approximation i.e. $R$ does not vary with time, the on-axis flux density ($\theta=0$) for the first harmonic can be estimated by (for the detailed calculation see Ref. [24])

$$\frac{d^2W}{d\Omega d\omega}\bigg|_{\theta=0} = \frac{e^2 N_u^2 \gamma^2}{4\pi\varepsilon_0 c} L\left(\frac{N_u \Delta\omega}{\omega}\right) F(K) \tag{2.49}$$

where $L\left(\dfrac{N\Delta\omega}{\omega}\right)$ is defined as so-called lineshape function

$$L\left(\frac{N\Delta\omega}{\omega}\right) = \frac{\sin^2(\frac{N\pi\Delta\omega}{\omega})}{N^2 \sin^2(\frac{\pi\Delta\omega}{\omega})} \tag{2.50}$$

and $F(K)$ is the on-axis angular energy distribution function

$$F(K) = \frac{K^2}{(1+K^2/2)^2} \left( J_1(\frac{K^2}{4(1+K^2/2)}) - J_0(\frac{K^2}{4(1+K^2/2)}) \right)^2 \tag{2.51}$$

with $J_0$ and $J_1$ as the Bessel functions of zeroth and first order, respectively. The equation (2.49) can be converted to the on-axis angular flux density i.e. the number of photons per mrad² per second per 0.1% bandwidth on-axis for the first harmonic for a planar undulator that in practical units is expressed as

$$\frac{d\dot{N}}{d\Omega}\bigg|_{\theta=0} [ph/s/mrad^2/0.1\%BW] = 1.74 \times 10^{14} N_u^2 E^2[GeV] I_b[A] F(K) \tag{2.52}$$

# 2.3 FEL Theory

The synchrotron radiation in an undulator is produced when electrons take an oscillatory trajectory due to the periodic magnetic field. For certain beam parameters and long enough interaction distance the radiated field can interact with the electrons, leading to an amplification of radiation. The process starts with an energy exchange between electrons and the co-propagating radiation field that makes a density modulation of electrons in the bunch on the scale of radiation wavelength. This process is called microbunching and results in an increase of coherent radiation. It can be regarded as macroparticles with charge $Q = Ne$ where $N$ is the number of electrons, which are concentrated into regions smaller than the radiation wavelength. Since for a fully bunched electron beam the radiation intensity scales with $N^2$, the radiation filed and the intensity of the radiation field grows exponentially as the electron microbunching increases along the undulator. It should be noted that the radiation intensity for the random spontaneous emission (like the undulator radiation) increases linearly along the undulator and scales like $N$. A sketch of microbunching and power growth inside an undulator is illustrated in Fig. 4.2.

In general, there are two modes of operation for an FEL regarding the initial amplification process: SASE FELs and Seeded FELs. In SASE (self-amplified spontaneous emission) case the spontaneous undulator emission in the first periods of a long undulator can start the FEL process. It also can be explained by existing white noise fluctuations in a bunch of random (uncorrelated) electrons, commonly called shot noise [16, 18]. For seeded FEL, the FEL process is initialized by an external coherent radiation source at the desired radiation wavelength (or a sub-harmonic in case of HGHG or EEHG [16]). Providing a high power external source at the resonance wavelength as a seed pulse can be done by using the FEL pulse itself as a seed pulse in a two-stage amplification process, which is known as a self-seeded FEL.
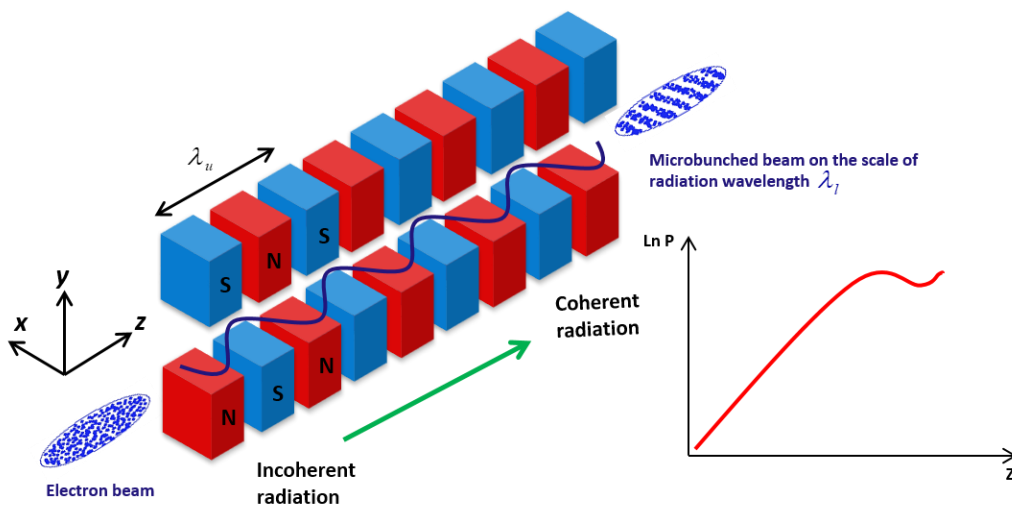


Figure 4.2: The power growth in the undulator due to the microbunching effect.

# 2.3.1 One Dimensional Theory of High-Gain FEL

In this section, to study the high-gain FEL we assume that the bunch charge density and radiation fields have no dependency on transverse coordinates x and y. Also, the electron bunch is considered to be infinitely long. The term high-gain is used in FEL physics when the amplification of radiation is achieved in a single pass through a long undulator unlike in the low-gain theory case where a small amplification occurs per pass through the undulator and the bunch needs to make many turns to let the radiation reach high output power [16]. The subsequent description of FEL theory closely follows the representation in Ref. [16].

## 2.3.1.1 FEL Resonance Condition

The change in the electron energy that takes an oscillation motion through an undulator and interacting with its own emitted radiation that co-operates with the electron is given by

$$\frac{d(\gamma mc^2)}{dt} = Fv = -e\,v_x(t)E_x(t) \tag{2.53}$$

Assuming $E_x(t) = E_{0x}cos\left(k_l z - \omega_l t + \phi_0\right)$ as the electric field of the co-operating radiation field and using above equation leads to:

$$\begin{aligned}\frac{d\gamma}{dt} &= -\frac{eKE_{0x}}{2\gamma mc}[\cos\left((k_u + k_l)z - \omega_l t + \phi_0\right) + \cos\left((k_u - k_l)z - \omega_l t + \phi_0\right)] \\ &= -\frac{eKE_{0x}}{2\gamma mc}[\cos\Phi + \cos\Theta]\end{aligned} \tag{2.54}$$

where $k_l$ is the wave number of radiation, $\omega_l$ is the radiation frequency and, $\phi_0$ is the phase offset between the radiation and sinusoidal trajectory of the electron. Here we defined the pondermotive phase as

$$\Phi = (k_u + k_l)z - \omega_l t + \phi_0 \tag{2.55}$$

It can be regarded as a longitudinal coordinate inside the bunch that characterizes the electron position relative to the phase of the radiation. Neglecting the second term in equation (2.54) (it can be expressed in terms of pondermotive phase and an oscillating term which has an average equal to zero per undulator period), it is clear that in order to have a constant energy transfer from the electrons to the radiation the pondermotive phase must remain constant i.e.

$$\frac{d\Phi}{dt} = (k_u + k_l)\bar{v}_z - \omega_l = 0 \tag{2.56}$$

Using the equation (2.35) for the average velocity and solving the above equation for the radiation wavelength we can obtain the resonance condition of the FEL as

$$\lambda = \frac{\lambda_u}{2\gamma^2}(1+\frac{K^2}{2}) \tag{2.57}$$

The interesting point is that the resonance condition gives the exactly the same radiation wavelength as the spontaneous undulator radiation at $\theta = 0$. Now it is clear why the spontaneous emission in the first undulator periods can start the FEL amplification process.

## 2.3.1.2 The Coupled First-Order Equations

In the High-gain regime the energy exchange between the electron and the radiation occurs in a single pass through the undulator and the radiation field amplitude grows considerably along the undulator and cannot be taken as a constant. Hence, we assume the electric field in the form of

$$\tilde{E}_x(z,t) = \tilde{E}_{0x}(z)\exp(i(k_l z - \omega_l t)) \tag{2.58}$$

Here $\tilde{E}_{0x}(z)$ is the complex field amplitude. By taking $\phi_0 = 0$ in the pondermotive phase, the initial position of the electron inside the bunch can be expressed with respect to the radiation field. Taking into account that the interaction between the electron and the radiation field leads to a periodic density modulation of the electron bunch, the current density can be expressed as

$$\tilde{J}_x(\Phi, z) = J_0 + \tilde{J}_1(z)\exp(i\Phi) \tag{2.59}$$

This equation for the current density and the equation (2.58) for the electric field can be inserted into the wave equation

$$[\frac{\partial^2}{\partial z^2} - \frac{1}{c^2}\frac{\partial^2}{\partial t^2}]\tilde{E}_x(z,t) = \mu_0 \frac{\delta \tilde{J}_x}{\delta t} + \frac{1}{\varepsilon_0}\frac{\partial \tilde{\rho}_x}{\partial x} \tag{2.60}$$

The transverse current density in equation (2.59) can be written in terms of the longitudinal one

$$\tilde{J}_x = \tilde{J}_z v_x / v_z \tag{2.61}$$

Neglecting the transverse dependence of the charge density (the transverse current density cannot be neglected due to the sinusoidal motion of the electron beam in the undulator) and also using the slowly varying amplitude (SVA) approximation leads to

$$\frac{d\tilde{E}_x}{dz} = -\frac{\mu_0 cK}{4\gamma}\tilde{J}_1(z) \tag{2.62}$$

Taking into account the z-dependence of the radiation field and also the longitudinal space charge field due to the charge density modulation, the energy-transfer, equation (2.53) can be expressed as

$$\frac{d\eta}{dz} = -\frac{e}{mc^2\gamma}\Re[(\frac{K_{jj}\tilde{E}_x}{2\gamma} + \tilde{E}_z)\exp(i\Phi)] \tag{2.63}$$

where $\eta = (\gamma - \gamma_r)/\gamma_r$ is the relative energy deviation with respect to the resonance energy (detuning) and $\gamma_r$ is the resonance energy. Here we used the modified undulator parameters $K_{jj}$:

$$K_{jj} = K[J_0(\frac{K^2}{4+2K^2}) - J_1(\frac{K^2}{4+2K^2})] \tag{2.64}$$

which takes the longitudinal velocity oscillation into account with $J_0$ and $J_1$ as the Bessel functions of zeroth and first order, respectively. Replacing the longitudinal space charge field $\tilde{E}_z$ by applying the Maxwell equation, then we can write the complete set of one-dimensional FEL equations as

$$\frac{d\Phi_n}{dz} = 2k_u\eta_n,$$

$$\frac{d\eta_n}{dz} = \frac{-e}{mc^2\gamma}\Re[(\frac{K_{jj}\tilde{E}_x}{2\gamma} - \frac{i\mu_0 c^2 \tilde{J}_1(z)}{\omega_l})\exp(i\Phi_n)]$$

$$\frac{d\tilde{E}_x}{dz} = -\frac{\mu_0 c K_{jj}}{4\gamma}\tilde{J}_1(z)$$

$$\tilde{J}_1(z) = \tilde{J}_0 \frac{2}{N}\sum_{n=1}^{N}\exp(-i\Phi_n)$$

$$\tag{2.66}$$

where $n = 1\ldots N$ denotes the individual particle within one radiation. This set of $2N+2$ coupled differential and algebraic equations describes the evolution of the electron beam energy and phase, as well as the evolution of the field amplitude as the electron travels through the undulator.

## 2.3.2 The Third-Order Equation

Due to the large number *N* of the electrons, the above equations cannot be solved analytically and so numerical methods must be used. To have an analytical solution we can assume that the periodic density modulation remains small and the quantities $\Phi_n$ and $\eta_n$ can be eliminated, giving a third-order differential equation as [16]

$$\frac{\tilde{E}_x'''}{\Gamma^3} + 2i\frac{\eta}{\rho}\frac{\tilde{E}_x''}{\Gamma^2} + ((\frac{K_p}{\Gamma})^2 - (\frac{\eta}{\rho})^2)\frac{\tilde{E}_x'}{\Gamma} - i\tilde{E}_x = 0 \tag{2.67}$$

Here $\Gamma$ is the gain parameter, $K_p$ is the space charge parameter and $\rho$ is the FEL parameter (Pierce parameter) that are defined as [16, 17]

$$\Gamma = \left( \frac{\mu_0 \pi e^2 n_e K_{jj}^2}{2m\gamma^3 \lambda_u} \right)^{1/3} \tag{2.68}$$

$$K_p = \left( \frac{4\mu_0 \pi e^2 n_e c}{m\gamma \lambda_u \omega_l} \right)^{1/2} \tag{2.69}$$

$$\rho = \frac{\Gamma \lambda_u}{4\pi} = \frac{1}{4\gamma}\left( \frac{I_P}{I_A}(\frac{K_{jj}\lambda_u}{\pi\sigma_r})^2 \right)^{1/3} \tag{2.70}$$

where $n_e$ is the electron density, $I_p$ is the peak current, $I_A \approx 17 KA$ is the Alfven current, and $\sigma_r$ is the rms transverse beam size in the undulator. The FEL parameter is the fundamental parameter of FEL. The main characteristics of the high-gain FEL systems can be described by ρ which is a dimensionless scaling parameter. It is a measure for the conversion efficiency from the power stored in the electron beam into the FEL radiation power.

The third-order equation can be simplified by assuming that the electron beam is on resonance $\eta = 0$, and neglecting the space-charge effect $K_p$=0 (that is a reasonable assumption for high energy beams)

$$\tilde{E}_x''' - i\Gamma^3 \tilde{E}_x = 0 \tag{2.71}$$

This equation can be solved for a trial function $\tilde{E}_x(z) = A\exp(\alpha z)$ with the solutions of the form

$$\alpha_1 = \frac{(i+\sqrt{3})\Gamma}{2}, \qquad \alpha_2 = \frac{(i-\sqrt{3})\Gamma}{2}, \qquad \alpha_3 = -i\Gamma \tag{2.72}$$

If we suppose that the FEL process starts by an initial monochromatic light field of the form

$$E_x(z,t) = E_{in}cos\left(k_l z - \omega_l t\right) \tag{2.73}$$

and using equation (2.61), the evolution of the FEL radiation wave is

$$\tilde{E}_x(z) = \frac{E_{in}}{3}(\exp(\frac{(i+\sqrt{3})\Gamma z}{2}) + \exp(\frac{(i-\sqrt{3})\Gamma z}{2}) + \exp(-i\Gamma z)) \tag{2.74}$$

which shows an exponential growth after a certain distance. Since $P(z) \propto \left|\tilde{E}_x(z)\right|^2$ we can express the radiation field power growth for $z \gg \Gamma^{-1}$ as

$$P(z) \cong \frac{P_{in}}{9} exp(z/L_{g0}) \tag{2.75}$$

Here we defined the power gain length as

$$L_{g0} = 1/\sqrt{3}\Gamma = \frac{\lambda_u}{4\pi\sqrt{3}\rho} \tag{2.76}$$

which determines the length over which the radiation field power grows by a factor of e (e-folding length). In some cases, the field gain length is defined as two times the power gain length. It must be noted that the index "0" shows that the above gain length is the one-dimensional gain length neglecting space charge forces. The exponential growth of the radiation field stops after some gain lengths and the intensity of the radiation stays more or less constant. Furthermore, electrons start to extract energy from the radiation field that results in oscillations of the radiation energy. Assuming maximum current density modulation $\left|\tilde{J}_1\right| \approx \left|J_0\right|$ at saturation and using equation (2.62) for one field gain length, the saturation power can be estimated as [16]

$$P_{sat} \approx \rho P_b \tag{2.77}$$

where $P_b = \gamma mc^2 I_p / e$ is the beam power. According to Ref. [17] the saturation distance can be approximated by a numerical factor times the power gain length. The numerical factor typically varies little from 16 to 20. So, the saturation length can be estimated by

$$L_{sat} \approx \frac{\lambda_u}{\rho} = 4\pi\sqrt{3}L_{g0} \tag{2.78}$$

After saturation the intensity of the radiation stays approximately constant. However, it is possible to gain more energy from the electron beam after saturation by reducing the undulator parameter K along the undulator to maintain the resonance condition [20].

## 2.3.3 Degrading Effects

In this section we explain the most important degrading effects like energy spread, the finite beam emittance and radiation diffraction. Including these degrading effects results in increasing the 1D gain length calculated in previous section for a mono-energetic beam. Deviations of the gain length from the ideal 1D limit, show to what extent these effects play a role in the FEL dynamics. Combining above degrading effects a fitting formula[2] has been derived by Xie [21] which expresses the 3D gain length of an x-ray FEL in terms of 1D gain length using the degradation factor $\Lambda$:

$$L_g = L_{g0}(1+\Lambda) \tag{2.79}$$

---

[2] Space charge is assumed to be negligible and detuning is optimized.

| | | | |
|---|---|---|---|
| $\alpha_1 = 0.45$ | $\alpha_6 = 2$ | $\alpha_{11} = 0.95$ | $\alpha_{16} = 1140$ |
| $\alpha_2 = 0.57$ | $\alpha_7 = 0.25$ | $\alpha_{12} = 3$ | $\alpha_{17} = 2.2$ |
| $\alpha_3 = 0.55$ | $\alpha_8 = 2.9$ | $\alpha_{13} = 5.4$ | $\alpha_{18} = 2.9$ |
| $\alpha_4 = 1.6$ | $\alpha_9 = 2.4$ | $\alpha_{14} = 0.7$ | $\alpha_{19} = 3.2$ |
| $\alpha_5 = 3$ | $\alpha_{10} = 51$ | $\alpha_{15} = 1.9$ | |

Table 2.1: Coefficients for the scaling function in equation (2.80).

The degrading factor or scaling function is expressed in terms of three scaled parameters: $\eta_\gamma$ energy spread, $\eta_\varepsilon$ emittance and $\eta_d$ diffraction. It is given by

$$
\begin{aligned}
\Lambda = {} & \alpha_1 \eta_d^{\alpha_2} + \alpha_3 \eta_\varepsilon^{\alpha_4} + \alpha_5 \eta_\gamma^{\alpha_6} \\
& + \alpha_7 \eta_\varepsilon^{\alpha_8} \eta_\gamma^{\alpha_9} + \alpha_{10} \eta_d^{\alpha_{11}} \eta_\gamma^{\alpha_{12}} + \alpha_{13} \eta_d^{\alpha_{14}} \eta_\varepsilon^{\alpha_{15}} \\
& + \alpha_{16} \eta_d^{\alpha_{17}} \eta_\varepsilon^{\alpha_{18}} \eta_\gamma^{\alpha_{19}}.
\end{aligned}
\tag{2.80}
$$

The scaled parameter $\eta_\gamma$ is the ratio of relative energy spread $\sigma_\eta$ and the FEL parameter

$$
\eta_\gamma = \frac{4\pi\sigma_\eta L_{g0}}{\lambda_u} = \frac{1}{\sqrt{3}} \frac{\sigma_\eta}{\rho}
\tag{2.81}
$$

A typical requirement for the tolerable rms energy spread can be expressed as

$$
\frac{\sigma_\eta}{\rho} < \frac{1}{2}
\tag{2.82}
$$

It gives the condition that the spread of the resonance wavelength due to the energy spread is less than the natural FEL bandwidth[3] [19].

The next scaled parameter $\eta_\varepsilon$ takes into account the emittance effect that for a constant beta function $\bar{\beta}$, is given by

$$
\eta_\varepsilon = \frac{4\pi\varepsilon L_{g0}}{\bar{\beta}\lambda_l}
\tag{2.83}
$$

The effect of emittance can be explained by the fact that the transverse velocity components of a beam with a finite emittance lead to a reduction of the average longitudinal velocity in equation (2.35) as [16]

$$
\bar{v}_z^\beta = (1 - \frac{1}{2\gamma^2}(1 + \frac{K^2}{2}))c - \frac{\varepsilon}{\bar{\beta}}c
\tag{2.84}
$$

---

[3] The bandwidth of the FEL is given by the FEL parameter ~ρ.

This reduction can be translated to an equivalent energy spread

$$\left(\sigma_\eta\right)_{eq} \approx \frac{\gamma^2 \varepsilon}{\bar{\beta}} \tag{2.85}$$

Taking into account the actual energy spread of the beam and using equation (2.62), an upper limit for the beam emittance can be obtained

$$\varepsilon < \frac{\bar{\beta}}{2\sqrt{2}\gamma^2} \rho \tag{2.86}$$

Also, by defining an emittance for a Gaussian light beam equation (2.45), and having the beam emittance in the range of radiation emittance, a general emittance criterion can be estimated as

$$\varepsilon \leq \frac{\lambda_l}{4\pi} \tag{2.87}$$

Thus, for the short wavelength FEL satisfying the emittance requirement would be more challenging.

The diffraction scaled parameter $\eta_d$, is the ratio of 1D gain length and Rayleigh length:

$$\eta_d = \frac{L_{g0}}{2S_R} \tag{2.88}$$

Here the Rayleigh length $S_R$ is defined as the length over which the beam cross section doubles[4]:

$$S_R = \frac{\pi\sigma_r^2}{\lambda_l} \tag{2.89}$$

It is important to have a good overlap of electrons and radiation field to increase the energy transfer. The widening of the radiation field can be compensated by reducing the gain length. Since both Rayleigh length and the gain length depend on the transverse beam size, there is a compromise that is given by

$$S_R \geq 2L_{g0} \tag{2.90}$$

Using equation (2.79) for 3D gain length, the saturation power can be estimated by [23]

$$P_{sat} = 1.6\rho\left(\frac{L_{g0}}{L_g}\right)^2 P_b \tag{2.91}$$

The saturation length is then determined by

---

[4] Since the electrons act as radiation source we use the electron transverse beam size $\sigma_r$.

$$L_{sat} = L_g \ln(\frac{9P_{sat}}{P_0})$$ (2.92)

where $P_0 = \gamma mc^3 \rho / \lambda$ is the SASE power [26].

The Xie fitting formula gives the advantage of having a quick estimation of FEL performance without numerical simulation and it is widely used in the FEL field as a preliminary tool for setup optimization and for choosing working points.

# 2.4 Laser Wakefield Accelerators

Laser wakefield accelerators (LPAs) use the enormous electric fields (100 GV/m) formed within plasma waves to accelerate charged particles to high energies in a fraction of distance needed in a conventional particle accelerator. The idea of using plasma to accelerate particles was proposed by Tajima and Dawson in 1979 [27]. They showed that an intense laser pulse can generate a wake of plasma oscillation through the non-linear ponderomotive force associated to the laser pulse. Electrons then can be accelerated through the very high electric field sustained by relativistic plasma waves driven by the laser. The longitudinal electric field in the plasma wave can be more than three orders of magnitude larger than that found in conventional radio frequency (RF) accelerators. Particles injected into the correct phase of the plasma wave can be accelerated to energies of order 1 GeV in only a few tens of millimetres. The plasma can be regarded as a converter which converts the transverse electric field of the laser pulse into a longitudinal accelerating field using the wake field generated by ponderomotive force. In this chapter the basic principle of Laser wakefield acceleration is very quickly reviewed.

## 2.4.1 Basic Concept

The process of acceleration is depicted in Fig. 5.2. When a high-power laser is passed through plasma the pondermotive force which is formed pushes the electron away from the front and back of the pulse thereby forming a trailing longitudinal density wave[5]. This pondermotive force in terms of normalized electromagnetic vector potential *a* is given by [28]

$$F_p = -\frac{mc^2}{2}\nabla a^2$$ (2.93)

---

[5] Here we consider the case that the electron bunch generated from the electrons inside the plasma by the intense enough driver lasers that is referred to the bubble regime. The electrons inside the plasma cannot get trapped if the intensity of the laser is not high enough. In this case an external source of electron is needed.
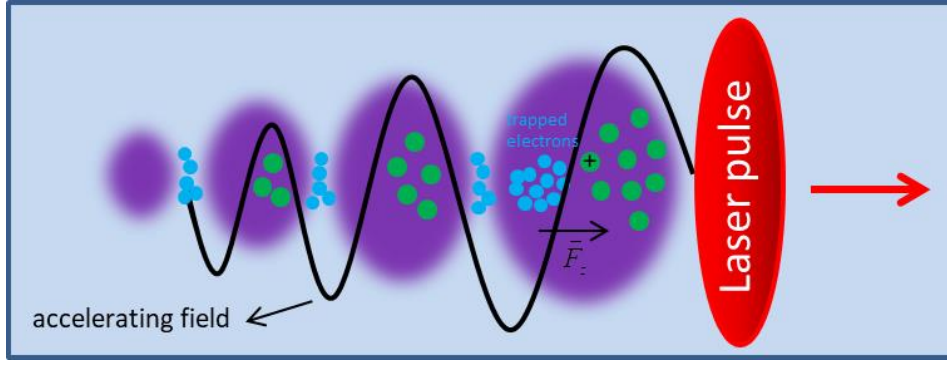
Figure 5.2: Propagation of laser pulse and generating axial electric field inside the plasma leads to an accelerating force in the direction of driving pulse.

where $a = eA/mc$. Ponderomotive motion for positive charges (heavy ions) can be neglected since it decreases quadratically with particle mass. The electrons experience a backward force because of the positively charged ions and then they start to oscillate with respect to their initial position. The frequency of that oscillation is known as plasma frequency

$$\omega_p^2 = \frac{e^2 n_0}{m\varepsilon_0} \tag{2.94}$$

with $n_0$ being the electron plasma density. These waves propagate near light speed behind the laser pulse with the wavelength approximately equal to the plasma wavelength [28, 29]

$$\lambda_p = \frac{2\pi c}{\omega_p} \approx 3.3 \times 10^{10} / \sqrt{n_0(cm^{-3})} \ [\mu m] \tag{2.95}$$

Only at one half of the wave the electron bunch is accelerating and in the other half it is decelerating so the length of the acc. bucket will be $\lambda_p / 2$ and the plasma-based accelerator would require a bunch duration $\tau_b < \lambda_p / c$. This shows that a femtosecond laser pulse produces femtosecond electron bunches. The axial electric field gradient on the laser axis due to the separation of the electrons and ions in the plasma wave can extend to 100 GV/m. An estimation of the field in a plasma is given by

$$E_0 [V/m] \approx 96 \sqrt{n_0 [cm^{-3}]} \tag{2.96}$$

This axial field can be used to accelerate electron bunches. The accelerated electron bunches can be formed inside the plasma (through the so-called self-injection process) with a high intensity laser or they can be injected externally behind the laser pulse. By increasing the plasma density, the accelerating gradient increases but the accelerating period becomes shorter.

The electron beam can also generate its own wake. As a consequence, the wake field generated by the laser can be perturbed and the acceleration gradient will be reduced. This effect is known as beam loading. Beside the beam loading the maximum energy gain is limited due to some factors like: laser diffraction, dephasing of the electrons and pump depletion [28]:

**Diffraction**: The peak amplitude of the laser pulse in the plasma decreases due to diffraction. Therefore, without any laser guiding the effective acceleration length will be limited to some distance on the order of the Rayleigh length.

**Electron dephasing:** Due to the velocity difference between the plasma wave and the relativistic electrons, the trapped electrons will overtake the wave and reach the decelerating region.

**Pump depletion:** The wakefield amplitude decreases as the laser pulse loses energy due to transferring its energy to the plasma wave. This effect is characterized by the pump depletion length that is the distance over which the pump loses a significant fraction of its energy.

# Chapter 3

# TGU Experiment at SINBAD

## 3.1 The SINBAD Facility

SINBAD (**S**hort **IN**novative **B**unches and **A**ccelerators at **D**ESY) is a dedicated, long-term accelerator research and development (R&D) facility and foreseen to host multiple independent experiments including production of ultra-short electron bunches and testing advanced acceleration techniques [11]. In the first stage, SINBAD will have two independent experiments: ARES (**A**ccelerator **R**esearch **E**xperiment at **S**INBAD) and AXSIS (Frontiers in **A**ttosecond **X**-ray **S**cience: **I**maging and **S**pectroscopy). The goal of the AXSIS project is to demonstrate a compact attosecond X-ray light source based on a fully THz-driven accelerator 30]. The ultra-compact, THz-driven, dielectric-loaded gun and traveling-wave structures will be used to generate and accelerate electron bunches. The electrons then are focused and collide with a high-power laser to create photons by coherent inverse Compton scattering. ARES is a conventional S-band linear RF accelerator that can provide low charge; short electron bunches, with excellent arrival-time stability and with the energy of 100 MeV [31, 32]. It consists of an S-band RF photoinjector and two S-band traveling wave structures (TWSs). The maximum beam energy operating on-crest mode is about 150 MeV but concerning the needed chirp for the bunch compression the final beam energy would be around 100 MeV. A schematic view of the ARES linac is depicted in Fig. 3.1.

The ARES linac was originally planned to provide beam for various experiments such as laser wakefield acceleration (LWFA), dielectric laser acceleration (DLA) and transverse gradient undulator (TGU) studies. In a future upgrade a third TWS was planned to be installed enabling an energy upgrade to 230 MeV when all three TWSs are operated on crest. Furthermore, a movable magnetic chicane is being designed and will be installed in the beamline. It supports t-
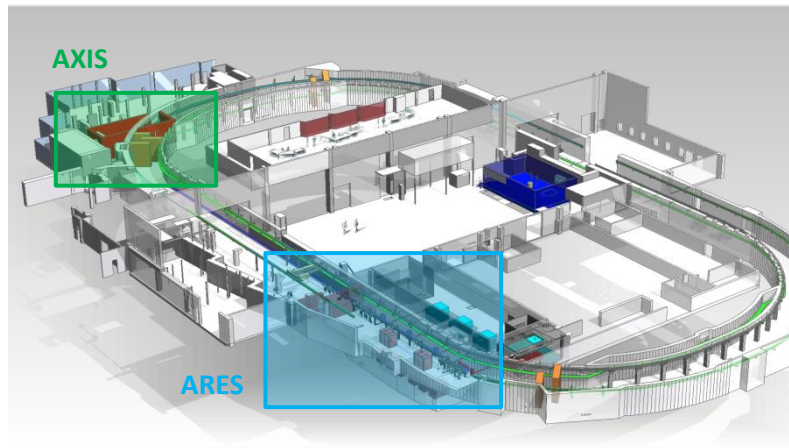
Figure 3.1: Overview of the SINBAD facility.

-he formation of femtosecond to attosecond bunches in the ARES linac which was planned to be optimized for external injection into a laser -driven plasma accelerator stage. Also, a second beamline (dogleg section) was planned to be added to the ARES beamline to inject the compressed electron bunches to a second experimental area. The current setup of the ARES linac and the current installation of ARES RF photoinjector are shown in Fig. 3.2 and Fig. 3.3, respectively [33]. The TGU experiment was planned to be conducted in the dogleg section of the ARES linac. The electron bunches would be generated in the RF photoinjector and accelerated by two TWSs. Using quadrupoles and two dipoles in the beamline the electron beam was planned to be sent through the undulator. The required dispersion is provided by the dipoles and is controlled by the downstream quadrupoles. For the chromatic effect compensation, a sextupole is considered in the beamline between the dipoles. Also, two correctors (beam steerers) are placed just before the undulator to control the initial beam position inside it. At the end, the produced radiation would be detected by a spectrometer behind the undulator. The layout of the beamline and the setup of the experiment are introduced in detail in section 3.3. In the following sections, the basic working principle of a TGU and technical details of this device are presented.
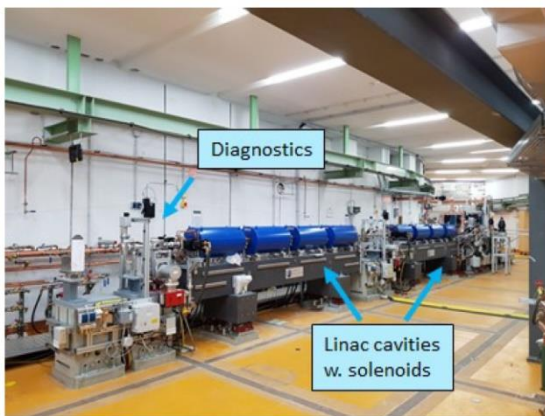


Figure 3.2:  Setup of the ARES linac.          Figure 3.3: ARES RF photoinjector.
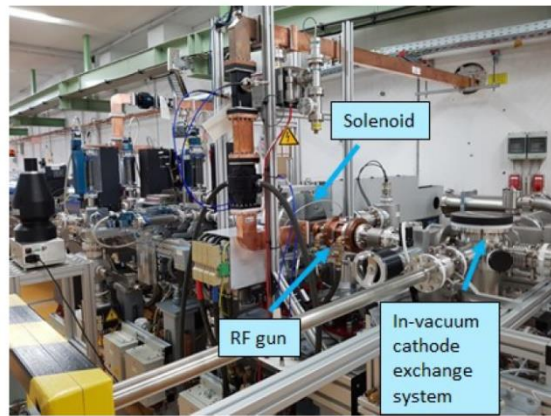
# 3.2 TGU Concept

Transverse Gradient Undulators were proposed in 1979 by Smith and collaborators as a scheme to reduce the effect of beam energy spread in FEL oscillators by introducing a transverse field gradient [9]. Although the idea at the beginning was proposed for low-gain FELs, it has been reconsidered in high-gain FEL concepts due to its ability to increase the FEL gain in the case of beams with large energy spread such as the beam from a laser-plasma accelerator (LPA) [10]. One of the main problems the LPA beams are suffering from is a large energy spread (1-10%) that results in FEL gain degradation. Combining the LPA that is capable to produce high energy, high peak current and low emittance beams with a TGU leads to possibility of having a compact x-ray FEL [34].

As we saw previously in section 2.2, when a monoenergetic beam passes through an undulator it starts emitting radiation at the resonance wavelength in the forward direction

$$\lambda = \frac{\lambda_u}{2\gamma^2}(1 + \frac{K^2}{2})$$

(3.1)

Considering a beam with a significant energy spread, the spectrum of the undulator radiation gets broadened and as a consequence the FEL gain decreases. The gain degradation can be explained by the process of exchanging energy and slippage distance between the electron and the radiation wave. The resonance condition i.e. the condition for sustained energy transfer from the electron to the radiation wave is satisfied when the radiation wave overtakes the electron in one undulator period by one resonant wavelength. The electron path inside the undulator can be described by its angle of excursion, $K / \gamma$. If there is a spread in average beam energies, the resonance condition would not be satisfied anymore and results in FEL gain degradation [16, 17] as shown in Fig. 3.4.
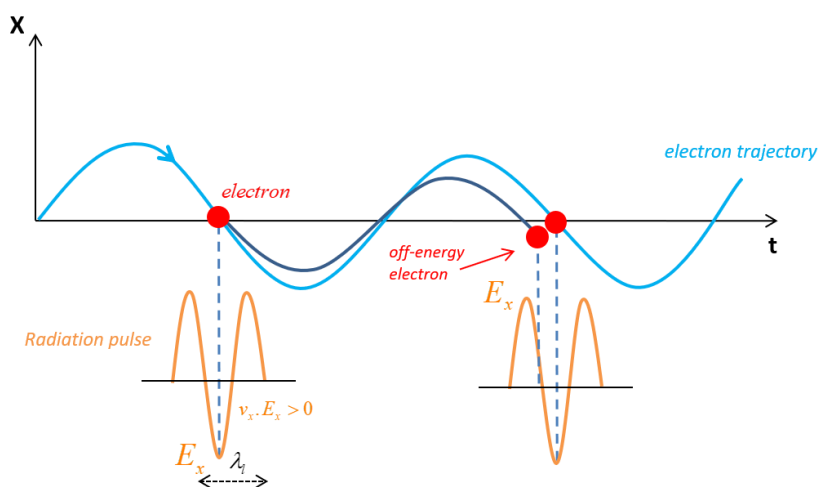


Figure 3.4:  Effect of energy spread on the resonance condition.

In order to compensate this effect, the scheme of a transverse gradient undulator was proposed. The idea is based on matching the electrons energy to the undulator magnetic field in a way that the resonance condition is satisfied for all particles. This can be done by introducing a linear transverse magnetic field gradient as

$$K(x) = K_0(1 + \alpha x)$$
(3.2)

where $K_0$ is the undulator parameter for the reference beam energy on-axis, $\gamma_0$ and $\alpha$ is the transverse gradient parameter. The electron energy can be a function of the transverse position x, by the dispersion function *D(s)*. By introducing some dispersion by a dispersive medium in particular a dipole, the electron's energy and position are correlated according to

$$x = D\delta = D\left(\frac{\gamma}{\gamma_0} - 1\right)$$
(3.3)

The energy $\gamma$, in the resonance condition can be eliminated by using equations (3.2-3) which in a linear approximation leads to an equation for a matched dispersion as

$$D = \frac{2 + K_0^2}{\alpha K_0^2}$$
(3.4)

Thus, by properly choosing the dispersion and keeping it constant along the TGU, the energy spread of the electron beam can be compensated and the resonance condition would be satisfied for electrons with different energies. Therefore, the modified undulator resonance equation for a transverse gradient undulator can be given by [35]

$$\lambda = \frac{\lambda_u}{2\gamma^2(x)}(1 + \frac{K^2(x)}{2}) \approx \text{constant}$$
(3.5)

The working principal of a TGU is depicted in Fig. 3.5.

## 3.2.1 TGU Layout

There are several possible geometries that can be used to generate a transverse magnetic field gradient. In the simplest case, the poles of the undulator are canted by an angle $\phi$ with respect to the x-z plane as shown in Fig. 3.5. The transverse gradient parameter $\alpha$ for a full can angle $2\phi$ is given by [10]

$$\alpha = 2\phi \frac{1}{K_0} \frac{\partial K_0}{\partial y} = 2\phi\left(\frac{5.47}{\lambda_u} - 3.6\frac{g}{\lambda_u^2}\right)$$
(3.6)

where g is the average gap of the canted poles. The maximum achievable transverse gradient
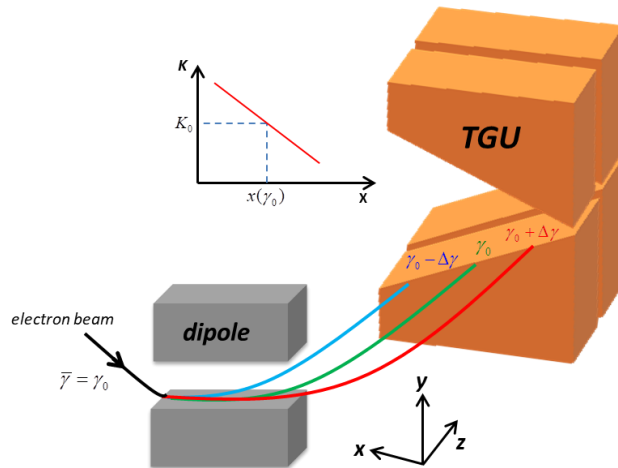
Figure 3.5: The working principal of a transverse gradient undulator with canted poles. Electrons with different energies enter the undulator at different transverse positions using a dipole. The energy of each particle is matched to the undulator field to satisfy resonance condition.

in this case is limited by an upper limit for the cant angle $\phi$ that for a realistic case is $\phi \leq 0.1$ rad [10, 36].

In Ref. [37] two possible geometries of a superconducting TGU were discussed. The first one is similar to the canted pole version but with superconducting (SC) wires. These SC wires are wound around the undulator poles which are tilted relative to the middle plane to produce the required field gradient. The second one is an undulator with cylindrical pole shape. In this case the curvature of the undulator coils produce the field gradient using SC wires wound around the two formers. Super conducting undulators (SCUs) can produce higher field amplitude than permanent magnet undulators for the same gap and period length. Also, by changing the current in the SC wires the undulator field strength can be changed without changing the undulator geometry. Moreover, the period length of the device in some special designs can be switched by changing the current direction in superconducting coils that are separately powered [38].

## 3.2.1.1 TGU40

The two above mentioned layouts were studied and investigated in detail at Karlsruhe Institute of Technology (KIT) by V. Afonso Rodriguez [39]. The goal was to develop and design a novel superconducting transversal gradient undulator (SCTGU) to create a compact radiation source with a laser wakefield accelerator. By optimization of both TGU models, the cylindrical TGU was chosen since higher transverse gradient can be achieved by this layout while keeping the relative deviation of radiation lower than the natural bandwidth i.e. $\Delta\lambda / \lambda < 1 / N_u$. Moreover, the required total dispersive beam splitting for a cylindrical TGU is much shorter ($\approx$ 4 mm) than the tilted version (> 10 mm).

| Parameter | Symbol | Value | Unit |
|---|---|---|---|
| Period Length | $\lambda_u$ | 10.05 | mm |
| Number of Periods | $N$ | 40 | - |
| Pole radius | $r$ | 30 | mm |
| Gap Width on symmetry axis | $g$ | 1.1 | mm |
| Gap Width at Beam Centre | $g(\gamma_0)$ | 2.4 | mm |
| Magnetic Field at Beam Centre | $B(\gamma_0)$ | 1.10 | T |
| Undulator Parameter at Beam Centre | $K(\gamma_0)$ | 1.078 | - |
| Undulator Transverse Gradient | $\alpha$ | 139.7 | 1/m |

Table 3.1: TGU40 parameters list.

Fig. 3.6 shows the full-scale prototype of the cylindrical TGU with 40 periods (TGU40) built at KIT. It consists of two cylindrical copper formers. Superconductor Niobium titanium Nb-Ti wires are wound on these two formers. The coil formers are supported by a copper support structure that basically defines the undulator gap. The TGU with the support structure is mounted inside a cryostat[1] with different thermal shields on the top of a plate heat exchanger as shown in Fig. 3.7. In order to keep the magnetic gap as small as possible the beam pipe is not foreseen in the layout [40, 41]. The main parameters of the TGU40 are given in Table. 3.1.

The TGU was originally built and optimized for an experimental test at the laser wakefield accelerator at the JETI high power laser at the university of Jena, Germany. Some further optimizations are needed to test it at SINABD with ARES linac. The major change will be changing the TGU gradient from vertically ($\hat{e}_y$) to horizontally ($\hat{e}_x$). In the current design as shown in Fig.3.6, a gradient is produced in vertical direction as it was needed for the beam line at Jena University with vertical dipoles. This gradient must be modified to a horizontal one sin-
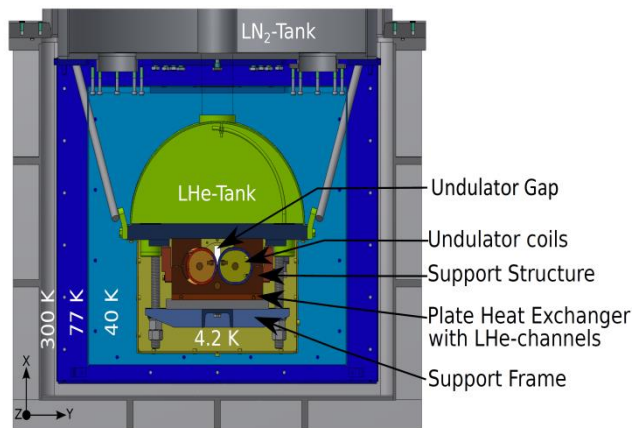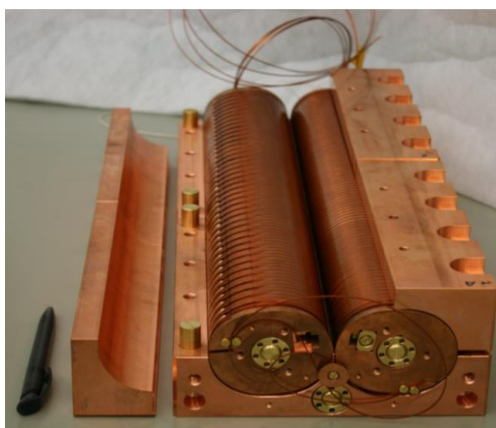


Figure 3.6: Prototype TGU40 in support frame [39].

Figure 3.7: Side view of the cryostat with TGU [39].

---

[1] The total length of the cryostat is 1.67 m. Mounting the TGU at the center, the distance from the center of the TGU to the entrance of the cryostat is 0.885 m.

-ce the dipoles in SINBAD beam line deflect the beam horizontally. Another optimization that should be considered here is the optimization for the correction coils (see section 3.2.3) for the reference beam energy of 80 MeV. In this thesis we assume that all these changes are done.

## 3.2.2 Magnetic Field calculation

The magnetic field of the cylindrical TGU can be estimated by assuming two infinitely long cylinders with external pole radius *r*, which are shifted by the undulator gap value *g*. Assuming a periodic potential in z-direction, the magnetic field for each cylinder can be calculated using Laplace's equation. The total magnetic field then can be approximated by the sum of the fields of both undulator halves [42]. For convenience we use cylindrical coordinates $(\rho, \phi, z)$ to calculate the undulator fields in the way that the two cylinders have their axis in different cylindrical coordinate system, upper and lower that are indexed by *u* (upper) and *l* (lower), respectively as shown in Fig. 3.8. Thus, the radial and azimuthal components for the upper and the lower cylindrical coordinate system can be expressed in terms of the Cartesian coordinates as

$$\rho_u = \sqrt{x^2 + \left(y - (r + \frac{g}{2})\right)^2} \tag{3.7}$$

$$\rho_l = \sqrt{x^2 + \left(y + (r + \frac{g}{2})\right)^2} \tag{3.8}$$

$$\phi_u = \tan^{-1}\left(\frac{y - (r + g/2)}{x}\right) \tag{3.9}$$

$$\phi_l = \tan^{-1}\left(\frac{y + (r + g/2)}{x}\right) \tag{3.10}$$

Using equations (3.9-10) the radial unit vector ($\hat{\rho}$) in cylindrical coordinate can be expressed in terms of Cartesian ones ($\hat{x}$ and $\hat{y}$) as:

$$\hat{\rho} = \cos\phi\,\hat{x} + \sin\phi\,\hat{y} \tag{3.11}$$

The magnetic field at point P(x, y, z) is the sum of the fields of both undulator halves. The magnetic field of each undulator half can be calculated by the scalar potential method [43]. The scalar magnetic potential $\Phi$, can be calculated using Laplace's equation in a cylindrical coordinate system

$$\nabla^2\Phi = \frac{1}{\rho}\frac{\partial}{\partial\rho}\left(\rho\frac{\partial\Phi}{\partial\rho}\right) + \frac{1}{\rho^2}\frac{\partial^2\Phi}{\partial\phi^2} + \frac{\partial^2\Phi}{\partial z^2} = 0 \tag{3.12}$$
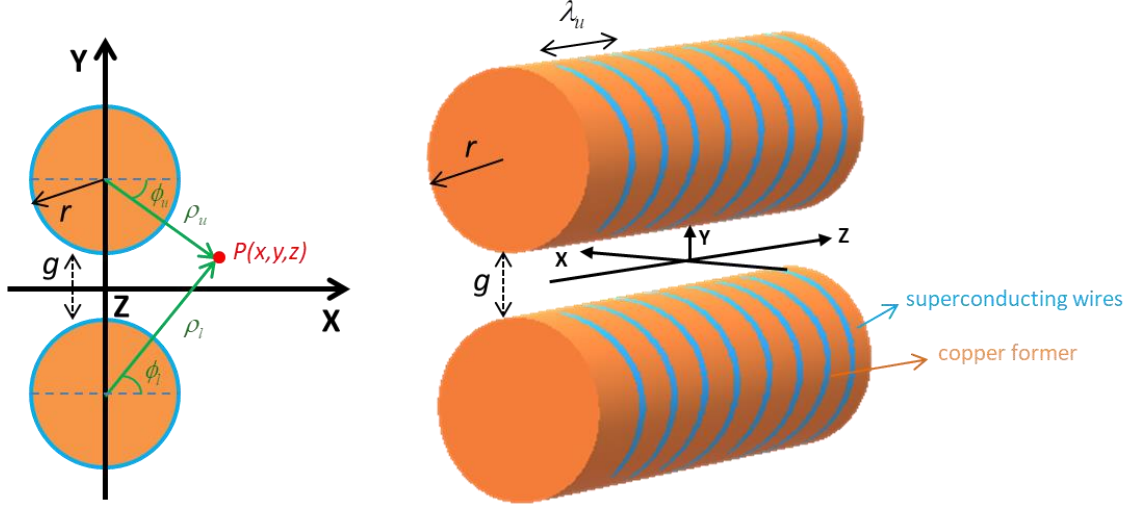
Figure 3.8: Schematic view of a cylindrical TGU with superconducting wires wound around the copper former and the coordinate system. The origins of the cylinders' local coordinate systems are at $r_{0,u}$ = *(0,(r + g/2),0)* and $r_{0,l}$ = *(0 ,-(r + g/2),0)*. Adopted from Ref. [31].

Using separation of variable techniques, equation (3.12) has a solution in the form of

$$\Phi(\rho,\phi,z) = \tilde{\Phi}_\rho(\rho)\tilde{\Phi}_\phi(\phi)\tilde{\Phi}_z(z) \tag{3.13}$$

Substituting equation (3.13) into equation (3.12) gives

$$\nabla^2\Phi = \sin(k_u z)\,\tilde{\Phi}_\phi\left(\frac{\partial^2\tilde{\Phi}_\rho}{\partial\rho^2} + \frac{1}{\rho}\frac{\partial\tilde{\Phi}_\rho}{\partial\rho} - k_u^2\tilde{\Phi}_\rho\right)$$

$$= \left(\frac{\partial^2\tilde{\Phi}_\rho}{\partial\rho^2} + \frac{1}{\rho}\frac{\partial\tilde{\Phi}_\rho}{\partial\rho} - k_u^2\tilde{\Phi}_\rho\right) = 0 \tag{3.14}$$

where we assumed $\tilde{\Phi}_z(z) = \sin(k_u z)$ [2] and $\tilde{\Phi}_\phi(\phi) = $ constant (for symmetry reasons).

Changing the variable $\rho$ to $k_u\rho$, equation (3.14) is the modified Bessel differential equation with the modified Bessel functions of the first, $I_0(k_u\rho)$ and the second kind, $K_0(k_u\rho)$ as the solutions. The solution must satisfy these two conditions

$$\lim_{\rho\to\infty}\tilde{\Phi}_\rho = 0$$

$$\forall\rho \to \frac{\partial\tilde{\Phi}_\rho}{\partial\rho} < 0 \tag{3.15}$$

---

[2] The z-dependence of the field is not purely sinusoidal and exhibits higher harmonics [39]. We just take the first term of the Fourier series expansion to calculate the magnetic field.

They both are only satisfied with $K_0(k_u\rho)$. Therefore, the complete solution reads

$$\Phi(\rho,\phi,z) = \Phi(\rho,z) = B^* K_0(k_u\rho)\sin(k_u z) \tag{3.16}$$

where $B^*$ is a constant. The magnetic field is expressed by

$$\vec{B} = -\vec{\nabla}\Phi(\rho,z) = -B^*\left(\frac{\partial}{\partial\rho}K_0(k_u\rho)\right)\sin(k_u z)\hat{\rho} - B^* k_u K_0(k_u\rho)\cos(k_u z)\hat{z} \tag{3.17}$$

Using the properties of the Bessel functions, i.e.

$$\frac{\partial}{\partial\rho}K_0(k_u\rho) = -k_u K_1(k_u\rho) \tag{3.18}$$

the magnetic field of one cylindrical half is

$$\vec{B} = B_0[K_1(k_u\rho)\sin(k_u z)\hat{\rho} + K_0(k_u\rho)\cos(k_u z)\hat{z}] \tag{3.19}$$

where $B_0 = -k_u B^*$. The total magnetic field is the sum of the two cylinders' field that yields [29]

$$\vec{B}_T = B_0\sin(k_u z)[K_1(k_u\rho_u)\hat{\rho}_u + K_1(k_u\rho_l)\hat{\rho}_l] + B_0\cos(k_u z)[K_0(k_u\rho_u) + K_0(k_u\rho_l)]\hat{z} \tag{3.20}$$

Here $\hat{\rho}_u$ and $\hat{\rho}_l$ are the radial unit vectors of the upper and the lower cylindrical coordinate systems, respectively. A 3D plot of the resulting magnetic fields on-axis in the deflection plane $B_y$, for one undulator period $\lambda_u$ = 0.0105 m, is plotted in Fig. 3.9.
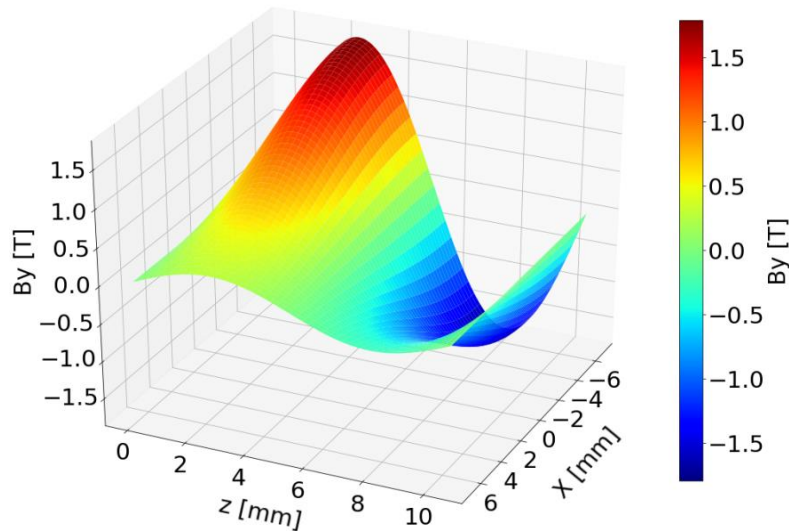


Figure 3.9: Magnetic field on axis $B_y$, as a function of transverse position $x$ and longitudinal position $z$ for one undulator period.
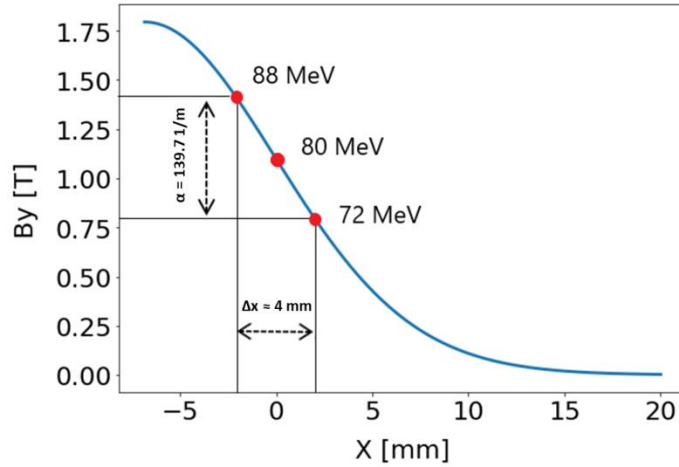
Figure 3.10: Magnetic field in the deflection plane *y = 0* as a function of transverse position *x* at *z = 7λ$_u$ /4.* The origin is shifted to the inflection point. The total dispersive beam splitting is around 4 mm.

For convenience *x=0* is chosen at the inflection point with B*(0, 0, λ$_u$ /4) = 1.1* T. In the locality of this inflection point the magnetic field $B_y$, is approximately linear. The width of this region is roughly $\Delta x \approx \pm 2\,\mathrm{mm}$ as shown in Fig. 3.10. In fact, considering overlap of the electrons' radiation cones with different energies [31] the maximum of total dispersive beam splitting for reference beam energy $E_0$, of 80 MeV with energy spread $\Delta E / E_0 = \pm 10\%$ is around $\Delta x_\gamma \approx 4\,mm$. It should be noted that the value of constant $B_0$, the field strength, in equation (3.20) is set such that the designed transverse gradient $\alpha$ = -139.7 1/m, in the vicinity of the inflection point is achieved. According to equation (3.4), with $\alpha$ = -139.7 1/m and $K_0$ = 1.078 a matched beam dispersion of *D* = -19.6 mm is needed. Assuming 80 MeV as the reference beam energy, the TGU is able to compensate the effect of energy spread on radiation broadening for a beam with $\Delta E = \pm 8\,\mathrm{MeV}$ .
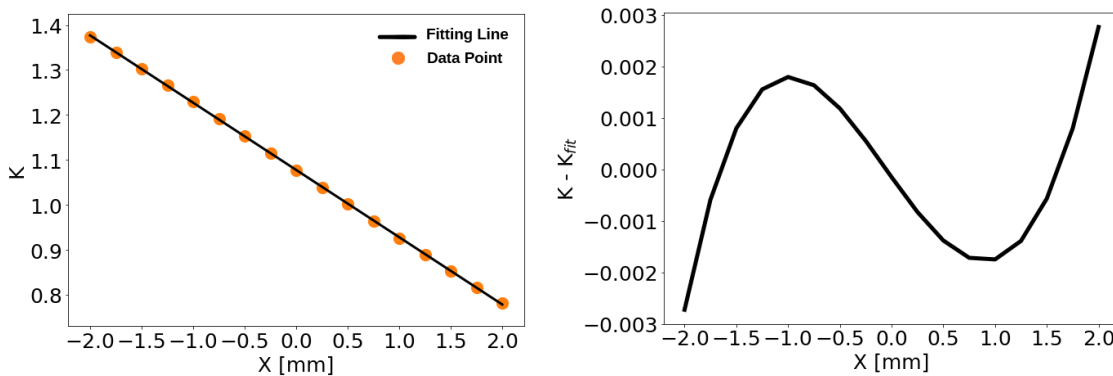


Figure 3.11: Left: Linear fit of the K values based on equation (3.20). Right: The difference between the K from fitting and the K from equation (3.20).
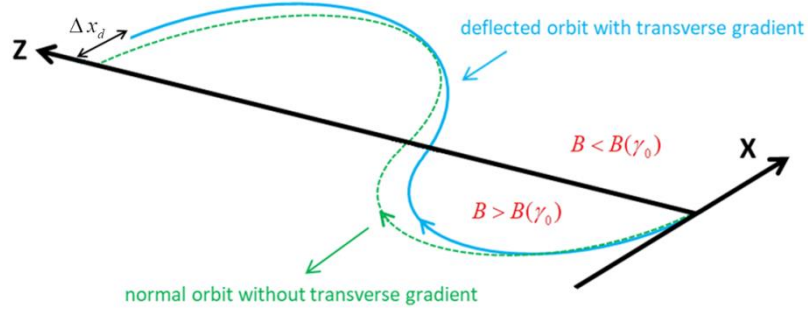
Figure 3.12: Ponderomotive drift due to the transverse magnetic field gradient in the deflection plane.

The transverse magnetic field gradient in the area $\Delta x \approx \pm 2\,\text{mm}$ is not completely linear. This can be seen from Fig. 3. 11 where the K value of the undulator at *z=7λ/4* as a function of transverse position x is plotted on the left side. By fitting the data points for the K values with a linear function based on equation (3.2), *α* = -139.8 1/m is obtained that is close to the designed parameter of TGU40. The difference between the K value from a linear fit and the calculated K based on equation (3.20) is plotted on the right side of Fig. 3.11.

## 3.2.3 Ponderomotive Drift

Due to the transverse gradient of the magnetic field inside the undulator, electrons experience a ponderomotive deflection. As the electron moves in *x-z* plane, in the first half of its oscillatory path it sees different magnetic fields than in the second half depending on the direction of its movement toward, higher or lower *x* values. This field difference results in a ponderomotive drift to the higher x values as shown in Fig. 3.12. The amount of this deflection can be estimated by using the Lorentz force equation for the reference particle [35]

$$\frac{d^2x}{dt^2} = \frac{e}{\gamma m} B_y(\gamma_0)(1+\alpha x(z))\sin(k_u z)\frac{dz}{dt} \tag{3.21}$$

Changing the variable from t to z in derivative and assuming $dz/dt = \beta c$ leads to

$$\frac{dx}{dz} = \frac{eB_y(\gamma_0)}{\gamma m\beta c}\int(1+\alpha x(z))\sin(k_u z)\,dz \tag{3.22}$$

Solving equation (2.31) for $x(z)$ and integrating the equation (3.22) for one period, the drift after one period can be approximated by
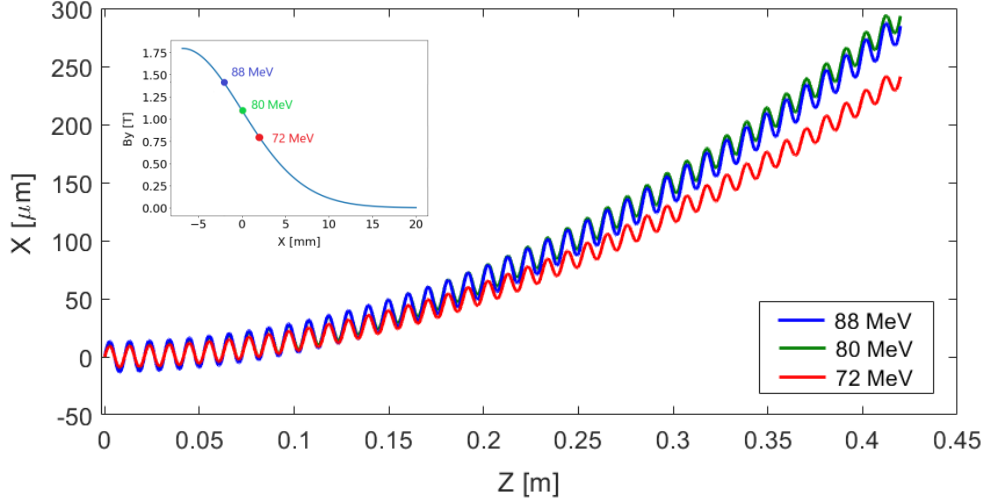
Figure 3.13: Relative electron trajectories for different energy values inside the TGU40. The Inset plot shows the initial transverse positions of the electrons with respect to the magnetic field $B_y$. The respective transverse starting points are shifted to zero.

$$\Delta x_d = -\frac{\alpha K^2(\gamma_0)\lambda_u^2}{2\gamma^2\beta^2} \qquad (3.23)$$

From equation (3.23) we can see that the ponderomotive drift depends on the local K value of the undulator and the energy of the incoming particle. Fig. 3.13 shows the drifts for different energies inside the undulator injected in different positions with different K values. The starting positions of the particles are shifted to zero to have a better comparison. Additionally, as a requirement for all insertion devices, the first and second field integrals should equal to zero [24]. This can be realized by using proper end field terminations. In the TGU40 the winding packages of the first and second coils at the beginning and at the end of the undulator, which are called matching coils, are modified to produce ¼ and ¾ of the field amplitude [35, 39]. These effects on the electron's trajectory must be compensated since the monochromaticity of the TGU radiation is linked to have a constant dispersion inside the undulator. The effect of the electron trajectory deviation is shown in Fig. 3.14 where the relative deviation of the peak radiation wavelength for 80 MeV beam $\lambda_0 = 338.65\ nm$, as a function of electron transverse displacement inside the undulator is plotted on the left. It shows how the peak energy of the emitted radiation changes depending on the transverse displacement inside the TGU40. Moreover, the flux density decreases due to missing overlap between the emitted radiation wavefronts as shown on the right side of Fig. 3.14 where the maximum on axis radiation flux at 100 m distance is plotted for different electron drift values inside the undulator. Here a linear increase or decrease of transverse displacement is assumed.
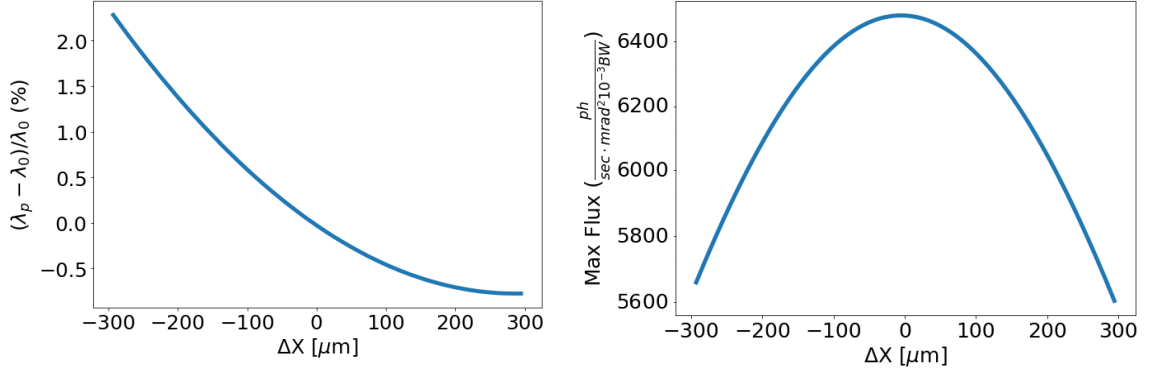
Figure 3.14: Left: Relative deviation of peak radiation wavelength with respect to that of 80 MeV for different transverse displacements. Right: Maximum radiation flux on axis as a function of transverse drifts inside the undulator.

## 3.2.3.1. Correction Coils

The electron displacement due to the ponderomotive force increases with increasing number of the undulator periods. Therefore, it is important to recover that after the first period. The trajectory drifts can be corrected using two racetrack coils inside the TGU coil formers which produce a "local dipole field" for different electron energies [37, 39]. The required dipole field must counteract exactly that single period drift and has to vary transversely but can be assumed to be constant in the *z* direction. Considering Δx(x) as the transverse drift in one undulator period the correction field $B_{yc}(x)$ can be estimated by

$$B_{yc}(x) = \frac{mc\gamma(x)}{e\, r_L(x)} \tag{3.34}$$

where $r_L(x)$ is the bending radius of the respective correction field and is given by

$$r_L(x) = \frac{\lambda_u^2 + (\Delta x(x))^2}{2\Delta x(x)} \tag{3.35}$$

The calculated values of the correction field $B_{yc}(x)$ for each transverse position can be fitted to a cubic function $B_{yc}(x) = P_1 x^3 + P_2 x^2 + P_3 x + P_4$ with coefficients

$$P_1 = 3239.36 \pm 58.21 \quad \text{T/m}^3$$
$$P_2 = -22.14 \pm 0.06 \quad \text{T/m}^2$$
$$P_3 = -0.08185 \pm 0.0017 \quad \text{T/m}$$
$$P_4 = 0.8896 \pm 0.00012 \quad \text{mT}$$

Fig. 3.15 shows the data points of $B_{yc}(x)$ and the fitted cubic function.
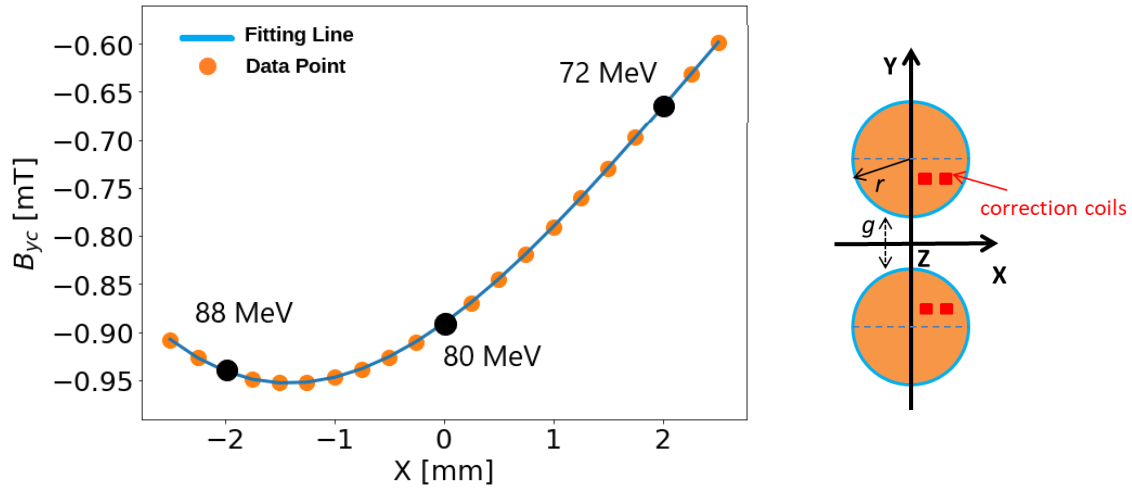
Figure 3.15: Correction field $B_{yc}(x)$ needed in the deflection plane for different energies. The blue line shows the cubic fit function. On the right the side view of the TGU with correction coils inside the formers is depicted.

The electron trajectories for the reference particle of 80 MeV before and after adding the correction field are plotted in Fig. 3.16 on the left and right side, respectively. The drift of the electron with correction field is reduced to $\Delta x < 2\,\mu m$ while without correction field the ponderomotive drift is around $\Delta x \approx 300\,\mu m$.

## 3.2.4 Realization of the TGU Concept

Taking into consideration the optimization for the matching coils and the correction coils, the proof of the TGU concept can be studied by looking at the radiation spectra and comparing the results with a normal undulator. Here we consider monochromatic beamlets with zero emittance and 10 pC charges (macroparticles). The reference beam energy is 80 MeV that goes
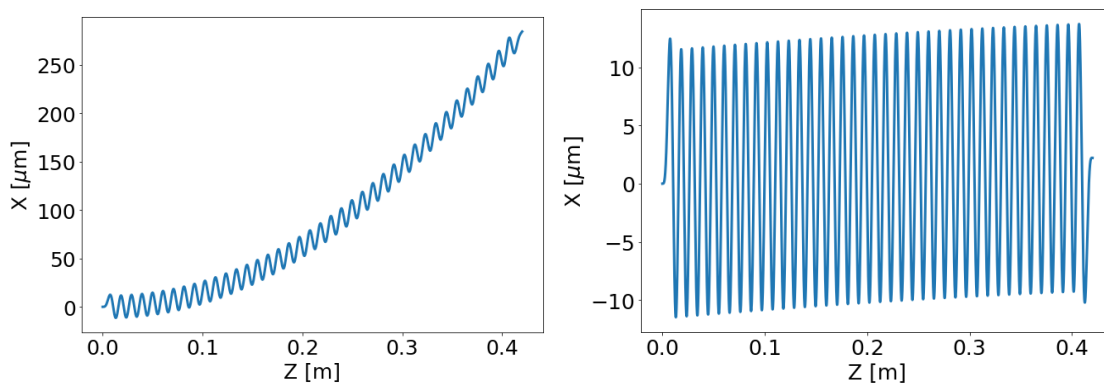


Figure 3.16: Electron trajectory in the deflection plane without (left) and with (right) correction coils for 80 MeV beam injected on the axis. The first and the last periods are influenced by the matching coils (¼ and ¾ of the field amplitude).

at the center of the undulator, x=0. For a bandwidth of energy of $\Delta E / E_0 = \pm 10\%$, the beamlets energies range from 72 to 88 MeV and are injected in the region $\Delta x \approx \pm 2\,\mathrm{mm}$. The matched dispersion according to equation (3.4) is *D* ≈ 20 mm and leads to 1 mm distance between the beamlets, assuming 5 beamlets. The TGU parameters are listed in Table. 3.1. The validity of the TGU concept is shown in Fig. 3.17 where the radiation spectra for a normal undulator (planer undulator) and the TGU as a function of relative deviation from the reference energy's radiation wavelength $\lambda(80\,\mathrm{MeV}) = 338.65$ nm are plotted. The radiation spectra are on axis and simulated by OCELOT at 100 m distance. For the planar undulator case the same parameters as TGU40 with *K*=1.078 (the same *K* value as the reference energy in the TGU40) are considered. As can be seen from Fig. 3.17 in the TGU case the total width of the radiation spectra is reduced with a full-width-half-maximum (FWHM) ≈4 % in comparison to the normal undulator case with FWHM ≈40 %.
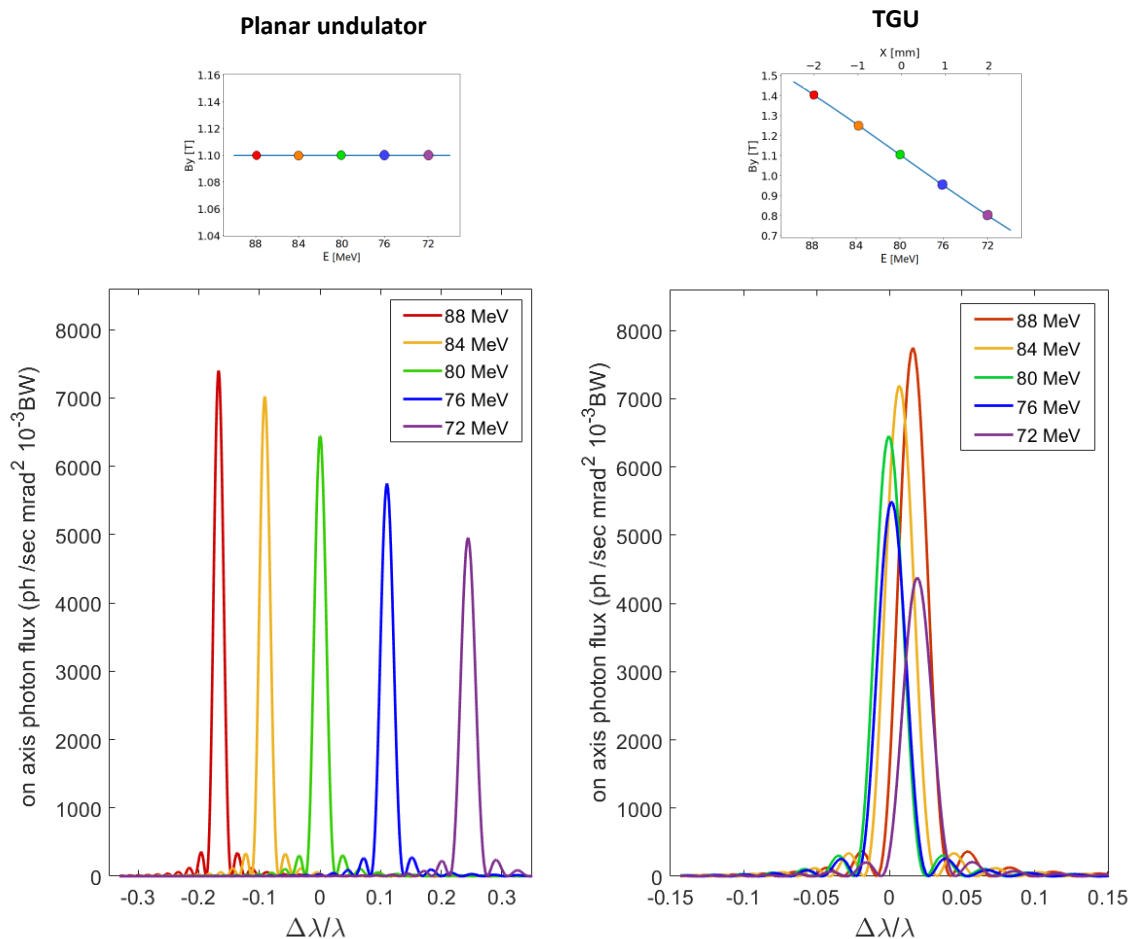


Figure 3.17:  Radiation spectra on axis at 100 m distance for 5 beamlets with different energies for a planar undulator with constant undulator parameter K=1.078 (left) and the TGU40 case with transverse field gradient *α* = -139.7 1/m (right). The top plots show the initial transverse position of each beamlet respect to the on axis magnetic field in the deflection plane.
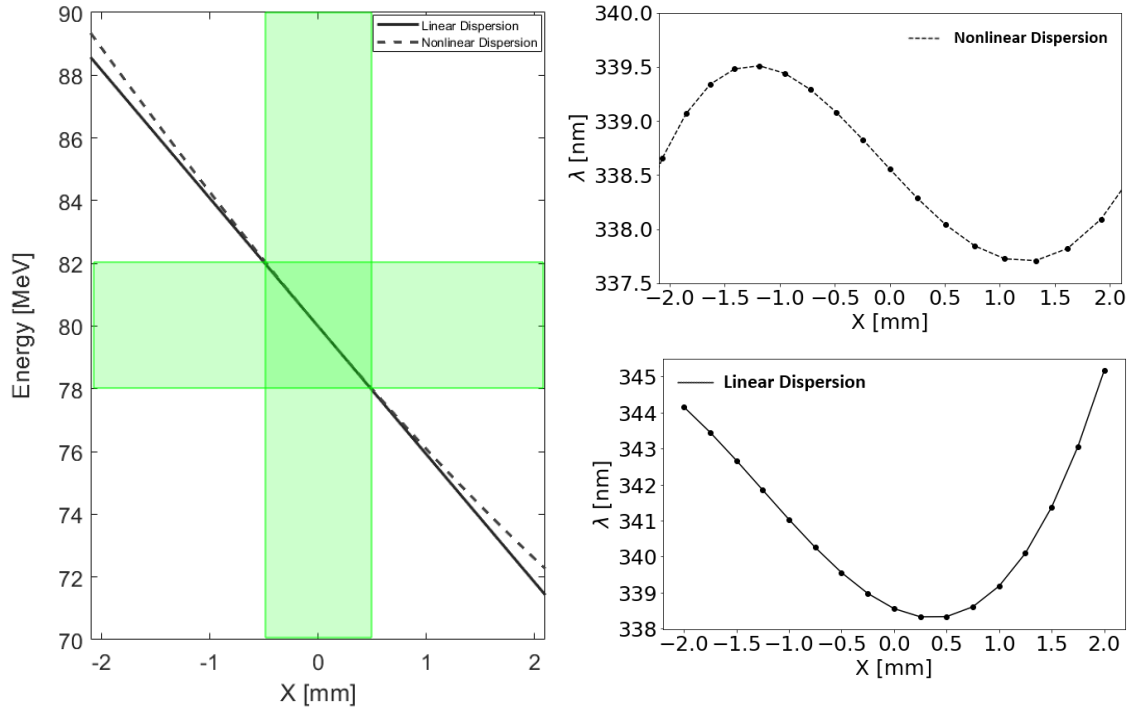
Figure 3.18: Left: Linear dispersion (solid line), equation (3.4), and nonlinear dispersion including higher order terms (dashed line), equation (3.26). The green area shows the region where linear approximation is valid. Right: The resulting radiation wavelength for both cases assuming a reference beam energy of 80 MeV at x=0.

In the TGU case, however, as it is expected, the radiation wavelengths for the beamlets should be the same as the radiation wavelength of the reference energy. The spread in the peak radiation wavelengths in the TGU case originates from neglecting higher order dispersion in equation (3.4). Solving equation (3.5) for *x* by assuming a linear *x* dependence of the undulator parameter *K* i.e. equation (3.2), yields

$$x(\delta) = \frac{1}{\alpha}\left(\sqrt{1+(\frac{2+K_0^2}{K^2})\delta(\delta+2)}-1\right) \tag{3.26}$$

The difference between a linear dispersion, equation (3.4), and nonlinear dispersion, equation (3.36), is plotted in Fig. 3.18 on the left. As can be seen, the assumption of having a linear matched dispersion is just valid for a small region around the origin that is shaded in green. The spread in the radiation wavelength for both cases with a reference beam energy 80 MeV at *x*=0 is depicted on the right side of Fig. 3.18.

The radiation spectra with a nonlinear dispersion according to equation (3.36) and assuming the same beamlets like the previous example are plotted in Fig. 3.19. In the case with nonlinear dispersion the width of the radiation spectra is decreased even more with a FWHM ≈2.3 % close to the natural bandwidth of the undulator.
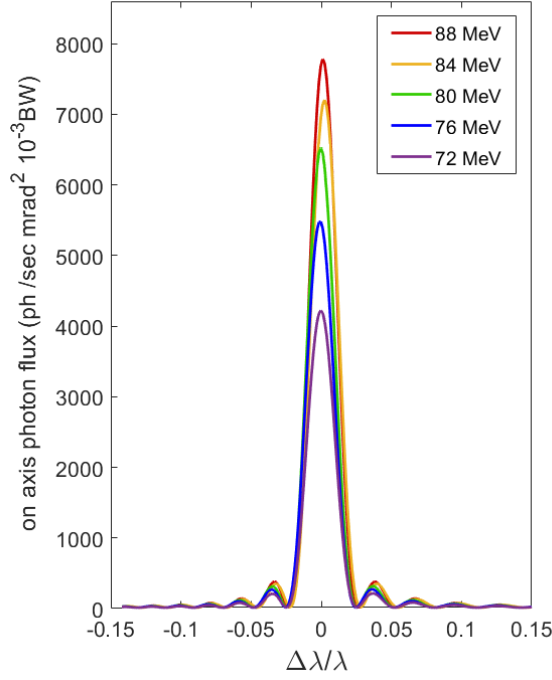
Figure 3.19: Radiation spectra for 5 beamlets with different energies for the TGU40 with a nonlinear dispersion according to equation (3.26) and a reference beam energy 80 MeV.

Furthermore, the transverse field gradient is not completely linear as shown in Fig. 3.11. The assumption of having purely sinusoidal field is the reason for this difference and higher harmonics must be considered in the analytical model. In fact, concerning higher harmonics in the Fourier series leads to a solution for the magnetic field of the form [39]

$$\vec{B}_T = \sum_{n=0}^{\infty} B_{F0}(\sin(nk_u z)[K_1(nk_u \rho_u)\hat{\rho}_u + K_1(nk_u \rho_l)\hat{\rho}_l]$$
$$+ \cos(nk_u z)[K_0(nk_u \rho_u) + K_0(nk_u \rho_l)]\hat{z})$$

(3.27)

Here $B_{F0}$ is a constant regarding Fourier coefficients of the magnetic field. These Fourier components can be calculated with a Finite-Element Method (FEM)-Software using a 3D simulation. This calculation is beyond the scope of this thesis and is not attempted in this study. In this thesis we use the first harmonic of the Fourier series and use equation (3.20) as the primary equation to simulate the magnetic field of the TGU40. This magnetic field is then imported as the field map into the OCELOT [44] to simulate the TGU radiation. The field measurement of the transverse field gradient of the TGU40 has been planned to be performed in 2021 at KIT. After the measurement, the real field map of the TGU40 can be imported instead of the analytical model field map to get more accurate results in the experimental test without any change in the setup of the experiment. The method of the experiment is described in section 3.3.

# 3.2.5 Undulator Focusing Properties

A planar undulator can be regarded as a vertically focusing element. The longitudinal magnetic field generated between the undulator poles is the reason for this focusing feature which is known as the vertical natural focusing of the undulator. The vertical motion of the electron inside the undulator can be expressed as [24, 45]

$$\frac{d^2 y}{dz^2} + K_u^2 y = 0 \tag{3.28}$$

with vertical focusing strength $K_u$, which in the case of a sinusoidal vertical magnetic field with amplitude $B_0$ averaged over one undulator period is given by

$$K_u = \frac{K k_u}{\sqrt{2}\gamma} \tag{3.29}$$

The undulator vertical natural focusing can be used to keep the vertical beam size constant through the undulator. For this purpose, proper beam matching at the entrance of the undulator is needed. The matching condition can be derived considering the undulator as a focusing element with a transfer matrix similar to a vertically focusing quadrupole. Having the beam waist at the undulator entrance i.e. $\alpha_y$=0, the matched vertical beta function to have a constant beam size (assuming emittance is conserved) along the undulator reads [46, 47]

$$\beta_y = \frac{1}{K_u} = \frac{\sqrt{2}\gamma}{K k_u} \tag{3.30}$$

In the TGU case, the overall vertical natural focusing can be approximated by [40]

$$K_u = \frac{K_0}{\sqrt{2}\gamma_0}(\sqrt{k_u^2 + \alpha^2}) \tag{3.31}$$

where $\alpha$ is the transverse gradient and the subscript 0 denotes the reference particle values. In the case of TGU40 with 80 MeV beam as the reference energy the matched beta function is $\beta_y$ = 0.334 m. It can be seen that the focusing strength varies with the magnetic field amplitude and also the particle energy. Considering the previous example in Sec. 3.2.4 with different beamlets but now with a finite emittance $\varepsilon_{nx} = \varepsilon_{ny} = \gamma\varepsilon = 1\mu\text{m-rad}$, the vertical focusing effect on the beam can be realized from Fig. 3.20 (a) where the vertical beta functions for these beams with different energy and different initial transverse position (i.e. different undulator parameter K) along the TGU40 are plotted. The initial beta function is taken from Fig.3.20 (b) that shows the final values of the vertical alpha and beta function at the end of the undulator for an 80 MeV beam (zero energy spread) as a function of the initial vertical beta fu-

(a)



(b)
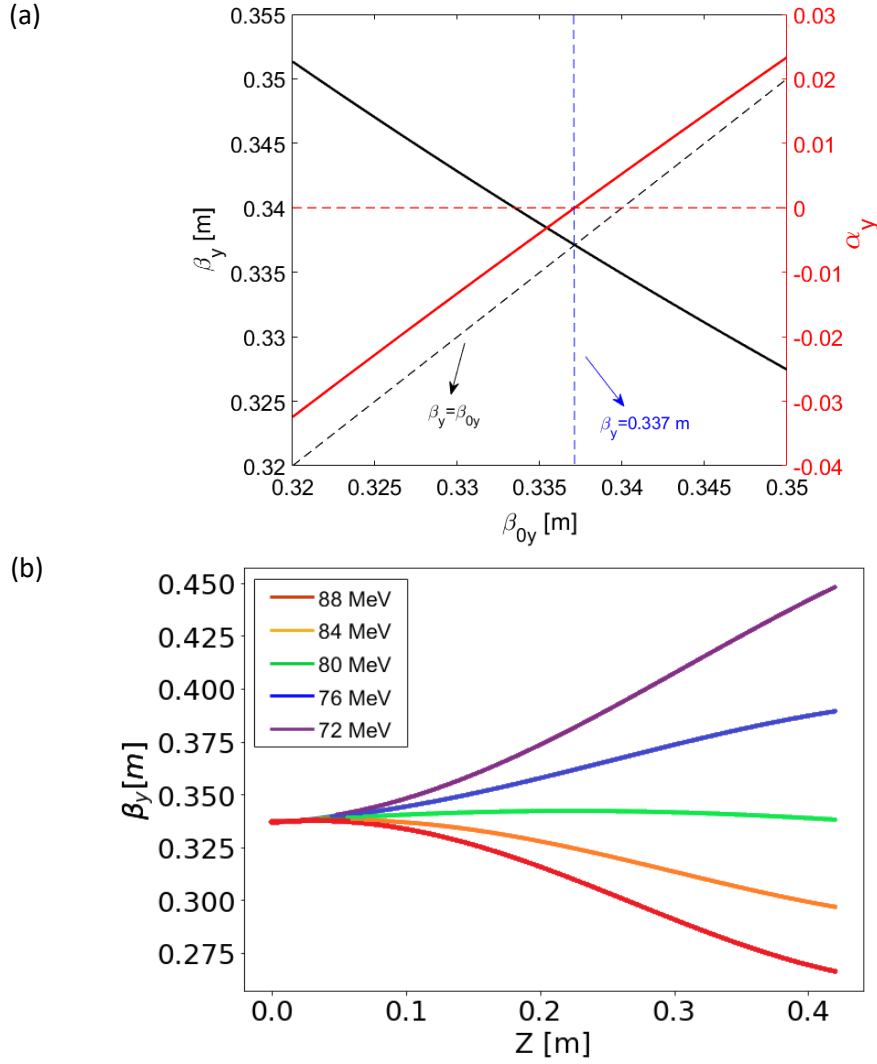


Figure 3.20: (a) final values of the vertical Twiss parameters as a function of the initial vertical beta function for an 80 MeV beam (zero energy spread) and 1μm-rad normalized emittance injected at x=0. (b) vertical beta function along the TGU40 for different beam energies injected in different transverse positions (see Fig. 3.17).

-nction $\beta_{0y}$, assuming $\alpha_{0y}$ =0 at the entrance of the TGU40. For $\beta_{0y}$ = 0.337 m, the initial and the final beta functions are equal with $\alpha_y$ =0, which is so close to the value predicted by equation (3.31). In the transverse plane x, TGU introduces a weak horizontal focusing [10]. The horizontal focusing strength $K_\beta$, of the TGU is given by [48]

$$K_\beta = \frac{K_0^2 \alpha}{\sqrt{2}\gamma_0(\sqrt{2+K_0^2})}$$

(3.32)

which for an 80 MeV beam as the reference beam, its betatron wavelength [10] is much larger than the TGU40 length and therefore can be neglected. Thus, in the transverse plane it can be

regarded as a drift section. Considering the beam waist at the center of the drift space i.e. $\alpha_w$=0, the evolution of the alpha and beta function after the center of the drift section of length 2$s$ can be calculated using equation (2.21) for a drift space

$$\beta(s) = \beta_w + \frac{s^2}{\beta_w}$$

$$\alpha(s) = -\frac{s}{\beta_w}$$

(3.33)

The minimum betatron function along the undulator can be reached by choosing the beta function at the waist as $\beta_w = L/2$, where L is the length of the undulator [13]. Therefore, the optimum initial values for the transverse alpha and beta functions are $\beta_{0x} = L$ and $\alpha_{0x} = 1$. The transverse beta functions for an 80 MeV beam with the optimum initial values in a drift section and along the TGU40 are plotted in Fig. 3.21. There is just a small difference between these two beta functions and therefore in a good approximation TGU40 transverse focusing can be neglected and it can be treated as a drift section.

## 3.2.6 Emittance Effects

In the previous section the beamlets are treated as zero- emittance macroparticles to generate the radiation. In fact, the transverse size of the electron beam leads to spectral broadening due to the transverse gradient in the TGU. The particles in lower or higher transverse positions will experience different magnetic fields and as a result the radiation wavelength will be differ-
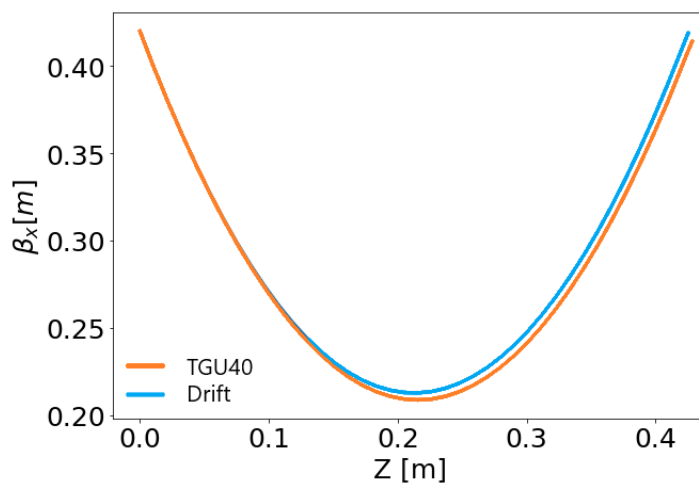


Figure 3.21: Transverse beta function along the TGU40 and a drift section with the same length. The beam energy is 80 MeV.

-ent from the reference particle that goes at the center. As an analytical rough estimation of the limit of the transverse beamlet width, the undulator natural bandwidth can be used as an upper limit for the relative wavelength deviation. In a linear approximation using Taylor series for equation (3.5) leads to

$$\lambda = \lambda(\gamma_0) + \left.\frac{\partial \lambda}{\partial x}\right|_{x=x(\gamma_0)} \Delta x = \lambda(\gamma_0) + \frac{\lambda_u}{2\gamma_0^2} K(\gamma_0) \left.\frac{\partial K}{\partial x}\right|_{x=x(\gamma_0)} \Delta x \tag{3.34}$$

where $\Delta x = x - x(\gamma_0)$. Considering the natural bandwidth of the undulator $\Delta\lambda/\lambda \approx 1/N_u$, an upper limit for the transverse beamlet width $\sigma_{xb}$ can be approximated as

$$\sigma_{xb} \ll \frac{2 + K^2(\gamma_0)}{2K^2(\gamma_0)\alpha N_u} \tag{3.35}$$

As an example, in the case of TGU40 with a reference beam energy of 80 MeV the tolerable range of the transverse beamlet size is estimated $\sigma_{xb} \ll 245\mu m$. The radiation bandwidth as a function of the transverse beamlet size for an 80 MeV beamlet using TGU40 is plotted in fig. 3.22. For the transverse beamlet width less than 170 $\mu m$ the radiation bandwidth stays below the upper limit $\Delta\lambda/\lambda = 1/N_u = 2.5\%$ as shown in Fig. 3.22.

The calculation of the maximum beamlet width has been done without including any energy spread in the beam. Clearly, the bandwidth of the radiation will be increased for a finite energy spread within the beam. The effect of the energy spread on the radiation bandwidth is shown in Fig. 3.23, where the bandwidth of the radiation is plotted as a function of the transverse energy spread i.e. the x-slice energy spread. Here, it is assumed that the beam has a zero-transverse size (i.e. as macroparticles) in order to exclude the effect of the beam width on the radiation bandwidth. As can be seen from the figure, the maximum effective energy spread that a zero-transverse size beam can have such that the radiation bandwidth stays below than the natural bandwidth of the undulator $\Delta\lambda/\lambda = 1/N_u = 2.5\%$ is around 0.3%. Therefore, in order to determine the minimum beam size, which can be regarded as a tolerable beam size such that the result radiation has a bandwidth less than the natural undulator bandwidth, the effect of the energy spread on the radiation bandwidth must be considered, while the finite beamlet size is taken into account.

In the former calculation the divergence of the particles was neglected. The effect of a finite beam size and divergence on the radiation can be studied by considering the beam emittance. The beam size and divergence are related to the beam emittance according to equation (2.14). Thus, using equation (3.35) leads to an approximated upper band for the emittance

$$\sigma_{xb} \approx \sqrt{\beta_x(\gamma_0)\varepsilon_x(\gamma_0)} \ll \frac{2 + K^2(\gamma_0)}{2K^2(\gamma_0)\alpha N_u} \tag{3.36}$$

where $\beta_x$ is the transverse betatron function and $\varepsilon_x$ is the transverse beam emittance.
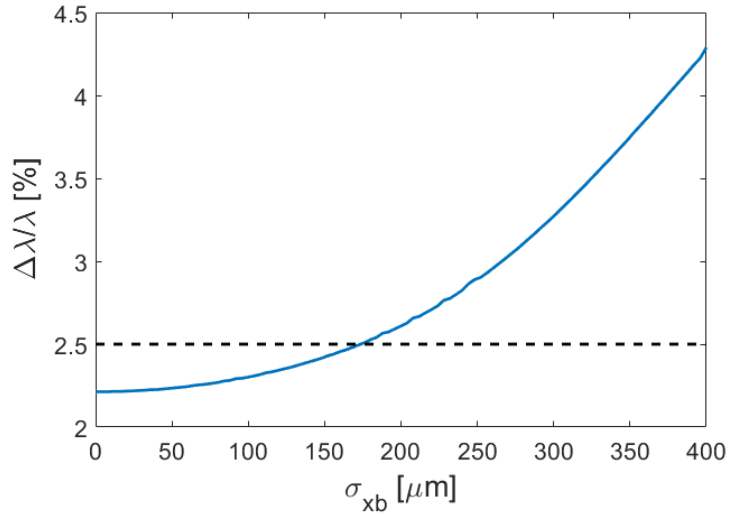
Figure 3.22: Radiation bandwidth as a function of the transverse beamlet size for the TGU40 and a reference beam energy of 80 MeV. The dashed line shows the natural undulator bandwidth.
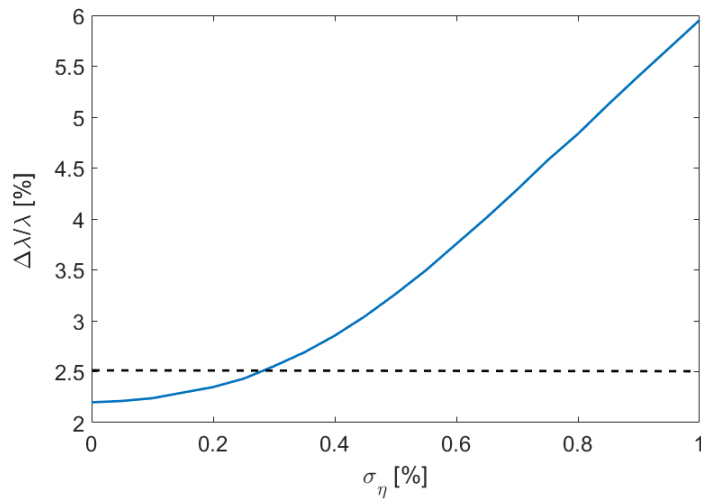


Figure 3.23: Radiation bandwidth as a function of the transverse energy spread (x-slice) for the TGU40 and a reference beam energy of 80 MeV. The dashed line shows the natural undulator bandwidth.

Furthermore, from equation (2.47) a general constraint on the electron beam divergence can be derived [35]:

$$\sigma'_{xb} \approx \sqrt{\frac{\varepsilon_x(\gamma_0)}{\beta_x(\gamma_0)}} \ll \frac{2 + K^2(\gamma_0)}{2\gamma^2 N_u} \tag{3.37}$$

48

The effect of a finite emittance on the radiation can be seen from Figs. 3.24-26. In Fig. 3.24 the particles in a monoenergetic beamlet with energy of 80 MeV are color-coded based on the relative deviation of the peak radiation wavelength respect to the radiation wavelength of the reference particle on axis and observed at 100 m distance. The reference energy is 80 MeV that leads to the radiation wavelength of the reference particle $\lambda_0 = 338.65$ nm using the parameters of TGU40. The beam is assumed to have a Gaussian distribution with normalized emittance of $\varepsilon_{nx} = \varepsilon_{ny} = \gamma\varepsilon = 1\mu$m-rad. The vertical beta function $\beta_y$= 0.337 m is chosen such that it takes a constant value inside the TGU utilizing the vertical focusing properties of the undulator. The transverse beta function $\beta_x$ is chosen to be symmetric with respect to the center of the undulator with the waist value of $\beta_x^{waist}$ = 0.21 m. A beam current of 10 pA represented by 2000 macroparticles is assumed here.

As may be noted from the phase space distribution of the beamlet at the entrance, center and exit of the undulator, there is a perceptible correlation between the radiation spectra and the X-XP phase space while such a correlation for the particles' radiation spectrum in Y-YP phase space does not exist. At the middle of the undulator, where we assumed the beam has its waist, the particle's transverse position determines the deviation of the emitted radiation wavelength from the reference energy wavelength. The transverse size of the beam at the waist is related to the $\beta_x^{waist}$. Therefore, small values of $\beta_x^{waist}$ lead to a narrower radiation spectrum. A smaller value of $\beta_x^{waist}$ demands larger initial beam divergence. Although the radiation wavelength is weakly correlated to the XP-coordinate, for some large values of the initial divergence this correlation becomes more important. This can be seen from Fig. 3.25,
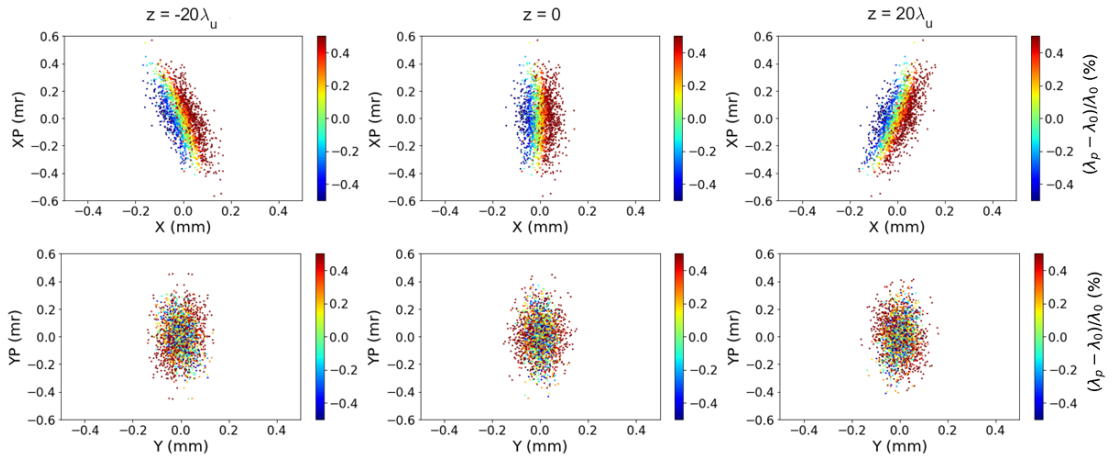


Figure 3.24: Phase space distribution at the entrance, middle and exit of the TGU40. The colorbar shows the deviation from the peak wavelength respect to the radiation wavelength of the reference particle with energy of 80 MeV. See the text for details.

where the normalized flux, ratio of the calculated flux to the flux for a zero-emittance beam, as a function of the normalized transverse emittance and the transverse beta function at the beam waist position is plotted. There is an optimum value of $\beta_x^{waist} \approx 0.1$ m for the range of the normalized transverse emittance shown in the plot.

In Fig. 3.26 the radiation spectra in the case of the previous example for the beamlet with a $\beta_x^{waist} = 0.21$ m is plotted for different values of the normalized transverse emittance. Increasing the normalized emittance leads to a reduction in the flux density and also an increase in the radiation bandwidth. For large values of the normalized emittance the radiation spectra are shifted towards longer wavelength as it is predicted by equation (2.47).

Besides the emittance as a degrading effect, TGU40 is restricted in the energy band acceptance. The linear part of the on axis vertical magnetic field in the transverse plane is limited in $\Delta x \approx \pm 2$ mm. Therefore, the maximum energy band with the designed transverse gradient parameter of $\alpha$ = -139.7 1/m will be $\Delta E / E_0 = \pm 10\%$. Assuming a beam with a Gaussian distribution, to be in the linear part of the transverse gradient, the maximum beam RMS energy spread should be around 5% (considering two standard deviations from the mean)[3].
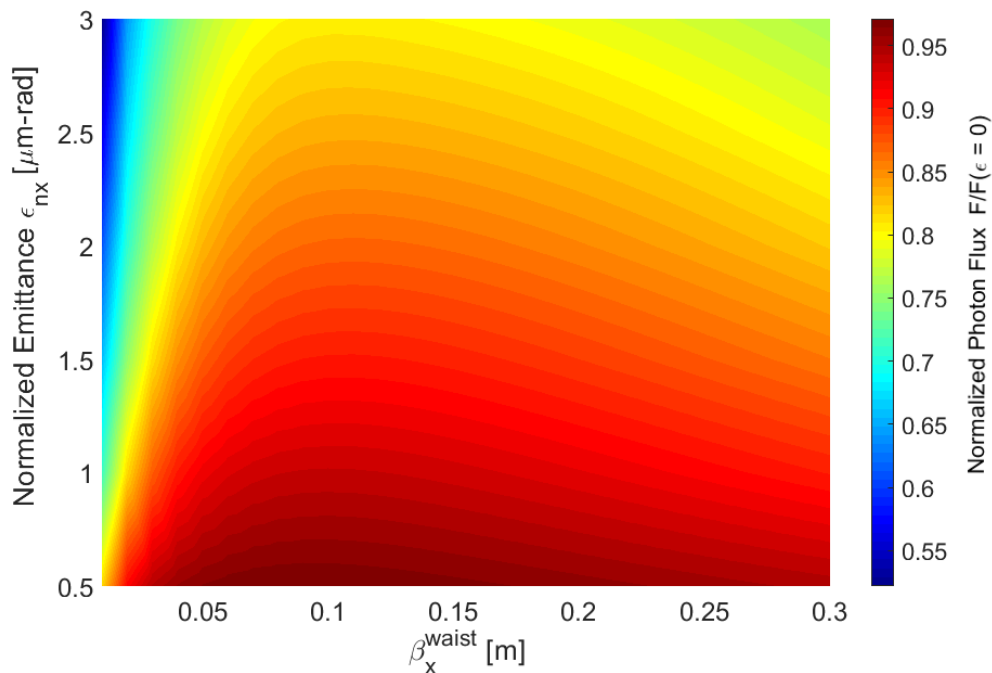


Figure 3.25: Normalized flux as a function of the normalized transverse emittance and beta function at the beam waist.

---

[3] For the Gaussian distribution, about 95% of the values lie within two standard deviations from the mean value.

For higher values of energy spread the resonance equation (3.5) is not satisfied for the particles with higher or lower energies in the dispersed beam i.e. the energy of the particles is not matched to the vertical magnetic field of the TGU and leads to a flux reduction and broadening of the radiation bandwidth. The reduction of the photon flux as a function of the RMS energy spread are plotted in Fig. 3.27 for two cases, TGU40 and a planar undulator (PU). Here a Gaussian beam with the energy of 80 MeV and normalized emittances $\varepsilon_{nx} = \varepsilon_{ny} = \gamma\varepsilon = 1\mu\text{m-rad}$ is assumed. For the planar undulator the same parameters as TGU40 with $K$=1.078 (the same $K$ value as the reference energy in the TGU40) are considered. In the TGU40 case the beam is dispersed in the transverse plane with the matched dispersion according to equation (3.4) i.e. $D$=-0.0196 m. As can be seen for the figure, maximum photon flux photon flux is dropped to 90% of its maximum value after reaching 5% RMS energy spread. The situation for the planar undulator is completely different and its photon flux falls just after a small increase in the energy spread. It should be noted that for each case the initial Twiss parameters are matched to the undulators according to equations (3.30) and (3.33).
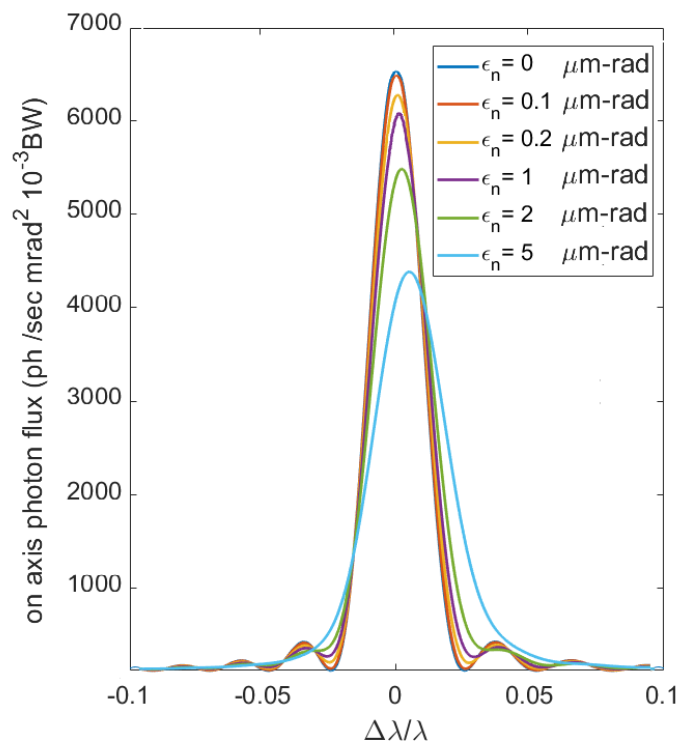


Figure 3.26: Right: On axis photon flux density for different values of the normalized transverse emittance at 100 m distance. The radiation spectrum for each particle in the beam is added incoherently. The beam parameters are the same as the former example (Fig. 3.24).
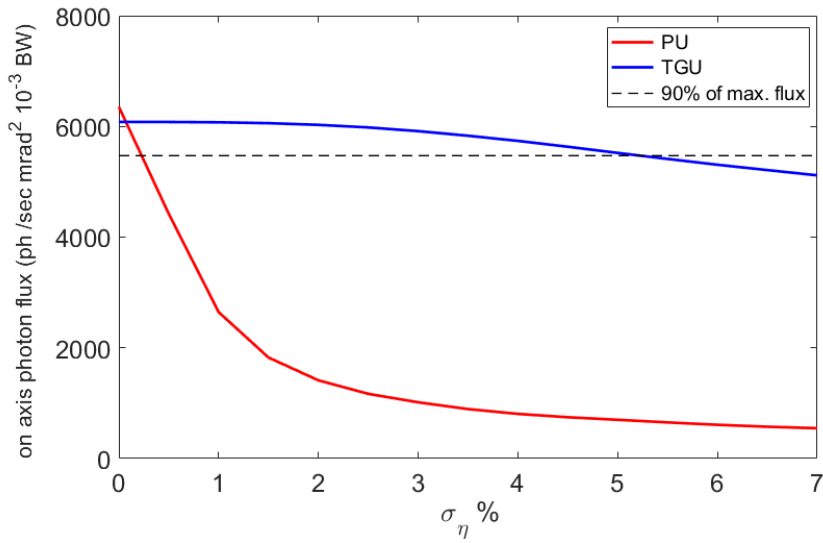
Figure 3.27: Maximum on axis photon flux at 100 m distance at 1 Hz VS initial RMS energy spread for a planar undulator with constant undulator parameter K=1.078 and the TGU40 with a dispersed beam. The beam energy is 80 MeV with a Gaussian distribution.

The effect of the non-linear transverse gradient magnetic field on radiation can also be seen from Fig. 3.28 where the deviation of the peak radiation wavelength respect to the reference particle radiation wavelength is plotted in terms of the transverse and vertical position inside the TGU.
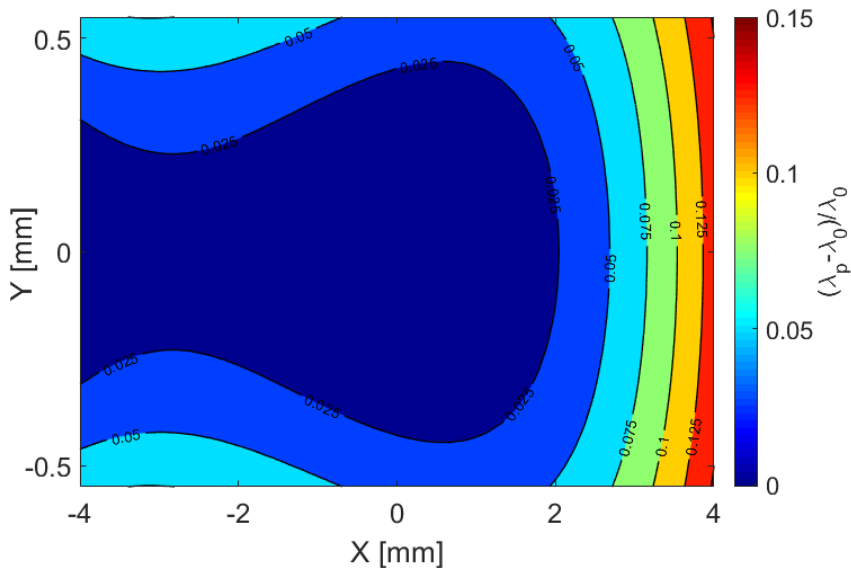


Figure 3.28: Deviation from the peak wavelength respect to the radiation wavelength of the reference particle with energy of 80 MeV as a function of the transverse and the vertical positions at the TGU entrance.

As can be seen, the radiation bandwidth stays below the natural bandwidth $\Delta\lambda/\lambda = 1/N_u = 2.5\%$ for the transverse positions in the linear part of the transverse gradient $\Delta x \approx \pm 2\,\text{mm}$. The deviation of the radiation wavelength in the vertical plane is due to the mismatching between the correction field and the transverse particle position. Particles with the same transverse coordinates but different vertical positions experience different vertical magnetic fields such that for the particles farther to the center the vertical magnetic field is higher. This variation in the transverse magnetic field causes spread in the emitted wavelengths and the radiation broadening. Furthermore, the calculation of the correction field has been done with a constant vertical magnetic field, which for the particles in different vertical positions with different vertical magnetic fields is not satisfied any more. The result uncorrected trajectories lead to the radiation deviation from the design wavelength.

# 3.3 TGU Experiment

It was originally planned to test the TGU40 with ARES linac at SINBAD facility at DESY. The experiment is in collaboration with KIT and the University of Jena. The plans have been changed due to a strategic reorientation of the SINBAD accelerator R&D plans. In the following we report the original plans. The TGU40 has been developed and built at KIT and will be transported to DESY after finishing the magnetic field measurement. The diagnostics for the radiation detection will be provided by the University of Jena. The main objective of the experiment is to validate the TGU capability of producing monochromatic radiation with a beam with a finite energy spread. The experiment is divided into three phases. The first phase is for alignment and also magnetic field verification of the TGU40. In this regard monoenergetic beams[4] produced by the ARES linac will be injected in different transverse positions inside the TGU. The transverse magnetic field can be verified for each transverse position by looking at the radiation spectra. For the second phase, monoenergetic beams with different energies are considered. Since the beam with a finite energy spread must be dispersed before entering the TGU, it can be regarded as a set of beamlets with different energies. The aim of the second phase of the experiment is to validate of the TGU scheme by constructing the real beam with finite energy spread using the beamlets with different energies. As the proof-of-principle experiment, the last phase is intended to demonstrate the enhancement in the flux and monochromaticity of the radiation by using a TGU as the source of the radiation. For that purpose, a beam with a finite energy spread will be produced by the ARES linac and will be dispersed by the dipole in the beamline before entering the TGU. The effect of the energy spread of the beam on the radiation and the TGU compensation can be

---

[4] However, in reality producing monoenergetic beam (beamlet) is impossible. Here monoenergetic beam is referred to a beam with very small energy spread ≪ 0.1 %.

studied by observing the detected radiation. In this section the phases of the experiment are discussed in detail and the experimental setup and the radiation diagnostics are presented.

# 3.3.1 Experimental Setup

In the ARES beamline the electrons are generated in a photoinjector. The main components of the photoinjector are a photocathode laser and a RF gun. As the laser hits the cathode, electrons are produced due to the photoelectric emission. The ARES photocathode laser is a 1 mJ Yb-doped laser with a transverse flat-top and a longitudinal Gaussian profile. The tunability of the laser pulse allows to produce electron bunches with tunable length between 80fs and 4.2ps. The minimum transverse-spot-size diameter on the cathode is 54μm. The amount of charge (0.5 to 30 pC) depends on the type of the photocathode. Due to the high quantum efficiency of semiconductor cathodes, a semiconductor cathode (e.g. caesium-telluride $Cs_2Te$) will be used for high charge applications. On the other hand, its relatively long emission time leads to generation of long bunches. A metallic (e.g. molybdenum Mo) photocathode is used for low average current applications since the quantum efficiency is relatively low but it allows to generate shorter bunches (<1ps) since it benefits of very short emission time. Once the electrons are generated, they will be accelerated in the RF gun. The RF gun at ARES is a 1.5 cell S-band operating at 2.998 GHz. With 6 MW peak input power in the cavity, electrons are accelerated with a final energy around 5 MeV. There are two solenoids around the RF gun for focusing and also emittance compensation in order to match the beam into the Linac [49]. Downstream of the photoinjector there are two traveling wave structures (TWSs) operating at a frequency of 2.998 GHz. Each of these 4.2 m long structures are powered by an independent RF station that allows a maximum energy gain of about 75 MeV per station. For the future energy upgrade a third TWS is planned to be installed that allows a final energy of 230 MeV when all three TWSs are operated on crest. The electron beams generated in the photoinjector are diagnosed and then injected into the TWSs for acceleration. For each TWS four solenoids with peak fields up to 0.1 T have been considered to provide focusing for space-charge defocusing effects. Following the TWSs are four quadrupoles as a matching region. The schematic view of the ARES linac is shown in Fig. 3.29.
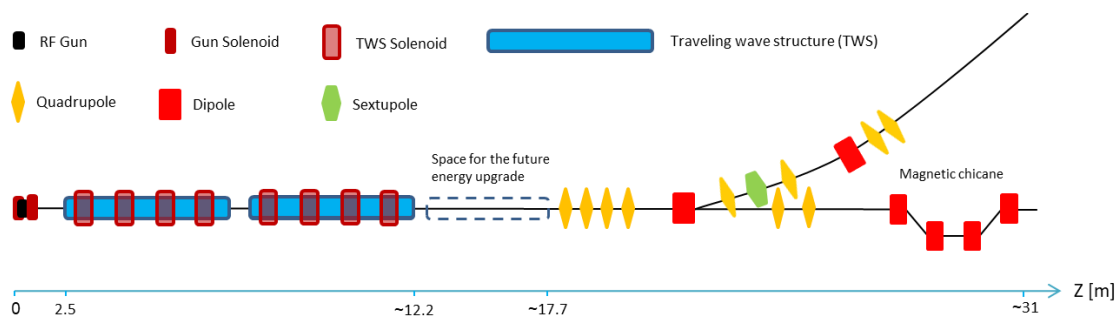


Figure 3.29: Sketch of the ARES linac, as planned for the TGU experiment.
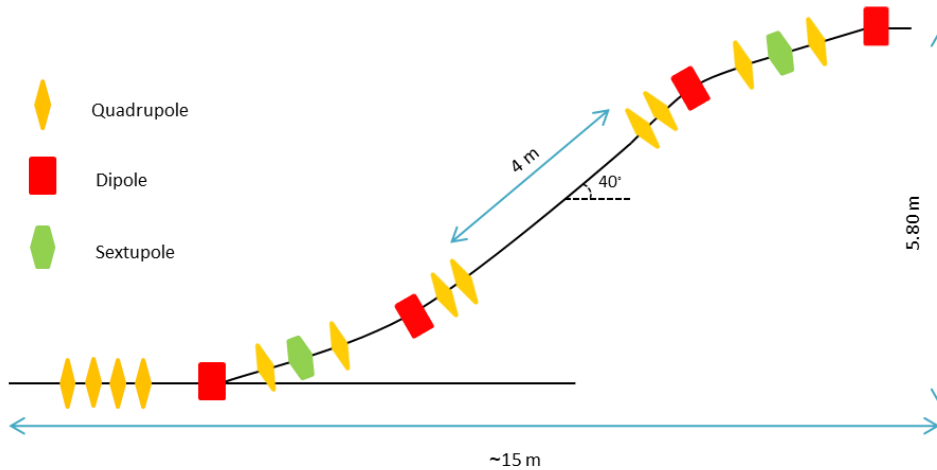
Figure 3.30: Schematic view of the dogleg section in the ARES, as planned for the TGU experiment.

A dogleg section is planned to be installed to deliver ultra-short electron bunches to the second beamline [50]. In this design, after the fourth quadrupole in the main beam line a dipole is placed to direct the beam to the dogleg section. The dogleg comprises of four rectangular dipole magnets, eight quadrupoles and two sextupoles. The test of the TGU40 will be done in the 4 m long straight part in the dogleg section in between the second and the third dipole. The layout of the dogleg is shown in Fig. 3.30.

Fig. 3.31 presents the experimental setup exclusively planned for the TGU experiment. In this regard two beam steerers have been considered before the TGU for transverse deflection. There are two removable screens before and after the TGU to aid alignment and to characterize the transverse profile of the electron beam. To separate the radiation and the electron beam an electron dipole dump is placed after the second screen. The radiation produced by the electrons in the undulator then can be focused at the entrance slit of spectrometer by a spherical achromatic lens (e.g. $CaF_2$ lens)[5]. The spectrometer is a Czerny-Turner spectrograph, which consists of an entrance slit, two flat turning mirrors and two spherical mirrors. The dispersive element of the spectrograph is a blazed grating. The grating period amounts 6.1 μm and 162.5 lines per mm. The grating size in the dispersive plane is 57 mm. Once the radiation passes the entrance slit the beam is first reflected by a flat turning mirror at the reflection angle close to 45 degrees. The beam is collimated by the first spherical mirror, which has a distance to the entrance slit equal to the focal length of the spherical mirror. The central reflection angle of the beam by the mirror is $\alpha=6.4°$. The reflected beam is then dispersed by the grating and goes to the second spherical mirror providing the same focal distance. The diameter of both spherical mirrors is 54 mm. By the focusing of the second spherical mirror the spectra are focused along the horizontal direction (dispersive plane). Using the second flat turning mirror the radiation is sent to a detector (e.g. CCD camera) [51].

---

[5] For high quality imaging a combination of a flat $CaF_2$ vacuum window and then a lens outside the vacuum is favored.
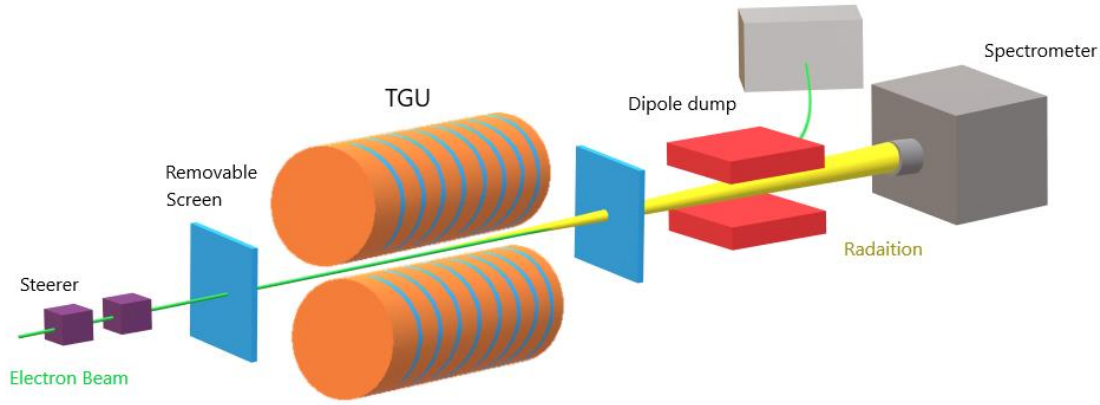
Figure 3.31: layout and the elements for the experiment.

# 3.3.2 Phases of the Experiment

The experiment is planned to be performed in three phases. For each phase, beams from the photocathode up to the exit of the linac were simulated and tracked by ASTRA [52] which includes space-charge effect. The optimization process for this part was performed by LISO [53]. The beam tracking and the optimization from the exit of the linac up to the entrance of the TGU were run by ELEGANT [54] which can model 1D coherent synchrotron radiation (CSR) force. At the end, the beams were tracked inside the TGU and the radiation simulation was done by OCELOT [44]. Besides, OCELOT is capable to include either space-charge or CSR effect and it was used to study space charge effects in this thesis. The central beam energy for the prototype TGU is assumed to be 80 MeV which results in the radiation wavelength in the UV region. Furthermore, a 10 pC beam charge has been considered for each stage to have a sufficiently high number of photons for the detection. The choice of the beam charge and the energy is based on an agreement with KIT and the University of Jena. The beam parameters and the method of the experiment are described in the following sub-sections in detail.

## 3.3.2.1 Phase 1

In the first phase of the experiment a beam with the energy of 80 MeV and 10 pC charge has been considered. In that sense, an 80 MeV quasi-monoenergetic beam and 10 pC charge was simulated by ASTRA using the LISO optimizer. To minimize the effect of the emittance on the radiation (see section 3.2.5) and to have low energy spread beam (monoenergetic beamlet) as much as possible, transverse emittance and energy spread were set to be the main objective parameters in the optimization process. Moreover, the minimum bunch length was limited to $\sigma_z \geq 100\,\mu\mathrm{m}$ as a constraint due to the CSR effect (for CSR and space charge effects see section 3.3.3). The beam parameters at the exit of the linac are listed in Table 3.2. The evolution of the beam parameters during the acceleration is depicted in Fig. 3.32.

| Beam Parameter | Value | Unit |
|---|---|---|
| Energy | *80* | *MeV* |
| Charge | *10* | *pC* |
| RMS Energy Spread | *0.03%* | */* |
| RMS Normalized Emittance (x/y) | *1.07* | *µm-rad* |
| RMS Beam Size (x/y) | *1.75* | *mm* |
| RMS Beam divergence (x/y) | *0.02* | *mrad* |
| RMS Beam Length | *0.1* | *mm* |

Table 3.2: Beam parameters at the exit of the linac simulated by ASTRA for the phase 1.
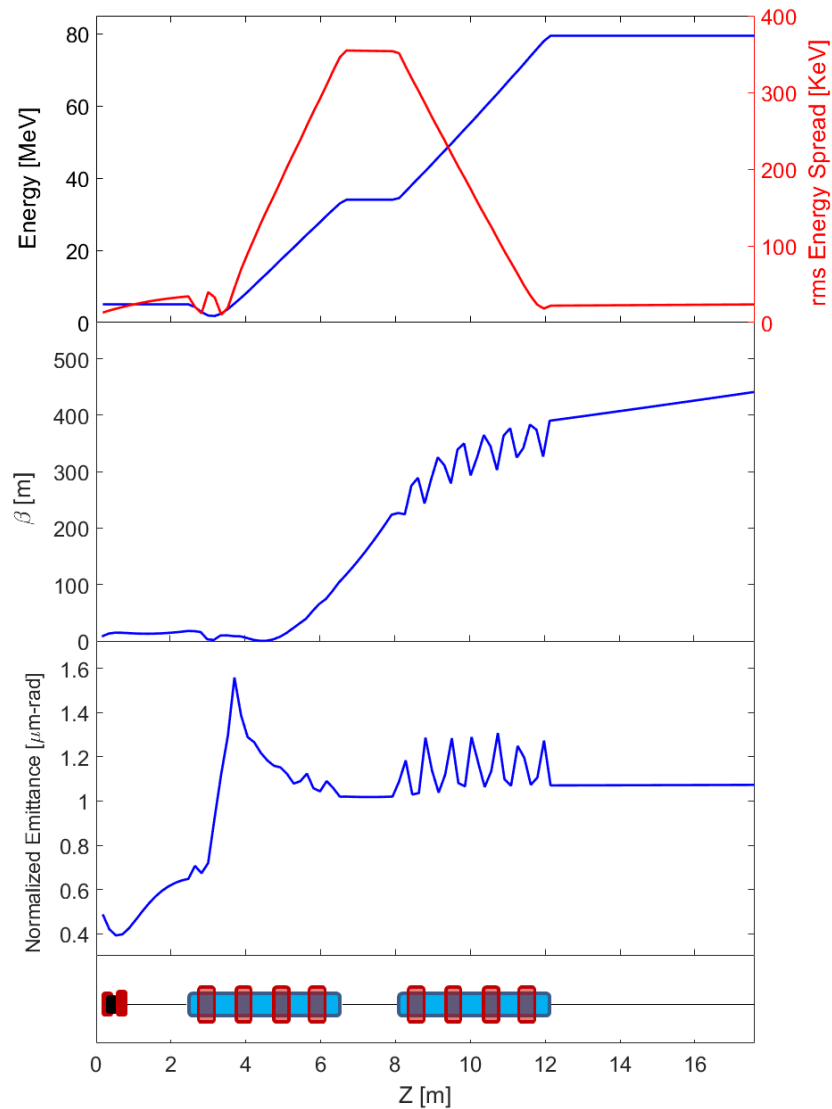


Figure 3.32: Evolution of energy, energy spread, beta and transverse emittance during the acceleration for the phase 1. The layout of the linac with RF gun (black rectangle), solenoid (red rectangle) and two TWSs (blue rectangle) is plotted at the bottom.
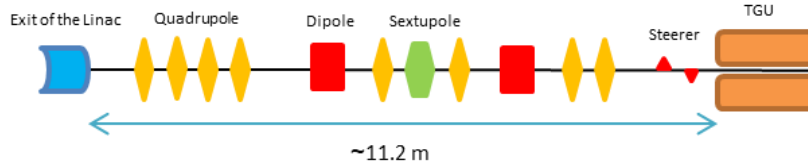
Figure 3.33: Sketch of the TGU beamline.

The beam distribution at the exit of the linac ($z \approx 17.6$) was imported to the ELEGANT code for tracking and optimization in the beam line up to the entrance of the TGU. The schematic view of the TGU beam line from the exit of the linac (including dogleg section) is depicted in Fig. 3.33. The Twiss parameters are matched to the TGU using quadrupoles in the beamline. The maximum flux can be achieved by taking $\beta_x^{waist} \approx 0.1$ m as shown in Fig. 3.25. This is equivalent to having $\beta_{0x} = 0.54$ m and $\alpha_{0x} = 2.1$ according to equation (3.33). In the vertical plane, the matching condition is given by $\beta_{0y} = 0.334$ m and $\alpha_{0y} = 0$ based on the equation (3.31). Since for the first phase of the experiment monoenergetic (low energy spread) beams are used, the beam is not needed to be dispersed to satisfy the resonance condition. Moreover, the transverse beam size should be small enough to have maximum photon flux and minimum radiation bandwidth (Fig. 3.22). For that purpose, the dispersion created by the first dipole is compensated by the quadrupoles between the two dipoles in such a way that after the second dipole it goes to zero. Since the beam has a very small energy spread, the sextupole, which is considered for the chromatic effect compensation, in this phase of the experiment can be neglected. The evolution of the beta functions and dispersion of the reference energy along the beam line is plotted in Fig. 3.34. The matched beam parameters at the entrance of the TGU and the Lattice functions[6] are listed in table 3.3.

| Beam Parameter | Value | Unit |
|---|---|---|
| Energy | 80 | MeV |
| Charge | 10 | pC |
| RMS Energy Spread | 0.03% | / |
| RMS Normalized Emittance (x/y) | 1.08/1.16 | μm-rad |
| RMS Beam Size (x/y) | 58 | μm |
| RMS Beam divergence (x/y) | 0.26/0.14 | mrad |
| RMS Beam Length | 0.1 | mm |

| Lattice Function | Value | Unit |
|---|---|---|
| Beta functions (x/y) | 0.54/0.334 | m |
| Alpha (x/y) | 2.1/0 | / |
| Dispersion | 0 | m |

Table 3.3: Beam and lattice parameters at the entrance of the TGU for the phase 1.

---

[6] Lattice functions are the designed parameters for the central energy particles and are only given by the elements in the beamline.
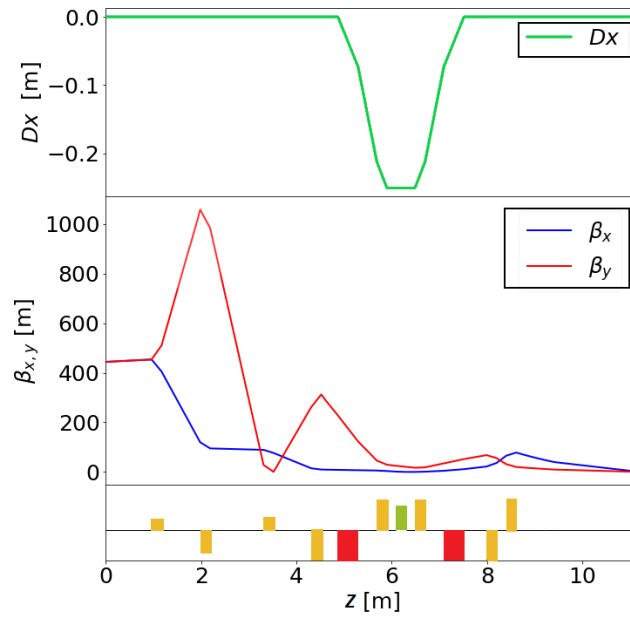
Figure 3.34: Dispersion Dx, and beta functions along the beam line for the phase 1 of the experiment. Layout of the beam transport with quadrupole (yellow), dipole (red) and sextupole (green) is plotted at the bottom.

The aim of the first phase is to attest the transverse magnetic field gradient inside the TGU. The transverse magnetic field can be verified for each transverse position by looking at the radiation spectra. In this regard, the former beam (80 MeV, 10 pC) is injected in different transverse positions inside the TGU. The steerer magnets in front of the TGU can deflect the beam transversely inside it. The sketch of the beam's positions with respect to the on axis vertical magnetic field and the side view of the TGU with initial beam's positions, which are separated by 1 mm, are depicted in Fig. 3.35. Since there is a field gradient inside the TGU the emitted radiation wavelength for each position would be different as shown in Fig. 3.36. In fact, by moving the beam transversely inside the TGU, the transverse magnetic field of the TGU can be certified by looking at the radiation spectrum.
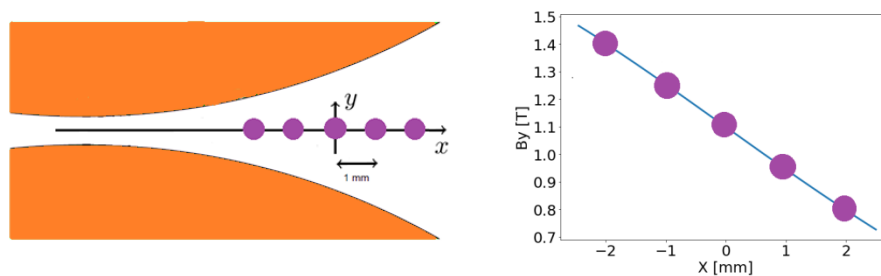


Figure 3.35: Left: Side view of the TGU with different initial beam's position. The 80 MeV beam (purple circle) is injected in different transverse positions inside the TGU. Right: The incoming beam's positions respect to the vertical magnetic field at $z=7\lambda/4$ (considering the matching coils as the first period).
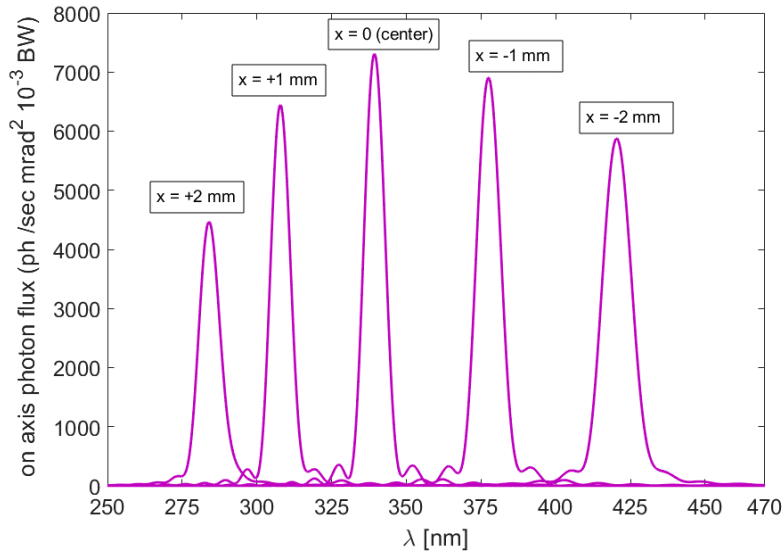
Figure 3.36: Radiation spectra on axis at 2 m distance at 1 Hz for the phase 1 with a beam with the parameters listed in Table 3.3. The beam is injected in different transverse positions inside the TGU (1 mm separation distance[7]).

## 3.3.2.2 Phase 2

A beam with a finite energy spread, which is dispersed transversely, can be regarded as monoenergetic beams that are well placed in transverse plane. In the other word, the electron beam can be divided into a set of monoenergetic beams which cover the energy range of the beam. Since the beam must be dispersed transversely at the entrance of the TGU with the matched dispersion, to construct the beam from the beamlets, the beamlets need to be placed in the transverse plane according to the dispersion equation *x=Dδ.* In this regard, for the second phase of the experiment the measurement of spectra is repeated by operating ARES at different energies and matching the beam's position to the according transverse position in the TGU. By doing this, a beam with a finite energy spread which is dispersed transversely can be constructed by monoenergetic beamlets allowing to analyze the monochromaticity of the radiation spectra by studying the incoherently added radiation spectrum for each beamlet as shown in section 3.2.4.

For the second phase, five beamlets with the energy of 72 MeV, 76 MeV, 80 MeV, 84 MeV and 88 MeV each having 10 pC charge are considered. For the TGU40 with $\alpha$ = 139.7 1/m and $K_0$ =1.078 and a reference energy of 80 MeV, 1 mm separation distance is required for these beamlets to resemble an 80 MeV beam with $\Delta E / E_0 = \pm 10\%$ which is dispersed in 4 mm linear part of the TGU's transverse field. Since the energies of the beamlets and the field gradient of

---

[7] For simplicity and having the same beamline layout, the matched vertical beta functions for the all deflected beams are taken as the central beam at x=0.
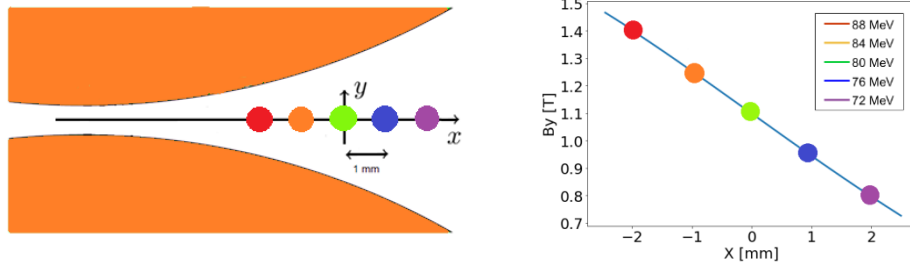
Figure 3.37: Left: Beamlets with different energies (coloured circles) are injected in different transverse positions (1 mm separation distance) inside the TGU. Right: The incoming beamlets' positions respect to the transverse magnetic field at *z=7λ/4* (considering the matching coils as the first period).

the TGU are matched, the expected radiation wavelength for all cases would be the same. The positions of the incoming beamlets inside the TGU (deflected by the steerers in the beam line) and respect to the on axis vertical magnetic field are demonstrated in Fig. 3.37. Table 3.4 lists the beams parameters which are simulated by ASTRA from the photocathode up to the end of the linac. The optimization was done to give the desired energy at the linac exit for each beam while transverse emittance and energy spread were set to be minimized in the optimization process. This allows minimizing the effect of the other parameters on the radiation when studying the radiation spectra. The matching conditions are the same as the first phase i.e. in the transverse plane, it is given by $\beta_x^{waist} \approx 0.1$ m as shown in Fig. 3.25. This leads to $\beta_{0x} = 0.54$ m and $\alpha_{0x} = 2.1$ according to equation (3.33). In the vertical plane, equation (3.31) with $K_0$ =1.078 and a reference energy of 80 MeV can be used for the beta matching. The matched Twiss parameters in the vertical plane then reads $\beta_{0y} = 0.334$ m and $\alpha_{0y}$ =0.[8]

| Parameter | Value (1) | Value (2) | Value (3) | Value (4) | Value (5) | Unit |
|---|---|---|---|---|---|---|
| Energy | 72 | 76 | 80 | 84 | 88 | MeV |
| Charge | 10 | 10 | 10 | 10 | 10 | pC |
| RMS Energy Spread | 0.05% | 0.045% | 0.03% | 0.062% | 0.047% | / |
| RMS Normalized Emittance (x/y) | 0.35 | 0.8 | 1.07 | 0.7 | 0.95 | μm-rad |
| RMS Beam Size (x/y) | 0.5 | 0.31 | 1.75 | 1.43 | 0.4 | mm |
| RMS Beam divergence (x/y) | 0.05 | 0.04 | 0.02 | 0.18 | 0.1 | mrad |
| RMS Beam Length | 0.22 | 0.33 | 0.1 | 0.12 | 0.24 | mm |

Table 3.4: Beam parameters at the exit of the linac simulated by ASTRA for the phase 2.

---

[8] The matching condition in the vertical plane for the beams with different energies is assumed to be the same to resemble the dispersed beam with a finite energy spread which has a matched vertical beta and alpha function as the central (reference) beam.

| Beam Parameter | Value (1) | Value (2) | Value (3) | Value (4) | Value (5) | Unit |
|---|---|---|---|---|---|---|
| Energy | 72 | 76 | 80 | 84 | 88 | MeV |
| Charge | 10 | 10 | 10 | 10 | 10 | pC |
| RMS Energy Spread | 0.05% | 0.045% | 0.03% | 0.062% | 0.047% | / |
| RMS Normalized Emittance (x/y) | 0.35 | 0.8 | 1.08/ 1.16 | 0.7 | 1/ 1.2 | μm-rad |
| RMS Beam Size (x/y) | 36/29 | 51/39 | 58 | 43/60 | 55/54 | μm |
| RMS Beam divergence (x/y) | 0.15/ 0.086 | 0.23/ 0.12 | 0.26/ 0.14 | 0.2/ 0.11 | 0.23/ 0.13 | mrad |
| RMS Beam Length | 0.21 | 0.34 | 0.1 | 0.12 | 0.24 | mm |

| Lattice Function | Value (1) | Value (2) | Value (3) | Value (4) | Value (5) | Unit |
|---|---|---|---|---|---|---|
| Beta functions (x/y) | 0.54/ 0.334 | 0.54/ 0.334 | 0.54/ 0.334 | 0.54/ 0.334 | 0.54/ 0.334 | m |
| Alpha (x/y) | 2.1/0 | 2.1/0 | 2.1/0 | 2.1/0 | 2.1/0 | / |
| Dispersion | 0 | 0 | 0 | 0 | 0 | m |

Table 3.5: Beam and lattice parameters at the entrance of the TGU for phase 2.

Since the initial beta and alpha functions for each case are different, the four quadrupoles before the first dipole (as the matching region) have been used to match the Twiss parameters of the incoming beam to the dogleg part as shown in Fig. 3.38. The quadrupoles' strengths (which are normalized by the momentum) downstream the dogleg would be the same as the first phase since the matching conditions are the same for the two phases. The beams and the lattice parameters for the tracked beams in the beamline are listed in Table. 3.5.
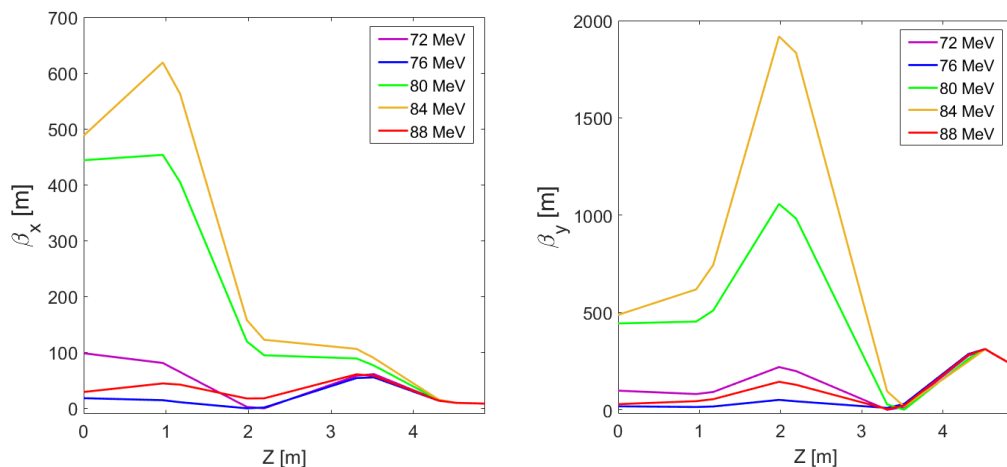


Figure 3.38: Evolution of the transverse beta functions after the exit of the linac up to the first dipole. The beta functions are matched to the dogleg section by the four quadrupoles downstream the linac.

The simulated radiation spectra for the second phase are plotted in Fig. 3.39. As a comparison with a normal undulator, which has a constant on axis vertical field in transverse plane, the radiation spectra for these beams with the same initial condition i.e. initial transverse position for a planar undulator with the same parameters as TGU40 are shown on the left side of fig. 3.39. For the planar undulator a constant on axis vertical field *B*=1.1 T is assumed. As can be seen from the figure, in the TGU40 case the wavelength of the emitted radiation for each beam with different initial transverse position (different initial K value) is close to the reference beam energy with $\lambda_0(80\,\mathrm{MeV}) = 338.65$ nm. Considering these beamlets as a beam with a finite energy spread which is dispersed transversely, the radiation bandwidth in the TGU40 case is reduced approximately by a factor of 6 with respect to the normal undulator case which has a bandwidth of $\Delta\lambda/\lambda_0 = 40\%$. The spectral broadening for this phase in comparison with the example shown in section 3.2.4 is due the finite emittance and energy spread of the beamlets which results also in a mismatch of the Twiss parameters respect to the design values. Moreover, to resemble a dispersed beam with a finite energy spread with these beamlets, the matching conditions (in the vertical plane) in this phase are just satisfied for the reference energy E=80 MeV, which results in the spectral broadening and flux reduction for the other beams with different energies and initial undulator parameters.
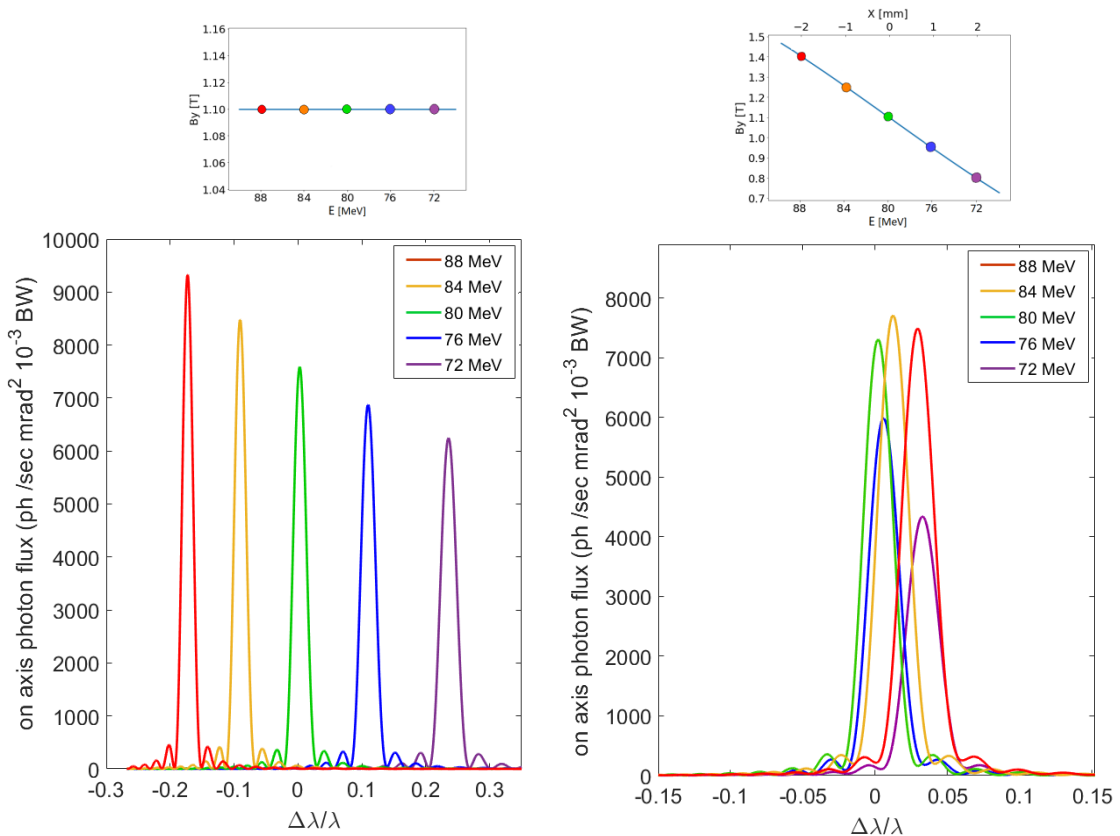


Figure 3.39: Radiation spectra on axis at 2 m distance at 1 Hz for the simulated beams of the second phase of the experiment for a planar undulator with constant undulator parameter K=1.078 (left) and the TGU40 case (right).

## 3.3.2.3 Phase 3

The main objective of the TGU experiment is to validate the TGU40 capability of producing monochromatic radiation with a beam with a finite energy spread. In this regard, for the third phase, an electron beam with considerably high energy spread will be produced by detuning the phases of the cavities of the Linac. The reference beam energy is $E_0$=80 MeV with 5% RMS energy spread. The RMS energy spread is chosen such that it covers the maximum energy band acceptance by the TGU40 i.e. $\Delta E / E_0 = \pm 10\%$. Moreover, 10 pC charge has been considered for this phase chosen for diagnostic purposes (sufficient number of photons for high resolution detection). The simulation of the beam from the photocathode up to the linac exit was done with ASTRA using the LISO optimizer. Fig. 3.40 shows the variation of the beam parameters during the acceleration.
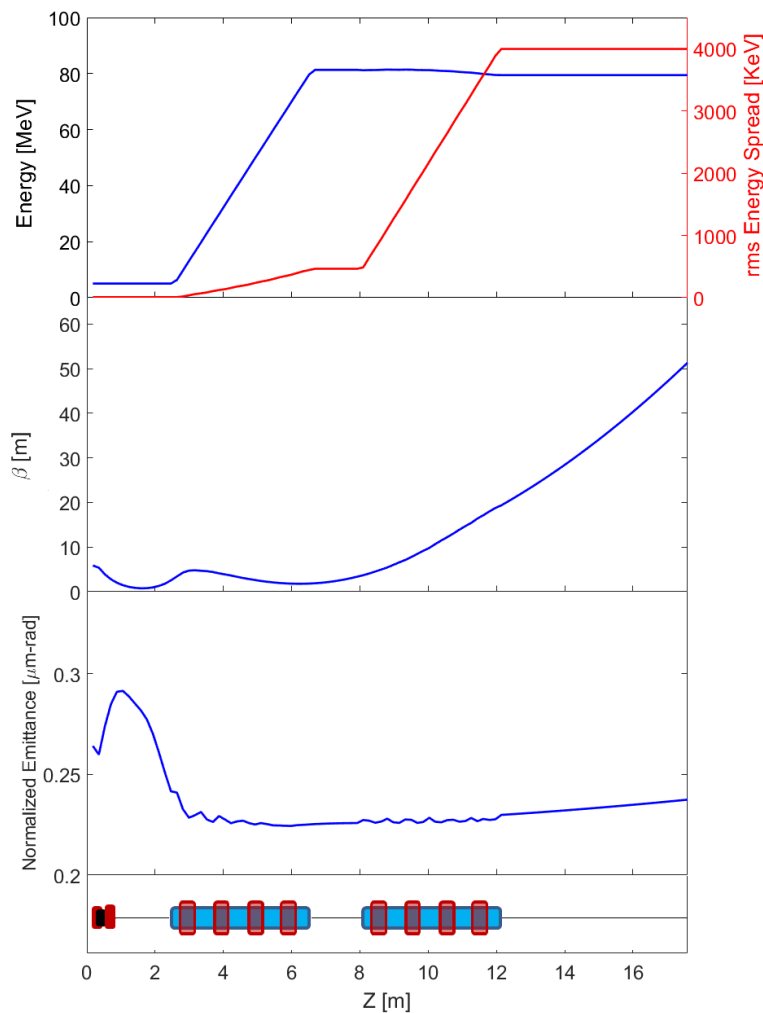


Figure 3.40: Evolution of energy, energy spread, beta and transverse emittances during the acceleration for the phase 3. The layout of the linac with RF gun (black rectangle), solenoid (red rectangle) and two TWSs (blue rectangle) is plotted at the bottom.

| Beam Parameter | Value | Unit |
|---|---|---|
| Energy | *80* | *MeV* |
| Charge | *10* | *pC* |
| RMS Energy Spread | *5%* | */* |
| RMS Normalized Emittance (x/y) | 0.22 | *µm-rad* |
| RMS Beam Size (x/y) | *0.28* | *mm* |
| RMS Beam divergence (x/y) | *0.02* | *mrad* |
| RMS Beam Length | *0.72* | *mm* |

Table 3.6: Beam parameters at the exit of the linac simulated by ASTRA for the phase 3.

The transverse emittances were set to be the main objective parameters to be minimized in the optimization process: reduce the radiation spectra broadening due the finite emittance of the beam (see section 3.2.6). Additionally, the minimum bunch length was limited as a constraint in the optimization for minimizing the CSR effect on the beam. The simulated beam parameters with ASTRA at the linac exit are listed in Table 3.6. The phase space plots of 200K macroparticles at the exit of the linac are shown in Fig. 3.41.
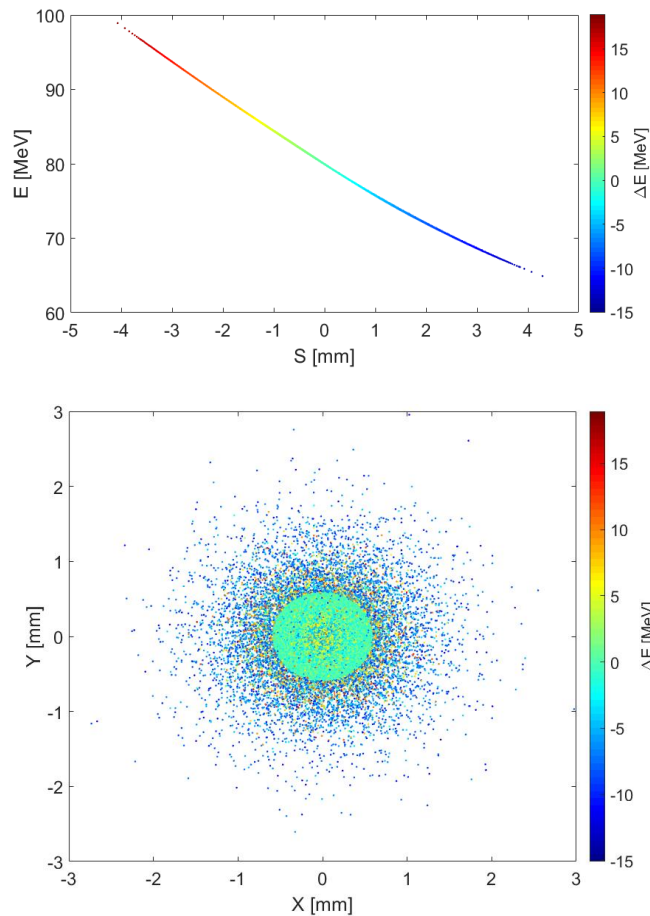


Figure 3.41: Phase space plots of 200K macroparticles at the linac exit for phase 3. The color code represents the energy changes with respect to the reference energy of $E_0$=80 MeV.
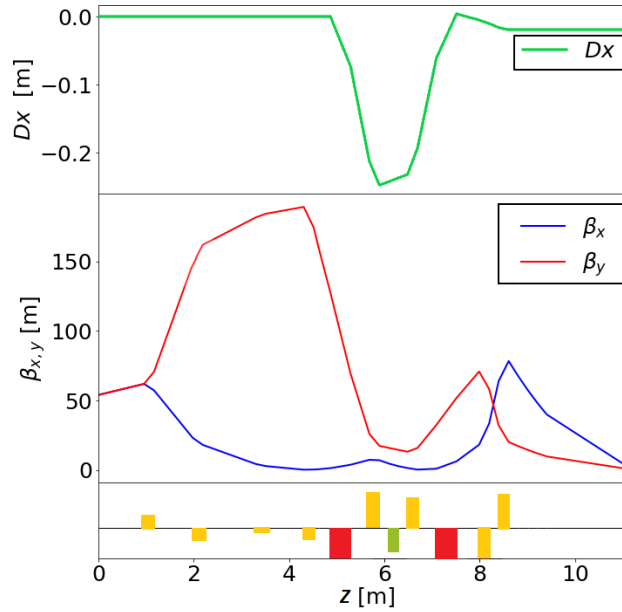
Figure 3.42: Dispersion Dx, and beta functions along the beamline for the phase 3 of the experiment. Layout of the beam transport with quadrupole (yellow), dipole (red) and sextupole (green) is plotted at the bottom.

The matching conditions for the vertical and horizontal beta and alpha functions are the same as the former phases i.e. in the transverse plane, it is given by $\beta_x^{waist} \approx 0.1$ m and in the vertical plane using equation (3.31) by $\beta_{0y} = 0.334$ m and $\alpha_{0y} = 0$. The transverse dispersion must be matched to the TGU according to the equation (3.4) such that for $\alpha$ = -139.7 1/m and $K_0$ = 1.078 it is calculated $D$ = -19.6 mm and D'=0. The dispersion created by the first dipole is matched to the TGU using the downstream quadrupoles[9]. The evolution of the beta functions and the transverse dispersion along the beamline are shown in Fig. 3.42. The position of the dispersed beam inside the TGU and respect to the on axis vertical magnetic field are illustrated in Fig. 3.43.
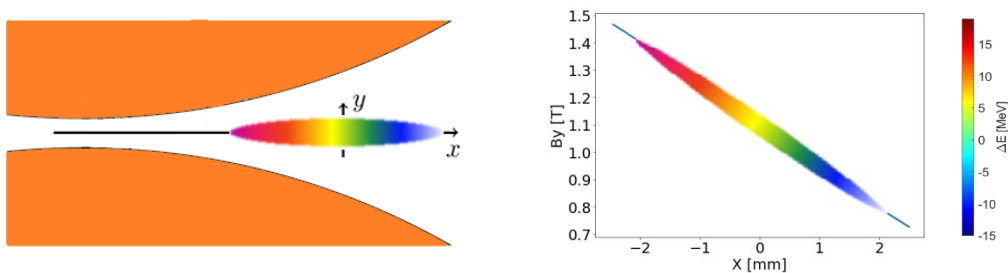


Figure 3.43: Left: Side view of the TGU with incoming dispersed beam (color-coded) injected at the center. Right: The incoming beam position respect to the transverse magnetic field at $z=7\lambda/4$ (considering the matching coils as the first period). The colorbar indicates the energy changes respect to the reference energy of $E_0$=80 MeV.

---

[9] The deflection angles of the dipoles are constant and cannot be changed.
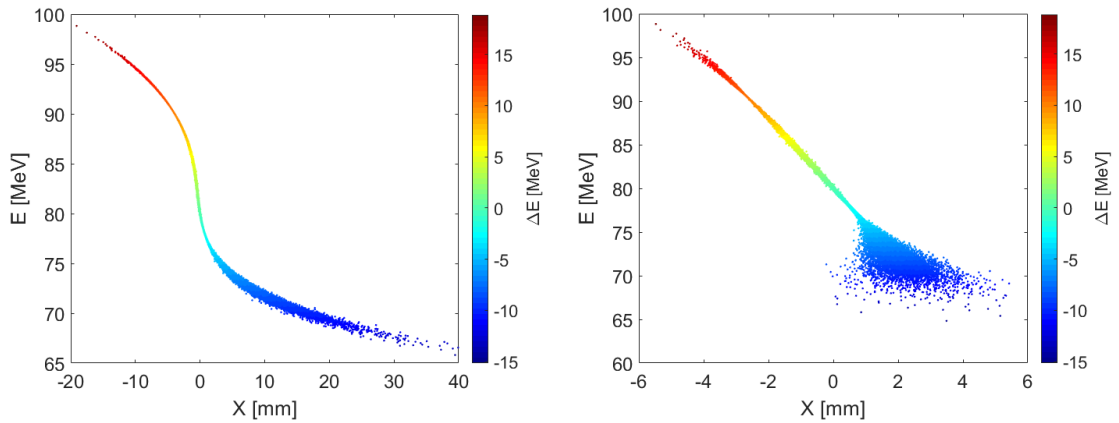
Figure 3.44: Dispersion distributions without the sextupole (left) and with the sextupole (right).

Since the beam suffers from a high energy spread chromatic correction is needed to compensate the chromatic emittance growth. As can be seen from Fig. 3.26, emittance growth leads to a reduction in the flux density and also an increase in the radiation bandwidth. Moreover, having particles with a large energy deviation from the reference energy causes a nonlinear effect on the beam dispersion, after focusing by the quadrupoles. The resonance condition equation (3.5), can only be satisfied by keeping the dispersion function constant along the TGU i.e. $D'$=0. Introducing a nonlinear dispersion due to the chromatic effect will break the resonant condition. For correction a sextupole is considered in the beamline to reduce the chromatic effects. The effect of the sextupole on the dispersion distributions at the entrance of the TGU is shown in Fig. 3.44. It can be observed that the nonlinearity in the dispersion is eliminated by using the sextupole. In Fig. 3.45 the evolutions of transverse normalized emittances (without dispersion contribution) along the beamline for two cases with and without chromatic correction are presented. With the sextupole, the chromatic transverse emittance growth is considerably suppressed.
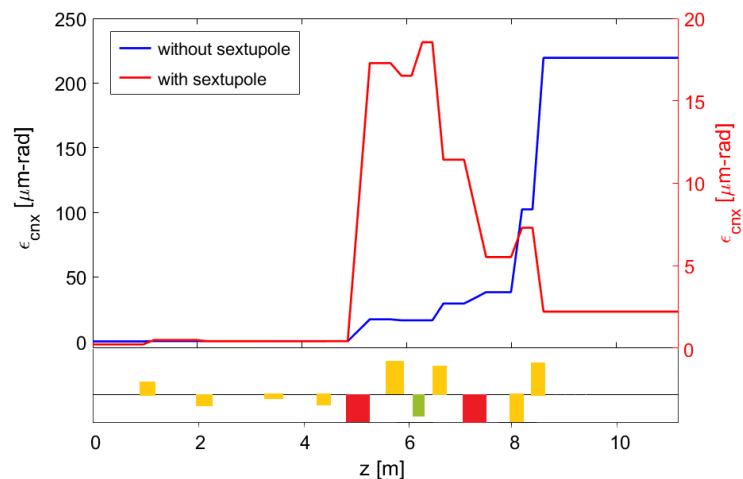


Figure 3.45: Evolution of the normalized transverse emittance along the beamline with and without the sextupole. The emittance is without dispersion contribution.

| Beam Parameter | Value | Unit |
|---|---|---|
| Energy | *80* | *MeV* |
| Charge | *10* | *pC* |
| RMS Energy Spread | *5%* | */* |
| RMS Normalized Emittance (x/y) | *35.28/2.63* | *μm-rad* |
| RMS Beam Size (x/y) | *0.97/0.31* | *mm* |
| RMS Beam divergence (x/y) | *0.28/0.06* | *mrad* |
| RMS Beam Length | *1.52* | *mm* |

| Lattice Function | Value | Unit |
|---|---|---|
| Beta functions (x/y) | *0.54/0.334* | m |
| Alpha (x/y) | *2.1/0* | */* |
| Dispersion | *-0.0196* | m |
| Dispersion slope | *0* | */* |

Table 3.7: Beam and lattice parameters at the entrance of the TGU for the phase 3.

The beam parameters and the lattice functions at the entrance of the TGU are listed in Table 3.7. The transverse size of the dispersed beam at the entrance of the TGU40 is larger than the transverse size of the linear part of the vertical magnetic field which is roughly $\Delta x \approx \pm 2\,\text{mm}$ with respect to the center of the TGU40. For this reason, a rectangular slit is considered in front of the TGU to remove the unwanted particles. In the transverse plane the slit has a width of $\Delta x = \pm 2\,\text{mm}$ similar to the width of the linear region. The vertical size of the slit is set to the minimum gap width of the TGU i.e. on the symmetry axis $\Delta y = \pm 0.55\,\text{mm}$. The beam transverse profile and the dispersion distribution for 200K macroparticles at the entrance of the TGU after passing the slit are depicted in Fig. 3.46.
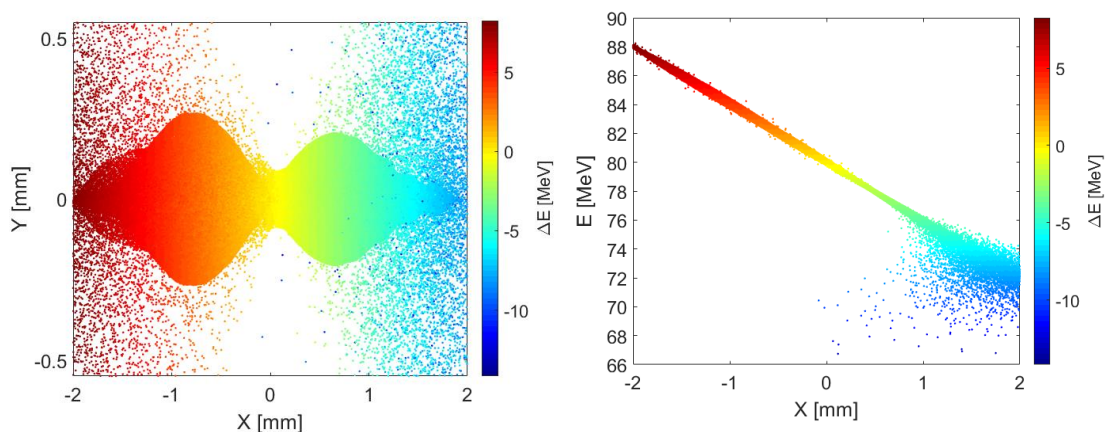


Figure 3.46: Phase space plots of 200K macroparticles at the entrance of the TGU after passing the ideal rectangular slit for phase 3. The color code represents the energy changes respect to the reference energy of $E_0$=80 MeV.

It should be noted that less than 6% of the particles are removed by the slit and the charge is dropped to 9.4 pC. Moreover, the effect of the collimator wakefields on the transverse phase space of the beam is neglected in the simulations. In fact, considering the beam parameters of the phase 3, the transverse emittance growth due to the collimator slit is negligible [55, 56].

The simulated radiation spectra for the third phase are plotted in Fig. 3.47. The spectra are on axis and calculated at 2 m distance at 1 Hz repetition rate. As a comparison with a normal planar undulator, the radiation spectra for a beam with the same parameters (Twiss parameters, emittances, charge, etc.) as the tracked beam without transverse dispersion are shown in Fig. 3.47. Here the planar undulator parameters are assumed to be the same as the TGU40 parameters with a constant on axis vertical field $B = 1.1$. In the TGU case, despite of having considerably large RMS energy spread $\sigma_\delta = 5\%$, the radiation bandwidth $\Delta\lambda / \lambda = 2.71\%$ is close to the natural bandwidth of the undulator $\Delta\lambda / \lambda = 1 / N_u = 2.5\%$. The spectral peak flux is not located at the reference energy wavelength of $\lambda_0(80\,\mathrm{MeV}) = 338.65\,\mathrm{nm}$ and is shifted towards longer wavelength at 340 nm. This spectral shift is the result of the finite emittance of the beam as explained in sec. 3.2.6. The TGU capability of producing monochromatic radiation is more evident by comparing it with the normal planar undulator case. As can be seen from Fig. 3.47, the radiation bandwidth in the planar case is increased by a factor of 9 respects to the TGU case. Likewise, the photon flux is dropped by a factor of 7.
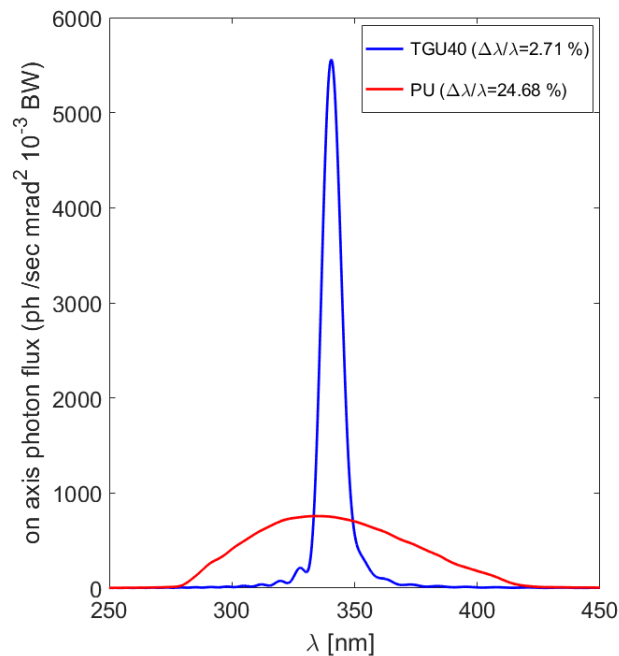


Figure 3.47: Radiation spectra on axis at 2 m distance at 1 Hz for the simulated beam of the third phase of the experiment for the TGU40 and a planar undulator (PU) with the same parameters. For the planar case a beam with the same parameters but without dispersion is assumed.

# 3.3.2.4. Collective Effects

Space charge forces and radiation effects can strongly affect the electron beam, changing the energy of the electrons inside the bunch and increasing the energy spread and beam emittance. Therefore, it is important to investigate the influence of these collective effects on the beam dynamics. Space-charge (SC) and coherent synchrotron radiation (CSR) are the most important ones, which are studied in this sub-section.

- **Coherent Synchrotron Radiation**

When charged particles undergo radial acceleration they generate electromagnetic radiation known as "synchrotron radiation". This typically happens in dipoles in the beam line, where the particles take a curved path. Generally, depending on the coherence of the emission, the synchrotron radiation can be divided into three main regimes as incoherent, fully coherent and partially coherent. Assuming an electron beam with normalized energy $\gamma$, containing $N_e$ electrons, which goes through a dipole with bending radius R, the total emitted power for these three cases are given by [57-59]

$$P_{ic} = N_e \frac{1}{6\pi\varepsilon_0} \frac{ce^2\gamma^4}{R^2},$$

(3.38)

$$P_{fc} = N_e^2 \frac{1}{6\pi\varepsilon_0} \frac{ce^2\gamma^4}{R^2},$$

(3.39)

$$P_{pc} \approx 0.0279 N_e^2 \frac{ce^2}{\varepsilon_0} \frac{1}{R^{2/3}\sigma_z^{4/3}}$$

(3.40)

respectively. For the partially coherent regime, the emitted power does not depend on the energy of the beam and it scales with the bending radius and the bunch length. Comparing equations (3.38-40) leads to an estimation of the bunch lengths where transitions between the regimes occur. The radiation from a bunch with length $\sigma_z$ can be considered as partially coherent when

$$N_e^{3/4} \gg \frac{\sigma_z}{\sigma_0} \gg 1$$

(3.41)

with $\sigma_0 = R/\gamma^3$. The upper and lower limits of equation (3.41) correspond to the incoherent and fully coherent cases, respectively. Assuming an electron beam that moves in a curved trajectory, the emitted radiation by the tail of the bunch can interact with the head of the bunch at the later time. As shown in Fig. 3.48, the path length difference between the straight line and the curved path for $\theta \ll 1$ can be approximated as

$$d = arc(AB) - AB = R\theta - 2R\sin(\frac{\theta}{2}) \approx \frac{R\theta^3}{24}$$

(3.42)
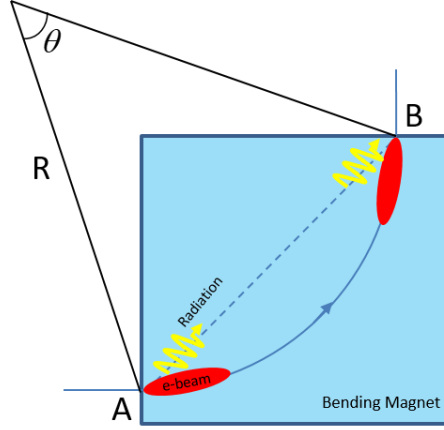
Figure 3.48: Illustration of bunch head and tail interaction due to CSR in a dipole.

For a bunch of length $\sigma_z$ equal or less than the path length difference $d$, the radiation generated in the bunch tail can overtake the head of the bunch. The overtaking length is defined as

$$L_o \equiv AB = (24\sigma_z R^2)^{1/3} \tag{3.43}$$

which is the length that light slips exactly over the bunch length. For a dipole with the length of $L_b > L_o$, all electrons will be located in the interaction region. The transferred energy from the tail to the head causes an induced energy change related to the longitudinal position of the electrons within the bunch. This can lead to a reduction of the beam mean energy and growth of the energy spread along the bunch. Furthermore, the energy modification along the bunch will cause a transverse emittance growth in the dispersive sections due to the change of transverse offset and divergence on the bending plane [60].

## • Space-Charge

The space-charge force is caused by the electromagnetic fields generated by the particles inside the beam itself. The transverse space-charge force for a symmetrical Gaussian beam in the cylindrical coordinate system is given by [61]

$$F_r(r,z) = \frac{e}{2\pi\varepsilon_0\gamma^2} \frac{q_0}{\sqrt{2\pi}\sigma_z} \exp(\frac{-z^2}{2\sigma_z^2}) \left( \frac{1-\exp(\frac{-z^2}{2\sigma_z^2})}{r} \right) \tag{3.44}$$

with the total charge $q_0$, the Lorentz relativistic factor $\gamma$ and the bunch length $\sigma_z$, which scales with $1/\gamma^2$ due to the focusing contribution of the azimuthal magnetic field. Equation (3.44) shows a nonlinear radially defocusing force for $r > \sigma_z$, which result in an emittance growth by distortion of the phase space.

71

In the longitudinal plane, space-charge forces can have a significant impact on the beam length and longitudinal energy distribution of the particles. For a beam with a uniform transverse distribution and an arbitrary non-uniform longitudinal profile $\lambda(z)$, the longitudinal space-charge force can be calculated as [61]

$$F_z(r,z) = \frac{-e}{4\pi\varepsilon_0\gamma^2}\left(1 - \frac{r^2}{\sigma_r^2} + 2\ln\frac{b}{\sigma_r}\right)\frac{\partial\lambda(z)}{\partial z} \tag{3.45}$$

where $\lambda(z)$ is the transverse beam size and $b$ is the beam pipe radius. Like the transverse space charge force, the longitudinal one also scales with $\gamma^{-2}$ and therefore can be neglected for high energy beams. The dependency of the longitudinal force on the slope of the density can result in an unwanted energy modulation along the bunch.

## • Simulation Study

The space-charge and the coherent synchrotron radiation effects have not been considered in the simulations so far. The optimization of each phase, considering the bunch length and charge, has been done such that these collective effects have the minimum impact on the beam and as a result on the radiation spectra. In order to study these effects in the beamline, OCELOT and ELEGANT, which include 3D SC and 1D CSR module, respectively, have been used. It should be noted that both modules at the same time cannot be taken into the account by neither of these codes. It is found that the SC and CSR both have negligible impact on the beam parameters. The beam parameters at the entrance of the TGU with and without space charge and CSR effects for the phase 3 are listed in table. 3.8. Moreover, the influence of these forces on the dispersion distribution is plotted in Fig. 3.49. As can be seen from the figure there is approximately no change in the dispersion by including the collective effects.

| Beam Parameter | Value (no SC/CSR) | Value (SC) | Value (CSR) | Unit |
|---|---|---|---|---|
| Energy | 80 | 80 | 80 | MeV |
| Charge | 10 | 10 | 10 | pC |
| RMS Normalized Emittance (x/y) | 35.28/2.63 | 36.51/2.62 | 36.46/2.63 | μm-rad |
| RMS Beam Size (x/y) | 0.97/0.31 | 0.94/0.31 | 0.94/0.31 | mm |
| RMS Beam divergence (x/y) | 0.28/0.06 | 0.30/0.06 | 0.30/0.06 | mrad |
| RMS Beam Length | 1.52 | 1.53 | 1.53 | mm |

Table 3.7: Beam and lattice parameters at the entrance of the TGU for the phase 3 with and without collective effects.
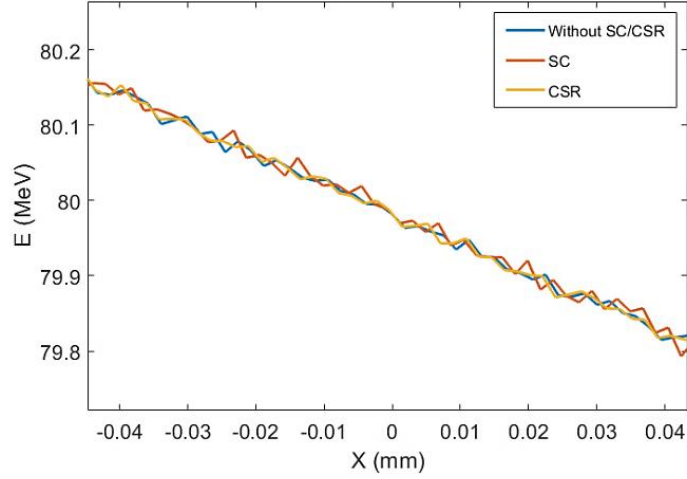
Figure 3.49: Beam transverse energy distribution at the entrance of theTGU with and without collective effects including space charge and CSR.

The tiny effect imposed by SC on the beam can also be realized by calculating the laminarity parameter, which is defined as the ratio between the space-charge term and the emittance contribution in the rms beam envelope equation. Using paraxial ray approximation $p_x \ll p_z$ for an axisymmetric beam with peak current $I^{peak}$, transverse size $\sigma$ and transverse normalized phase space emittance $\varepsilon_n$, the rms envelope equation in the absence of any external focusing forces reads [62, 63]

$$\sigma'' + \frac{\gamma'}{\gamma}\sigma' - \frac{K_{sc}}{(\beta\gamma)^3\sigma} - \frac{\varepsilon_n^2}{(\beta\gamma)^2\sigma^3} = 0 \tag{3.46}$$

where $K_{sc} = I^{peak}/2I_A$ is the beam perveance, $I_A$ is the Alfven current (~17 kA) and $\beta$ and $\gamma$ are the normalized velocity and the normalized energy, respectively. Therefore, the laminarity parameter is given by the ratio between the third term (SC contribution) and the fourth term (emittance contribution) in equation (3.46) [64]

$$\rho = \frac{I^{peak}}{2I_A\beta\gamma}\frac{\sigma^2}{\varepsilon_n^2} \tag{3.47}$$

For the values of $\rho < 1$ the space-charge effects can be neglected and the evolution of the beam envelope is dominated by the beam emittance. In the case of an asymmetric beam $(\sigma_x \gg \sigma_y)$ and assuming no energy change, two envelope equations for $\sigma_x$ and $\sigma_y$ become [65]

$$\sigma_x'' = \frac{I^{peak}}{I_A(\beta\gamma)^3(\sigma_x + \sigma_y)} + \frac{\varepsilon_{nx}^2}{(\beta\gamma)^2\sigma_x^3} \tag{3.48}$$

$$\sigma_y'' = \frac{I^{peak}}{I_A(\beta\gamma)^3(\sigma_x + \sigma_y)} + \frac{\varepsilon_{ny}^2}{(\beta\gamma)^2\sigma_y^3} \tag{3.49}$$

and the laminarity parameter can be defined for each plane separately. This is shown in Fig. 3.50, where the evolutions of the laminarity parameters along the beam line are plotted. Both parameters stay below 1 during the transport. Due to the increased transverse beam size after the dipole, the emittance terms in equations (3.48-49) are largely dominant over the space charge terms and the beam is so-called emittance dominated.
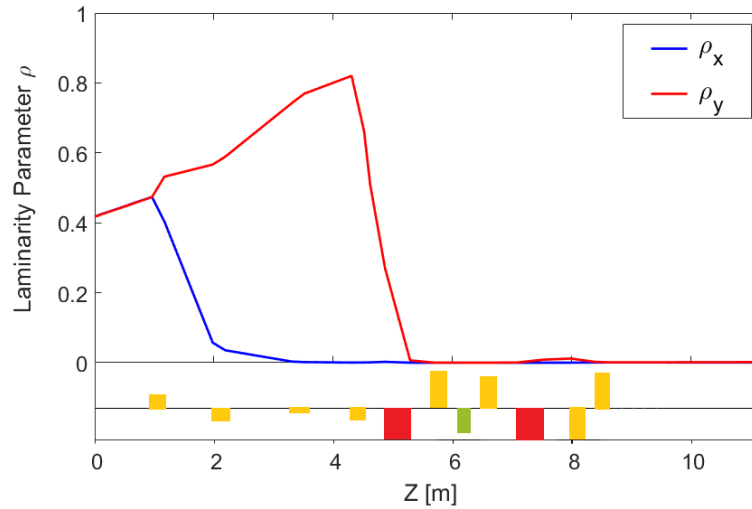


Figure 3.50: Laminarity parameters for each plane according to equations (3.58-59) along the beam line.

# 3.4 Conclusion

Conventional undulators can produce radiation with a narrow relative spectral width if the electron beam has a relatively small energy spread. The electron beams generated in more compact electron sources like laser plasma accelerators (LPAs), which can produce high quality beams for Free electron lasers (FELs), suffer from a large energy spread. This limitation leads to a degrading effect in the FEL gain and power and prohibits FEL lasing. In order to overcome this limitation, modified undulator schemes, so-called transverse gradient undulators (TGUs), were proposed and a first superconducting TGU was built at Karlsruhe Institute of Technology (KIT), Karlsruhe, Germany.

In this chapter, the concept of the transverse gradient undulator has been studied in detail. The concept relies on fulfilling the resonance condition for different particles' energy in an electron beam with a large energy deviation from the mean value. The energies of the particles in the incoming beam, which is dispersed transversely, are matched to the transverse magnetic field gradient of the TGU such that the resonance condition is satisfied for the all particles with different energies that results in a narrow radiation bandwidth.

The transverse magnetic field gradient can be generated by using two cylinders with superconducting wires wound around them. This layout was used to build a first superconducting TGU at KIT with 40 periods (TGU40). A collaboration between KIT, University of Jena and DESY was formed to prepare a first experimental test with TGU40 at the ARES Linac at SINBAD. In this regard, a test experiment has been designed in the dogleg section of the ARES to validate the capability of the TGU40 in producing monochromatic radiation.

The experiment is divided into three phases and for each phase start-to-end simulations have been performed. The first two phases are for the aligning and also magnetic field verification of the TGU40 while the purpose of the third phase of the experiment is to validate the TGU concept by demonstrating the TGU capability in the enhancement of the flux and monochromaticity of the radiation. The phases of the experiment and the experimental setup have been presented in detail in this chapter and the simulation results have been shown for each phase of the experiment. The simulation results prove that the TGU scheme can compensate the energy spread in the electron beam and produce monochromatic radiation with a bandwidth in the order of natural undulator bandwidth.

# Chapter 4

# Generation of FEL Radiation Using Transverse Gradient Undulator

In this chapter the possibility of using transverse gradient undulators for generating FEL radiation is studied. The goal of this study is to investigate the required beam parameters for generating FEL radiation with a laser plasma accelerator using a transverse gradient undulator. After a successful test of the TGU40 one can perform an experiment by attaching the TGU to a laser plasma accelerator and demonstrating FEL lasing. For the undulator parameters the same parameter set as for the TGU40 is assumed, but with a longer undulator length of 5 m. The nominal LPA beam parameters are chosen based on the currently achievable parameters from the laser plasma accelerators, but the combination of all parameters might be still challenging. In this regard, the study has been done by scaling the parameters over a reasonable range which can be reached by optimizing the LPA setup.

## 4.1 FEL Challenges

Free electron lasers are recognized as the premier source of tunable, intense and coherent radiation, from the far infrared down to the hard X-ray regime. In an FEL a relativistic electron beam passes through an undulator which has a periodic magnetic field. The wiggled electrons then emit synchrotron radiation that can interact with the electrons in the beam. An energy modulation (density modulation) on the scale of the radiation wavelength occurs that leads to coherent radiation with an exponentially raising power. The dependency of the radiation wavelength on the undulator period and the electron beam energy makes the FEL a tunable radiation source. This transformation of the kinetic energy of the electron beam into tunable, intense and coherent electromagnetic radiation in the X-ray region with a peak power in the

Gigawatt range have established FELs as powerful light sources in the X-ray regime. They have become powerful tools for scientific experimentation [66].

The efficiency of the FEL radiation output is often determined through the FEL parameter (Pierce parameter) $\rho$, which is a measure of the FEL performance with respect to the electron beam quality at the undulator. In order to maximize the output power and to decrease the gain length the FEL parameter should be maximized. The FEL beam requirements can also be obtained based on the FEL parameter which is given by equation (2.70). As a first requirement, a high peak current electron beam is needed to have a larger $\rho$ and shorter gain length. By reducing the FEL gain length the output power can be saturated in a shorter distance, that means shorter undulator length and less space is needed. The FEL parameter also can be maximized by reducing the transverse beam size which is usually expressed in terms of the transverse emittance. Having a beam with lower emittance allows maintaining a small beam size over the undulator length. Moreover, lower emittance leads to having an efficient overlap between the electrons and the radiation, see equation (2.87). The third requirement is given by equation (2.82) which demands a very low initial energy spread within the electron beam. For a typical value of the FEL parameter $\rho=10^{-3}$ an energy spread of 0.05% is needed, showing the importance of having a large FEL parameter.

These three requirements of the X-ray FEL beam i.e. high peak current, low emittance and small energy spread can be met by conventional RF based accelerators. On the other hand, providing all requirements simultaneously needs some consideration in the setup of the linac. For example, due to the low initial energy of the electrons in the gun region the space charge prevents having high charge beam after extraction of the electron from the cathode. Therefore, to increase the current bunch compressors are implemented in the beamline after the RF cavities. Even with the bunch compressors in the beamline the achievable peak currents are on the order of a few kA[1] [67].

Another limiting factor in conventional accelerators is the maximum achievable gradient by the RF cavities. The maximum accelerating electrical field provided by the RF cavities is on the order of 100 MV/m due to the RF breakdown [68, 69]. Operating the X-ray FEL in the nanometer to angstrom range needs energies on the order of 1-10 GeV. Accelerating an electron beam with RF cavities to this energy requires at least an accelerator length of 10-100 m. Moreover, with a few kA peak current and GeV energy range an undulator with typical length of 100 meters is needed to reach FEL saturation power.

Hence the main problem of such photon sources is the large size of the facility including long accelerators along with the beam transport line and the undulator section which extends over ten to a hundred meters. The large-scale, accompanied by high cost and space requirements, limit, the availability of these radiation sources. Therefore, the need for new technologies particularly in the acceleration part is inevitable to overcome these problems. In this regard,

---

[1] The limitation is due to the CSR effect in the magnetic chicane and the upper band of tolerable energy spread of the FEL.

novel acceleration techniques have been developed during the past decades reduces the size and the cost [70]. Aiming to reach high accelerating gradient above the GeV/m-range to reduce the size of the accelerator, different innovative acceleration methods like terahertz-driven accelerators (THzAs) [71], dielectric laser accelerators (DLAs) [72] and plasma-based accelerators (PBAs) [28] have been proposed.

Although with these new acceleration techniques a high accelerating gradient in the GeV/m-range can be realized in a short distance, due to the limitations related to the maximum achievable peak current, only the laser plasma accelerators seem to be a good match for the FEL. The combination of having an ultra-short acceleration distance with high peak current of multiple kA and small transverse emittance electron beam makes laser plasma accelerators a favorable accelerator for the next generation of compact FEL light sources [73, 74].

The greatest obstacle that prevents successful FEL lasing using such sources is the electron beam energy spread which is typically about 1-5%. While in recent years the energy spread of the produced beams has been reduced down to one percent, it is still the major limiting factor in an FEL concept in combination with the other beam parameters like the transverse emittance and peak current. In fact, increasing the peak current into the multi kA-range while keeping the energy spread lower the percent level is challenging for current laser plasma-based accelerators and has remained an issue for FELs' applications.

Several techniques have been studied to minimize the energy spread by mitigating the correlated energy spread induced by the steep slope of the accelerating fields [75-78]. Even with those concepts the energy spread of PBAs generated beams remains of a few percent-ranges. Other concepts use beam phase space manipulation techniques to reduce local energy spread by passing the electron beam through a chicane. The electrons are sorted by their energies, leading to a reduction of the slice energy spread and also minimizing the FEL performance degradation due to slippage effect [74 -81].

Another approach to handle the large energy spread is using a transverse gradient undulator as it was proposed in early FEL days by Smith et al. to reduce the sensitivity to the electron energy jitter for FEL oscillators [9]. The scheme is based on mitigating the energy spread problem by properly dispersing the electron beam and matching the energy of the particles to the transverse field of the undulator. The matching can be done by introducing a linear transverse field dependence in the undulator. The compensation of the energy spread leads to an increase in the saturation power and shortening the gain length. In the following sections the TGU concept from an FEL point of view is presented in detail followed by a scaling of the nominal LPA beam parameters to investigate the minimum beam requirement for the FEL lasing demonstration experiment.

## 4.1.1 Energy Spread Effect

In the case of a mono-energetic beam which is on resonance $\eta=0$ and neglecting the space charge $K_p=0$ the power increase of an FEL can be described by three eigenvalues which are given by equation (2.72). It can be shown that the eigenvalue equation for a beam with energy spread $\sigma_\eta > 0$ including space charge and detuning $\eta$ in the 1D case is given by [16]

$$\alpha = (i\Gamma^3 - k_p^2 \alpha) \int_{-\delta}^{+\delta} \frac{F_0(\eta)}{(\alpha + i2k_u\eta)^2} d\eta \tag{4.1}$$

where $\Gamma$ is the gain parameter, $K_p$ is the space charge parameter and $F_0(\eta)$ is the energy distribution of the electron beam. Defining normalized energy spread as $\Delta = \sigma_\eta / \rho$ the above equation can be solved analytically for a Gaussian energy distribution in two cases: $\Delta \gg 1$ and $\Delta \ll 1$ regarding the optimum detuning [18]. These two asymptotic cases can be approximated by the eigenvalue of the form [2][21]

$$\Re(\alpha_1) \approx \frac{\sqrt{3}\Gamma}{2(1+\Delta^2)} \tag{4.2}$$

The typical FEL beam energy spread requirement, equation (2.82), can be realized from Fig. 4.1, where the growth rate function is defined as

$$f_{gr} = 2\Re(\alpha_1)L_{g0} \tag{4.3}$$

with $L_{g0}$ to be the one-dimensional gain length. It is plotted as a function of normalized energy spread $\Delta = \sigma_\eta / \rho$. As can be seen from the figure for $\Delta = 0.5$ the growth rate decreases to 80% of its maximum. For an energy spread $\sigma_\eta \approx \rho$ the gain length is doubled with respect to the 1D ideal gain length $L_{g0}$.

In a simplified view the requirement can be understood as the need that the change of the resonance wavelength due to the beam energy spread must be less than the natural FEL bandwidth. Since the FEL bandwidth can be approximated by the FEL parameter $\rho$, taking equation (2.47) into account leads to

$$\frac{\Delta\lambda}{\lambda} < \rho \;\rightarrow\; \frac{2\Delta\gamma}{\gamma} < \rho \;\rightarrow\; \sigma_\eta < \frac{\rho}{2} \tag{4.4}$$

If this condition is satisfied, the contribution of off-resonant electron energies in the change of pondermotive phase over one gain length is much less than unity [19].

---

[2] The power growth is realized by the real part of $\alpha_1$, $P(z) \propto \exp(2\Re(\alpha_1)z)$.
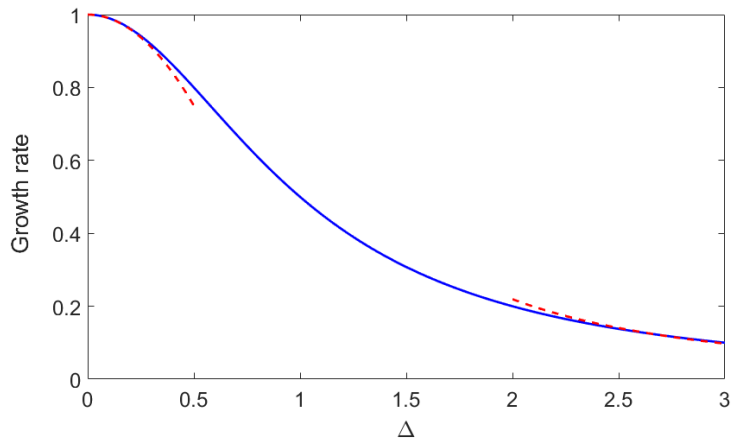
Figure 4.1: Growth rate as a function of normalized energy spread Δ according to equation (4.2). The dashed lines show the asymptotic cases for small and large normalized energy spread.

Fig. 4.2 shows the FEL power drop and gain length increase along the undulator for different values of the normalized energy spread. The power and the undulator length are normalized by the saturation power and saturation length in the case of a zero-energy spread electron beam, respectively.

For a linear accelerator based FEL the typical Pierce parameter is about $\rho \approx 10^{-3}$-$10^{-4}$ and therefore the energy spread requirement for the FEL lasing is challenging. The importance of having low energy spread beam is more pronounced for FELs operating in the X-ray regime due their to having small Pierce parameter [82, 83].
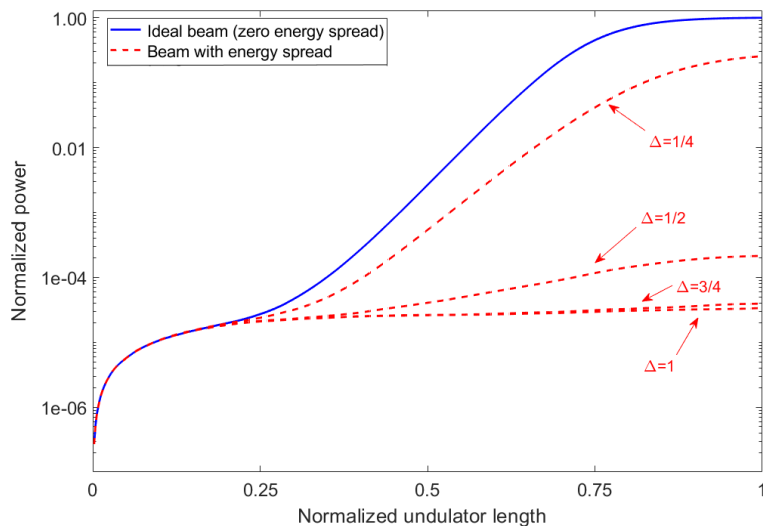


Figure 4.2: FEL power as a function of normalized undulator length for different values of normalized energy spread.

# 4.2 TGU FEL

Including the effect of a finite energy spread (Gaussian) in the electron beam the gain length can be described by [10]

$$L_g \approx \frac{\lambda_u}{4\pi\sqrt{3}\rho}\left(1+\frac{\sigma_\eta^2}{\rho^2}\right) \tag{4.5}$$

However, In the TGU case the beam is dispersed transversely and the beam size after the dispersive medium is given by the dispersion $D$ and the energy spread $\sigma_\eta$

$$\sigma_T = (\sigma_x^2 + D^2\sigma_\eta^2)^{1/2} = \sigma_x\left(1+\frac{D^2\sigma_\eta^2}{\sigma_x^2}\right)^{1/2} \tag{4.6}$$

Since the FEL parameters $\rho$ is proportional to $\rho \propto \sigma_x^{-1/3}$ this increased beam size and the reduction of the beam density lead to an effective FEL parameter as

$$\rho_T^{\mathrm{eff}} = \rho\left(1+\frac{D^2\sigma_\eta^2}{\sigma_x^2}\right)^{-1/6} \tag{4.7}$$

where the index $T$ stands for the TGU case. Moreover, the local energy spread decreases due the stretching of the bunch in the transverse plane which results in an effective energy spread

$$\sigma_\eta^{\mathrm{eff}} = \sigma_\eta\left(1+\frac{D^2\sigma_\eta^2}{\sigma_x^2}\right)^{-1/2} \tag{4.8}$$

Thus, the equivalent 1D gain length for a TGU reads [67]

$$L_g^T \approx \frac{\lambda_u}{4\pi\sqrt{3}\rho_T^{\mathrm{eff}}}\left(1+\frac{\sigma_\eta^{\mathrm{eff}\,2}}{\rho_T^{\mathrm{eff}\,2}}\right) \tag{4.9}$$

By increasing the dispersion $D$ both $\rho_T^{\mathrm{eff}}$, $\sigma_\eta^{\mathrm{eff}}$ and as well as their ratio decrease which induces a gain length reduction with respect to the case without TGU (normal planar undulator) for $\Delta = \sigma_\eta/\rho$ when energy spread is the dominant effect. This is shown in Fig. 4.3 where the gain length ratio i.e. the gain length including the energy spread effect over the ideal gain length $L_{g0}$ as a function of normalized energy spread $\Delta$ is plotted on the left. For $\Delta = \sigma_\eta/\rho$ the gain length increases due to the energy spread being mostly compensated by the TGU. The right plot shows the effect of the TGU on the growth rate function, equation (4.3), in comparison with a normal planar undulator. Note that the TGU cases are plotted for optimum dispersion (see below).
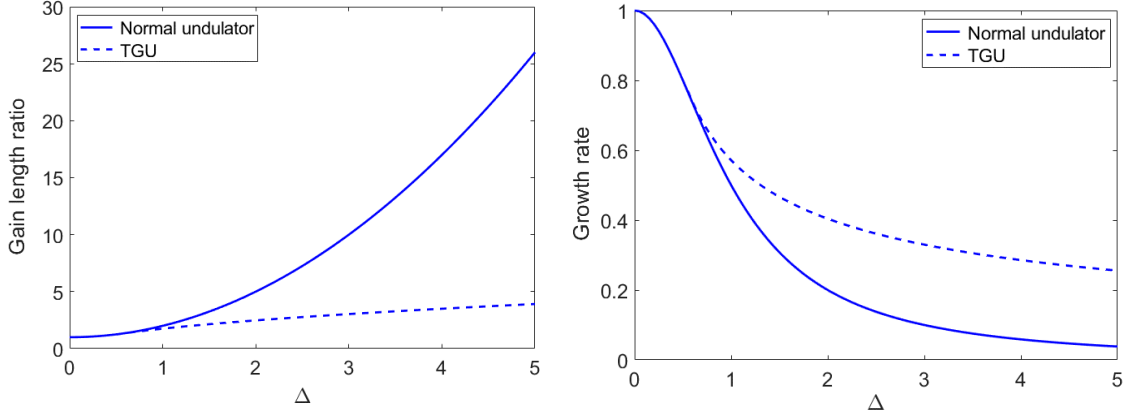
Figure 4.3: Left: Gain length ratio vs normalized energy spread for a TGU and a normal planar undulator. Right: Growth rate as a function of normalized energy spread for a TGU and a normal planar undulator. In both plots the TGU case is plotted for optimum dispersion.

By introducing the parameter n as the ratio of dispersed beam size and initial beam size

$$n = \frac{\sigma_T}{\sigma_x} \tag{4.10}$$

and using normalized energy spread $\Delta = \sigma_\eta / \rho$, then equation (4.9) can be written as [85]

$$L_g^T = L_{g0}\left(n^{1/3} + \frac{\Delta^2}{n}\right) \tag{4.11}$$

which can be minimized for optimum n

$$n_{\mathrm{opt}} = 3^{3/4}\Delta^{3/2} \tag{4.12}$$

Therefore, the minimum gain length can be estimated as

$$L_{g,\min}^T \approx 1.75\,L_{g0}\Delta^{1/2} \tag{4.13}$$

which is a function of normalized energy spread. The ratio of the ideal 1D gain length over the 1D TGU gain length as a function of the normalized energy spread Δ and the bunch length ratio n is illustrated in Fig. 4.4. The red line shows the optimum n for each Δ value. As can be seen from the figure for the large value of Δ the effect of the TGU on the gain length reduction is more pronounced and the rapid gain length increase due to the energy spread is compensated considerably. In fact, this plot is an extended version of Fig. 4.3 right, including the parameter n. For n=1 and n=n$_{opt}$ it exhibits the normal undulator and the TGU cases in Fig. 4.3, respectively.
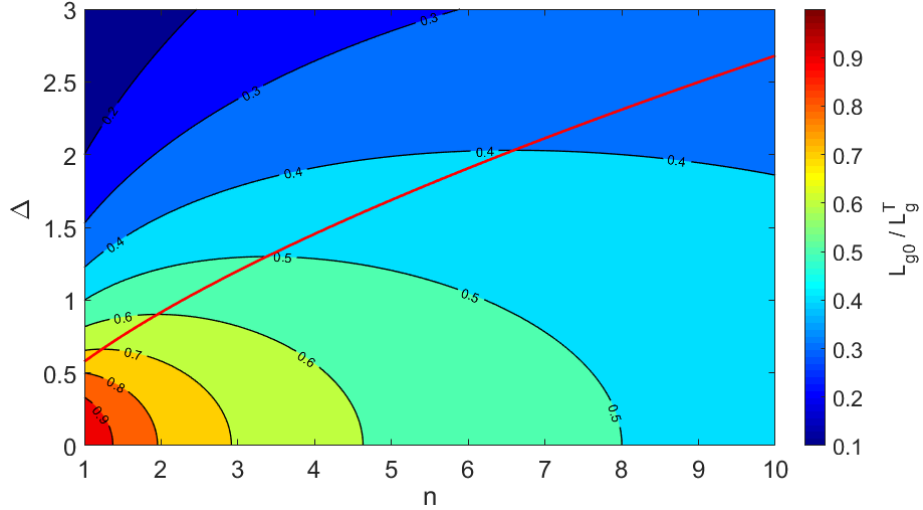
Figure 4.4: Normalized gain length vs the normalized energy spread Δ and the bunch length ratio n. The red line shows the optimum n for a given initial energy spread. A gain length reduction is possible for cases of Δ > 0.6.

The optimum bunch length ratio also can be expressed in terms of the dispersion and the beam size which results in an optimum dispersion as [86]

$$D_{\text{opt}} \approx 2.28 \frac{\sigma_x \sigma_\eta^{1/2}}{\rho^{3/2}} \tag{4.14}$$

It can be shown that by including 3D effects like diffraction the optimum dispersion is shifted to higher values [84]. Indeed, the optimum dispersion is a compromise between the impact of the effective FEL parameter and the effective energy spread on the FEL gain length. In the other word, at the expense of the current density reduction[3] the fast increase in the gain length can be compensated by decreasing the local energy spread in the transverse plane. Therefore, the influence of both effective parameters on the gain length results in a stationary point (a minimum) in terms of the bunch length ratio or dispersion.

This can be seen from Fig. 4.5 where the normalized effective parameters $\rho_T^{\text{eff}} / \rho$ (dashed line) and $\sigma_\eta^{\text{eff}} / \sigma_\eta$ (solid line) are plotted in terms of the bunch length ratio n. By increasing n both normalized effective parameters decrease but for some values of n the gain length ratio $L_g^T / L_{go}$ (equation 4.11) shows an optimum which depends on the normalized energy spread $\Delta = \sigma_\eta / \rho$ as shown on the right axis of Fig. 4.5 for two cases Δ=1 (solid line) and Δ=1.5 (dashed line). In fact, for a bunch length ratio n smaller than the optimum the energy spread is the main effect while for values of n larger than optimum, the FEL parameter is the dominant effect which results in a steadier increase of the gain length.

---

[3] By dispersing the beam, the peak current stays constant while the local current density (in the transverse plane) decreases.
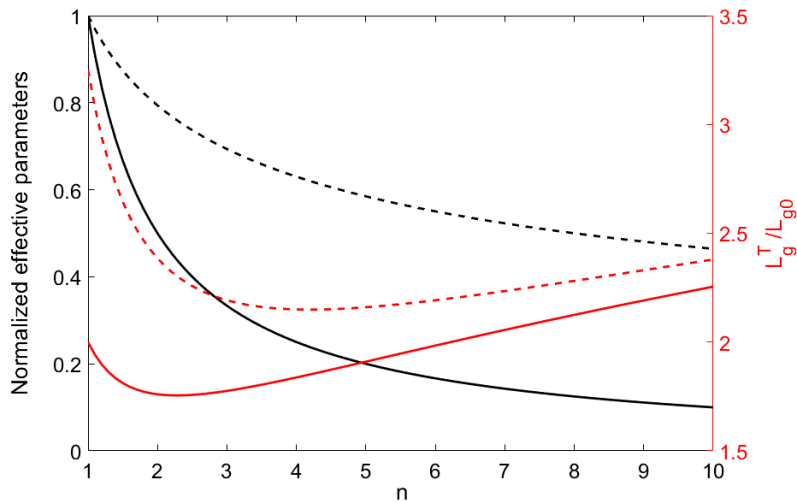
Figure 4.5: Left axis: Normalized effective parameters $\rho_T^{\text{eff}} / \rho$ (dashed line) and $\sigma_\eta^{\text{eff}} / \sigma_\eta$ (solid line) vs bunch length ratio n. Right axis: gain length ratio for two cases Δ=1 (solid line) and Δ=1.5 (dashed line).

# 4.2.1 Parameter Choice

It is envisioned to perform an FEL lasing experiment by means of a transverse gradient undulator and a laser plasma accelerator beam after a successful test of TGU40. The LPA beam requirement allowing for FEL amplification is investigated in this section. Up to now, from an FEL point of view and generating X-ray radiation several laser plasma parameter sets have been studied. The sets are based on the expected capability of the LPAs and also experimentally demonstrated beam have been studied. Table. 4.1 lists some LPA based beam parameter sets which have been discussed recently.

| Parameter | SLAC [10] | LUX [87,88] | LUNEX5 [81, 89] | SIOM [90] | Peking University [91] | Unit |
|---|---|---|---|---|---|---|
| Energy | 1000 | 230-410 | 400 | 200-600 | 500 | MeV |
| Charge | 50 | 20-60 | 20 | 10-80 | 40 | pC |
| RMS Energy Spread | 1% | 1-10% | 1% | 0.4-1.2% | 1% | / |
| RMS Normalized Emittance (x/y) | 0.1 | 0.5-2 | 1 | 0.5-1.4 | 0.3 | µm-rad |
| RMS Beam divergence (x/y) | 0.05 | 0.5-1 | 1.25 | 0.2 | 0.3 | mrad |
| RMS Beam Length | 1.5[4] | 1-2 | 0.6 | 1-3 | 1 | µm |

Table 4.1: LPA beam parameters based on experiments and simulations.

---

[4] Flattop bunch size.

For this thesis the parameter set is chosen such that it becomes independently achievable by LPAs but the combination of all parameters might be still challenging. Likewise, the FEL parameter should be smaller than the beam energy spread to have the possibility of using a TGU to improve the FEL gain and power compared to a normal planar undulator. Therefore, based on the parameter sets listed in Table. 4.1 and the expected capability of the LPAs the nominal parameter set, which are presented in Table. 4.2 was chosen as reference parameter set in this thesis. Since the aim of this chapter is to explore the possibility of FEL lasing by using a TGU, each of these nominal parameters are scaled over a reasonable range to inspect the minimum LPA beam requirement for the first FEL demonstration experiment.

Demonstration of FEL amplification requires reaching an output power at the end of the undulator knowingly higher than the purely spontaneous emission. In this regard, a limit of $P_{total}/P_{spont.} \geq 10$ has been considered as a requirement for the demonstration experiment. The spontaneous power at the end of the undulator is obtained from a linear fit before the exponential regime and calculating the power line at the end of the undulator. Such a limit and spontaneous power calculation are already introduced in Ref. [92]. The difference is that here the spontaneous power is calculated at the end of the undulator while in the former reference the shot noise power is calculated as the spontaneous power.

The undulator parameters are assumed to be the same as the TGU40 parameters except the length which is set to $L_u$ =5 m. The longer undulator length allows reaching saturation power. For the first FEL demonstration experiment it can also be shorter since the goal of the experiment is reaching the output power one order of magnitude higher than the spontaneous power. The TGU parameters are listed in the Table. 4.2.

The bunch is assumed to have a Gaussian distribution both in energy and space. Any initial energy chirp has been neglected since the beam needs to be dispersed in the transverse plane which results in vanishing initial energy chirp (it is transformed to the transverse plane).

The effect of the beam transport on the electron beam parameters, specifically the growth of the emittance, and the collective effect like CSR are not included in the simulations. The design study of the beamline transport including the collective effects is presented in chapter 5. In this chapter a perfect matching condition at the undulator entrance is assumed. In the vertical plane the electron beam optic is matched to the natural focusing of the TGU according to equation (3.45). Thus, the Twiss parameters of the matched beam are $\beta_{0y} = \sqrt{2}\gamma / K \sqrt{k_u^2 + \alpha^2} \approx 1.26$ m and $\alpha_{0y} = 0$. In the transverse plane the TGU can be regarded as a drift section with a transfer matrix (2.10). For optimized FEL performance the average beta function along the undulator should be minimized. Using equation (2.21) the average beta function in a drift section can be calculated as

$$\beta_{x,ave} = \beta_{0x} - \alpha_{0x}L_u + \frac{(1+\alpha_{0x}^2)L_u^2}{3\beta_{0x}} \tag{4.15}$$

| Beam Parameter | Value | Unit |
|---|---|---|
| Energy | *300* | *MeV* |
| Charge | *65* | *pC* |
| Peak Current | *8* | *kA* |
| RMS Energy Spread | *1%* | */* |
| RMS Normalized Emittance (x/y) | 0.5 | *μm-rad* |
| RMS Beam Length | *1* | *μm* |

| TGU Parameter | Value | Unit |
|---|---|---|
| Period Length | *10.05* | *mm* |
| Undulator Length | *5* | *m* |
| Undulator Parameter | *1.07* | */* |
| Undulator Transverse Gradient | *139.7* | *1/m* |

| TGU FEL Parameter | Value | Unit |
|---|---|---|
| Radiation Wavelength | *24* | *nm* |
| Pierce Parameter | *55×10^{-4}* | */* |
| TGU FEL Parameter | *38×10^{-4}* | */* |

| Lattice Function | Value | Unit |
|---|---|---|
| Beta functions (x/y) | *5.77/1.26* | m |
| Alpha (x/y) | *1.73/0* | */* |
| Dispersion | *0.0196* | m |

Table 4.2: LPA beam parameters used as reference parameters, parameter list of the TGU, FEL parameters and lattice functions.

Equation (4.15) can be solved for initial beta and alpha functions which gives the minimum average beta function along the undulator. For $L_u$ =5 m the matched initial Twiss parameters in the transverse plane are $\beta_{0x} = 2L_u / \sqrt{3} \approx 5.77$ m and $\alpha_{0x} = \sqrt{3} \approx 1.73$. As a result, the nondispersive rms beam sizes at the TGU entrance would be $\sigma_x \approx 70\,\mu m$ and $\sigma_y \approx 33\,\mu m$.

The parameter set listed in Table 4.2 and concerning the matching conditions leads to a $\rho$ value of approximately 55×10^{-4}, which is almost half of the rms energy spread. Such a small FEL parameter in comparison with the initial rms energy spread can be seen as a show stopper for a normal planar undulator. This raises the importance of using a TGU to compensate the energy spread effect and to improve FEL gain. In the following sections simulation studies regarding the power growth by using the TGU in comparison with a normal undulator and the scaling of the electron beam parameters with respect to the initial parameters are presented. All TGU FEL simulations have been done in SASE mode with a modified version of GENESIS [93] which includes transverse gradient parameter, using the time-dependent mode of the GENESIS.

## 4.2.1.1 Dispersion

As it was previously mentioned, the compromise between the effective parameters $\rho_T^{\text{eff}}$ and $\sigma_\eta^{\text{eff}}$ leads to an optimum value of the dispersion. The optimum value, which minimizes the gain length, is predicted in both 1D and 3D gain length theory. Fig. 4.6 shows the gain length as a function of the dispersion for the reference LPA parameters listed in Table. 4.2. The 1D case is based on 1D gain length, equation (4.11), while the 3D gain lengths are obtained by time-dependent GENESIS simulations averaged over 10 runs with different initial shot-noise seeds. For each value of dispersion, the TGU gradient $\alpha$, which satisfies the matched dispersion, equation (3.4), is assumed. The inset plot shows the region where the dispersion reaches its optimum value. The simulation steps in terms of dispersion are reduced to find the exact optimum case. The error bars in the inset plot mark one standard deviation of the fluctuation in calculated gain length due to the different shot-noise seeds.

Both cases show an optimum dispersion which gives the minimum gain length. The ideal dispersion in the 1D case is about $D \approx 40$ mm while in the case of the GENESIS simulation, which includes 3D effects, the optimum dispersion is shifted to lower values, which in this case is about $D \approx 21$ mm, as shown in the inset plot of Fig. 4.6. The minimum gain length that can be achieved by choosing the optimum dispersion is then $L_g^T \approx 0.41$ m. The optimum dispersion is so close to the designed value of the TGU40, $D=0.0196$ m. In fact, as can be seen from the inset plot the designed dispersion value and the optimum one result in approximately the same value of the gain length.
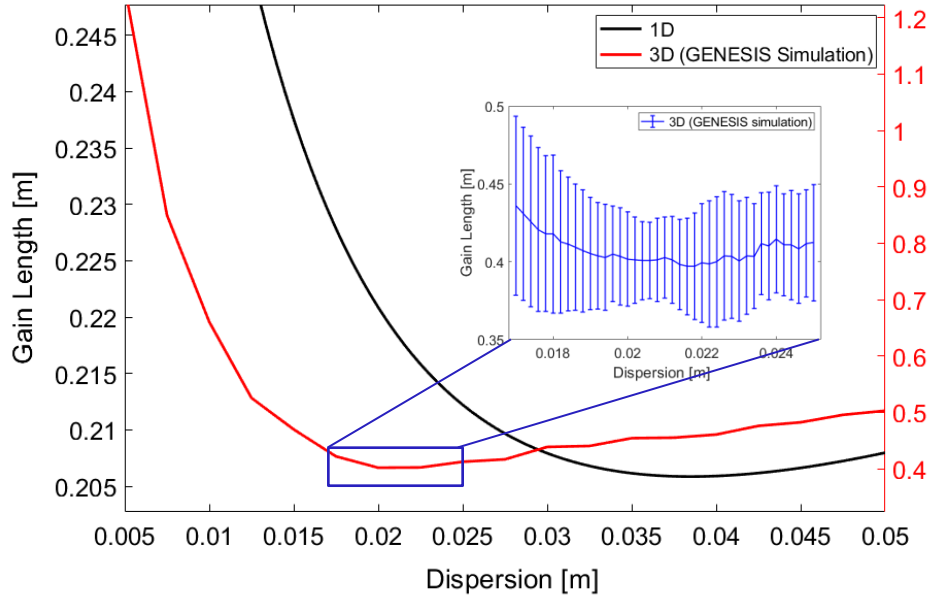


Figure 4.6: Gain length as a function of dispersion. The inset plot shows the region with optimum dispersion. The data of GENESIS are obtained by the time-dependent mode and averaged over 10 runs with different shot-noise seeds.

In order to have the same parameters as the TGU40 and to keep the transverse gradient unchanged $\alpha$ = 139.7 1/m, succeeding simulations are performed with the design dispersion of $D$ = 0.0196 m.

The optimum dispersion will depend on the initial normalized emittance. It should be noted that by changing the initial normalized emittance the initial bunch size, divergence and of course the FEL parameter $\rho$ will be changed as well. Fig. 4.7 shows the gain length as a function of dispersion for different values of normalized emittance. The initial normalized emittances for the x and y planes are assumed to be the same. In the left plot the gain lengths are calculated by the simulation data from GENESIS while the right plot shows the gain curves based on 1D theory. As shown in Fig. 4.7 the gain length curves follow the same pattern as the 1D case. The difference is that the ideal dispersion predicted by 1D theory is larger than the optimum dispersion obtained by GENESIS simulation which includes 3D effects. Such a gain length vs dispersion curve, which includes 3D effects, is reported in Ref. [84] using a variational technique but for a different set of parameters.
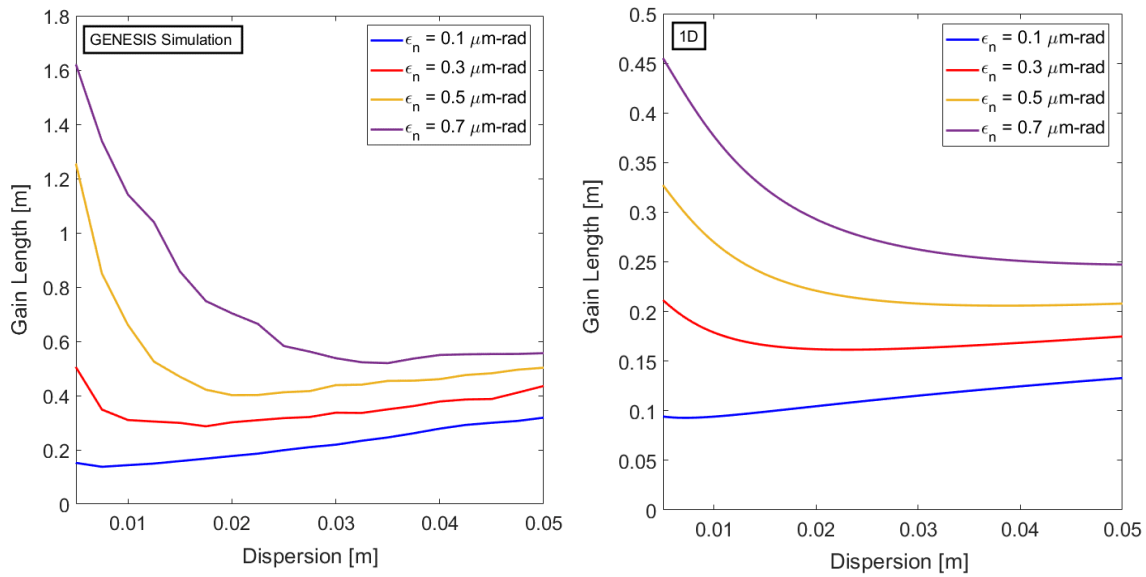


Figure 4.7: Gain length as a function of dispersion for different values of the normalized emittance. Left: data are obtained by the GENESIS simulation averaged over 10 independent runs. Right: gain length curves according to equation (4.11).

## 4.2.2 TGU VS Normal Undulator

In this section TGU FEL performance in the case of the reference beam parameters listed in Table. 4.2 are compared to a normal planar undulator with the same parameters as the TGU but without any transverse gradient. The simulations have been done with GENESIS in time-dependent mode and are averaged over 10 independent runs with different initial shot-noise seeds. The simulations here do not involve any beamline transport before the undulator and a perfect matching of the electron beam to the undulator is assumed for both cases.

A comparison of the power growth along the undulator for two cases, a TGU with a dispersed beam $D$ = 0.0196 m and a normal planar undulator with a non-dispersed beam is presented in Fig. 4.8. The TGU parameters and the beam parameters are listed in Table. 4.2. The dashed line shows the spontaneous power which is estimated by a linear fit to the lethargy regime and calculated at the end of the undulator. As can be seen from the figure the gain length and the power gain have been significantly improved by compensating the energy spread effect using the TGU. In the normal undulator case the gain length is about 1.2 m which is almost 4 times larger than the TGU case. Also, the TGU is able to reach a maximum power at the end of the undulator of about 35 MW which is 35 times higher than the 1 MW in the normal undulator case. Fig. 4.9 shows the maximum power normalized to the spontaneous power along the undulator.
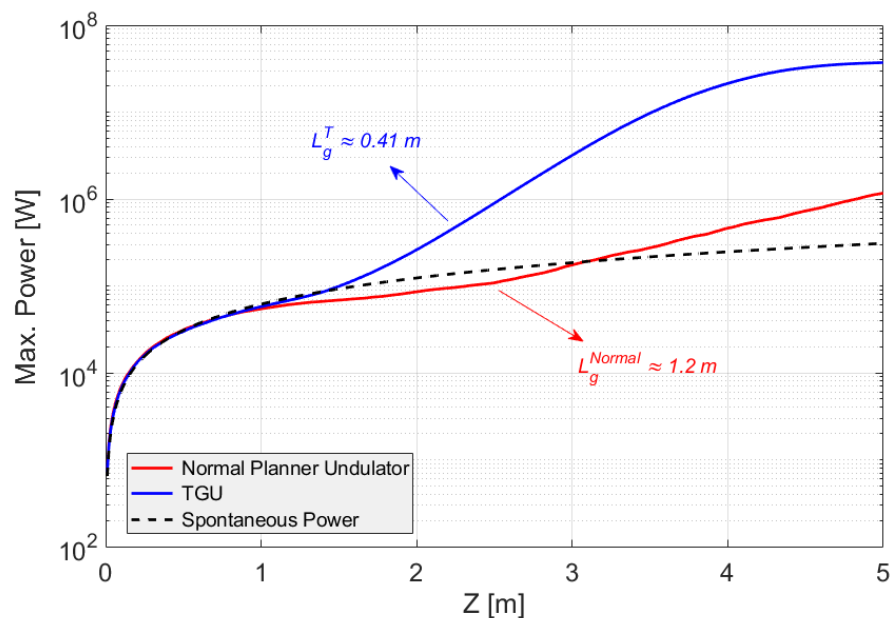


Figure 4.8: Power growth along the undulator for the TGU and the normal a planar undulator. The dashed line shows the spontaneous power. The data are averaged over 10 runs with different shot-noise seeds.
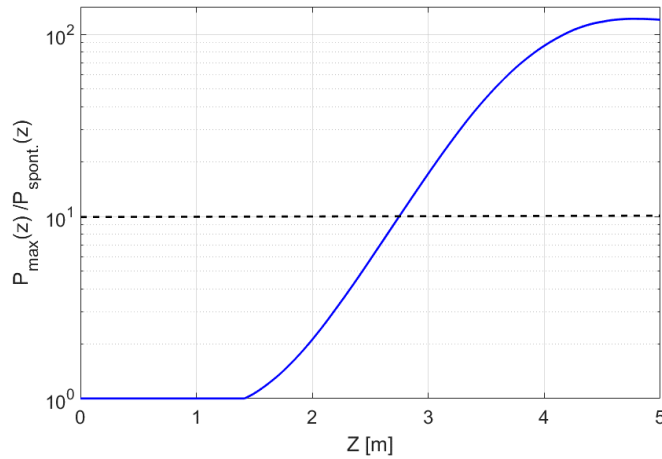
Figure 4.9: Normalized power as a function of the longitudinal position along the undulator. The dashed line shows the design goal $P_{total}/P_{spont.} \geq 10$ which is reached after approximately L = 2.7 m and increases up to $P_{total}/P_{spont.} \approx 120$ at the end of the undulator.

An exponential power growth with respect to the spontaneous emission can be observed roughly after L = 1.5 m such that at the end of the undulator the normalized power reaches approximately $P_{total}/P_{spont.} \approx 120$ which fulfils the design goal by a factor of 12. The radiation spectrum of the TGU and a normal planar undulator are depicted in Fig. 4.10 on the left. For the normal undulator case a beam with the same parameters but without the dispersion is assumed. The spectrum in the TGU case shows a single coherent spike while in the normal undulator case the radiation bandwidth is increased by a factor of 16 with respect to the TGU case.
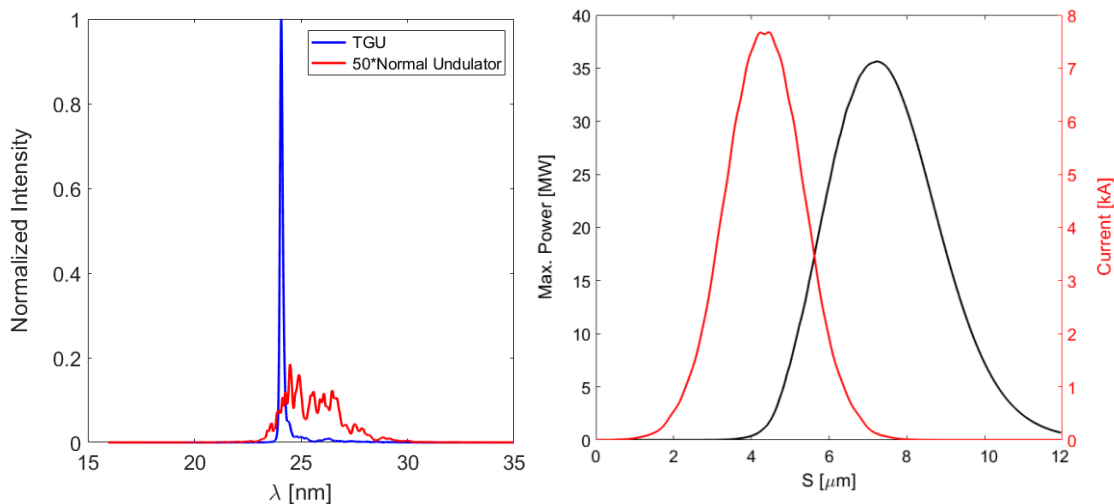


Figure 4.10: Left: Radiation spectrum of the FEL for the TGU and the normal planar undulator. Right: Radiation pulse at the end of the undulator as a function of the bunch coordinate. The right axis shows the current profile of the beam.

| Parameter | TGU | Normal Undulator | Unit |
|---|---|---|---|
| Max. Power | 35 | 1 | MW |
| $P_{max.}/P_{spont.}$ (end) | 120 | 3.5 | / |
| 3D Gain length | 0.41 | 1.2 | m |
| 1D Gain length | 0.127 | 0.087 | m |
| Pierce Parameter | $38\times10^{-4}$ | $55\times10^{-4}$ | / |
| Radiation Spectrum Bandwidth (FWHM) [5] | 0.6 | 10 | % |

Table 4.3: FEL output parameters for the TGU and a normal undulator.

On the right side of Fig. 4.10 the maximum radiation power is plotted as a function of the bunch coordinate. For reference purposes the current profile of the bunch is shown on the right axis. As can be seen from the figure, the radiation at the end of the undulator is significantly shifted with respect to the electron beam. This large slippage effect prevents the FEL to reach the saturation power (see section 4.2.4).

Nevertheless, energy spread compensation in the TGU case leads to an exponential power gain which is higher than the design goal and is sufficient enough for the first TGU FEL demonstration experiment. A comparison between the FEL output in the TGU case and the normal planar undulator is presented in Table. 4.3. The comparison between the two cases shows the TGU capability in suppressing the energy spread and introduces a possible candidate for FEL lasing in the case of a large energy spread beam generated in LPAs.

## 4.2.3 Coherence Properties of the Radiation

Coherence is a statistical property of a radiation source and describes the phase relation between two points either in time or space. The mathematical description of the coherence properties can be described by the so-called mutual coherence function [94],

$$\Gamma(r_1, r_2, t_1, t_2) = \left\langle E(r_1, t_1) E^*(r_2, t_2) \right\rangle = \left\langle E(r_1, t) E^*(r_2, t + \tau) \right\rangle \tag{4.16}$$

where $r_1$ and $r_2$ are the transverse coordinates, $\tau = t_2 - t_1$ is the time difference between the points in time $t$ at a particular z location, $E(r, t)$ is the electric field of the propagated radiation and brackets <…> show an ensemble average. The transverse and the temporal coherence of the radiation then can be characterized by the mutual coherence function as $\Gamma(r_1, r_2, 0)$ and $\Gamma(0, 0, \tau)$, respectively. While the former shows the correlation between the radiation fields

---

[5] For the normal undulator case the spectrum is approximated by a Gaussian profile.

at the same time but at different points, the latter indicates how the optical fields are correlated at different times at the same point.

- **Transverse Coherence**

In the SASE FEL case due to the mode competition process (mode cleaning), the fundamental $TEM_{00}$ mode will grow faster than the other modes due to having major overlap with the electron beam, although at the beginning of the exponential gain regime higher modes would be present. At the saturation regime the domination of the $TEM_{00}$ mode makes the SASE FEL as a fully coherent source in the transverse dimension. After the saturation regime, the modes that are not saturated yet would continue to grow along the undulator and as a result the degree of the transverse coherence decreases [95]. However, for the TGU case the increased beam size in the transverse plane leads to growth of multiple FEL modes in the exponential gain regime and as a result the transverse coherence of the radiation will be degraded [84].

In order to investigate the transverse coherence of the TGU radiation we assume that the field *E (r, t)* is quasi-monochromatic so that the time delay due to the path length difference from $r_1$ and $r_2$ can be eliminated and we can neglect the time dependence in the mutual coherence function. Therefore, a single parameter, which ranges between 0 and 1, can be used to characterize the total degree of transverse coherence by normalization of the coherence function as [96]

$$\zeta = \frac{\iint |J_{12}|^2 \, dr_1 dr_2}{P^2}$$

(4.17)

where *P* is the radiation power and

$$J_{12} = J(r_1, r_2) = \Gamma(r_1, r_2, 0)$$

(4.18)

is the mutual intensity function. As result of calculation the degree of the transverse coherence by using the simulated radiation field from GENESIS is presented in Fig. 4.11 where the degree of the transverse coherence is plotted along the undulator distance for a TGU and a normal undulator with the nominal beam parameters listed in Table. 4.2. As a comparison, the case of a beam with a very low energy spread and a normal undulator is also plotted. For the normal undulator cases, non-dispersed beams (*D*=0) and TGU gradient $\alpha$ = 0 are assumed. While due to the large energy spread and relatively low gain the transverse coherence for a normal undulator is very poor, in the TGU case a relatively good transverse coherence $(\zeta \sim 0.5)$ is achieved. Nevertheless, because of the increased beam size the maximum transverse coherence that is established close to the saturation is far below the optimum case, where the beam energy spread is very low.

The inverse of the degree of transverse coherence can be used to determine the number of transverse modes $M_{\perp}$ in the radiation pulse
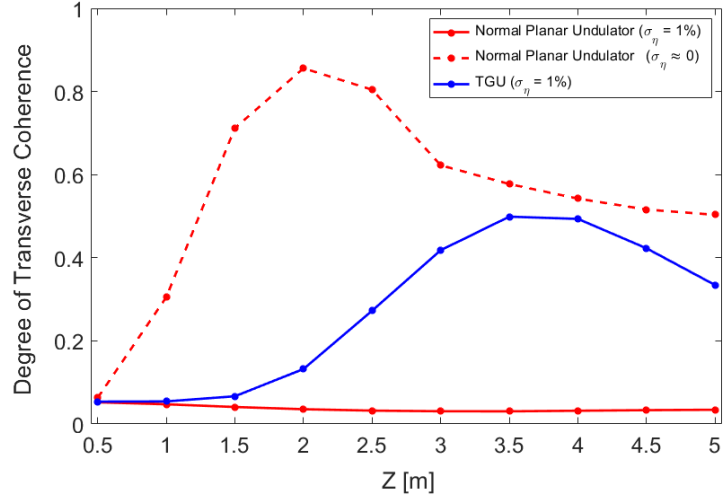
Figure 4.11: Degree of transverse coherence along the undulator distance for the TGU (blue line), a normal undulator (red line) and a normal undulator with a beam with a very low energy spread (red dashed line). For the normal undulator cases, non-dispersed beams (*D*=0) and $\alpha$ = 0 are assumed.

$$M_\perp = \frac{1}{\zeta} \tag{4.19}$$

The transverse mode patterns at the end of the exponential gain regime and close to the saturation for the cases in Fig. 4.11 are illustrated in Fig. 4.12. (a-c). As can be seen from the figure, in the TGU case (a), even with such a large energy spread of $\sigma_\eta = 1\%$ a relatively good transverse coherence can be achieved compared to the poor transverse coherence in the normal undulator case (b).



(a)                          (b)                          (c)
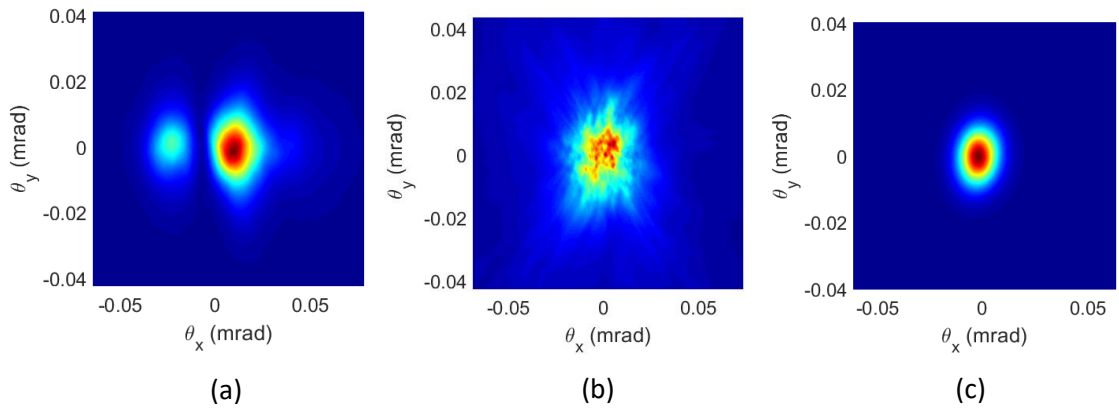
Figure 4.12: Transverse mode patterns for (a) the TGU, (b) a normal undulator and (c) a normal undulator with a beam with a very low energy spread at the end of the exponential gain regime consistent with Fig. 4.11. For the normal undulator cases, non-dispersed beams (*D*=0) and $\alpha$ = 0 are assumed.
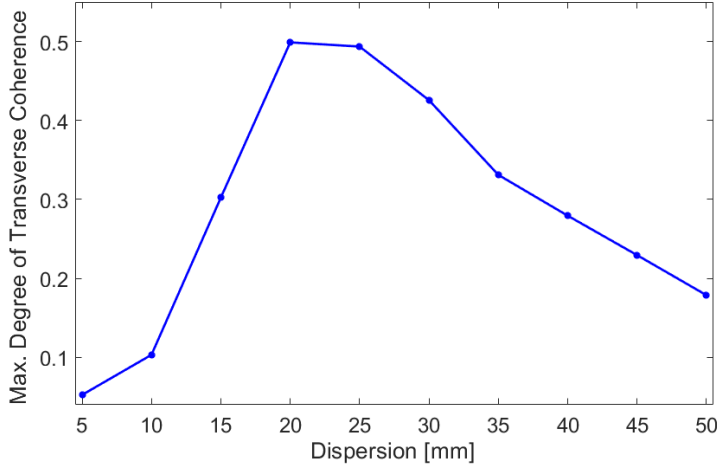
Figure 4.13: Maximum degree of the transverse coherence along the undulator in terms of the beam dispersion and a fixed transverse gradient of $\alpha$ = 139.7 1/m.

The maximum degree of the transverse coherence as a function of the beam dispersion for a fixed value of the transverse gradient $\alpha$ = 139.7 1/m, is illustrated in Fig. 4.13. As it is expected, the maximum value of the transverse coherence is reached close to the matched dispersion, where the resonance condition is satisfied.

- **Temporal Coherence**

Temporal coherence is characterized by the coherence time [97]

$$\tau_c = \int_{-\infty}^{+\infty} |g_1(\tau)|^2 d\tau \tag{4.20}$$

where the first-order temporal normalized correlation function $g_1(\tau)$ is given by

$$g_1(r,\tau) = \frac{\left\langle E(r,t)E^*(r,t+\tau)\right\rangle}{\left[\left\langle |E(r,t)|^2\right\rangle\left\langle |E(r,t+\tau)|^2\right\rangle\right]^{1/2}} \tag{4.21}$$

which in the stationary case is a function of only the time difference $\tau = t_2 - t_1$. The average number of longitudinal modes (spikes) can be approximated by [16]

$$M_\parallel = \frac{T_{bunch}}{\tau_c} \tag{4.22}$$

where $T_{bunch}$ is the bunch length. The coherence time as a function of the undulator length for three cases; the TGU and a normal undulator with the parameters listed in Table 4.2 and also an optimum case where the energy spread of the beam is very low is depicted in Fig. 4.14. While the coherence time in the normal undulator case ($\sigma_\eta = 0.01$) stays below 0.5 *fs*, due to

94
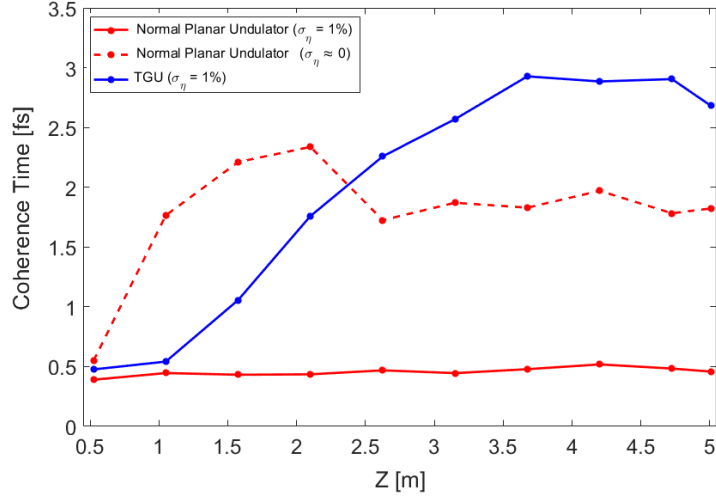
Figure 4.14: Coherence time along the undulator distance for the TGU (blue line), a normal undulator (red line) and a normal undulator with a beam with a very low energy spread (red dashed line). For the normal undulator cases, non-dispersed beams (*D*=0) and $\alpha$ = 0 are assumed.

the energy spread compensation in the TGU case, a coherence time close to the bunch length of $T_{bunch} = 3.3\,fs$ is obtained, which shows just one temporal mode in the radiation pulse (see Fig. 4.10 left). It is worth noting that, similar to the degree of transverse coherence, the maximum coherence time is reached at the end of the exponential gain regime and close to the saturation.

## 4.2.4 Slippage Effect

The saturation power in the TGU case analogous to equation (2.91) can be estimated by [84]

$$P_{sat}^T = 1.6\rho_T^{\text{eff}}\left(\frac{L_T}{L_g}\right)^2 P_b \qquad (4.23)$$

where $P_b = \gamma mc^2 I_p / e$ is the beam power, $L_T = \lambda_u / 4\pi\sqrt{3}\rho_T^{\text{eff}}$ and $L_g$ is the 3D gain length. According to equation (4.23) the saturation power for the TGU case is about 1.5 GW which is almost 50 times larger than the achieved power at the end of the TGU. The effect of the large slippage can be reduced by using the seeding technique which allows reaching saturation power in a shorter distance [98]. A measure for the slippage effect is given by the cooperation length. Recalling that the radiation slips ahead of the electrons per undulator wavelength by one radiation wavelength, the cooperation length is defined as the slipped distance by the radiation in one gain length with respect to the electrons [99]

$$L_c = \frac{L_g}{\lambda_u} \lambda_l \tag{4.24}$$

The cooperation length can be interpreted as the length over which the amplified noise signals are correlated and communication between the electrons within the bunch can happen during one gain length. Defining the parameter $K_s$, which is so called "superradiance" parameter, as the ratio between the cooperation length and the bunch length [100]

$$K_s = \frac{L_c}{\sigma_z} \tag{4.25}$$

the electron pulse can be regarded as a short and long pulse when $K_s \geq 1$ and $K_s \ll 1$ respectively. For the case of $K_s \ll 1$, the FEL is operating in the steady state regime where the gain length is not affected by the slippage. For short electron pulses $K_s \geq 1$, the emitted radiation could quickly escape from the electron pulse which deters the FEL process due to the reduction of interaction between the bunch and the radiation field which leads to a reduction of saturation effect within the bunch. The slippage effect can be reduced by decreasing the cooperation length for a given bunch length. This can be done by either decreasing the gain length or the radiation wavelength. Fig. 4.15 shows the cooperation length normalized by the bunch length for the parameter set of the reference beam listed in Table. 4.2, which are scanned for each parameter while keeping the other parameters the same as the reference one. The dispersion is $D$ = 0.0196 and the corresponding transverse gradient according to equation (3.4) is set to $\alpha$ = 139.7 1/m. For the case of the undulator parameter scan Fig. 4.15 (d), the dispersion is changed for each value of the undulator parameter according to equation (3.4) while the transverse gradient is assumed to be constant. For the reference beam parameter set the cooperation length is about the bunch length $L_c / \sigma_z \approx 1$. Since $L_c \propto L_g \propto \rho^{-1}$, any increase in the FEL parameter i.e. by increasing the charge (peak current) or the undulator parameter for a fixed radiation wavelength or any decrease in the gain length i.e. by decreasing the energy spread or the beam emittance results in a cooperation length reduction. As can be seen from the Fig. 4.15 (a) increasing the charge up to the 100 pC results in the same cooperation length as the reference one while the effect of reducing the beam charge below the reference charge of 65 pC has a large impact on the cooperation length. This can be explained by the fact that for fixed values of the energy spread and dispersion, the rate of reduction in gain length decreases for large values of the FEL parameter, as shown in Fig. 4.16 left. Fig. 4.15 (b) shows the case of varying the energy spread for a fixed value of the FEL parameter, which results in increasing normalized gain length, as illustrated in Fig. 4.16 right. This dependency of the gain length on the FEL parameter and the energy spread can be seen from equation (4.9). The cooperation length also can be decreased by reducing the beam emittance and the gain length as well, as shown in Fig. 4.15 (c). Since larger undulator parameters result in longer radiation wavelengths and on the other hand larger FEL parameter, the interplay between these two effects shows an optimum value for the undulator parameter as illustrated in Fig. 4.15 (d).
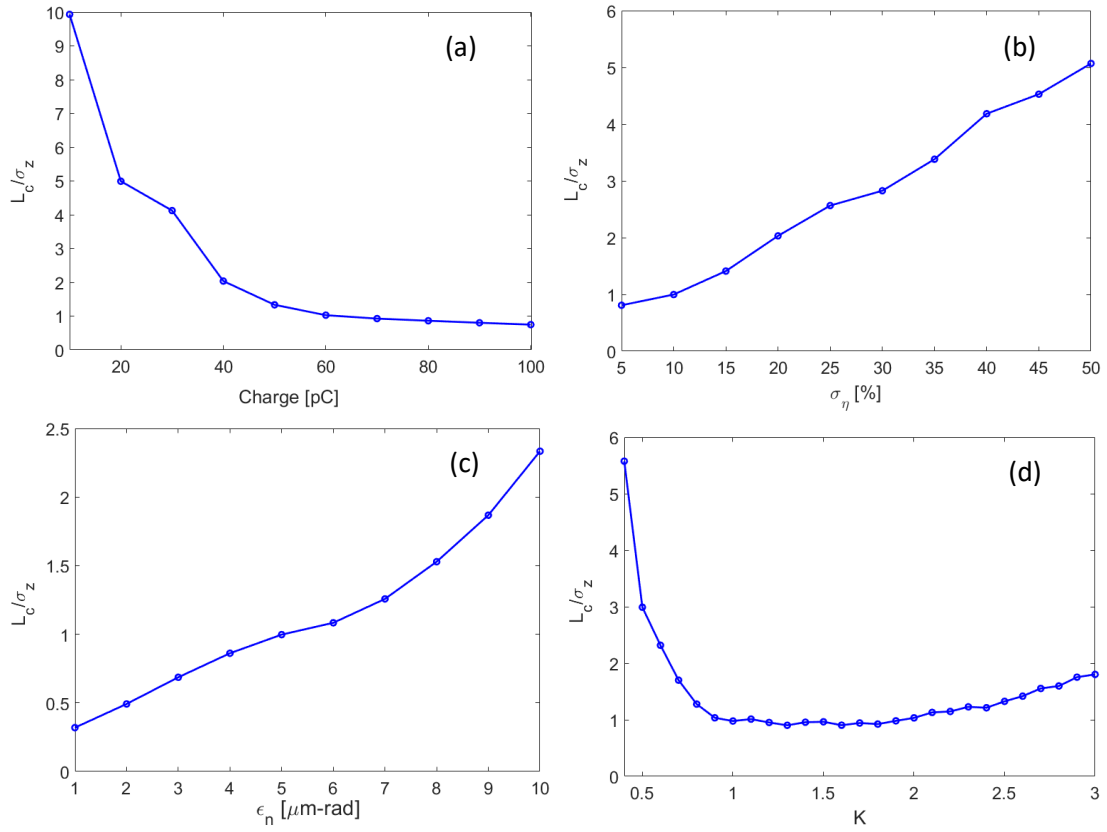
Figure 4.15: Normalized cooperation length as a function of (a) charge, (b) energy spread, (c) normalized emittance and (d) undulator parameter for the reference beam parameters listed in Table. 4.2.
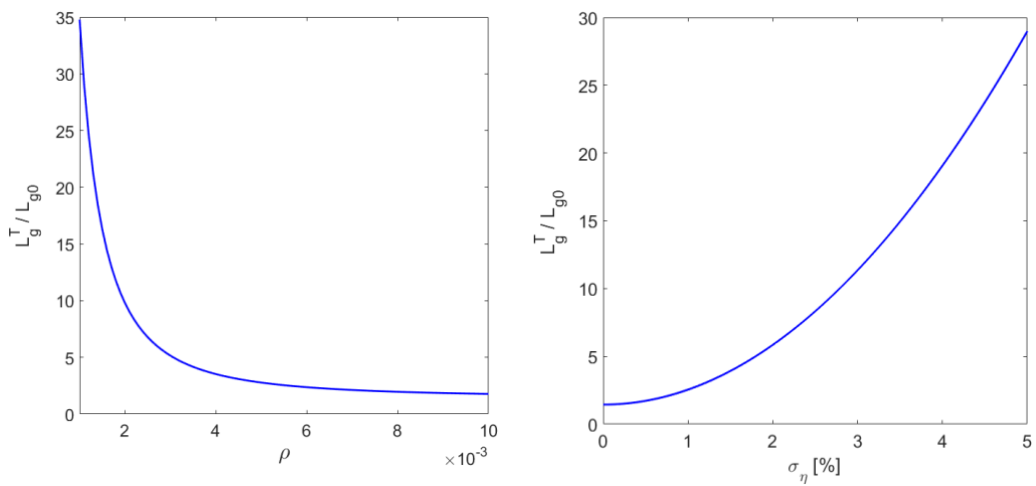


Figure 4.16: Normalized gain length $L^T_g/L_{g0}$ as a function of the FEL parameter (left) and the energy spread (right) according to the equation (4.11) for n=3.

# 4.3. Parameter Scaling

In this section the reference LPA beam parameters are scaled to investigate the effect of changing a parameter on the FEL output. This allows finding the minimum FEL beam requirement to demonstrate TGU FEL amplification. In this regard, the scaling is done by scanning two parameters for each case and as a requirement for demonstration of FEL lasing $P_{total}/P_{spont.} \geq 10$ is considered. The study shows how a decrease or increase in a parameter can be compensated by changing the other parameters to achieve the power requirement for the FEL demonstration experiment. It should be noted that, for the mesh plots in this section interpolated coloring is used in order to fill the gaps between the simulated data points.

## 4.3.1 Energy

One of the main advantages of LPAs is generating high gradient accelerating field in a short distance. This allows producing high energy beams at GeV level. However, since the FEL parameter is inversely proportional to the energy $\rho \propto \gamma^{-1}$ increasing the electron beam energy leads to having a low FEL parameter and as a result a larger gain length and saturation length. Moreover, lower output power is expected in this case. A moderate beam energy of $E = 300$ MeV which has been already achieved experimentally, is considered here. Such a low energy beam with a large FEL parameter allows reaching saturation in a shorter distance, which in our case is 5 m, and gives the possibility to reduce other parameters if needed. On the other hand, the radiation wavelength is inversely proportional to the energy $\lambda_r \propto \gamma^{-2}$. Therefore, to generate short pulse FEL (ultraviolet and X-ray range) a compromise between these parameters needs to be considered.

Fig. 4.17 shows the maximum FEL power along the 5 m long TGU for different beam energies. As can be seen from the figure only the 300 MeV beam reaches its saturation in 5-meter distance. Furthermore, only beams of 300 MeV and 400 MeV can achieve an output power above the design goal $P_{total}/P_{spont.} \geq 10$ as shown in Fig. 4.18, left axis. For the 300 MeV beam the maximum power at the end of the TGU is more than 2 orders of magnitude higher than the spontaneous power. A larger FEL parameter allows having shorter gain length. This is plotted on the right axis of Fig. 4.18. Shorter gain length provides starting exponential gain in a shorter distance, which is favorable for the first FEL lasing experiment, since it allows using a shorter TGU in case of necessity. The data are averaged over 10 runs with different shot-noise seeds and the error bars mark one standard deviation of the shot-to-shot power fluctuation. The electron beam energy acceptance for the normalized power limit can be increased by going to higher values of the undulator parameter. This can be seen from Fig. 4.19, where the normalized power as a function of beam energy and the undulator parameter is plotted.
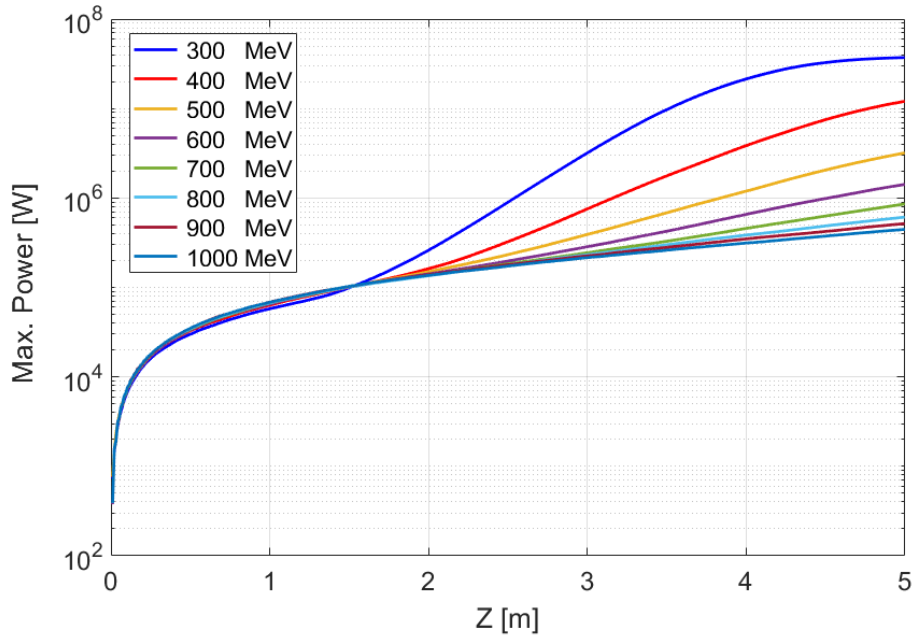
Figure 4.17: FEL peak power growth along the undulator for different values of energy. For the lower energies the exponential gain starts in a shorter distance due to having shorter gain length. The data are averaged over 10 runs with different shot-noise seeds.
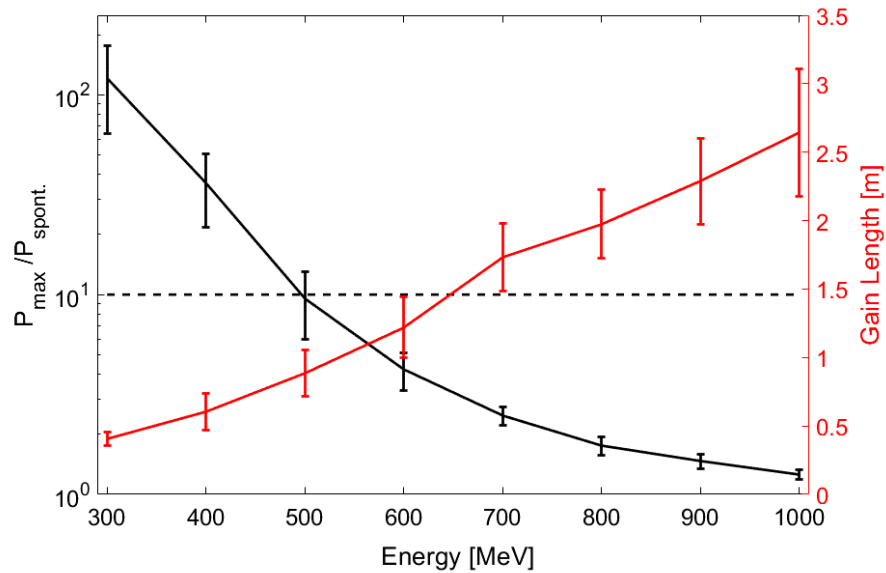


Figure 4.18: Normalized power at the end of the undulator as a function of the beam energy. Only beams with the energy of 300 and 400 MeV reach a normalized power higher than the design goal which is shown by the dashed line. The corresponded gain lengths are plotted on the right axis. The error bars indicate one standard deviation of the shot-to-shot power fluctuation due to the different initial shot-noise seeds for 10 runs.
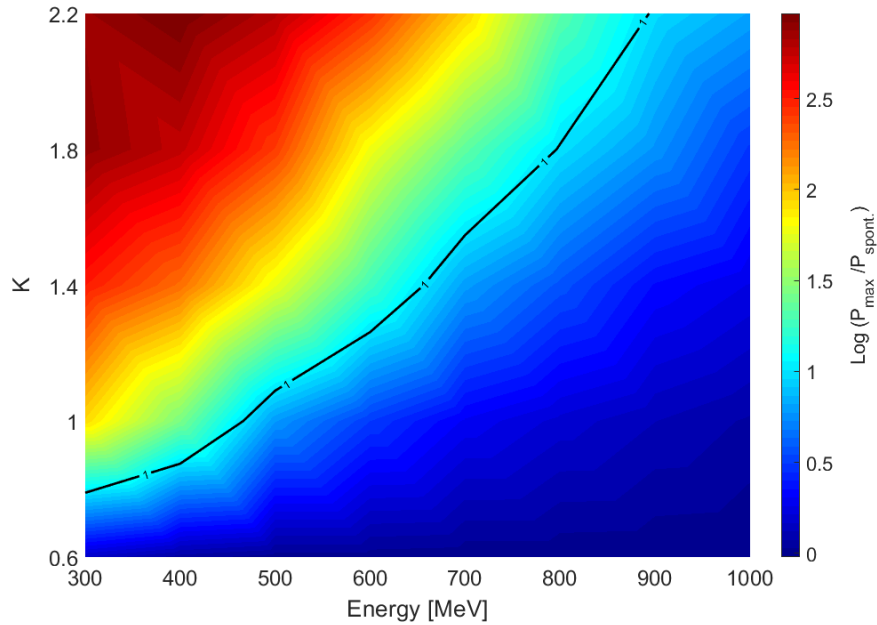
Figure 4.19: Normalized power (log scale) as a function of the beam energy and the undulator parameter. The design power limit is indicated by the contour line. The data are averaged over 10 runs with different shot noise seeds.

The contour line, which shows the power limit $P_{total}/P_{spont.}$ = 10, divides the plot into two regions of acceptable energies in terms of the undulator parameters. The beam energy can be increased up to 900 MeV for an undulator parameter of K= 2.2. Furthermore, for the case of 300 MeV, the minimum undulator parameter to reach the power goal is around K= 0.8. All of these combinations of energy and undulator parameter give the possibility of going to higher or lower radiation wavelengths as shown in Fig. 4.20.
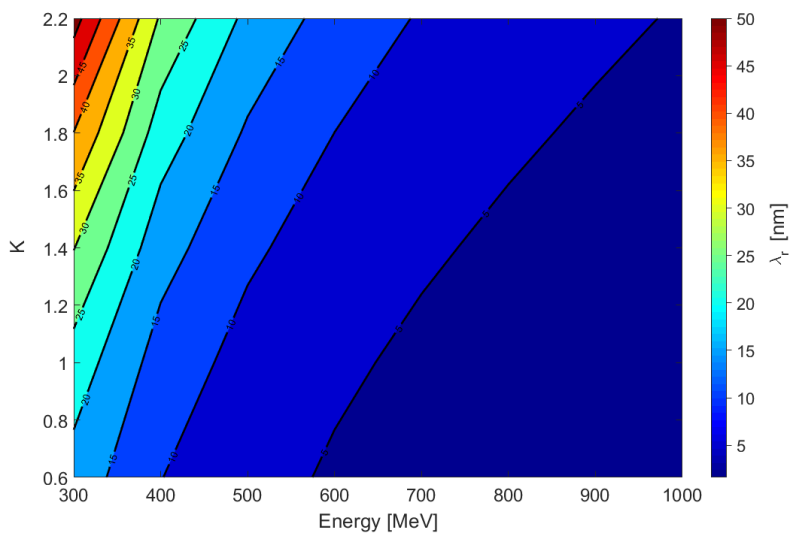


Figure 4.20: Radiation wavelength as a function of the energy and the undulator parameter.

## 4.3.2 Charge

The current profile of the bunch is assumed to be Gaussian with a bunch length of 1 μm. To have more accurate results the maximum charge is limited to $Q$ < 100 pC, since the GENESIS code is not able to correctly model the dynamic space-charge-driven debunching for ultrahigh currents [92, 93]. This leads to a peak current limit of $I$ < 12 kA which for the reference beam is about $I_{peak}$ ≈ 8 kA. It should be noted that since the beam is dispersed transversely the effect of local space charge is reduced in comparison with the non-dispersed beam and a normal undulator case. Therefore, the above-mentioned limit is considered as a reasonable range for the charge scaling and the corresponding peak current.

The normalized power as a function of initial charge for different values of rms energy spread is plotted in Fig. 4.21. The dashed line shows the limit for demonstration of FEL amplification $P_{total}/P_{spont.}$ = 10. For the case of 1 percent rms energy spread the minimum charge requirement is nearly 50 pC while the initial charge can be reduced down to 25 pC for the case of 0.5 percent initial rms energy spread. Regarding the reference beam parameter set the maximum energy spread that can be considered as a show stopper is 2.5 percent with 100 pC charge. Confining the initial charge to its reference value the initial rms energy spread can be increased up to 1.5 percent.
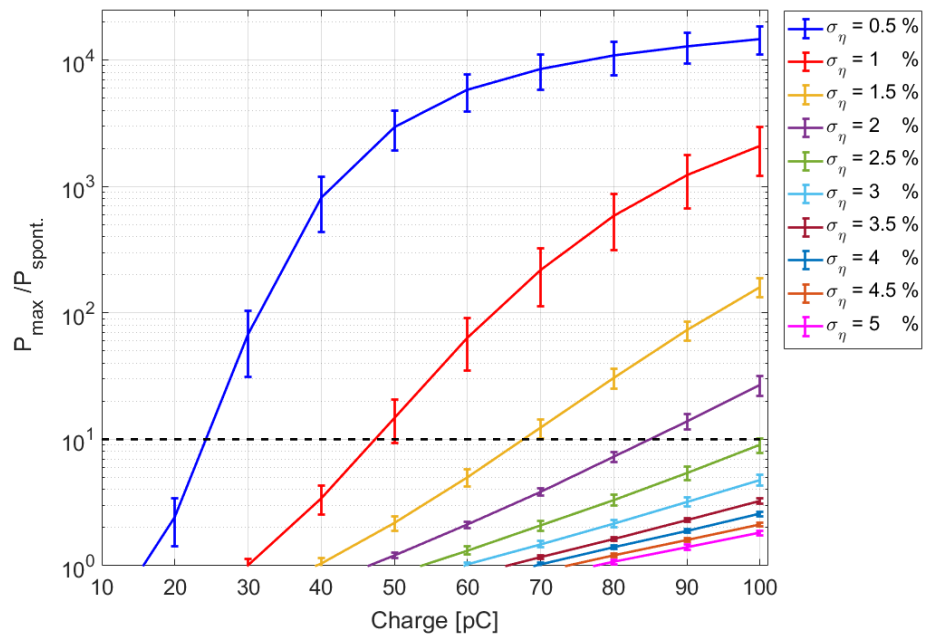


Figure 4.21: Normalized power vs charge for different values of projected rms energy spread. The dashed line shows the power limit for the FEL amplification. The data are averaged over 10 runs with different shot-noise seeds and the error bars show one standard deviation of the shot-to-shot power fluctuation.
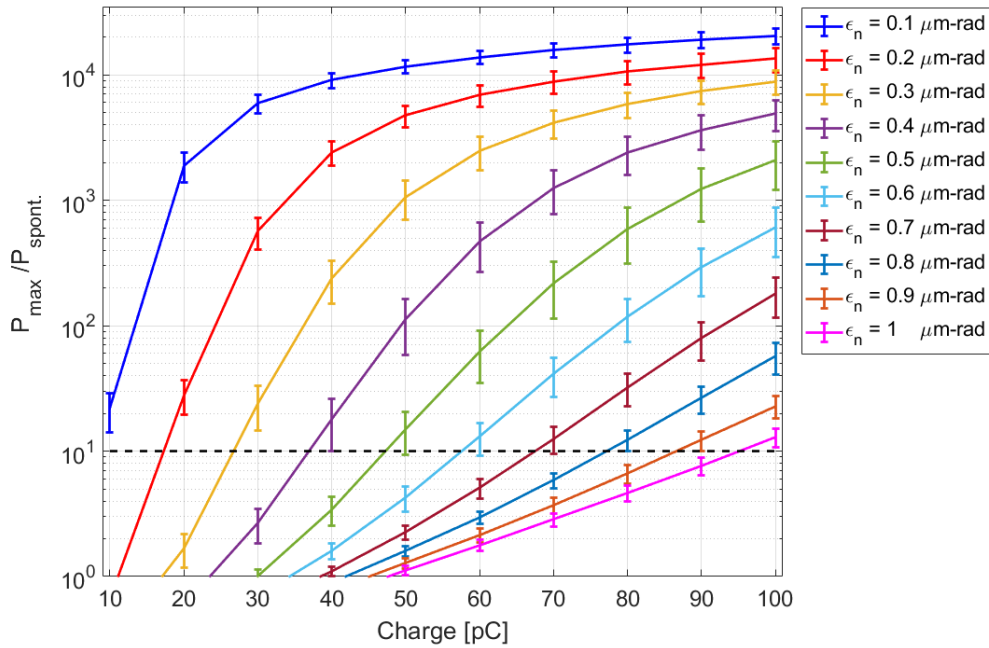
Figure 4.22: Normalized power at the end of the undulator as a function of charge and initial normalized emittances at the undulator entrance. The design power limit is indicated by the dashed line. The error bars indicate one standard deviation of the shot-to-shot power fluctuation due to the different initial shot-noise seeds for 10 runs.

Fig. 4.22 shows the normalized FEL power at the end of the undulator in terms of initial beam charge for different values of initial normalized emittance averaged over 10 independent runs. The emittance values are without dispersion contribution and are considered to be the same in both transverse and horizontal planes. As can be seen from the figure for the reference charge of 65 pC ($I_{peak} \approx 8$ kA), the maximum tolerable emittance (at the undulator entrance) is less than 0.7 μm-rad. Lower emittances allow having less charge such that for emittance of 0.1 μm-rad the initial charge can be reduced down to 10 pC, still reaching the design power limit which is shown with the dashed line on the plot.

The reduction in beam charge also can be compensated by increasing the undulator parameter as well. As shown in Fig. 4.23, the beam charge can be reduced down to 40 pC using an undulator with higher magnetic field which is the case of a superconducting undulator. It should be noted that for this case the TGU gradient is set to $\alpha$ = 140 1/m and the dispersion values are changed for each undulator parameter according to equation (3.4). However, considering the reference parameter set the undulator parameter larger than 0.6 is needed even with increasing the charge up to 100 pC. For the higher K values, the rate of the change of the power levels for a given charge decreases. As show in Fig. 4.15 (d), increasing the undulator parameter leads to an increase in the cooperation length which makes the emitted radiation slipping out the bunch in a short distance and the FEL process being hindered by the slippage effect.
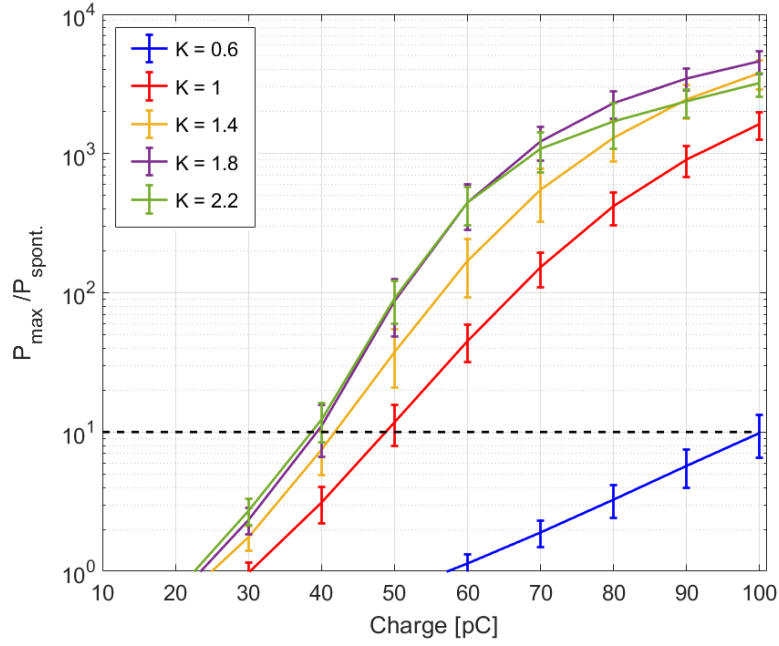
Figure 4.23: Normalized FEL power at the end of the undulator in terms of the initial charge and the undulator parameter. The design power limit is indicated by the dashed line. The error bars show one standard deviation of the power fluctuation originating from 10 runs with different shot-noise seeds.

## 4.3.3 Energy Spread

The main obstacle of achieving FEL lasing by using LPA beam is the relatively large energy spread of the generated beams from these accelerators. The typical range of the energy spread for these accelerators is about 1-5%. Although in recent years an energy spread of less than 1 percent has been achieved, the combination of such a low energy spread with the other parameters like charge, emittance and peak current is favorable from an FEL point of view but is still challenging. The reference beam energy spread for this study has been set to 1 percent as the projected energy spread and any initial energy chirp (expected from LPAs) has been neglected since the beam needs to be dispersed transversely before entering the TGU. The scanning is done in the range of 0.5-5% which allows investigating the maximum energy spread that can be tolerated for the demonstration of the TGU FEL amplification.

The effective energy spread, equation (4.8), can be written in terms of the bunch size ratio n, and the initial energy spread as

$$\sigma_\eta^{\text{eff}} = \frac{\sigma_\eta}{n} \approx \frac{\sigma_x}{D} \tag{4.19}$$

where for the final approximation we assumed $\sigma_T \gg \sigma_x$, which is the TGU operation regime.

Equation (4.19) shows that by increasing the energy spread for a fixed amount of dispersion the effective energy spread stays roughly constant. On the other hand, the transverse current which is proportional to $n^{-1}$ drops[6]. This is shown in Fig. 4.24 where the transverse current (left axis) and the effective energy spread (right axis) are plotted as a function of the initial energy spread for the reference parameter set. As can be seen from the figure, while the effective energy spread for $\sigma_\eta \geq 1\%$ is almost constant, the transverse current decreases to less than 1 kA for $\sigma_\eta = 5\%$. This drop in the transverse current results in a reduction of the FEL parameter $\rho$, which translates to the gain length increase and FEL power drop. In other words, increasing the transverse bunch size by increasing the initial energy spread, causes the effective FEL parameter to decrease while the effective energy spread stays constant, resulting in the FEL gain degradation.

Fig. 4.25 shows the contour plot of the normalized FEL peak power at the end of the undulator versus rms energy spread and initial charge. The beam with the reference parameter set is shown by the red dot. The data are averaged over 10 independent runs with different shot-noise seeds. Fig. 4.25 is a contour plot of the data in Fig. 4.21 which shows more clearly the region of permitted parameter range. The contour line of the normalized power equal to 1 splits the plot into two areas of permitted and unpermitted parameter sets in terms of charge and rms energy spread where the power limit is satisfied. Moreover, the contour lines show the points where the ratio of the charge to the energy spread stays constant. This feature can be used to study the CSR effect in the beam line transport [101].
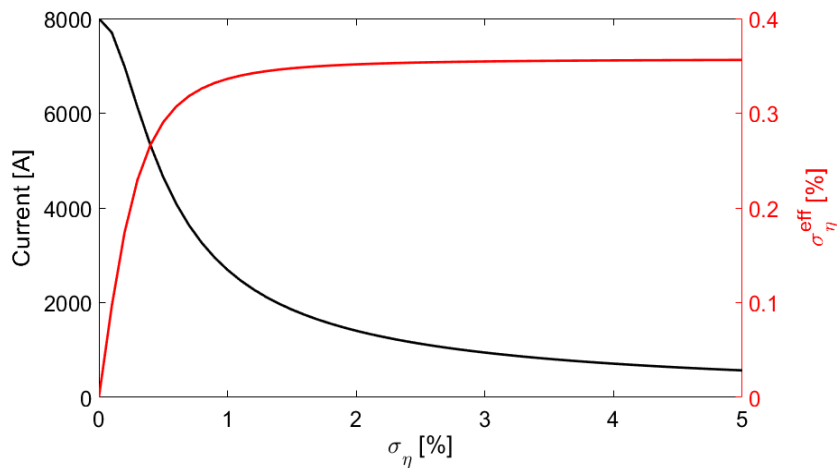


Figure 4.24: Transverse current as a function of the initial energy spread for the reference parameter set. On the right axis the effective energy spread is plotted. Increasing the initial energy spread for a fixed value of dispersion leads to a reduction of the FEL parameter.

---

[6] Increasing the energy spread for a fixed value of the dispersion leads to an increase of the transverse bunch size, equation (4.6).
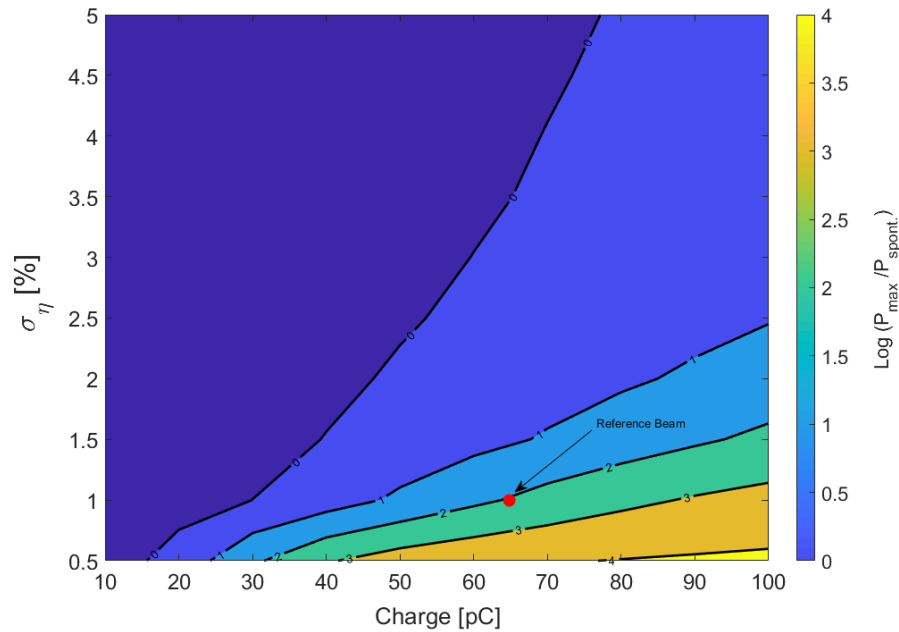
Figure 4.25: Contour plot of the normalized FEL power at the end of the undulator in terms of the initial charge and rms energy spread. The normalized power is in log scale. The reference beam is shown by the red dot. The data are averaged over 10 runs with different shot-noise seeds.

The interplay between the energy spread and the normalized emittance is shown in Fig. 4.26 where the normalized power as a function of normalized emittance is plotted for different values of the energy spread. As can be seen from the figure, having beams with lower normalized emittance than the reference beam can significantly increase the energy spread acceptance for the demonstration experiment such that for a beam with normalized emittance of $\varepsilon_n = 0.2$ μm-rad the rms energy spread can be increased up to 4%, which in the case of the normal undulator even with such a low value of emittance can be regarded as a show stopper.

The acceptable energy spread for achieving a maximum power at the end of the undulator one order of magnitude larger than the spontaneous power can be improved by going to higher values of undulator parameter as shown in Fig. 4.27. An energy spread of $\sigma_\eta = 2.2$ % can be regarded as the maximum tolerable limit for the case of a relatively large undulator parameter of $K$=2.2.
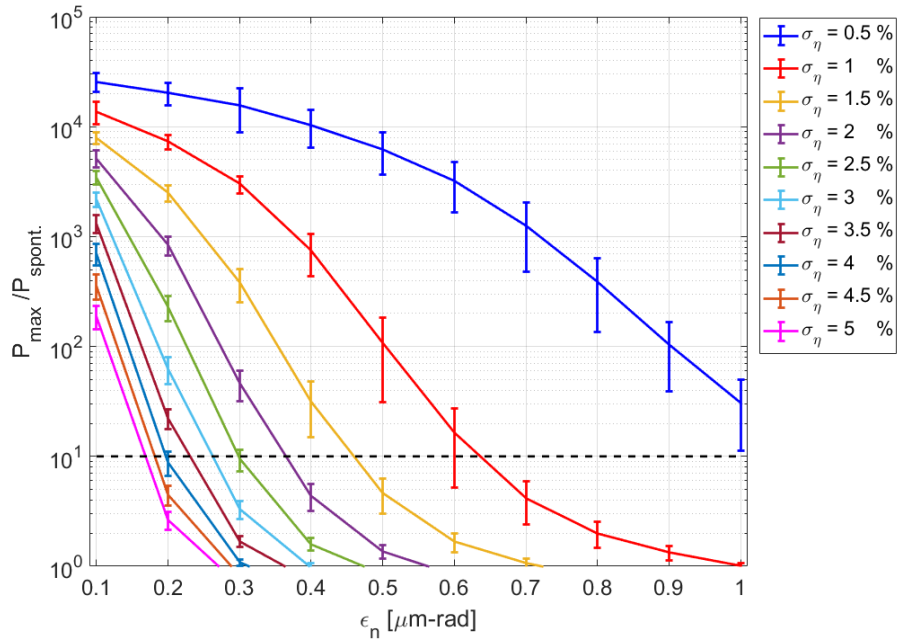
Figure 4.26: Normalized power as a function of normalized emittance and rms energy spread. The error bars indicate one standard deviation of the shot-to-shot power fluctuation due to the different initial shot-noise seeds for 10 runs. The design power limit is indicated by the dashed line.
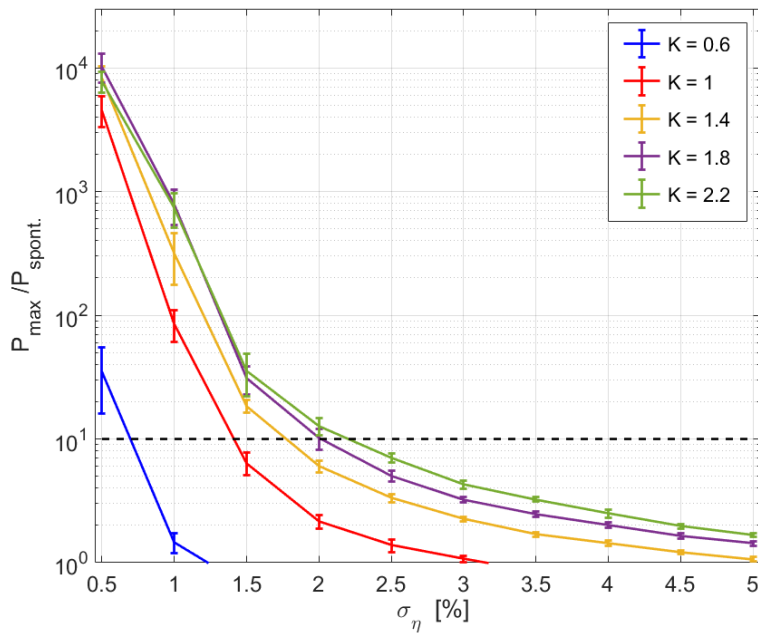


Figure 4.27: Normalized power as a function of energy spread and undulator parameter. The dashed line shows the power limit for the FEL amplification. The data are averaged over 10 runs with different shot-noise seeds and the error bars show one standard deviation of the shot-to-shot power fluctuation.

## 4.3.4 Emittance

The presence of relatively large energy spread in the beam generated in an LPA leads to an additional emittance growth in the beamline from the LPA to the undulator entrance. The normalized emittance of $\varepsilon_n$ = 0.5 µm-rad as the reference beam emittance is regarded without any transport line emittance growth contribution and is assumed to be the same in the both transverse and vertical planes. The importance of the emittance scaling is more prominent in the beamline design since a significant emittance growth by the beamline is expected due to the large energy spread within the electron beam. A detailed study of the effect of the beamline transport on the beam parameter and the collective effect like CSR and space charge is presented in chapter 5. All these effects will increase the beam emittance and affect the beam phase space properties. The dependency of the normalized power on the beam normalized emittances is plotted in Fig. 4.28 where the normalized power at the end of the undulator is plotted for different values of the initial normalized transverse emittances (non-dispersed beam) for the reference beam parameters. The transversely dispersed beam shows more emittance sensitivity in the dispersive plane, which must be considered in the optimization of the beam line transport (see chapter 5). The maximum tolerable normalized emittance bound is illustrated by the contour line in Fig. 4.28. For the case of $\varepsilon_{nx}$ = $\varepsilon_{ny}$, a normalized emittance of $\varepsilon_n$ ≈ 0.7 µm-rad can be regarded as the tolerable limit.
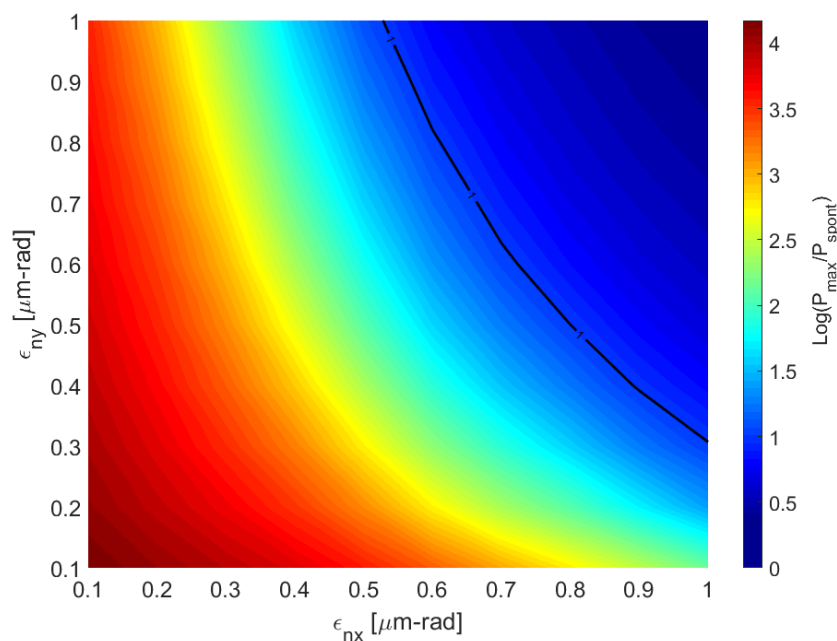


Figure 4.28: Normalized power as a function of the normalized transverse and horizontal emittances. The contour line shows the power limit for the FEL amplification. The data are averaged over 10 runs with different shot-noise seeds.
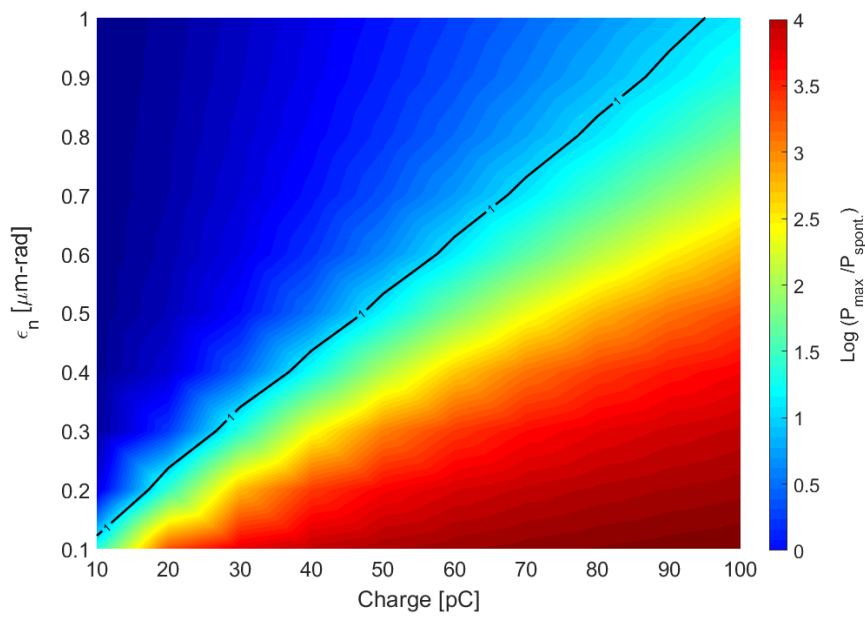
Figure 4.29: Normalized power as a function of the charge and the normalized emittance. The contour line shows the normalized power goal design. The data are averaged over 10 runs with different shot-noise seeds.
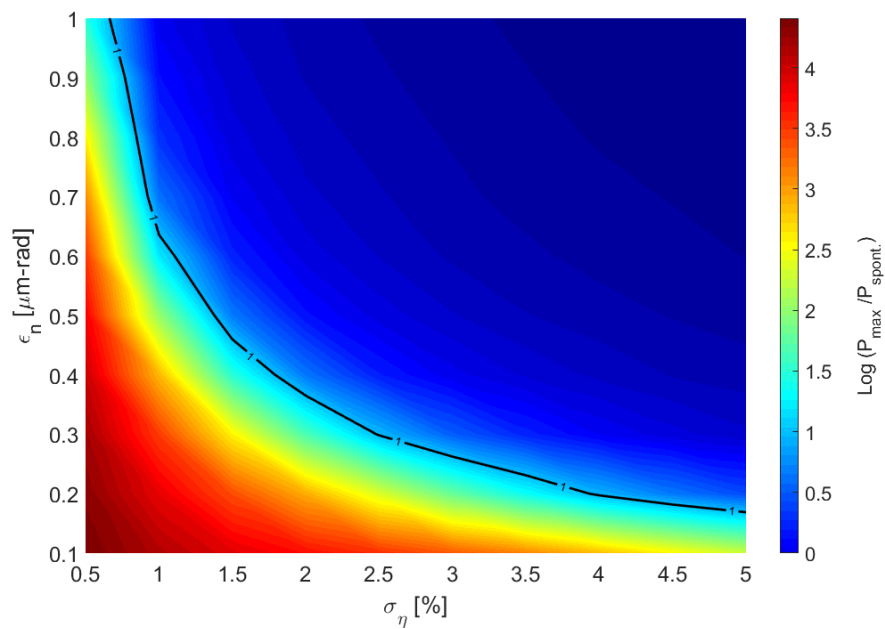


Figure 4.30: Normalized power as a function of the rms energy spread and the normalized emittance. The contour line illustrates the power goal bound. The data are averaged over 10 runs with different shot-noise seeds.
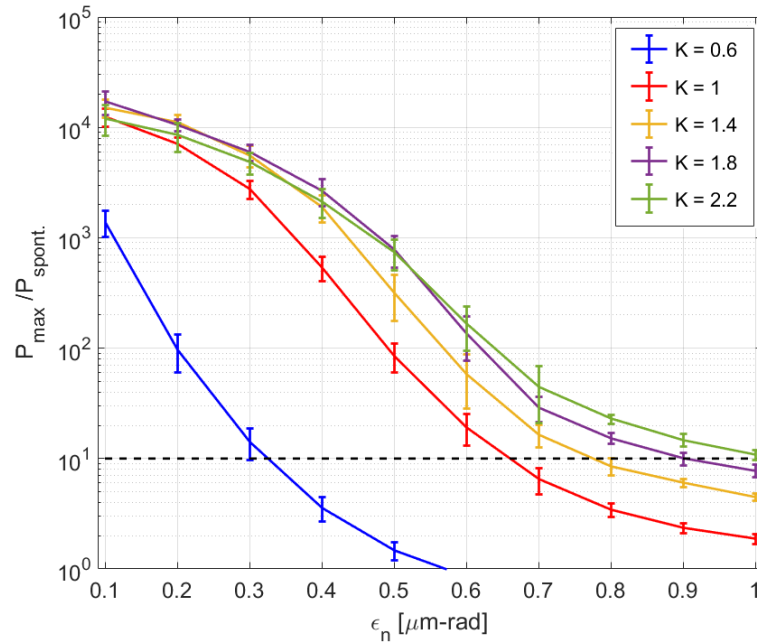
Figure 4.31: Normalized power vs normalized emittance for different values of undulator parameter. The dashed line shows the power limit for the FEL amplification. The data are averaged over 10 runs with different shot-noise seeds and the error bars show one standard deviation of the shot-to-shot power fluctuation.

Fig. 4.29 shows the normalized power vs normalized emittance and charge. The contour line shows the design power limit which increases linearly in terms of both free parameters. It shows that any relative increase or decrease in normalized emittance or charge can be compensated by roughly the same amount of relative change in the other parameter i.e. 50% reduction of the charge can be compensated by 50% decrease in the normalized emittance.

Decreasing the normalized emittance also allows for a larger rms energy spread range. Normalized power as a function of the normalized emittance and the rms energy spread is shown in Fig. 4.30. The area of the acceptable parameters, which is determined by the contour line, in comparison with the other plots covers a small portion of the parameter set in terms of the normalized emittance and the energy spread. However, beams with higher energy spread suffer more emittance growth in the beamline. This shows the importance of preserving the emittance during the beam transport when the energy spread is the dominant factor (see chapter 5).

Besides the beam parameters, the emittance acceptance range can be increased by the larger undulator parameters. As show in Fig. 4.31, increasing the undulator parameter up to $K$=2.2 results in a tolerable normalized emittance of nearly $\varepsilon_n$ = 1 µm-rad. For a large value of K, the normalized power curves tend to reach the same power level since the cooperation length for the higher K values increases as shown in Fig. 4.15 (d).

## 4.3.5 Bunch Length

The reference bunch length is assumed to be $\sigma_z$=1 μm with a Gaussian distribution. A beam with such a short length can undergo a significant slippage effect (see section 4.2.3), which leads to a gain length increase and a reduction in the saturation power since the radiation originated at the bunch tail would outrun the electron beam before reaching the saturation. The effect of the short bunches on the FEL gain can be estimated by the bunch length scaling law as [102]

$$L_g(\sigma_z) = L_{g0}(1 + \Lambda_z) \qquad (4.26)$$

where $L_{g0}$ is the 1D gain length and $\Lambda_z$ is the correction parameter

$$\Lambda_z = b_1 \exp\left(b_2\left(\frac{\sigma_z}{L_{c,1D}}\right)^{b_3}\right) \qquad (4.27)$$

with the fit parameters

$$b_1 = 16.7512, \qquad b_2 = -3.0420, \qquad b_3 = 0.3267 \qquad (4.28)$$

and 1D cooperation length

$$L_{c,1D} = (L_{g0}/\lambda_u)\lambda_l \qquad (4.29)$$

The normalized growth rate $L_{g0}/L_g(\sigma_z)$ in terms of normalized bunch length is depicted in Fig. 4.32. For bunch length much longer than the cooperation length the gain length converges to the ideal 1D gain length while for the bunch length on the order of cooperation length the gain length ratio drops due to slippage effect.
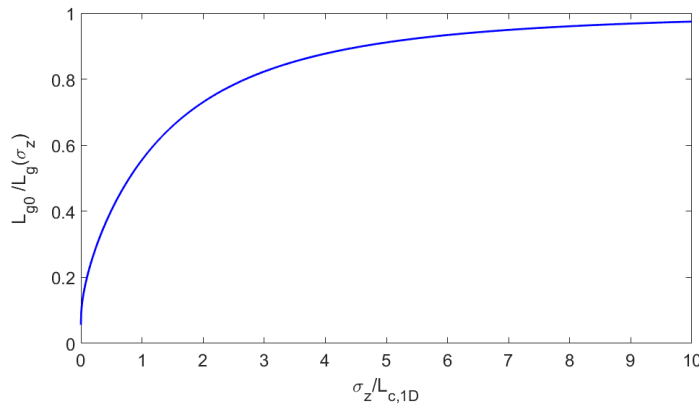


Figure 4.32: Normalized gain as a function of the normalized bunch length according to equation (4.26).

A combined scaling including both the energy spread and slippage effects can be done by using an effective cooperation length given by the corrected gain length of the energy spread scaling and using this effective cooperation length for the bunch length scaling. For this purpose, in the TGU case with a dispersed beam, the 1D cooperation length must be replaced by the effective one as

$$L_c^T = (L_g^T / \lambda_u)\lambda_l \tag{4.30}$$

Thus, the combined scaling regarding the energy spread and the bunch length effects in the TGU case can be calculated by

$$L_g^{T,\sigma_z} = L_{g0}\left(1 + b_1 \exp\left(b_2\left(\frac{\sigma_z}{L_c^T}\right)^{b_3}\right)\right)\left(n^{1/3} + \frac{\Delta^2}{n}\right) \tag{4.31}$$

The reduction of the gain length due to energy spread compensation leads to a decrease of the cooperation length resulting in a gain length reduction in the combined scaling. A contour plot of the normalized gain $L_{g0}/L_g^{T,\sigma_z}$ as a function of the normalized energy spread $\Delta = \sigma_\eta / \rho$ and the normalized bunch length $\sigma_z / L_{c,1D}$ for n=1 (non-dispersed beam) and n=$n_{opt}$ is illustrated in Fig. 4.33. The comparison shows a significant gain length reduction especially for the higher values of the normalized energy spread while for low energy spread beam the two cases show the same behavior in terms of the gain length reduction. It should be noted that the optimum bunch size ratio n, is roughly independent of the normalized bunch length and equation (4.12) was used for the optimum case (bottom plot) in Fig. 4.33[7].

For reference beam parameters, the effect of the bunch length on the normalized power has been studied by GENESIS simulations, as shown in Fig. 4.34. To minimize the effect of the other parameters and emphasis on the slippage effect on the normalized power, the charge value is scaled such that the same peak current ($I_{peak} \approx 8$ kA) is ensured for all bunch length values. Moreover, due to the limitation of modelling space-charge effects in GENESIS the peak current is assumed to be the same in the case of the short and the long bunches as well. As can be seen from the figure, increasing the bunch length leads to an increase in the normalized power due to decreasing the slippage effect. The minimum bunch length resulting in a normalized power above the design goal (for $I_{peak} \approx 8$ kA) is about $\sigma_z$=0.7 μm. Below this range the slippage has a strong effect on the power gain and the achievable power is not sufficient for the demonstration of the FEL amplification. On the right axis of the Fig. 4.34 the corresponded gain lengths are plotted. For the bunch length of $\sigma_z \geq 1$ μm the gain lengths are almost the same resulting in the same cooperation lengths. This shows that for a fixed value of the peak current of $I_{peak} \approx 8$ kA a bunch length of $\sigma_z$=1 μm can be chosen as the optimum case reg-

---

[7] For the values of Δ<0.6 the optimum bunch size ratio is n=1 since regarding the gain length scaling included the energy spread effect, a gain length reduction is possible just for cases with Δ>0.6 (Fig. 4.4).
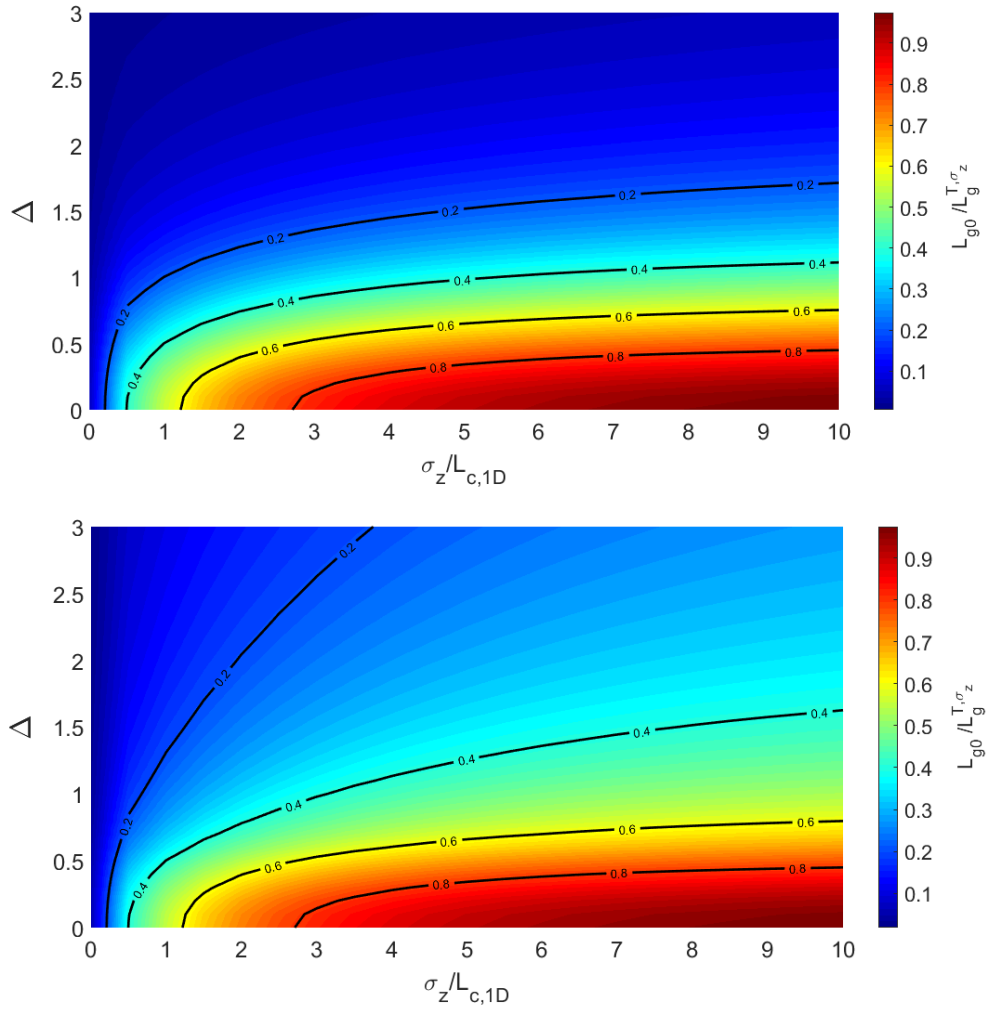
Figure 4.33: Normalized gain as a function of the normalized bunch length and the normalized energy spread for n=1 (top) and n=$n_{opt}$ (bottom) according to equation (4.31). A substantial gain length reduction in comparison with the non-dispersed beam can be expected particularly for the large values of the normalized energy spread.

-arding the slippage effect. However, the normalized power grows for long bunches due to having more interaction region with the radiation.

Increasing the bunch length in LPAs (external injection regime) typically results in an increase in the initial energy chirp which is assumed to be the same as the projected energy spread. In fact, positioning the beam at the slope of the longitudinal field during the acceleration process leads to an energy chirp caused by the finite bunch length. Fig. 4.35 shows the normalized power as a function of the bunch length (assuming the same peak current of $I_{peak} \approx 8$ kA) and the energy spread for the reference beam parameters. The contour line shows the maximum tolerable energy spread for each bunch length value in the case of reaching the power goal limit. In the long bunch case of $\sigma_z$=2 µm the maximum tolerable energy spread imposed by the LPA in order to reach the normalized power design is around 2.5%.
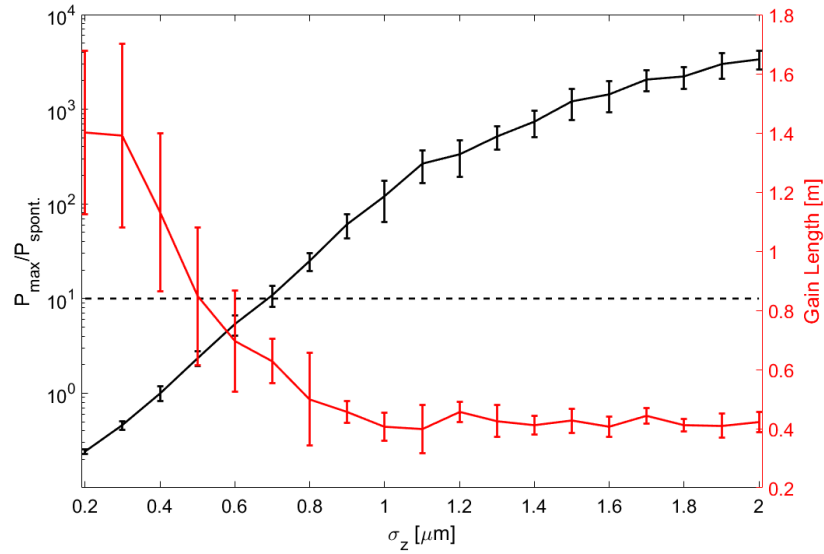
Figure 4.34: Normalized power as a function of the bunch length for a fixed amount of the peak current (different charges) of $I_{peak} \approx 8$ kA. The design power goal is indicated by the dashed line. On the right axis the corresponded gain lengths are plotted. The data are averaged over 10 independent runs with different shot-noise power seeds and the error bars show one standard deviation in the power fluctuation.
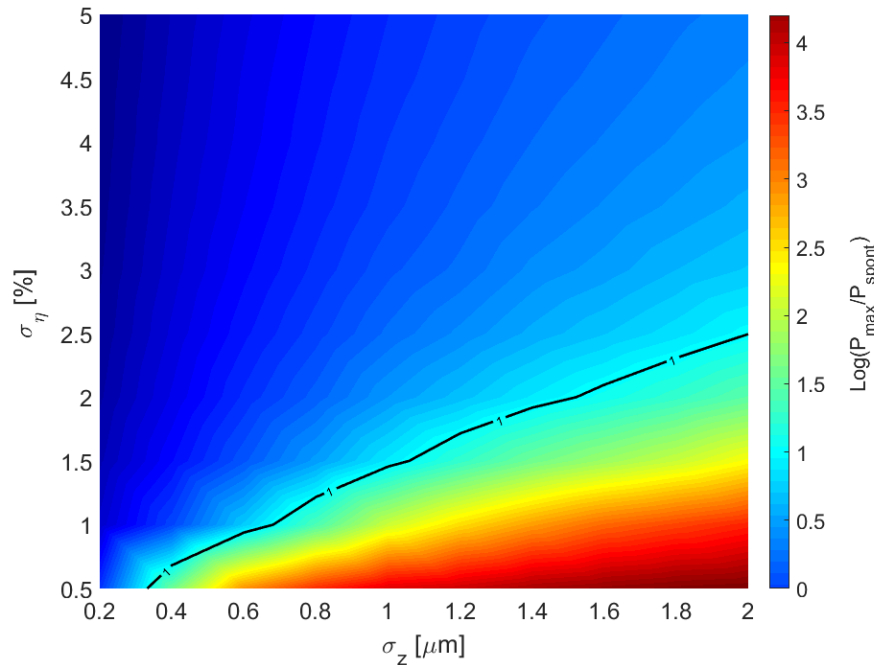


Figure 4.35: Normalized power vs the bunch length and the rms energy spread for a fixed amount of the peak current of $I_{peak} \approx 8$ kA. The contour line illustrates the power goal bound. The data are averaged over 10 runs with different shot-noise seeds.
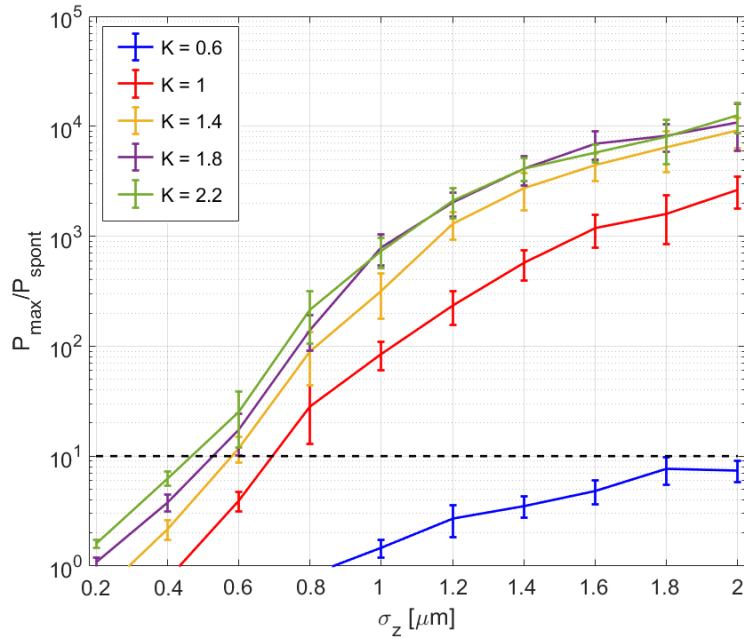
Figure 4.36: Normalized power vs bunch length for different values of the undulator parameter. The dashed line shows the power limit for FEL amplification. The data are averaged over 10 runs with different shot-noise seeds and the error bars show one standard deviation of the shot-to-shot power fluctuation.

As shown in Fig. 4.15 (c), the compromise between the FEL parameter and the radiation wavelength leads to an optimum value for the undulator parameter regarding the cooperation length. This can also be seen from Fig. 4.36 where the normalized power is plotted as a function of the bunch length and the undulator parameter. Increasing the undulator parameter for a given bunch length results in a smooth increase in the normalized power for large K values. For the long bunch case of $\sigma_z$ = 2 µm the undulator parameter can be decreased down to K > 0.6, while for short bunches of $\sigma_z$ < 0.5 µm the power goal design cannot be reached even for the high K value of K = 2.2. This clearly shows the strong slippage effect in the short bunch length cases.

As shown in Fig. 4. 15 (a), beams with the charge in the range of 50 pC < $Q$ < 100 pC approximately results in the same cooperation length. In this regard, the effect of increasing the bunch length on the FEL power for a given cooperation length can be studied by scanning the bunch length for the charge values in the range of 50 pC < $Q$ < 100 pC. As can be seen from Fig. 4.37, increasing the bunch length leads to a drop of the FEL power for all charge values. Although increasing the bunch length reduces the slippage effect by increasing the interaction time between the electrons and the radiation field, the reduction of the peak current and local charge density has a stronger effect on the FEL power output.
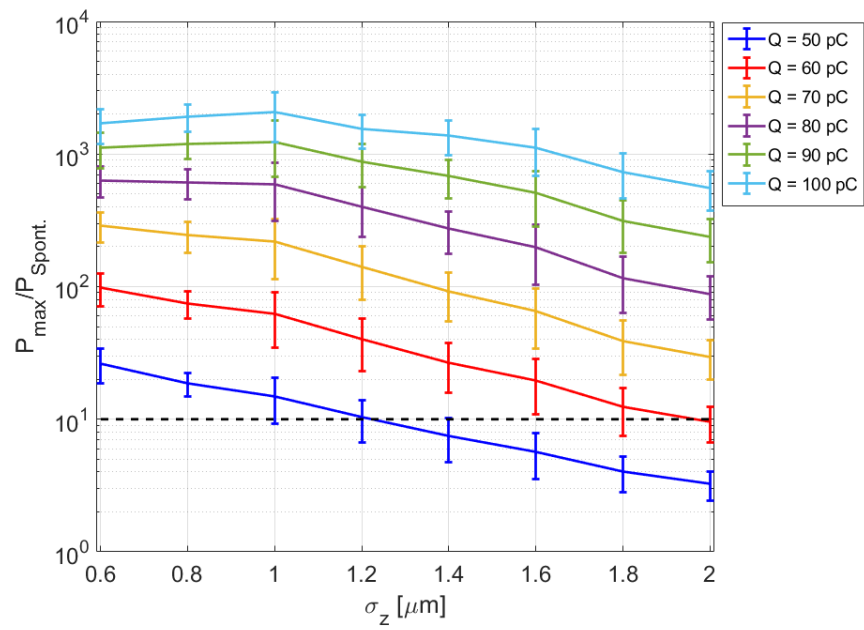
Figure 4.37: Normalized power vs bunch length for different values of the beam charge. The dashed line shows the power limit for the FEL amplification. The data are averaged over 10 runs with different shot-noise seeds and the error bars show one standard deviation of the shot-to-shot power fluctuation.

# 4.4 Conclusion

In this chapter, the transverse gradient undulator concept from an FEL point of view has been studied. The major limitation of using the beams generated in laser plasma accelerators the relatively large energy spread within the beam which is on the percent-level. Such a large energy spread hinders the FEL process and prevents the produced radiation to be amplified. The TGU scheme is based on a reduction of the local energy spread at the cost of a reduction of the local current density. The beam, which is dispersed transversely, enters the TGU with a transverse field gradient. The energy of the particles is matched to the TGU transverse gradient which results in an increase of the power gain. A comparison between the TGU and a normal planar undulator shows a significant improvement in the power gain and the gain length for the TGU case.

It is planned to perform the first FEL lasing by a TGU after a successful test of the TGU40. For the demonstration experiment, the TGU will be attached to a laser plasma accelerator as the beam generator and the radiated power at the end of the undulator will be used as a measure for demonstrating the FEL amplification. In this regard, a nominal LPA beam parameter set has been chosen based on the currently achievable parameters from the laser plasma accelerators. The minimum FEL beam requirement has been investigated by scaling the reference parameter set over a possible range which can be reached by an optimized LPA setup.

Sensitivity study has been done in terms of energy, charge, energy spread, normalized emittance and bunch length. Although it is possible to achieve the design goal power $P_{total}/P_{spont.} \geq 10$, with the reference beam, the scaling studies allow to address any variation of the reference parameter set. Since the combination of all parameters might be still challenging for current LPAs, the scaling also shows how a reduction in a specific parameter can be compensated by changing the other parameters to reach the normalized power design goal. Besides, the undulator parameter has been included in the scaling studies as the setup parameter for cases in which the power goal limit cannot be achieved by variation in the LPA beam parameters.

# Chapter 5

# *Beam Transport System*

Besides the energy spread as a major problem of electron beams generated in laser plasma accelerators, the LPA beams usually suffer from a large divergence in the milliradian range. Such a large divergence must be compensated by using focusing elements as close as possible to the LPA exit. The chromatic emittance growth due large energy spread poses serious challenges for capturing and transporting the beam while preserving the beam quality, which is characterized by its emittance. Therefore, it is important to investigate the impact of the beam line on the beam properties and to study the evolution of the beam parameters during the transport. In the following sections, the major points that need to be considered in the design of a beam line for a TGU are addressed and an optimized compact beam line is proposed. At the end of this chapter, a start-to-end FEL based TGU simulation is performed in order to investigate the effect of the beam line on the final FEL power, while the collective effects are included during the transport.

## 5.1 Chromatic Emittance Growth

The emittance is the measure of the spread of the particle distribution in 6-D volume in phase space $(x, p_x, y, p_y, z, p_z)$ which is enclosed by an appropriate fraction of the particle distribution, usually one standard deviation. The projected phase space emittance in $x - p_x$ plane is defined as [103]

$$\varepsilon_{ph} = \frac{1}{\langle p_z \rangle} \sqrt{\langle x^2 \rangle \langle p_x^2 \rangle - \langle x p_x \rangle^2} \qquad (5.1)$$

117

A more practical parameter which is preserved with acceleration is the normalized emittance,

$$\varepsilon_{n,ph} = \frac{\varepsilon_{ph}\langle p_z\rangle}{m_0 c} \tag{5.2}$$

in which $m_0$ is the electron rest mass and $c$ is the speed of light. The emittance can also be defined in the trace space $(x, x', y, y', z, \delta)$ as

$$\varepsilon_{tr} = \sqrt{\langle x^2\rangle\langle x'^2\rangle - \langle xx'\rangle^2} \tag{5.3}$$

with $x' = p_x / p_z$ and the corresponding normalized emittance,

$$\varepsilon_{n,tr} = <\beta\gamma> \varepsilon_{tr} \tag{5.4}$$

where $\beta$ and $\gamma$ are the normalized velocity and the Lorentz relativistic factor, respectively. For conventional accelerators with relatively low energy spread the beam equation (5.4) might generally be the case, but for beams with a large energy spread, like the electron beams generated in the laser plasma accelerators, the normalized emittance must be calculated by using the general normalized emittance definition in phase space as

$$\varepsilon_{n,ph} = \sqrt{\langle x^2\rangle\langle \beta^2\gamma^2 x'^2\rangle - \langle x\beta\gamma x'\rangle^2} \tag{5.5}$$

Assuming that there is no correlation between the energy and transverse position and defining the relative energy spread $\sigma_E$,

$$\sigma_E^2 = \frac{\langle \beta^2\gamma^2\rangle - \langle \beta\gamma\rangle^2}{\langle \gamma\rangle^2} \tag{5.6}$$

the *intrinsic normalized emittance* for relativistic electrons ($\beta = 1$) reads [104,105]

$$\varepsilon_{n,intr} = \langle \gamma\rangle\sqrt{(\sigma_E^2\sigma_x^2\sigma_{x'}^2 + \varepsilon_{tr}^2)} \tag{5.7}$$

which in the case of low energy spread reduces to the usual expression of normalized emittance in the trace space, equation (5.4). In the case of $\alpha = 0$ i.e. the beam is in a waist and assuming a long drift ($\sigma_x(L) \approx \sigma_{x'}L$), the emittance growth in a drift of length $L$ can be approximated by

$$\varepsilon_{n,intr} = \langle \gamma\rangle\sqrt{(\sigma_E^2 L^2\sigma_{x'}^4 + \varepsilon_{tr}^2)} \tag{5.8}$$

While the normalized phase space emittance increases through a drift section with the initial beam divergence and energy spread, the trace space emittance remains constant due to the
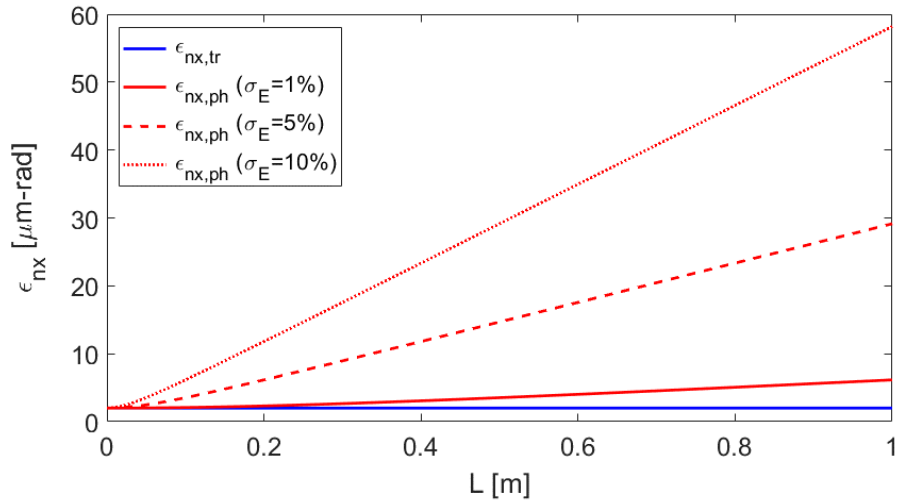
Figure 5.1: Comparison of the evolution of the normalized phase space emittance and the trace space emittance over 1-meter drift section for different values of the initial energy spread, simulated by ELEGANT.
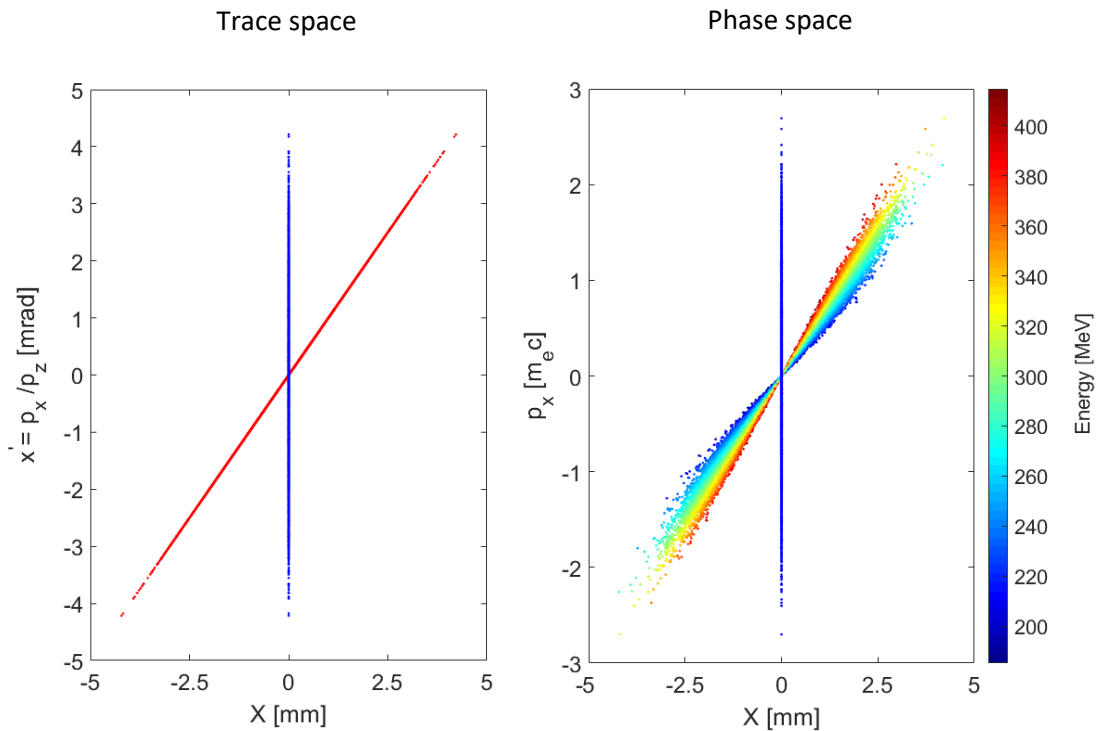


Figure 5.2: Evolution of the beam in the trace space (left) and the phase space (right) after 1-meter drift for the case of the initial energy spread of 10%. During the drift, particles with different energies rotate with different velocities in the phase space which causes emittance worsening [83].

119

normalization to $p_z$. This can be seen from Fig. 5.1 where the evolution of the normalized equation (5.8), the normalized phase space emittance is not constant in the drift and its growth scales with the initial energy spread. Here, a beam with the energy of 300 MeV, 1 mrad initial divergence and normalized emittance of 2 µm-rad is assumed. For the three cases of different energy spread the normalized trace space emittance (equation 5.4) remains constant. The difference behaviour of the normalized emittances in a drift can be understood by looking at the beam distribution in these spaces. Fig. 5.2. shows the beam distributions after 1-meter drift in the trace space (left) and the phase space (right) for the beam with initial energy spread of 10% shown in Fig. 5.1. In the trace space $(x, x')$, due to the normalization to $p_z$, the energy spread effect cannot be seen and the normalized emittance remains constant. On the other hand, in the phase space particles with different energies sheer according to their energies and as a result the phase space emittance will not be a constant during the drift.

As discussed in detail in Ref. [106], the two emittances show different behaviour in a transfer line, as we saw earlier in a drift part. When the transverse and longitudinal distributions are independent[1], the evolution of the phase space and trace space emittances through a thin quadrupole of length $l$ and focusing strength $k$ are given by

$$\varepsilon_{tr}^2 - \varepsilon_{tr0}^2 = k^2 l^2 \sigma_E^2 \sigma_{x0}^4 \tag{5.9}$$

$$\varepsilon_{ph} = \varepsilon_{ph0} \tag{5.10}$$

with the initial values at the lens entrance subscripted by 0. Unlike the drift section, the phase space emittance stays constant while the beam in the trace space emittance suffers an emittance dilution scaled with the beam energy spread, beam size and integrated normalized gradient $kl$ [107].

However, if there is no correlation between longitudinal and transverse distributions, it can be shown that to the first order in $dp/p_0$ the two normalized emittances are related as [106]

$$\varepsilon_{n,ph}^2 = \varepsilon_{n,tr}^2 \left(1 + \alpha^2 \sigma_E^2\right) \tag{5.11}$$

where $\alpha$ is the Twiss parameter. Equation (5.8) shows that the difference between the two normalized emittances are more pronounced for the cases of higher energy spread and more divergent or convergent beams. Although the validity of equation (5.11) in the presence of a strong focusing lens is lost, in the case of $\alpha = 0$ i.e. at the beam waist, the two normalized emittances are always equal.

This can be seen in Fig. 5.3 where the evolution of the normalized emittances and the Twiss parameter $\alpha$, are plotted in the drift section of the previous example followed by a quadrupole at L=1 m. While the trace space emittance is constant in the drift part, it jumps aft-

---

[1] In the presence of strong focusing elements this assumption is not valid anymore.
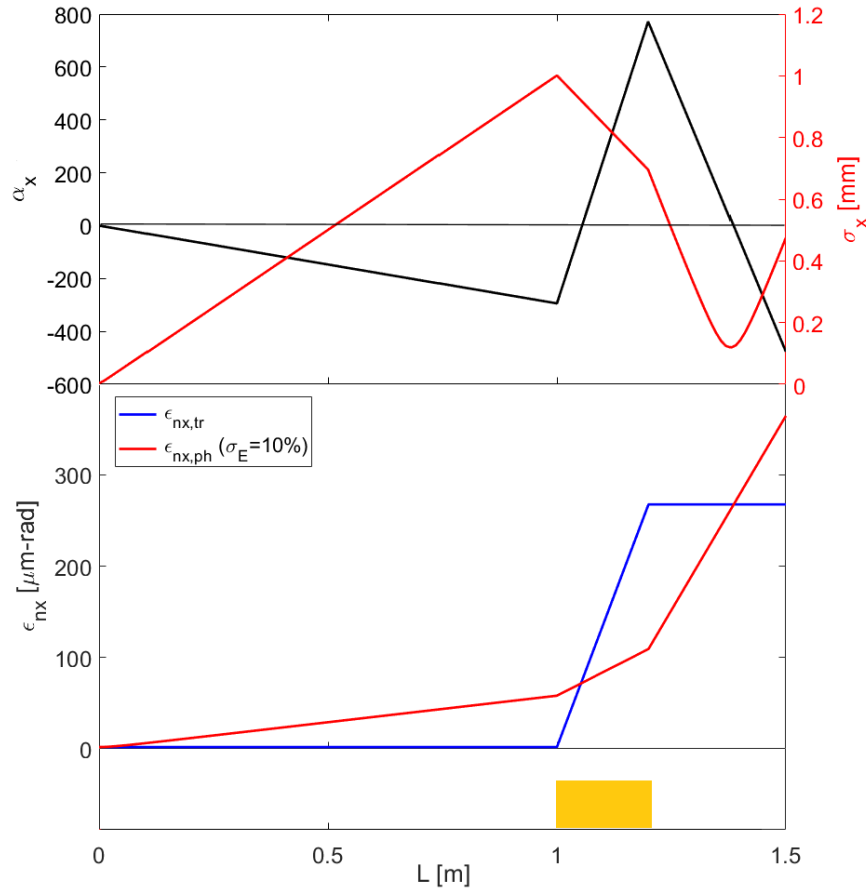
Figure 5.3: Evolution of the phase space emittance and the trace space emittance over a drift followed by a quadrupole (yellow rectangular). The top plot shows the corresponded beam size and the Twiss parameter $\alpha$. The two normalized emittances are equal where $\alpha = 0$ i.e. at the beam waist where the beam changes from convergent to divergent at L=1.39.

-ter the quadrupole. The quadrupole focuses the beam and the beam waist ($\alpha = 0$) is achieved at L=1.39, where two normalized emittances are equal. It should be noted that the evolution of the parameters inside the quadrupole is not shown here.

The different behaviour of the normalized emittances emphasizes the calculation of normalized phase space emittance rather than the trace space emittance in tracking simulations. Since the trace space shows an unphysical behaviour, in order to get meaningful results, the phase space emittance should be used for the optimization of the beam line [103]. Furthermore, it is clear that the locations of the beam waist in the beam line can be regarded as the favourable points for emittance measurement. It should be mentioned that, the emittance values quoted in this work are normalized phase space emittances, unless otherwise specified.

# 5.2 Beam Line Design

In this section, a study of designing a beam line for a TGU with an electron beam generated in an LPA is presented. Unlike the conventional beam lines, the TGU beam line must include at least one dispersive element (a dipole) to introduce dispersion, which needs to be matched to the TGU gradient, according to equation (3.4). Since the LPA beam suffers from a large energy spread, the bunch length increases after the dipole resulting in a reduction in peak current. Moreover, due to the large divergence and the energy spread of the LPA beam, the focusing elements should be as close as possible to the LPA exit to control the beam expansion and chromatic emittance growth which increases the difficulty of designing such a beam line, specially from an FEL point of view.

## 5.2.1 Bunch Lengthening

One of the advantages of the LPA beams is high peak current up to tens of kA. Preserving such a high peak current in the beam line transport can be challenging specially in the TGU case. The electron beam must be dispersed transversely before entering the TGU. This can be done by including bending magnets in the beam line which introduce required dispersion for the TGU radiation. The effect of the bending magnet (dipole) on the bunch length can be studied by the transfer matrix (2.11), which for the longitudinal offset $z$, reads

$$z = z_0 - \sin\theta x_0 - R(1-\cos\theta)x_0' + (l/\gamma^2)\delta - R(\theta - \sin\theta)\delta \tag{5.12}$$

For small bending angles $\theta \ll 1$, and assuming relativistic particles i.e. $1/\gamma^2 \approx 0$ equation (5.12) is approximated as

$$z = z_0 - \theta x_0 - \frac{l\theta}{2}x_0' - \frac{l\theta^2}{6}\delta \tag{5.13}$$

with $l = R\theta$ being the length of the dipole magnet, $\delta$ the relative energy deviation, $x_0$ and $x_0'$ the transverse offset and slope before the dipole. For the LPA beam with a large energy spread and a short bunch length, the increase of the bunch length is more pronounced resulting in a reduction of the peak current and FEL gain degradation.

The bunch lengthening after the dipole can be minimized by proper choosing of the initial Twiss parameters at the dipole entrance. Multiplying both sides of the equation (5.13) by $z$ and taking average leads to

$$\sigma_z^2 = \sigma_{zz_0} - \theta\sigma_{zx_0} - \frac{l\theta}{2}\sigma_{zx_0'} - \frac{l\theta^2}{6}\sigma_{z\delta} \tag{5.14}$$

with $\sigma_{ij} = \langle ij \rangle$ being the covariance term and $\sigma_i^2 = \langle ii \rangle$. The covariance terms can be calculated by multiplying both sides of the equation (5.13) by the corresponding value and by taking an ensemble average over the all particles in the bunch. Assuming that the initial longitudinal position is uncorrelated with the other variables i.e. $\sigma_{zj} = \langle zj \rangle = 0$ and that there is no energy correlation in the initial distribution i.e. $\sigma_{\delta j} = \langle \delta j \rangle = 0$, the covariance terms using equation (2.19), are given by

$$\sigma_{zz_0} = \sigma_{z_0}^2,$$
$$\sigma_{zx_0} = \theta\varepsilon(\frac{l\alpha}{2} - \beta),$$
$$\sigma_{zx_0'} = \theta\varepsilon(\alpha - \frac{l}{2\beta} - \frac{l\alpha^2}{2\beta}),$$
$$\sigma_{z\delta} = \theta\varepsilon(-\frac{l\theta}{6\varepsilon}\sigma_\delta^2)$$

(5.15)

where $\varepsilon$ is the initial beam emittance (trace space) with $\alpha$ and $\beta$ the initial Twiss parameters at the dipole entrance. Therefore, the bunch length after the dipole can be approximated as

$$\sigma_z^2 = \sigma_{z_0}^2 + \left(\frac{l\theta^2}{6}\right)^2 \sigma_\delta^2 + \theta^2\varepsilon\left(\beta - l\alpha + \frac{l^2}{4\beta} + \frac{l^2\alpha^2}{4\beta}\right)$$

(5.16)

Equation (5.16) shows a bunch lengthening after the dipole in terms of the energy spread and the initial Twiss parameters, which for a given energy spread can be minimized by minimizing the third term (positive value). While there is no absolute minimum for that, for the large values of $\alpha$ it can be minimized by

$$\beta \approx \left(\frac{l}{2}\right)\alpha$$

(5.17)

This can be seen from Fig. 5.4 where the bunch length after a dipole with $\theta = 0.1\,rad$ and $l = 0.1\,m$ is plotted as a function of the initial Twiss parameters, $\alpha$ and $\beta$ for a 300 MeV beam with 1% uncorrelated energy spread. The initial bunch length and the normalized emittance are $\sigma_{z_0} = 1\,\mu m$ and $\varepsilon_{nx} = 0.5\,\mu rad$, respectively. The red line shows the local minima estimated by equation (5.16). Besides the initial Twiss parameters, the bending angle and the initial energy spread affect the bunch length according to the equation (5.16). Fig. 5.5 shows the final bunch length after passing the dipole as a function of dipole bending angle for different values of the initial energy spread. The beam parameters are the same as the former example with the optimum Twiss parameters $\alpha = 20$ and $\beta = 1$ according to equation (5.17). As can be seen from the figure, in the case of a beam with a large energy spread small bending angles are favored to avoid bunch lengthening by the dipole.
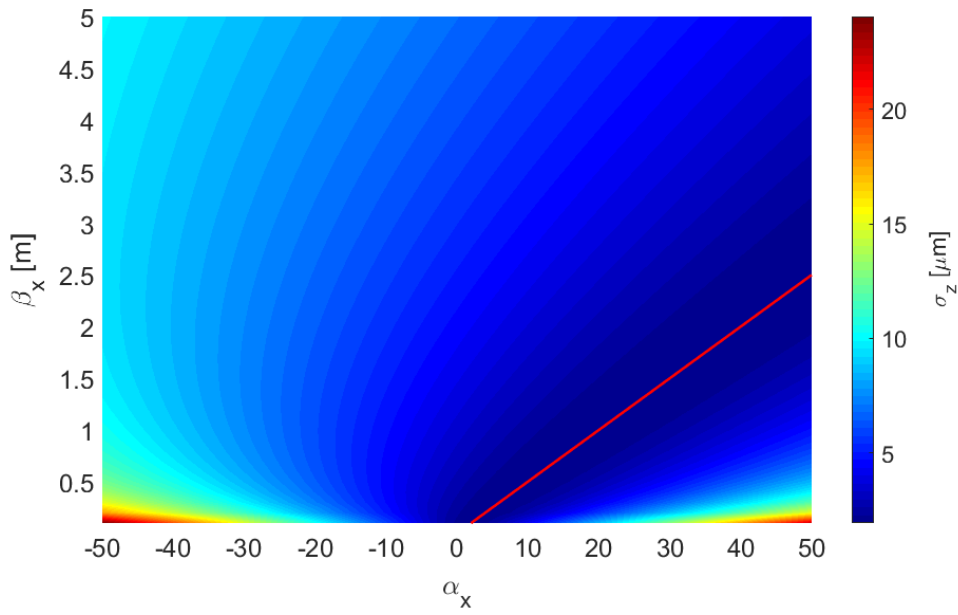
Figure 5.4: Bunch length after a dipole as a function of the initial Twiss parameters $\alpha$ and $\beta$ at the dipole entrance for the initial bunch length $\sigma_{z_0} = 1\,\mu m$. The red line shows the local minima. See the text for details.
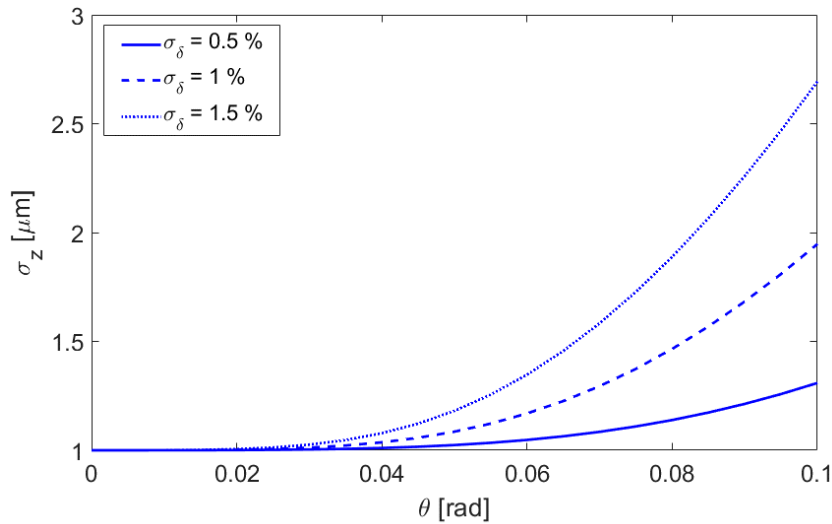


Figure 5.5: Bunch length after a dipole as a function of the dipole bending angle for different values of the energy spread. For small bending angles, the bunch lengthening is much smaller than for large bending angles.

Including an energy chirp in the initial distribution as [108]

$$\delta = h z_0 + \delta_u \qquad (5.18)$$

with $h$ the energy chirp factor and $\delta_u$ the uncorrelated energy spread along the bunch length, equation (5.13) can be written as

$$z = \left(1 - \frac{l\theta^2 h}{6}\right) z_0 - \theta x_0 - \frac{l\theta}{2} x_0' - \frac{l\theta^2}{6}\delta_u \qquad (5.19)$$

Then the bunch length after the dipole is given by

$$\sigma_z^2 = \left(1 - \frac{l\theta^2 h}{6}\right)^2 \sigma_{z_0}^2 + \left(\frac{l\theta^2}{6}\right)^2 \sigma_{\delta_u}^2 + \theta^2 \varepsilon \left(\beta - l\alpha + \frac{l^2}{4\beta} + \frac{l^2\alpha^2}{4\beta}\right) \qquad (5.20)$$

Equation (5.20) shows that for "*full compression*" where $h = 6/l\theta^2 = -1/R_{56}$ the final bunch length is given by the uncorrelated energy spread in the bunch. It should be noted that, assuming an initial chirp does not change the optimum values of the initial Twiss parameters, the equation (5.17) is still valid. However, the bunches generated in the LPAs usually have a negative energy chirp which results in an increase of the bunch length by passing the dispersive element in the beam line. Fig. 5.6 shows the bunch length after passing a dipole as a function of the initial chirp for a beam with the same parameters as the previous example with the optimum Twiss parameters $\alpha = 20$ and $\beta = 1$ according to equation (5.17). The blue line shows the case of an unchirped beam and the dashed line illustrates the initial bunch length before the dipole. As can be seen from the figure, for the negative chirp values the bunch lengthening is larger than the unchirped beam, while the increase of the bunch length due to the initial energy spread can be reduced by imposing an initial positive chirp.
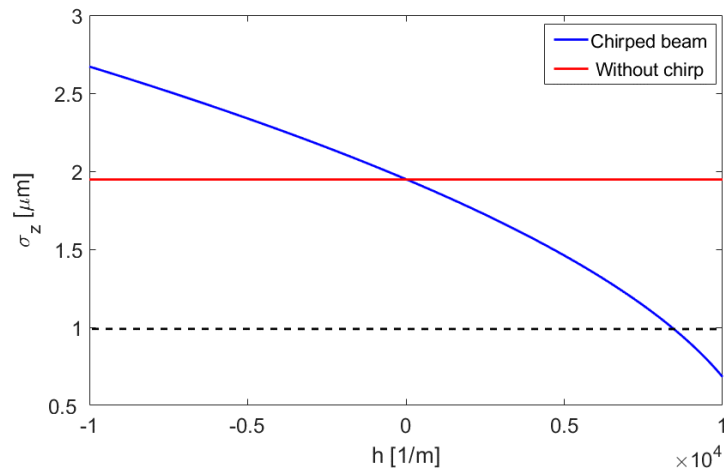


Figure 5.6: Bunch length after a dipole as a function of the initial chirp. The dashed line shows the initial bunch length.

## 5.2.2 Chromatic Correction

The focusing strength $k$, of a quadrupole is inversely proportional to the particle momentum $p$, which results in a change of focusing strength due to the energy deviation as

$$k = \frac{e}{p}\frac{\partial B_y}{\partial x} = \frac{e}{p_0(1+\delta)}\frac{\partial B_y}{\partial x} \approx k_0(1-\delta) \tag{5.21}$$

with $p_0$ being the reference particle energy. Considering a beam, which goes through a quadrupole magnet with strength $k$ and length $l$, the angular kicks by a transversely focusing quadrupole on the particle with the transverse position $x$ and the vertical position $y$ in the thin lens approximation can be expressed as

$$\Delta x' = -k_0 lx(1-\delta), \tag{5.22}$$

$$\Delta y' = k_0 ly(1-\delta) \tag{5.23}$$

which shows an additional kick on the particle corresponding to its energy deviation from the reference energy. Therefore, the focal point of a quadrupole will be shorter for lower energy particles than the particles with a positive energy deviation, as shown schematically in Fig. 5.7 (a). For a dispersed beam with dispersion $D$ and relative energy spread $\delta$, this chromatic focal point change causes an additional dispersion $\Delta D(\delta)$, downstream of the quadrupole, which leads to a nonlinear correlation of $x-p$ [98]. The dispersion evolution after a transversely focusing quadrupole with initial value $D_0$ can be approximated by

$$D = D_0, \tag{5.24}$$

$$\Delta D' = -D_0 k_0(1-\delta) \tag{5.25}$$

which shows an energy dependent kick on the beam dispersion leading to an additional dispersion $\Delta D(\delta)$. Since the TGU concept needs a linear dispersion for optimum functioning, the nonlinearity in the $x-p$ correlation results in a degradation of the TGU gain due to the mismatching between the particles energy and the undulator parameter. Therefore, sextupole magnets must be included in the beam line. The magnetic field components of a sextupole are expressed as [109]

$$B_x = \frac{\partial^2 B_y}{\partial x^2}xy, \tag{5.25}$$

$$B_y = \frac{1}{2}\frac{\partial^2 B_y}{\partial x^2}(x^2 - y^2) \tag{5.26}$$

$$B_z = 0 \tag{5.27}$$
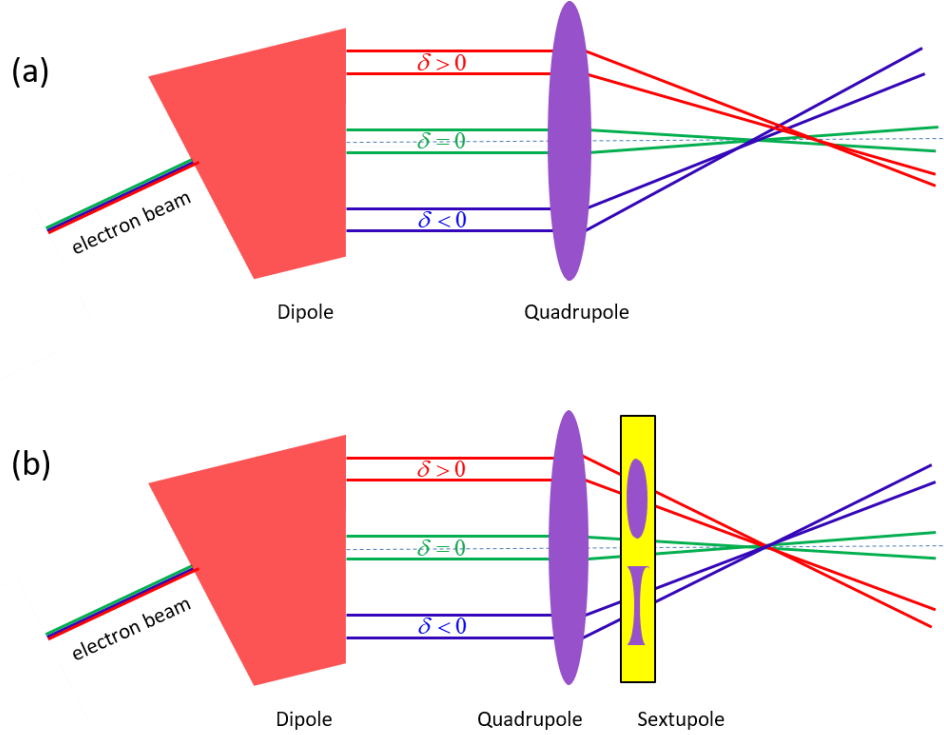
Figure 5.7: Chromatic aberration correction by a sextupole. (a): The focal length of a quadrupole is different for different energies. (b): sextupole with an appropriate strength can provide additional focusing (defocusing) depending on the energy of the particle resulting in the same focal length for all particles with different energies. Adopted from Ref. [109].

and the angular kicks from a sextupole with strength $m$, see equation (2.5), and length $L$, is given by [110]

$$\Delta x' \simeq \frac{\Delta p_x}{p} = -\frac{eLB_y}{p} = -\frac{1}{2}mL(x^2 - y^2), \qquad (5.26)$$

$$\Delta y' \simeq \frac{\Delta p_y}{p} = \frac{eLB_x}{p} = mLxy \qquad (5.27)$$

In fact, a sextupole acts like a quadrupole with a focusing strength related to the transverse particle position i.e.

$$k_{sext} = mx \qquad (5.28)$$

which in the case of a dispersed beam with $x = D\delta$, can be used to reduce chromatic aberrations by correcting the focusing of an off-energy particle, as shown in Fig. 5.7 (b). The additional dispersion $\Delta D(\delta)$ due to the energy dependent quadrupole kick can be decreased by the proper choice of the sextupole strength, which leads to linear $x - p$ correlation. Moreover, by implementing the sextupole, the trace space emittance growth due to a focusing element, equation (5.9), can be eliminated along with the nonlinear dispersion in the beam line [98].

# 5.2.3 Layout Optimization

The goal of the study performed here is to design a compact transport line to guide the beam from the laser plasma accelerator to the entrance of the TGU. The beam and the undulator parameters are assumed to be the same as the ones used in the reference case in chapter. 4, Table. 4.2, in order to maintain consistency with the study presented in that chapter. The beam line must be designed in a way that the electron beam has minimum emittance growth during the transport along with the other constraints concerning bunch lengthening and dispersion matching as well as matching of the Twiss parameters at the undulator entrance. However, some parameters, as elements length and maximum gradient are considered as fixed values to facilitate the optimization process. Table 5.1 lists all the fixed and the free parameters considered in the optimization.

It is assumed that the beam with a Gaussian distribution and without any initial energy correlation leaves the plasma at the waist with $\beta_{x,y} = 0.0095$ m and $\alpha_{x,y} = 0$. Since the beam after the plasma exit expands rapidly due to the large divergence, a focusing stage, which is composed of two quadrupoles, is used to capture the beam along with the third quadrupole for matching purposes for the subsequent stage. A dipole is placed after the focusing stage to introduce dispersion, which is controlled by the matching stage with three quadrupoles to match the Twiss parameters and the dispersion at the undulator entrance. For cancelling the chromatic emittance growth and nonlinear dispersion, sextupoles are included in the beam line as a chromatic correction stage. The number of the sextupoles after the dipole is given by the optimization, regarding the available space between the quadrupoles. However, the number of sextupoles can be increased by increasing the minimum distance between the elements in the matching section.

| Fixed Parameters | Value | Unit |
|---|---|---|
| Magnets Length | *0.1* | *m* |
| Maximum Quadrupole Strength | *100* | *1/m* |
| Maximum Sextupole Strength | *4000* | *1/m²* |
| Minimum Distance between elements | *0.1* | *m* |
| Maximum Distance between elements | *1* | *m* |
| Distance Between the first Quadrupole and the Plasma exit | *0.1* | *m* |

| Free Parameters | Value | Unit |
|---|---|---|
| Quadrupole Strength | *-100 ~ 100* | 1/m |
| Sextupole Strength | *-4000 ~ 4000* | *1/m²* |
| Dipole Bending Angle | */* | rad |
| Distance between elements | *0.1 ~ 0.5* | *m* |

Table 5.1: Fixed and the free parameters considered in the optimization.

The first constraint that should be considered is the Twiss matching at the dipole entrance due to the bunch lengthening imposed by the dipole on the beam. Therefore, according to equation (5.17), the transverse beta function should be related to the transverse alpha function at the entrance of the 0.1-m dipole by $\alpha = 20\beta$. Moreover, the dispersion created by the dipole must be matched to the TGU with the gradient $\alpha = 139.7$ 1/m along with the condition of a constant dispersion inside the TGU. So, the dispersion matching reads $D = 19.6$ mm and $D' = 0$. The Twiss parameters also need to be matched at the undulator entrance to have the minimum beam size along the undulator. The optimum Twiss parameters at the TGU entrance (see Sec. 4.2.1) are $\beta_x = 5.77$ m, $\beta_y = 1.26$ m $\alpha_x = 1.73$ and $\alpha_y = 0$. Likewise, the emittance growth must be maintained as low as possible. As six parameters should be matched at the end of the beam line along with a constraint at the dipole entrance, the transfer line should include six quadrupoles with variable drift sections. The optimization function that must be minimized is the quadratic sum of the relative differences to the optimum values of the Twiss parameters and the dispersion. For the emittance case, the relative difference is regarded respect to the initial emittances. Although the final power shows more sensitivity with respect to the emittance in the dispersive plane, the final emittances are optimized to have the same values in order to have a better comparison with the results obtained in chapter. 4. It should be noted that the optimum case is selected over 1000 runs with different initial values to avoid the local minima in the optimization. The initial values are chosen randomly over the range given by the maximum and the minimum of the corresponded values. The optimization and tracking have been done with the tracking code ELEGANT. The results of the optimization are presented in Table. 5.2, where the initial beam parameters at the exit of the plasma and the final beam parameters at the entrance of the TGU (at *z* = 2.67 m) are listed.

| Beam Parameter | Initial Value | Final Value | Unit |
|---|---|---|---|
| Energy | *300* | *300* | *MeV* |
| Charge | *65* | *65* | *pC* |
| RMS Energy Spread | *1%* | *1%* | */* |
| RMS Normalized Emittance (x/y) | *0.5* | *31/0.68* | *μm-rad* |
| RMS Beam Size (x/y) | *2.85* | *208/33* | *μm* |
| RMS Beam divergence (x/y) | *0.3* | *0.02/0.03* | *mrad* |
| RMS Beam Length | *1* | *1.2* | *μm* |

| Lattice Function | Initial Value | Final Value | Unit |
|---|---|---|---|
| Beta functions (x/y) | *0.0095* | *5.77/1.26* | m |
| Alpha (x/y) | *0* | *1.73/0* | / |
| Dispersion | *0* | *0.0196* | m |

Table 5.2: Initial and the final beam (at the TGU entrance) and the lattice parameters.

The beam line parameters including the drifts length and the magnets strength are listed in Table. 5.3. The compact design of the beam line allows to achieve the matched values at z = 2.67 m. The evolution of the beta functions and the dispersion for the reference beam energy along the beam line is plotted in Fig. 5.8. The dispersion introduced by the dipole is controlled by the quadrupole in the matching stage and is matched to the TGU as well as the Twiss parameters.

The effect of the chromatic correction stage with three sextupoles can be seen in Fig. 5.9, where the evolution of the normalized emittances (without dispersion contribution) are plotted for two cases, with and without sextupoles. The emittance growth is significantly suppressed by the sextupoles, but not completely. Although sextupoles correct the chromatic aberration, due to introducing geometric aberration they must be implemented in pairs in the beam line to avoid any new geometric aberration [88]. Moreover, sextupoles are able to reduce the additional dispersion $\Delta D(\delta)$, imposed by the quadrupoles on the off-energy particles. This is shown in Fig. 5.10, where the dispersion distribution at the undulator entrance is plotted in the cases of with and without sextupole correction. The non-linear dispersion distribution in the absence of the sextupoles is effectively mitigated when the sextupoles are included in the beam line. The moderate increase in the rms bunch length from 1 $\mu m$ to 1.2 $\mu m$ in comparison with the layout in Ref. [98] is the result of the matching of the transverse Twiss parameters at the dipole entrance, while in the aforementioned reference, the beam waist is matched at the position of the dipole.
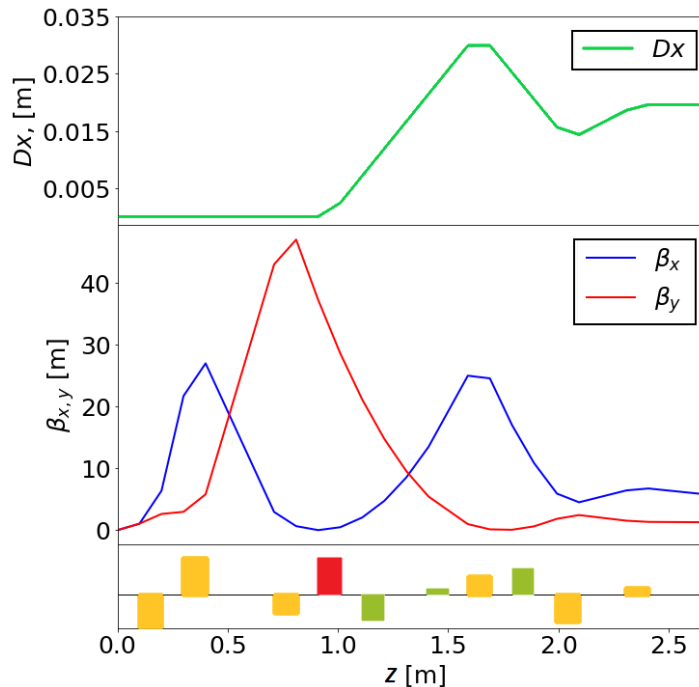


Figure 5.8: Dispersion Dx, and the beta functions along the beamline for the reference beam energy. Layout of the beam transport with quadrupole (yellow), dipole (red) and sextupole (green) is plotted at the bottom.

| Drift | Value | Unit |
|---|---|---|
| D1 length | *0.1* | *m* |
| D2 length | *0.1* | *m* |
| D3 length | *0.310* | *m* |
| D4 length | *0.102* | *m* |
| D5 length | *0.1* | *m* |
| D6 length | *0.178* | *m* |
| D7 length | *0.1* | *m* |
| D8 length | *0.1* | *m* |
| D9 length | *0.105* | *m* |
| D10 length | *0.215* | *m* |
| D11 length | *0.268* | *m* |

| Dipole | Value | Unit |
|---|---|---|
| Bending angle | *47.64* | mrad |
| Length | *0.1* | m |

| Quadrupole | Value | Unit |
|---|---|---|
| Q1 strength | *-65.76* | $1/m^2$ |
| Q1 strength | *62.52* | $1/m^2$ |
| Q1 strength | *-30.34* | $1/m^2$ |
| Q1 strength | *30.79* | $1/m^2$ |
| Q1 strength | *-46.37* | $1/m^2$ |
| Q1 strength | *10.31* | $1/m^2$ |
| All length | *0.1* | m |

| Sextupole | Value | Unit |
|---|---|---|
| S1 strength | *-3614.12* | $1/m^3$ |
| S2 strength | *903.08* | $1/m^3$ |
| S3 strength | *3771.90* | $1/m^3$ |
| All length | *0.1* | m |

Table 5.3: Parameters of the optimized beam line. All elements are consequently numbered. Here positive/negative values of the quadrupole strength refer to a transversely (x) focusing/defocusing quadrupole.
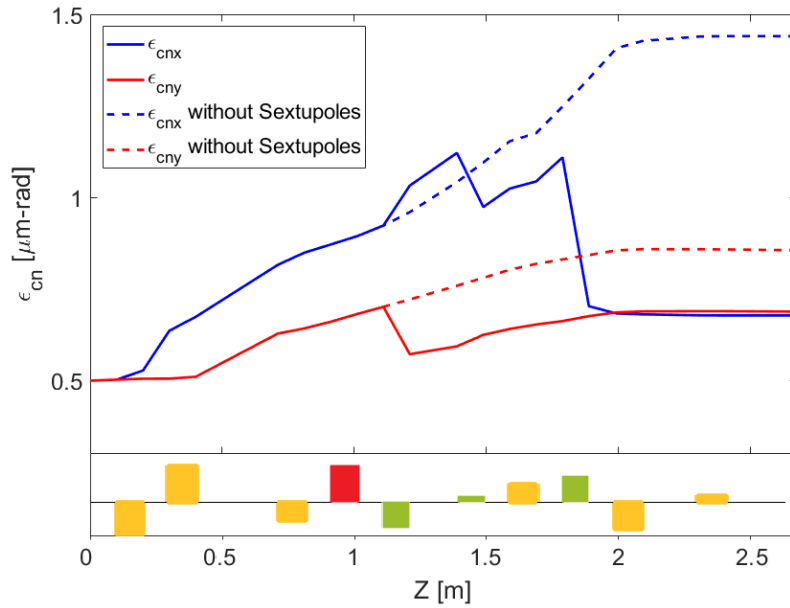
Figure 5.9: Evolution of the normalized emittances with and without sextupoles along the beam line. The chromatic emittance growth is effectively suppressed by implementing sextupoles in the beam line. The emittances are without dispersion contribution. Layout of the beam transport with quadrupole (yellow), dipole (red) and sextupole (green) is plotted at the bottom.
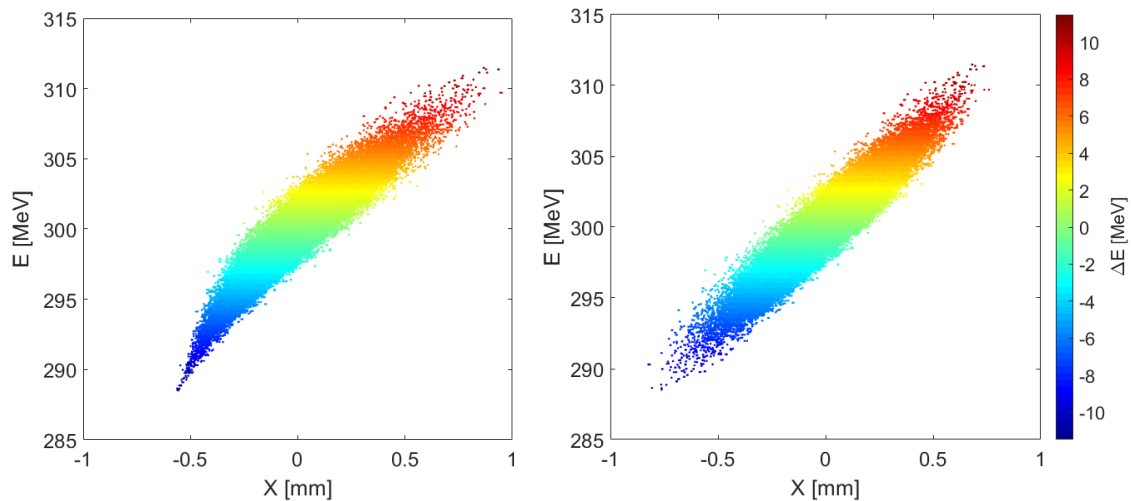


Figure 5.10: Dispersion distributions without the sextupole (left) and with the sextupole (right) at the entrance of the undulator. Nonlinear dispersion leads to a mismatching of the resonance condition inside the TGU. Using sextupoles magnet reduces the nonlinearity in the final dispersion. The color code represents the energy changes respect to the reference energy of $E_0$=300 MeV.
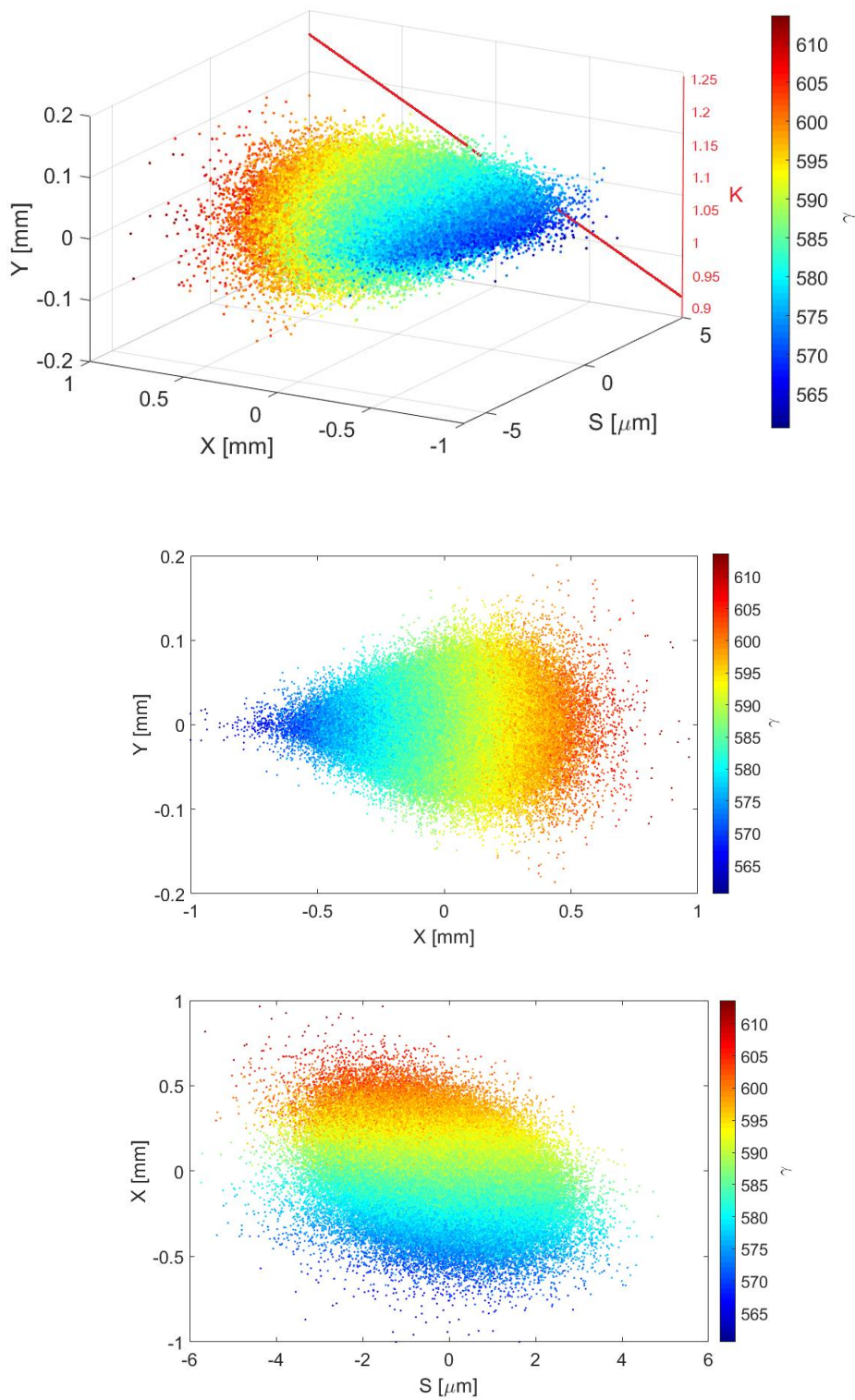
Figure 5.11: Distribution of the electrons inside the bunch at the entrance of the TGU. The undulator transverse gradient is shown with the red line in the top plot. The energies of the incoming particles are matched to the TGU gradient in a way that the resonance condition is satisfied for all particles with different energies.

# 5.3 Collective Effects

In order to study the relevant collective effects, i.e. space charge (SC) and coherent synchrotron radiation (CSR), which can affect the beam parameters, OCELOT and ELEGANT are used, respectively. OCELOT includes a three-dimensional Poisson equation solver in the bunch frame to model the space charge forces along with the transport matrices to track the particles [111]. For the simulation of the CSR effect, ELEGANT, which includes a 1D CSR module, is used.

The effect of the SC and CSR on the beam properties at the entrance of the undulator are shown in Fig. 5.12 (a)-(f). While including the CSR in the beam line does not change the peak current, the effect of SC on the beam peak current is more pronounced. Combination of a short bunch length with a high peak current results in a 20 percent reduction of the final peak current due to the SC effect [112], as shown in Fig. 5.12 (a). The effective energy spreads i.e. the x-slice energy spread, equation (4.8), are plotted in Fig 5.12 (b). In the CSR case, the electron beam will significantly suffer more energy spread growth than in the case of including only the SC. This is due to the different induced energy modulation in these two cases, as shown in Fig 5.12 (c). Since there is a linear correlation in x-z phase space (Fig. 5.11), the energy chirp imposed by SC and CSR will be transferred in the transverse plane as well. The average energy as a function of the particle transverse position in the bunch is depicted in Fig. 5.12 (d), which also shows a negative correlation between the transverse and longitudinal positions when compared with the results of Fig. 5.12 (c). The energy loss due to CSR will shift the radiation wavelength to higher values (see section 5.4). As shown in Figs. 5.12 (e) and (f), the transverse and the vertical emittances are more affected by the SC force, mainly due to the increase of the bunch size by the SC. The final beam parameters at the undulator entrance including the SC and CSR effect during transport in the beam line are listed in Table. 5.4.

| Final Beam Parameter | Value (no SC/CSR) | Value (SC) | Value (CSR) | Unit |
|---|---|---|---|---|
| Energy | 300 | 300 | 298 | MeV |
| Charge | 65 | 65 | 65 | pC |
| RMS Energy Spread | 1% | 1.13% | 1.05% | / |
| RMS Normalized Emittance (x/y) | 31/0.68 | 39/0.82 | 30.5/0.68 | µm-rad |
| RMS Normalized Emittance Without Dispersion Contribution (x/y) | 0.68/0.68 | 0.98/0.82 | 1.06/0.68 | µm-rad |
| RMS Beam Size (x/y) | 208/33 | 211/24 | 203/33 | µm |
| RMS Beam divergence (x/y) | 0.02/0.03 | 0.03/0.06 | 0.02/0.03 | mrad |
| RMS Beam Length | 1.2 | 1. 3 | 1.18 | µm |

Table 5.4: Final beam parameters at the entrance of the TGU.
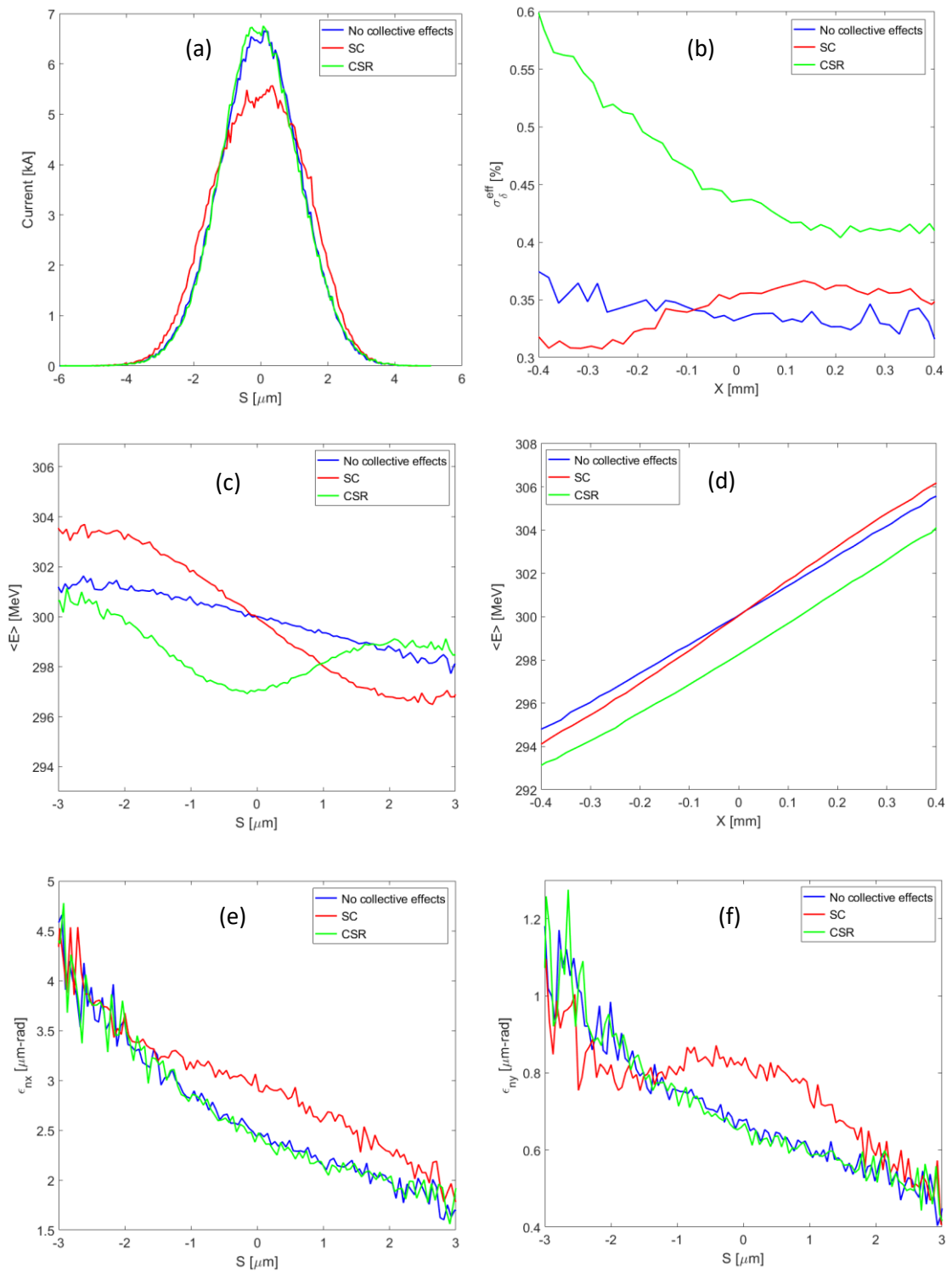
Figure 5.12: Final beam properties at the TGU entrance with and without collective effects. (a) current distribution, (b) effective energy spread, (c) longitudinal average energy distribution, (d) transverse average energy distribution, (e) slice normalized transverse emittance and (f) slice normalized vertical emittance.

The deviation of beam dispersion and Twiss parameters from the designed values, which are shown in Fig. 5.8, causes a reduction of the FEL power. In the dispersion case, due to mismatching between the transverse gradient of the TGU and the energy of the particles, the resonance condition will be lost, which results in broadening of the radiation spectrum and FEL power drop. As shown in Fig. 5.13 (a), both CSR and SC effects have a major impact on the initial beam dispersion at the undulator entrance, which is one order of magnitude smaller than the designed value. Moreover, the initial beam dispersion decreases along the undulator and even reaches lower values at the end.

Besides the dispersion matching, the evolution of the beam envelope along the undulator, which is given by the initial Twiss parameters, has a significant impact on the FEL performance. The designed Twiss parameters are calculated such that the minimum average beam size along the undulator is achieved, in order to maximize the FEL parameter (see section 4.2.1). Any deviation from the design values changes the beam size and divergence, leading to a reduction of FEL power and gain length [113]. The evolution of the beam beta functions along the undulator is presented in Figs. 5.13. (b) and (c). Due to the increase of beam emittance by the SC effect, the beam suffers more deviation from the ideal matching achieved with the design values of the Twiss parameters. Even for the case of non-collective effects included, both beta functions in the transverse and vertical planes deviate from the design values due to the large energy spread in the beam, which causes chromatic emittance growth accompanied by a change of the Twiss parameters.

In order to reduce the collective effects mentioned above, either setup parameters or the initial beam parameters can be changed. It is more convenient to keep the setup of the beam line unchanged and investigate the effect of SC and CSR by varying the initial beam parameters. Alongside the beam energy, bunch length and the beam charge are the most effective parameters, concerning SC and CSR, which can affect the beam during the transport. According to the data in Fig. 5.12, the bunch length and the transverse emittances are mostly affected by the SC effect, while the effective energy spread is highly influenced by CSR. Moreover, the initial dispersion at the undulator entrance is significantly changed by both effects. The scaling of the initial bunch length and charge has been done for the case that has the most influence on the beam. The results of the scaling are shown in Figs. (5.14) and (5.15) for the SC case and the CSR case, respectively. In all cases, as it is expected, starting with longer bunches and lower beam charges (lower peak current) results in reducing the collective effects. It should be noted that the dispersion values in these plots are first order and higher orders are not shown here. In both cases the optimum dispersion cannot be achieved, even with larger bunch lengths and charges, the dispersion values are far from the matched case of $D$=0.0196 m, for short bunches with high charge. However, these effects should be characterized in terms of their impact on the FEL output power. The consequences of the collective effects on the final FEL power are presented in section 5.4.
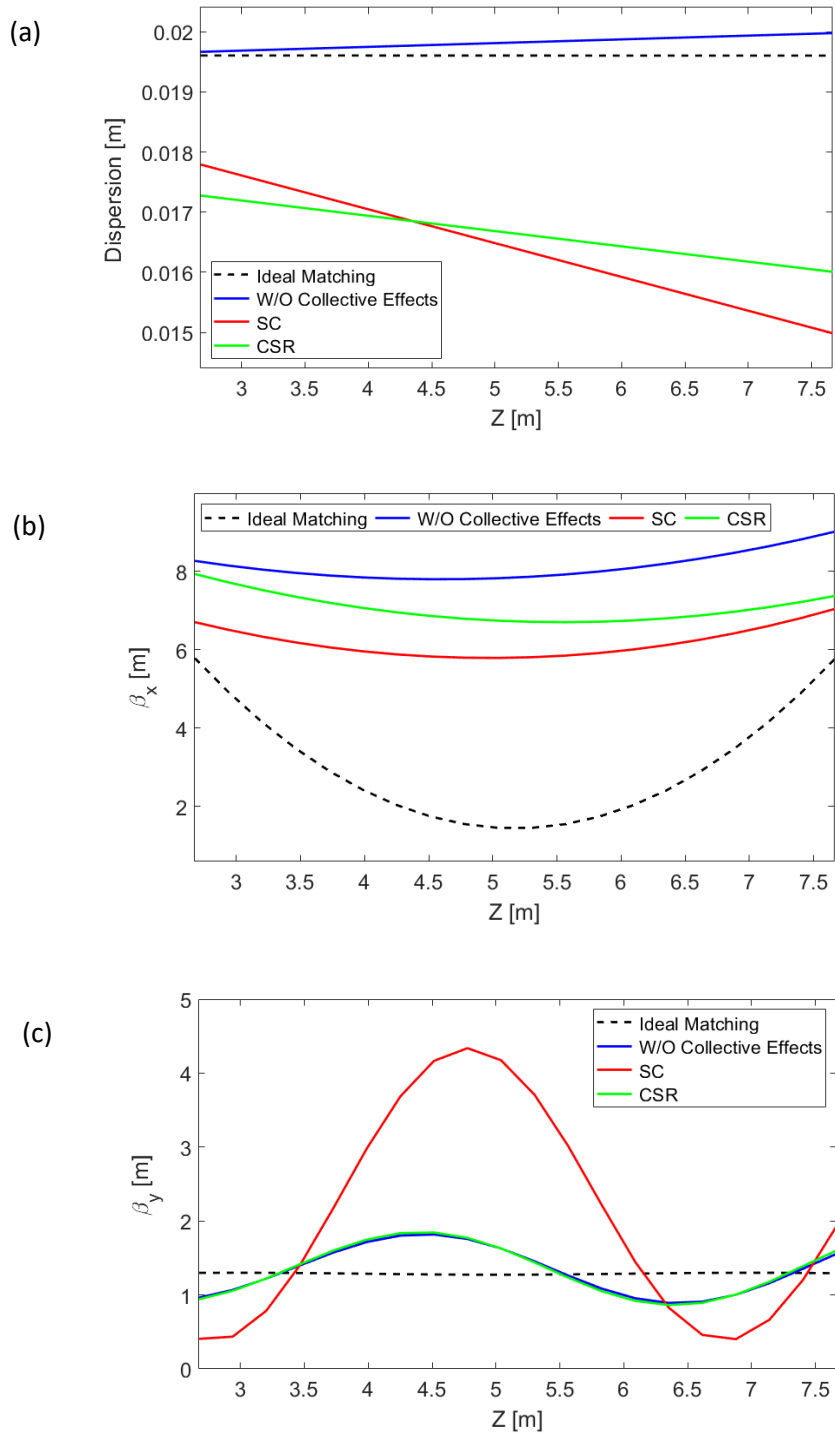
Figure 5.13: Beam dispersion (a), transverse beta function (b) vertical beta function (c) along the TGU of the tracked beam with and without including collective effects in the beam line. The dashed line shows the case with ideal matching.
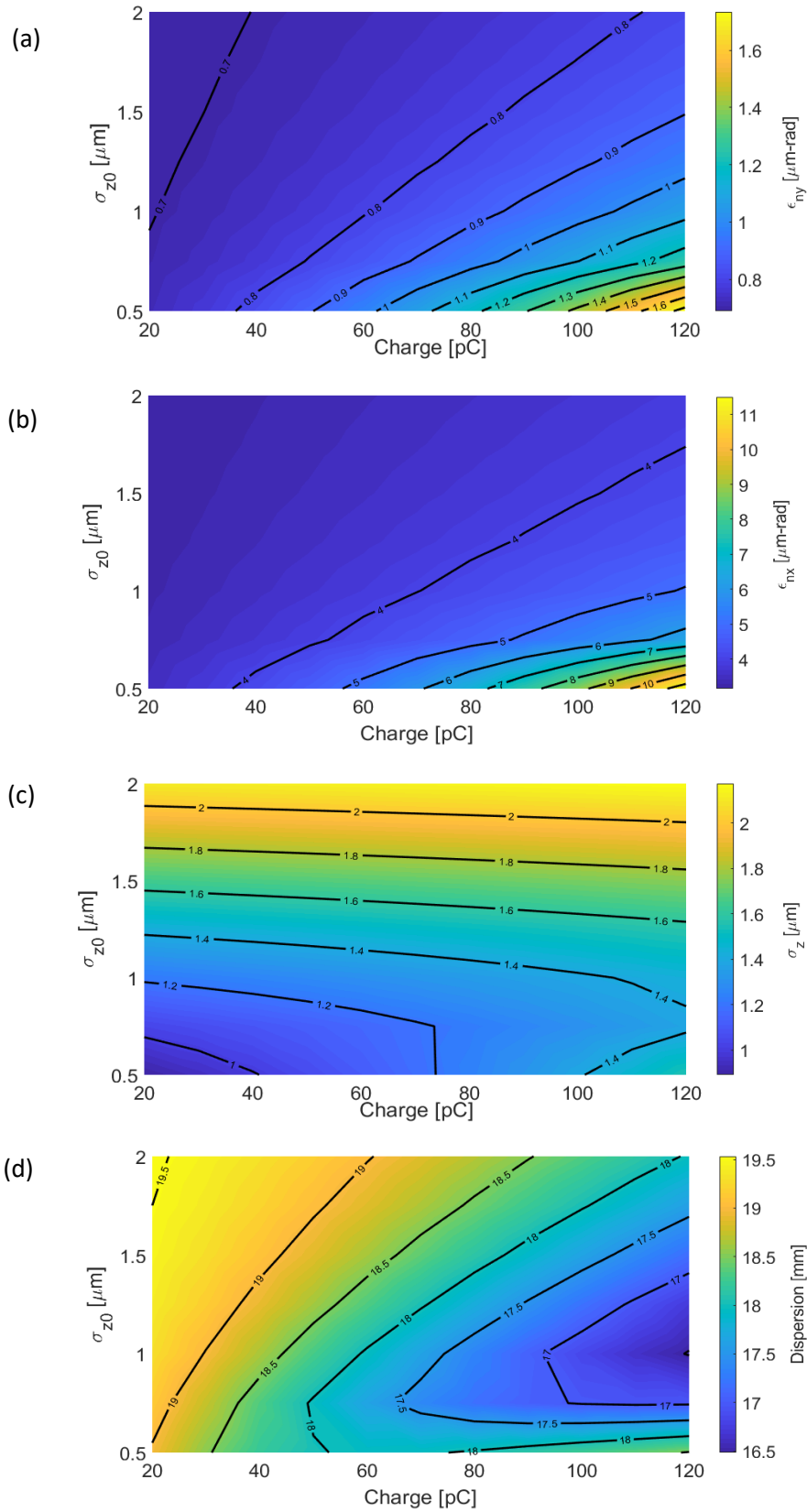
Figure 5.14: Beam properties as a function of the initial bunch length and charge in the SC case.
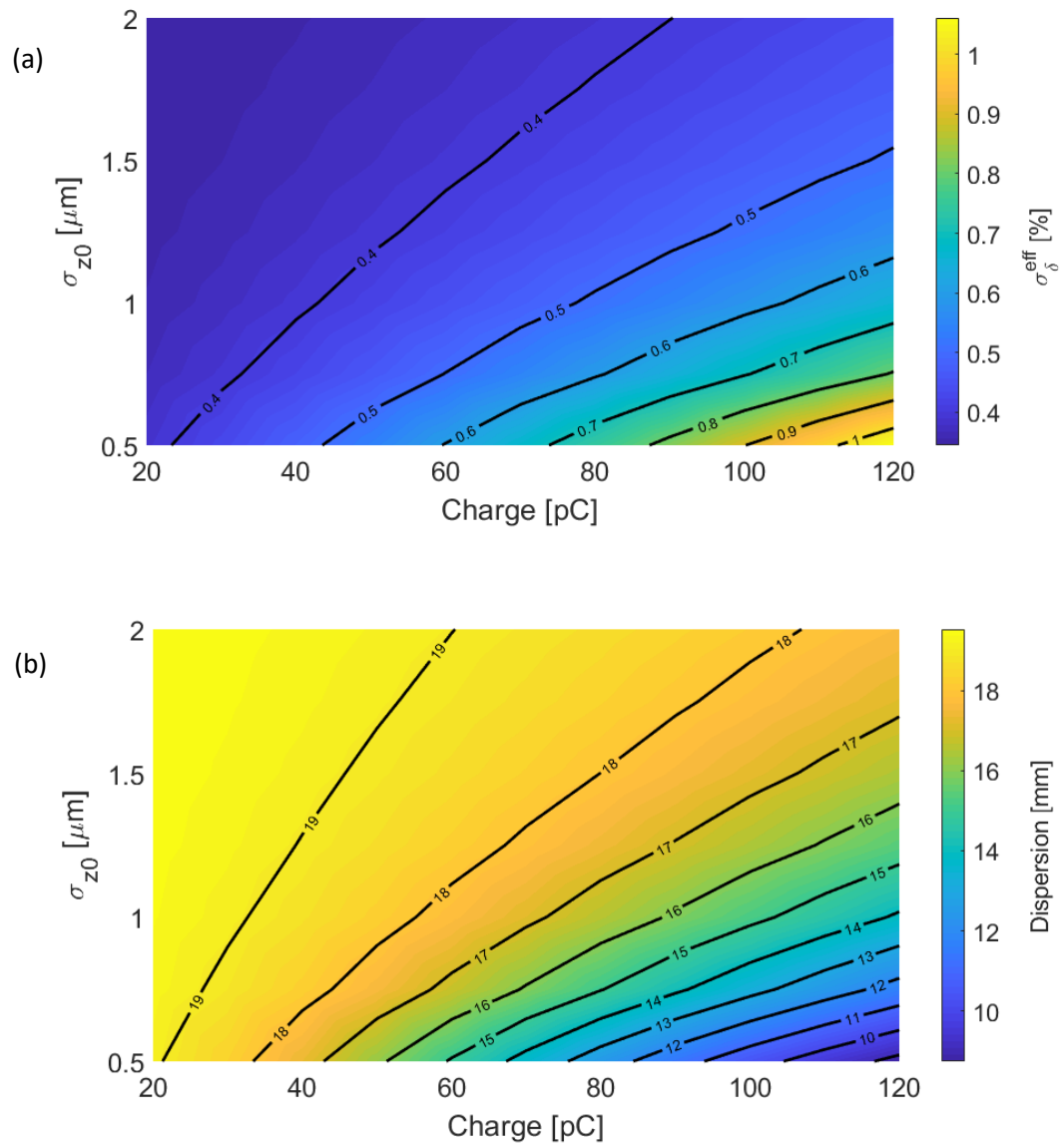
Figure 5.15: Beam properties as a function of the initial bunch length and charge in the CSR case.

# 5.4 Start-to-End Simulation

In order to further investigate the effect of the compact beam line, which was designed and optimized in the previous section, on the beam and the FEL radiation as well, on FEL simulation with a TGU has been done by GENESIS for the tracked beam, with the collective effects i.e. SC and CSR. The initial beam parameters as well as the TGU parameters are the same as the parameters used in Chap. 4, which are listed in Table. 5.5. Therefore, the simulation results can be compared to the data obtained in Chap. 4 in order to study the impact of the transfer line on the final FEL output. Moreover, it allows to explore the criteria, which must be considered to reach the final FEL power goal for the first TGU FEL demonstration experiment.

The schematic view of the LPA beam line including TGU at the end is depicted in Fig. 5.16. It is worth noting that, in order to eliminate the laser pulse after the LPA jet, laser can be focused into a concentrated spot at the LPA gas jet, and will afterwards diverge rapidly. Then a foil at the first quadrupole magnet with a small hole in the center can be used to let the electron beam pass while it blocks the laser and just a very small portion of the diverged laser pulse with low intensity would go through the magnets [114]. Another option is using a thick liquid crystal plasma mirror, which reflects a substantial portion of the laser to prevent damage to downstream components, without electron beam emittance degradation [115]. For the case discussed here, the effect of laser out coupling is neglected and it is supposed that the beam emittance does not change in the first drift after the plasma jet (only the chromatic emittance growth is considered in the simulations).

| LPA Beam Parameter | Value | Unit |
|---|---|---|
| Energy | *300* | *MeV* |
| Charge | *65* | *pC* |
| RMS Energy Spread | *1%* | */* |
| RMS Normalized Emittance (x/y) | *0.5* | *μm-rad* |
| RMS Beam Size (x/y) | *2.85* | *μm* |
| RMS Beam divergence (x/y) | *0.3* | *mrad* |
| RMS Beam Length | *1* | *μm* |

| TGU Parameter | Value | Unit |
|---|---|---|
| Period Length | *10.05* | *mm* |
| Undulator Length | *5* | *m* |
| Undulator Parameter | *1.07* | */* |
| Undulator Transverse Gradient | *139.7* | *1/m* |

Table 5.5: LPA beam parameters and the TGU parameters used for the simulation.
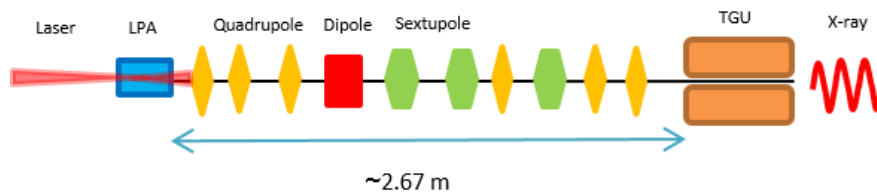
Figure 5.16: Cartoon of the TGU beam line with a beam generated in an LPA.

With the purpose of keeping all details of the phase space distribution 200K macroparticles have been imported into GENESIS to simulate the FEL radiation. GENESIS is modified to include transverse gradient undulator parameters. For each GENESIS simulation, the data are averaged over 10 independent runs with different initial shot-noise seeds.

The results of the simulation are presented in Fig. 5.17, where the evolution of the SASE FEL peak power is shown for two cases. The power goal design i.e. $P_{total}/P_{spont.} \geq 10$ will not be satisfied for the both cases with SC and CSR effects included in the beam line. Although even for the SC case an exponential FEL power growth can be seen, the final power is just 2.5 times larger than the spontaneous power, which is far below the power goal. The main degrading effect on the beam during the transport to the TGU is the emittance growth imposed by the SC forces which is translated to a nonlinear dispersion growth and results in a reduction of the FEL parameter, increasing the gain length. By including the space charge, the gain length is about 1.35 m. Furthermore, the induced energy chirp in both SC and CSR cases will introduce nonlinear dispersion terms, which makes particle fall out of resonance.

The radiation spectra for these cases are plotted in Fig. 5.18. The spectrum in the CSR case deviates from its single spike mode due to energy loss by CSR in the beam, which results in a redshift of the radiation wavelength. Moreover, due to the deterioration of the phase space in x-p plane, which causes a mismatching between the dispersion and the TGU gradient, the spectra have a large bandwidth, especially in the SC case where the bandwidth is much larger than the CSR case and also has much less intensity.

As discussed in the previous section, initial bunch length and the beam charge have the most impact when introducing SC and CSR effects in the beam line. The normalized FEL power as a function of the initial bunch length and the beam charge for the cases of including SC and CSR in the beam line are plotted in Figs. (5.19) and (5.20), respectively. As can be seen in Fig. 5.19, by including only CSR in the beam line the design power goal can be satisfied for high charge cases, while in the SC case the normalized power stays below than the limit even for the high charge beams with increased bunch length, as shown in Fig. 5.20.
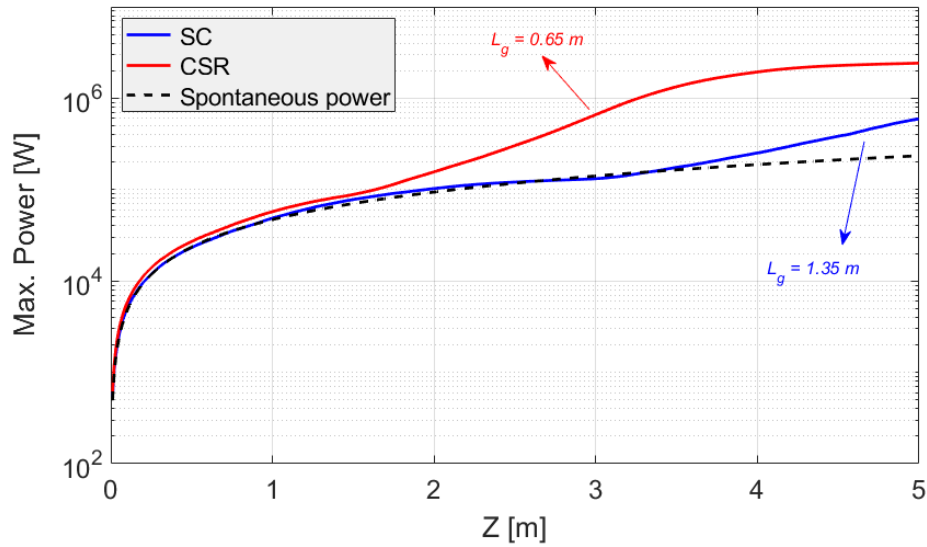
Figure 5.17: FEL peak power growth along the undulator for the cases of SC and CSR effects included in the beam line. The dashed line shows the spontaneous power in the SC case. The gain length in the SC case is about two times larger than the CSR case. The power goal limit is not satisfied in both cases.
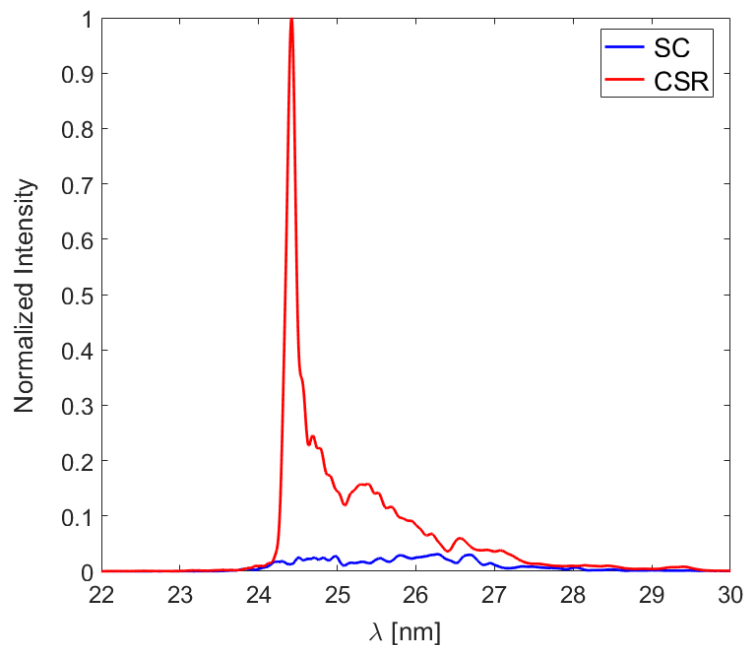


Figure 5.18: Radiation spectrum of SASE FEL for the cases of SC and CSR effects included in the beam line. The redshift of the radiation in the CSR case is due to the induced energy chirp during the transport.
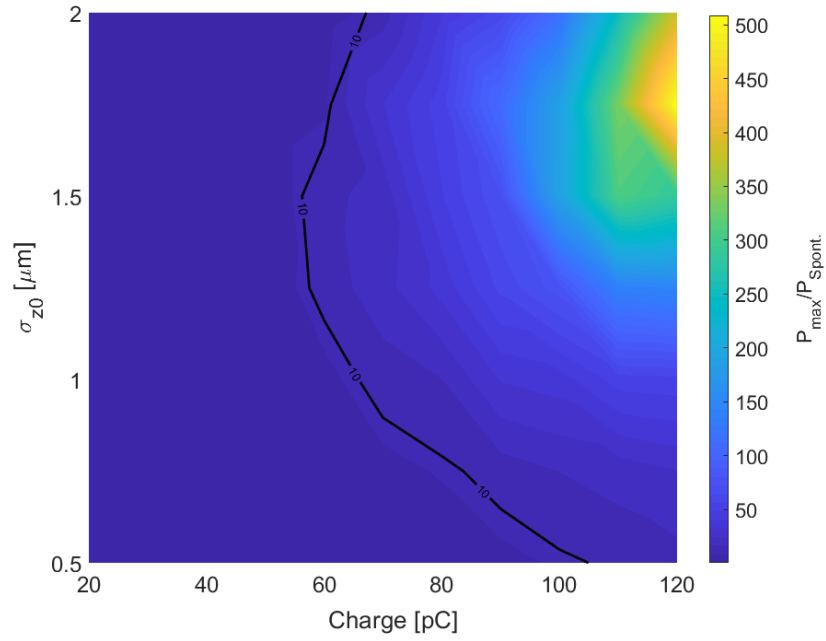
Figure 5.19: Normalized FEL power as a function of the initial bunch length and beam charge in the case of including CSR in the beam line. The contour line shows the power goal limit for the FEL demonstration experiment.
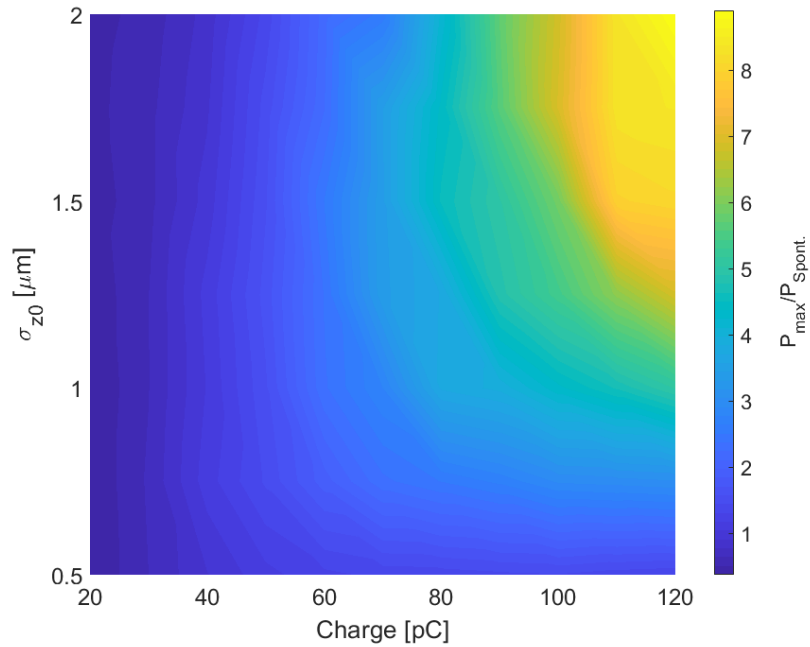


Figure 5.20: Normalized FEL power as a function of the initial bunch length and beam charge in the case of including SC in the beam line. The power goal limit is not satisfied even for high charge cases.

In order to reduce the effects of SC in the beam line, the initial energy of the beam can be increased. Moreover, the increase of the normalized emittances due to the SC effects has a major impact on reduction of the final FEL power. For this purpose, the interplay between the energy and the initial normalized emittances should be considered. This is shown in Fig. 5.21, where the normalized power as a function of the beam energy and the initial normalized emittance are plotted for two cases with the initial bunch length of (a) $\sigma_z = 1\,\mu m$ and (b) $\sigma_z = 2\,\mu m$. Decreasing the initial emittance for the fixed initial Twiss parameters results in a smaller initial beam divergence and as a consequence the SC effect will be more dominant after the exit of the plasma. Moreover, for a given initial normalized emittance, it is expected that by increasing the beam energy the output power decreases due to reduced FEL parameter, which scales with $\gamma^{-1}$. Because of the presence of SC (especially for lower energies), increasing the beam energy will reduce the SC effects and will result in an optimum value. As can be seen from Fig. 5.21, considering the range of the normalized emittances shown on the plot, for the cases of $\sigma_z = 1\,\mu m$ and $\sigma_z = 2\,\mu m$ the beam energies of $E = 600\,\mathrm{MeV}$ and $E = 400\,\mathrm{MeV}$ can be regarded as optimum energies, respectively.

With the optimum energies in the two cases of $\sigma_z = 1\,\mu m$ and $\sigma_z = 2\,\mu m$, the effect of the SC for different bunch charges can be studied. The normalized power as a function of bunch charge for different values of the normalized emittances for the two cases of $\sigma_z = 1\,\mu m$ and $\sigma_z = 2\,\mu m$, with the beam energies of $E = 600\,\mathrm{MeV}$ and $E = 400\,\mathrm{MeV}$ are plotted in Fig. 5.22. (a) and (b), respectively. For the two cases, considering the reference beam charge of 65 pC, the maximum affordable initial normalized emittances are about 0.3 $\mu m$-rad, in order to achieve the power goal design. Although the beams with the normalized emittances of 0.4 $\mu m$-rad can reach the power goal limit, the minimum bunch charge in this case must be increased up to 90 pC.

The above results show that in order to achieve our normalized power goal, some modifications in the initial beam parameters must be done. The main changes are related to the beam energy and the normalized emittances. For the case of SC the power limit can be reached by a bunch length of 1 $\mu m$, However, in order to reduce the CSR effect, the bunch length needs to be increased as well. The change of the normalized power at the end of the undulator can be compared with its ideal case i.e. without CSR (and SC). This is shown in Fig. 5.23 where the normalized power ratio is plotted as a function of beam charge for the above cases of $\sigma_z = 1\,\mu m$ and $\sigma_z = 2\,\mu m$, with the beam energies of $E = 600\,\mathrm{MeV}$ and $E = 400\,\mathrm{MeV}$. For the two cases a normalized emittance of $\varepsilon_n = 0.2\,\mu m$-rad is assumed. Here the parameter $P_n$ is defined as the ratio between the normalized powers in the case of without CSR (ideal case) and including CSR in the beam line i.e. $P_n = (P_{max}^{ideal} / P_{spont.}^{ideal}) / (P_{max}^{CSR} / P_{spont.}^{CSR})$. As can be seen from the figure, for the long bunch case the effect of the CSR decreases and this reduction is less for the low charge bunches.
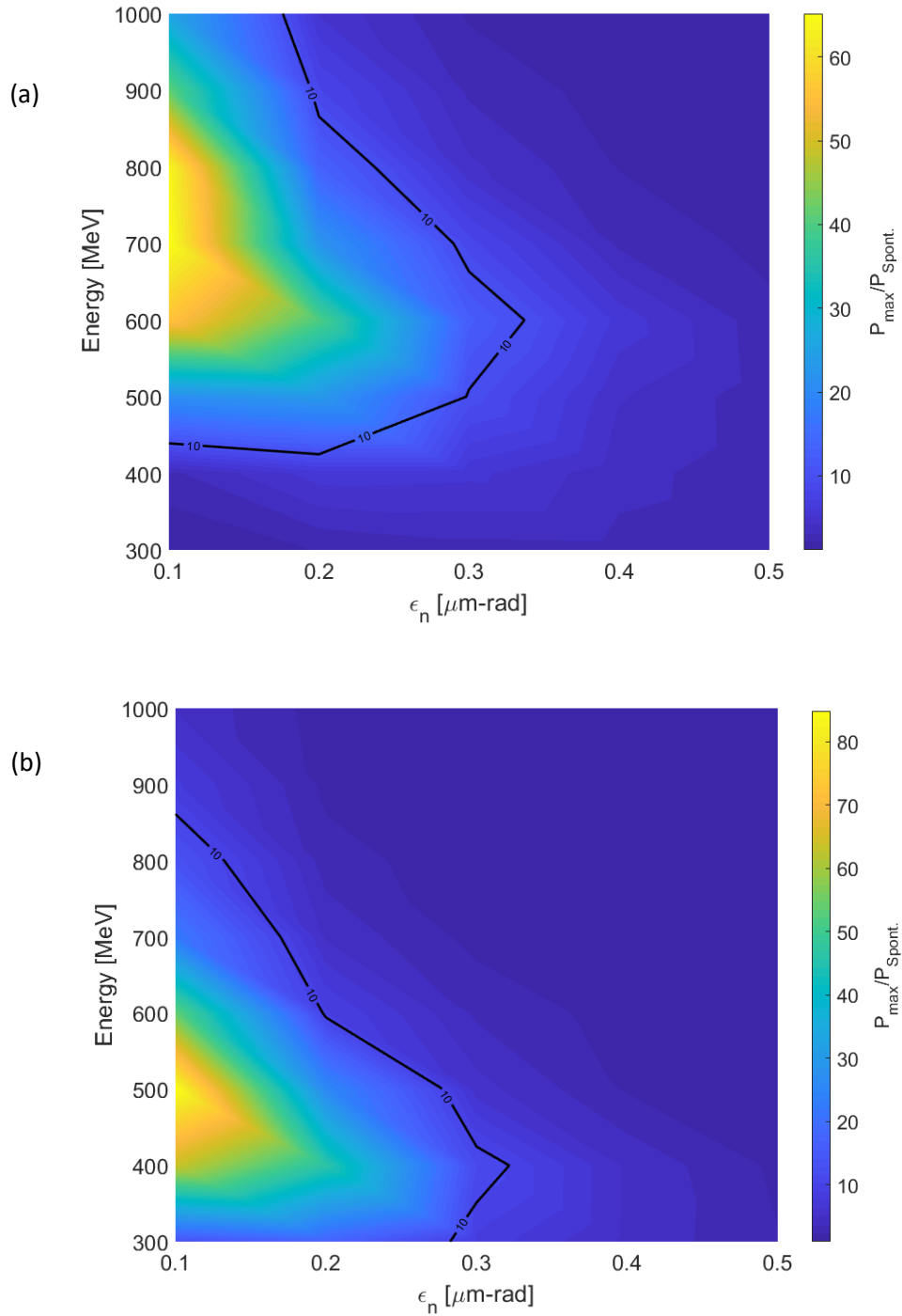
Figure 5.21: Normalized FEL power as a function of the initial beam energy and the beam emittance for two cases of different initial bunch length (a) 1 *μm* and (b) 2 *μm* in the case of including SC in the beam line. The power goal limit is shown with the contour line on the plots. The optimum beam energies result from balancing the competing influences of the FEL parameter, which scales with $1/\gamma$, and induced emittance growth due to SC effect on the final FEL power. It should be mentioned that the interpolated coloring is used in order to fill the gaps between the simulated data points.
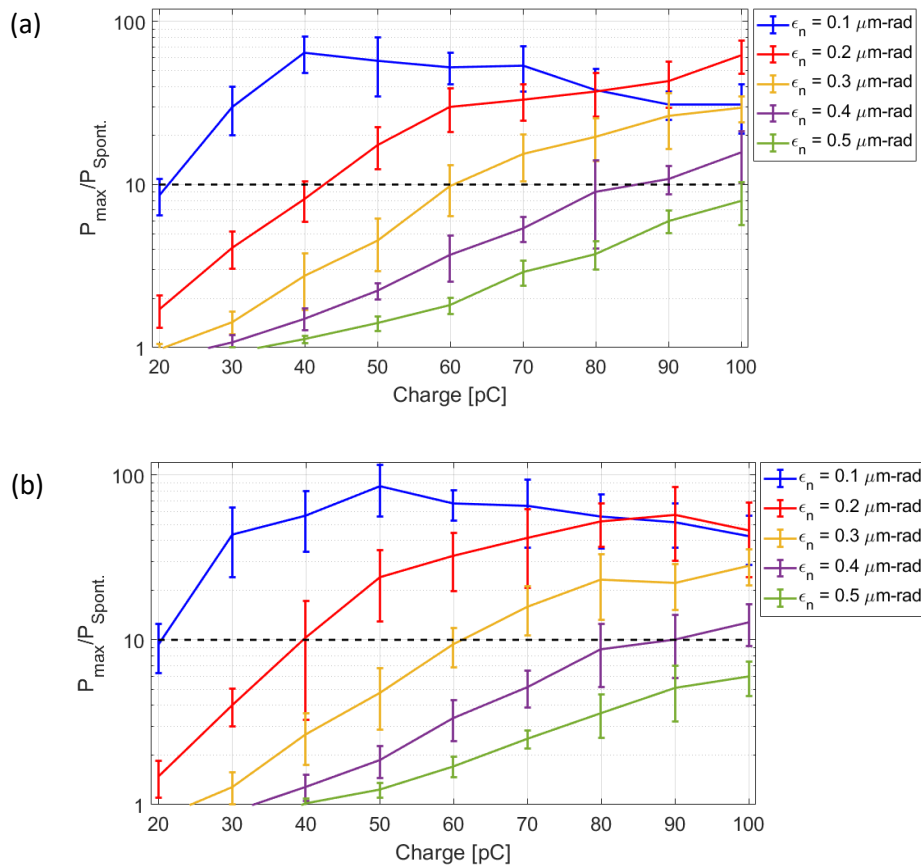
Figure 5.22: Normalized FEL power as a function of the bunch charge for different values of the initial normalized emittance in the cases of the initial bunch length of (a) 1 $\mu m$ with the beam energy of 600 MeV and (b) 2 $\mu m$ with the beam energy of 400 MeV including SC in the beam line. The power goal limit is shown with the dashed line.
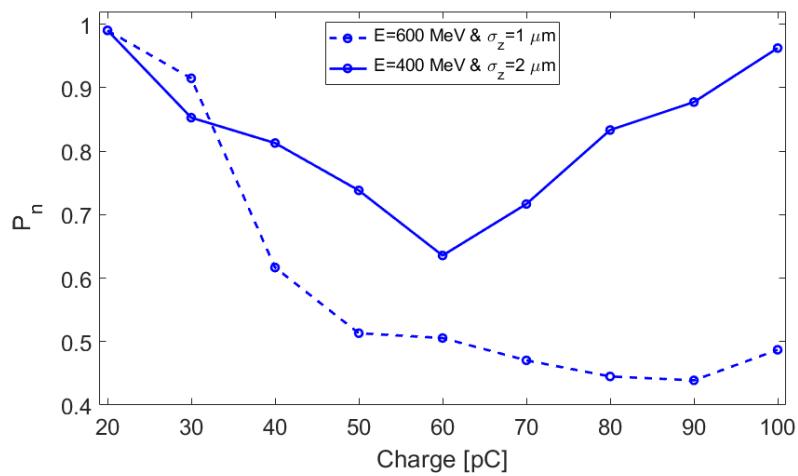


Figure 5.23: Normalized power ratio as a function of the bunch charge. See text for detail.

Nevertheless, considering the power goal limit, the beam charge cannot be decreased to very low values. Furthermore, for the case of $\sigma_z = 2\,\mu\mathrm{m}$, the normalized power ratio increases for the bunch charges larger than 60 pC. Therefore, assuming a beam with the energy of $E = 400\,\mathrm{MeV}$, the normalized emittance $\varepsilon_n = 0.2\,\mu\mathrm{m}\text{-rad}$, the length of $\sigma_z = 2\,\mu\mathrm{m}$, 65 pC charge with 1% energy spread, the power goal design can be achieved while minimizing the collective effects imposed by the beam line on the beam. Figure 5.24 shows the results of a start-to-end simulation where the evolution of the FEL peak power along the undulator with the abovementioned beam parameters is plotted for two cases of SC and CSR included in the beam line. For comparison the case of the beam with $\sigma_z = 1\,\mu\mathrm{m}$ and $E = 600\,\mathrm{MeV}$ is shown with the dashed line. Although in the SC case both beams with different lengths reach approximately the same power at the end of the undulator, the CSR effect is more pronounced for the shorter bunch length and the final power is more affected in this case. However, the FEL power in the SC case increases up to 76 MW, which is more than 2 orders of magnitude larger than the spontaneous power, shown by the dotted line in the Fig. 5.24.

It should be mentioned that the beam parameter set used here is one of the possible combinations of parameters, which can be used to show the FEL lasing. The TGU parameters also can be modified to relax the constraints on the LPA beam parameters. Increasing the undulator parameters or using a longer TGU can result in a more flexible parameter set. However, the main point, which was addressed here, is the TGU ability for compensation of the energy spread of the LPA beam and for increase of the FEL gain and power.
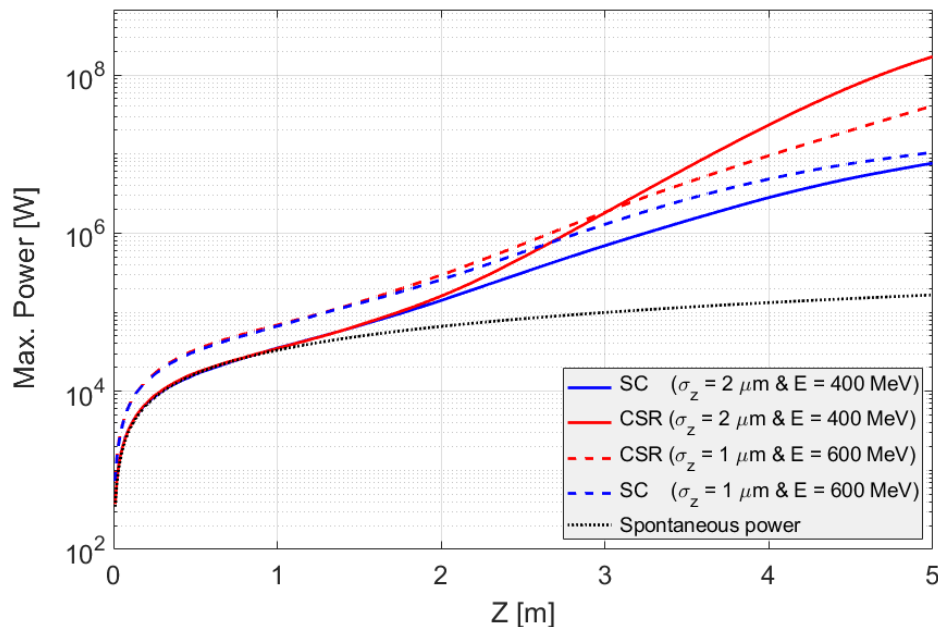


Figure 5.24: Evolution of the FEL peak power along the undulator. The data are averaged over 10 shots with different shot-noise seeds.

# 5.5 Conclusion

In this chapter, the most important issues that need to be considered in the design of a beam transport system for a TGU with a beam generated in an LPA have been addressed. Due to the large energy spread and the large divergence of the LPA beam the design of a beam line transport for such electron beams is very challenging. Degradation of the emittance due to chromatic emittance growth is the main problem which in combination with the initial large divergence poses serious challenges in transport of the LPA beam. Moreover, the beam needs to be dispersed before entering the TGU with the matched dispersion that makes the design of the beam line even more difficult.

An optimized compact beam line has been proposed. The design has been done such that it allows to minimize the degrading effects while preserving the beam quality. The compactness of the beam line also gives a chance of having a table top free electron laser in combination with the small size of the laser-plasma accelerators.

Furthermore, the influence of the collective effects like space-charge and coherent synchrotron radiation on the beam properties during the transport to the TGU have been studied. It has been shown that the beam with the reference parameter set greatly suffers from the collective effects and the power goal limit for demonstration of the FEL amplification cannot be reached. Therefore, considering the impact of the collective effects on the beam properties and the final FEL power the reference parameter set has been optimized in order to achieve the power goal design. The start-to-end simulation shows that the FEL power amplification can be achieved with this new parameter set.

# *Chapter 6*

# ***Conclusion and Outlook***

In this thesis the concept of the transverse gradient undulator has been studied in detail and a test experiment was designed in order to examine the TGU capability of producing monochromatic radiation. In addition, the possibility of using a transverse gradient undulator for generating FEL radiation has been studied. Also, a scaling study for a nominal LPA beam parameter set has been done in order to investigate the minimum FEL beam requirement for demonstration of FEL lasing by using a TGU as a source of radiation. Moreover, a compact beam line transport from a laser plasma accelerator to a transverse gradient undulator has been designed and the effect of the beam line on the beam properties and the final FEL power has been investigated.

The electron beams generated in laser plasma accelerators typically have energy spreads on the order of several percent. Such a large energy distribution of the electrons within the beam hinders the FEL performance, resulting in a reduction of the gain and FEL power. To address this the use of a transverse gradient undulator was proposed. The proposed scheme to mitigates the effect of energy spread by decreasing the local energy spread at the cost of reducing the local current density. The concept of the TGU relies on fulfilling the resonance condition for different particles' energy in an electron beam with a large energy deviation from the mean value. The energies of the particles in the incoming beam, which is dispersed transversely, are matched to the transverse magnetic field gradient of the TGU such that the resonance condition is satisfied for all particles with different energies

In order to prove the TGU concept, a 40-period prototype superconducting TGU was built at Karlsruhe Institute of Technology (KIT) and was planned to be tested with the ARES linac at SINBAD facility at DESY. The main objective of the experiment was to validate the TGU capability of producing monochromatic radiation with a driver beam that has large energy spread. The experiment simulations show that the TGU is able to reach a photon flux much

higher than a normal undulator and the produced radiation bandwidth is much smaller in comparison with the normal case.

In recent years, the TGU idea has been reconsidered in high-gain FEL concepts due to its ability to increase the FEL gain in the case of beams with large energy spread such as the beam from a laser-plasma accelerator. Therefore, after a successful test of the prototype TGU, it is planned to perform an experiment with a full-scale TGU and a beam generated in an LPA to demonstrate FEL lasing. For the envisioned parameter set and by using the TGU scheme the FEL performance can be improved by some orders of magnitude. In order to find the minimum FEL beam requirement to demonstrate TGU FEL amplification, the nominal parameter set of the LPA beam was scaled over a range which can be reached by an optimized LPA setup. The scaling has been done in terms of energy, charge, energy spread, normalized emittance and bunch length. Although it is possible to achieve the design goal power $P_{total}/P_{spont.} \geq 10$, with the reference beam, the scaling studies allow to address any variation in the reference parameter set and show how a reduction in a specific parameter can be compensated by changing the other parameters to reach the normalized power design goal. Besides, the undulator parameter has been included in the scaling studies for cases when the power goal limit cannot be fulfilled by variation in the LPA beam parameters. According to the study, the demonstration of FEL amplification is possible over a wide range of LPA parameters and therefore, can be shown experimentally with currently available LPA setups.

However, due to the presence of collective effects like, space-charge and CSR in addition to chromatic emittance growth due to large energy spread of the beam, the beam properties will be affected by the beam line during the transport from the LPA to the TGU. It has been shown that the beam with the nominal parameter set will experience a large degrading effect during the transport and the collective effects have a great impact on the beam properties in addition to the chromatic emittance growth imposed by the beam line on the beam. Although it is tried to optimize the beam line in order to minimize the emittance growth during the transport, the increase of the chromatic emittance is unavoidable. Regarding all of these degrading effects, the reference beam parameter set was optimized in terms of energy, emittance and bunch length in order to achieve the power goal design for the demonstration FEL amplification experiment.

In summary, the ability of energy spread compensation with transverse gradient undulators, makes them promising candidates for future generation synchrotron light sources, including a laser plasma accelerator in cm scale that generates beam with a large energy spread on the order of some percent.

# Bibliography

[1] A. Sessler, E. Wilson," Engines Of Discovery: A Century Of Particle Accelerators", World Scientific, (2007).

[2] H. Winick and S. Doniach, Synchrotron radiation research. Springer Science & Business Media, (2012).

[3] A, Hofmann, "The Physics of Synchrotron Radiation". Cambridge University Press. (2004).

[4] R. Bonifacio, L. De Salvo Souza, Claudio Pellegrini, ''High Gain, High Power Free Electron Laser: Physics and Application to TeV Particle Acceleration", Elsevier, (2012).

[5] V. Shiltsev. "A phenomenological cost model for high energy particle accelerators". In: Journal of Instrumentation 9.07 (2014).

[6] A.R. Maier, M. Kirchen, F. Grüner, "Brilliant Light Sources Driven by Laser-Plasma Accelerators". Synchrotron Light Sources and Free-Electron Lasers: Accelerator Physics, Instrumentation and Science Applications, (2020).

[7] B. McNeil, N. Thompson, X-ray free-electron lasers. Nature Photon 4, 814–821 (2010).

[8] S. Di Mitri, G. Perosa, "Electron Beam Transport in Plasma-Accelerator-Driven Free-Electron Lasers in the Presence of Coherent Synchrotron Radiation and Microbunching Instability." Physics 2.4 (2020)

[9] T. I. Smith, L. R. Elias, J. M. J. Madey, and D. A. G. Deacon, "Reducing the sensitivity of a free electron laser to electron energy," J. Appl. Phys., vol. 50, p. 4580, (1979).

[10] Z. Huang, Y. Ding, and C. B. Schroeder, "Compact X-ray free-electron laser from a laser plasma accelerator using a transverse-gradient undulator," Phys. Rev. Lett., vol. 109, p. 204801, (2012).

[11] U. Dorda et al. "Status and objectives of the dedicated accelerator R&D facility "SINBAD" at DESY". Nucl. Instr. Meth. Phys. Res. A 909, (2018).

[12] K. Wille. "The Physics of Particle Accelerators: An Introduction" (2001).

[13] H. Wiedemann, "Particle Accelerator Physics I - Basic Principles and Linear Beam Dynamics". Springer (2003).

[14] S. Y. Lee. "Accelerator Physics". World Scientific, New Jersey, (2004).

[15] D. Attwood. "X-Rays and Extreme Ultraviolet Radiation", (2000).

[16] P. Schmuser et al., "Free-Electron Lasers in the Ultraviolet and X-Ray Regime", Springer International Publishing, (2014).

[17] Z. Huang and K.-J. Kim. "Review of x-ray free-electron laser theory". Phys. Rev. ST Accel. Beams, 10:034801, (2007).

[18] E. L. Saldin, E. A. Schneidmiller, and M. V. Yurkov. "The Physics of Free Electron Lasers". Springer, Berlin, 2000.

[19] K. Kim, Z. Huang, and R. Lindberg. "Synchrotron Radiation and Free-Electron Lasers: Principles of Coherent X-Ray Generation". Cambridge: Cambridge University Press. (2017).

[20] N. M. Kroll, P. L. Morton, and M. Rosenbluth. "Free-electron lasers with variable parameter wigglers". Quantum Electronics, IEEE Journal of, (1981).

[21] Ming Xie, "Exact and variational solutions of 3D eigenmodes in high gain FELs", Nucl. Instrum. Meth. A 445, 59-66, (2000).

[22] K.-J. Kim, "Brightness, coherence and propagation characteristics of synchrotron radiation". Nuclear Instruments and Methods in Physics Research Section A: Accelerators, Spectrometers, Detectors and Associated Equipment 246, 71–76 (1986)

[23] M. Xie, "Design Optimization for an X-Ray Free Electron Laser Driven by SLAC LINAC", Proc. of Particle Acc. Conf. 95, 183{185, Dallas, Texas, (1995).

[24] J. A. Clarke. "The science and technology of undulators and wigglers". Oxford series on synchrotron radiation. OUP Oxford, (2004).

[25] C. Pellegrini, A. Marinelli, and S. Reiche. "The physics of x-ray free-electron lasers". Rev. Mod. Phys., 88:015006, (2016).

[26] M. Xie, "Transverse coherence of self-amplified spontaneous emission" Nucl. Instrum. Methods Phys. Res., Sect. A 445, 67 (2000).

[27] T. Tajima and J. M. Dawson. Laser electron accelerator. Phys. Rev. Lett., 43:267-270, (1979).

[28] E. Esarey, C. B. Schroeder and W. P. Leemans. "Physics of laser-driven plasmabased electron accelerators". In: Rev. Mod. Phys. 81, pp. 1229–1285. (2009).

[29] E. Esarey, P. Sprangle, J. Krall, and A. Ting, "Overview of plasma-based accelerator concepts", IEEE Trans. Plasma Sci. 24, 252–288 (1996).

[30] N. Matlis, et al., Acceleration of electrons in THz driven structures: first steps towards AXSIS, Nucl. Instrum. Methods Phys. Res. A. (2017).

[31] B. Marchetti et al., "Electron-Beam Manipulation Techniques in the SINBAD Linac for External Injection in Plasma Wakefield Acceleration", Nucl. Instr. and Methods in Physics A,vol. 829, pp. 278-283, (2016).

[32] Zhu J et al. "Sub-fs electron bunch generation with sub-10-fs bunch arrival-time jitter via bunch slicing in a magnetic chicane" Phys. Rev. ST Accel. Beams 19 (2016)

[33] E. Panofski et al., "Status Report of the SINBAD-ARES RF Photoinjector and Linac Commissioning", presented at the 10th Int. Particle Accelerator Conf. (IPAC'19), Melbourne, Australia, (2019).

[34] T. Liu et al. "Compact beam transport system for free-electron lasers driven by a laser plasma accelerator", Phys. Rev. ST Accel. Beams, vol. 20, no. 20, p. 020701, (2017).

[35] A. Bernhard et al., "Radiation emitted by Transverse Gradient Undulators" Physical Review Accelerators and Beams, vol. 19, p. 090704, (2016).

[36] T. Seggebrock. "Conceptual design of a Laser-Plasma Accelerator driven Free-Electron Laser demonstration experiment", PhD thesis, Ludwig-Maximilians university Munchen. (2015)

[37] G. Fuchert et al. "A novel undulator concept for electron beams with a very large energy spread", Nucl. Instrum. Methods Phys. Res., Sect. A 672, 33 (2012).

[38] S. Casalbuoni et al., "superconducting undulator coils with period length doubling", presented at the 10th Int. Particle Accelerator Conf. (IPAC'19), Melbourne, Australia, (2019).

[39] V. Afonso Rodriguez, "Electromagnetic Design, Implementation and Test of a Superconducting Undulator with a Transverse Gradient Field Amplitude". PhD thesis, Karlsruhe Institute of Technology (KIT) (2015).

[40] V. Afonso Rodriguez, et al. "Construction and First Magnetic Field Test of a Superconducting Transverse Gradient Undulator for the LaserWakefield Accelerator in Jena". In Proceedings of the IPAC 2014, page WEPRO036 (2014).

[41] V. Afonso Rodriguez et al. "Development of a Superconducting Transverse-Gradient Undulator for Laser-Wakefield Accelerators". IEEE Transactions on Applied Superconductivity, 23(3):4101505–4101505. (2013).

[42] G. Fuchert. "Modelle für supraleitende Undulatoren an kompakten Synchrotron-strahlungsquellen mit Laser-Wake_Field-Beschleunigern". Master's Thesis, KIT, (2009).

[43] J. D. Jackson. Classical electrodynamics. Wiley, (1975).

[44] I. Agapov, G. Geloni, S. Tomin, I. Zagorodnov. NIM. A. 768 pp. 151-156 (2014).

[45] R. P. Walker, PCAS - CERN Accelerator School: 5th Advanced Accelerator Physics Course, pp.807-835. (1995).

[46] S. Reiche, CERN Yellow Reports: School Proceedings, Vol. 1/2018, CERN-2018-001-SP pp.347-354 (2018)

[47] C. Widmann, "Simulation and First Experimental Tests of an Electron Beam Transport System for a Laser Wakefield Accelerator" PhD thesis, Karlsruhe Institute of Technology (KIT) (2016).

[48] P. Baxevanis et al., "3D theory of a high-gain free-electron laser based on a transverse gradient undulator" Phys. Rev. ST Accel. Beams, vol. 17, no. 2, p. 020701, (2014).

[49] B. Marchetti, R. Assmann, U. Dorda and J. Zhu. `Conceptual and technical design aspects of accelerators for external injection in LWFA'. Applied Sciences 8, (2018).

[50] J. Zhu. "Design study for generating sub-femtosecond to femtosecond electron bunches for advanced accelerator development at SINBAD". Dissertation. University of Hamburg, (2017).

[51] I. Uschmann, Jena University, private communication. (2020).

[52] K. Floettmann. ASTRA: A space charge tracking algorithm. 3.2. DESY. (2017).

[53] J. Zhu, LISO. 0.1.0, Github (2018).

[54] M. Borland. elegant: A exible SDDS-compliant code for accelerator simulation. Tech. rep. Advanced Photon Source, (2000).

[55] J. Resta-Lpez, "Single-bunch Transverse Emittance Growth due to Collimator Wakefield Effects", http://arxiv.org/pdf/1309.0480.pdf (2013).

[56] A. Brynes, B. Spataro, O. Frasciello, A. Marcelli, and G. Castorina, "Studies of geometric wakefields and impedances due to collimators", Tech. Rep. INFN-16- 10/LNF (2016).

[57] M. Dohlus, T. Limberg and P. Emma. "Bunch compression for linac-based FEL's. Electron bunch length compression". In: ICFA Beam Dyn. Newslett. 38 (2005).

[58] E. L. Saldin, E. A. Schneidmiller, and M. V. Yurkov. "On the coherent radiation of an electron bunch moving in an arc of a circle". Nucl. Instrum. Methods Phys. Res. Sect. A, 398:373, (1997).

[59] Y. Derbenev, J. Rossbach, and E. L. Saldin. "Microbunch radiative tail-head interaction". TESLA FEL-Report 1995-05, (1995).

[60] J. Zhu. "Design Study for Generating Sub-femtosecond to Femtosecond Electron Bunches for Advanced Accelerator Development at SINBAD". PhD thesis, University of Hamburg, (2017).

[61] M. Ferrario, M. Migliorati and L. Palumbo. "Space charge effects". In: CAS -CERN Accelerator School: Advanced Accelerator Physics Course (Trondheim,Norway). (2013).

[62] M. Reiser, "Theory and Design of Charged Particle Beams" (Wiley, New York, 1994).

[63] L. Serafini and J. B. Rosenzweig. "Envelope analysis of intense relativistic quasilaminar beams in rf photoinjectors: A theory of emittance compensation". Phys. Rev. E 55, pp. 7565 (1997).

[64] S. G. Anderson, J. B. Rosenzweig, G. P. LeSage and J. K. B. "Space-charge effects in high brightness electron beam emittance measurements". Phys. Rev. ST Accel. Beams 5, (2002).

[65] J. B. Rosenzweig, S. Anderson and L. Serafini, "Space charge dominated envelope dynamics of asymmetric beams in RF photoinjectors," *Proceedings of the 1997 Particle Accelerator Conference (Cat. No.97CH36167)*, Vancouver, BC, Canada, (1997).

[66] E. A. Seddon et al. "Short-wavelength free-electron laser sources and science: a review" Rep. Prog. Phys. 80 115901(2017).

[67] M. Altarelli, R. Brinkmann, M. Chergui, W. Decking, B. Dobson, et al. "XFEL: The European X-Ray Free-Electron Laser: Technical design report". Technical report, Deutsches Elektronen-Synchrotron (DESY), Hamburg, (2006).

[68] S. Dobert. "Gradient limitations for high-frequency accelerators", Linear accelerator Proceedings, 22nd International Conference, Linac, Luebeck, Germany (2004).

[69] T. Argyropoulos et al., "Design, fabrication, and highgradient testing of an X-band, traveling-wave accelerating structure milled from copper halves", Phys. Rev. Accel. Beams Vol. 21, p. 061001, (2018).

[70] M. Ferrario and R.W. Aßmann, "From Dreams to Reality: Prospects for Applying Advanced Accelerator Technology to Next Generation Scientific User Facilities", in Proc. IPAC'19, Melbourne, Australia, (2019).

[71] E. A. Nanni et al. "Terahertz-driven linear electron acceleration". In: Nature communications 6, p. 8486 (2015).

[72] R. J. England et al. "Dielectric laser accelerators". In: Rev. Mod. Phys. 86, pp. 1337–1389, (2014).

[73] Grüner, F., Becker, S., Schramm, U. et al. Design considerations for table-top, laser-based VUV and X-ray free electron lasers. Appl. Phys. B 86, 431–435 (2007).

[74] A. R. Maier, A. Meseck, S. Reiche, C. B. Schroeder, T. Seggebrock, and F. Grüner Phys. Rev. X 2, 031019. (2012).

[75] G. Manahan et al. "Single-stage plasma-based correlated energy spread compensation for ultrahigh 6D brightness electron beams". Nat. Comm. 8.15705 (2017).

[76] R. Brinkmann et al. "Chirp Mitigation of Plasma-Accelerated Beams by a Modulated Plasma Density". Phys. Rev. Lett. 118 p. 214801 (2017).

[77] A. Döpp et al. "Energy-Chirp Compensation in a Laser Wakefield Accelerator". Phys. Rev. Lett. 121, p. 074802 (2018).

[78] Y. P. Wu et al. "Phase Space Dynamics of a Plasma Wakefield Dechirper for Energy Spread Reduction". Phys. Rev. Lett. 122 (2019).

[79] A. Loulergue et al. "Beam manipulation for compact laser wakefield accelerator based free-electron lasers" New Journal of Physics 17.2 p. 023028 (2015).

[80] T. Seggebrock , A. Maier, I. Dornmair and F. Grüner  "Bunch decompression for laser-plasma driven free-electron laser demonstration schemes" Phys. Rev. Spec. Top.-Accel. Beams, 16 (7) p. 070703 (2013).

[81] M. E. Couprie, A. Loulergue, M. Labat, R. Lehe and V. Malka "Towards a free electron laser based on laser plasma accelerators" J. Phys. B: At. Mol. Opt. Phys., 47 (23) p. 234001 (2014).

[82] W. Ackermann, G. Asova, V. Ayvazyan, A. Azima, N. Baboi, et al." Operation of a free-electron laser from the extreme ultraviolet to the water window". Nature Photonics, 1:336, (2007).

[83] P. Emma, R. Akre, J. Arthur, R. Bionta, C. Bostedt, et al. "First lasing and operation of angstrom-wavelength free-electron laser". Nature Photonics, 4:641, (2010).

[84] P. Baxevanis, Z. Huang, R. Ruth, and C. B. Schroeder "Eigenmode analysis of a high-gain free-electron laser based" on a transverse gradient undulator" Phys. Rev. ST Accel. Beams 18, 010701, (2015).

[85] T. Seggebrock, A. R. Maier, I. Dornmair, and F. Grüner. Bunch decompression for laser-plasma driven free-electron laser demonstration schemes. Phys. Rev. ST Accel. Beams, 16:070703, (2013).

[86] C. B. Schroeder et al., in Proceedings of the 35th International Free-Electron Laser Conference, New York, (2013).

[87] A. R. Maier et al. "Decoding Sources of Energy Variability in a Laser-Plasma Accelerator" Phys. Rev. X 10, 031039, (2020).

[88] A.R. Maier, LUX, DESY, private communication, (2020).

[89] M. E. Couprie et al. "Strategies towards a compact XUV free electron laser adopted for the LUNEX5 project", Journal of Modern Optics, 63:4, 309-323, (2016).

[90] W. T. Wang et al. "High-Brightness High-Energy Electron Beams from a Laser Wakefield Accelerator via Energy Chirp Control " Phys. Rev. Lett. 117, (2016).

[91] Weilun Qin et al. "Study of a free-electron laser driven by a laser-plasma accelerated beam at Peking University", Nuclear Instruments and Methods in Physics Research Section A: Accelerators, Spectrometers, Detectors and Associated Equipment, Volume 925, Pages 193-198, (2019).

[92] A. R. Maier, A. Meseck, S. Reiche, C. B. Schroeder, T. Seggebrock, and F. Grüner "Demonstration Scheme for a Laser-Plasma-Driven Free-Electron Laser". Phys. Rev. X 2, 031019 (2012).

[93] S. Reiche. GENESIS 1.3: a fully 3D time-dependent FEL simulation code. Nucl.Instrum. Methods Phys. Res. Sect. A, 429:243, (1999).

[94] J. W. Goodman, "Statistical Optics" 2nd Edition, Wiley, (2015).

[95] E. Schneidmiller and M. Yurkov, "Transverse Coherence and Fundamental Limitation on the Pointing Stability of X-ray FELs" Proceedings, 7th International Particle Accelerator Conference (IPAC 2016).

[96] Y. Ding, Z. Huang, S.A. Ocko, "Transverse-coherence properties of the FEL at the LCLS". FEL 2010 - 32nd International Free Electron Laser Conference. 151-154. (2010).

[97] E.L. Saldin, E.A. Schneidmiller, M.V. Yurkov. "Coherence properties of the radiation from X-ray free electron laser". Optics Communications. 281. 1179-1188. 10.1016/j.optcom.2007.10.044. (2007).

[98] T, Liu, T, Zhang, D, Wang, and Zh. Huang, "Compact beam transport system for free-electron lasers driven by a laser plasma accelerator" Phys. Rev. Accel. Beams 20, 020701, (2017).

[99] R. Bonifacio, L. De Salvo, P. Pierini, N. Piovella, and C. Pellegrini. Spectrum, "Temporal structure, and fluctuations in a High-Gain Free-Electron Laser Starting from Noise". Phys. Rev. Lett., 73:70, (1994).

[100] R. Bonifacio, B. W. J. McNeil, and P. Pierini "Superradiance in the high-gain free-electron laser" Phys. Rev. A 40, 4467 (1989).

[101] J. van Tilborg, S. K. Barber, F. Isono, C. B. Schroeder, E. Esarey, and W. P. Leemans. "Free-electron lasers driven by laser plasma accelerators", AIP Conference Proceedings 1812, 020002 (2017).

[102] S. Bajlekov. "Towards a Free-Electron Laser Driven by Electrons from a Laser- Wakefield Accelerator: Simulations and Bunch Diagnostics". PhD thesis, University of Oxford, (2011).

[103] K. Floettmann, "Some basic features of the beam emittance" Phys. Rev. ST Accel. Beams, 6:034202, (2003).

[104] P. Antici, et al. "Laser-driven electron beamlines generated by coupling laser-plasma sources with conventional transport systems". Journal of Applied Physics 112, 044902 (2012).

[105] M. Migliorati et al. "Intrinsic normalized emittance growth in laser-driven electron accelerators" Phys. Rev. ST Accel. Beams 16, 011302, (2013).

[106] Xi. Li, A. Chancé, and P. A. P. Nghiem, "Preserving emittance by matching out and matching in plasma wakefield acceleration stage" Phys. Rev. Accel. Beams 22, 021304, (2019).

[107] J. Buon, "Beam phase space and emittance, in CERN Accelerator School: 5th General Accelerator Physics Couse", 1992, edited by S. Turner (Geneva, 1994), Vol. I, p. 89 (CERN Accelerator School Report No. CERN 94–01, 1994).

[108] T. P. Wangler. RF linear accelerators. (2008).

[109] A. Wolski. "Beam Dynamics in High Energy Particle Accelerators", (2014).

[110] D. C. Carey, "The Optics of Charged Particle Beams". Harwood Academic Publishers, Chur. London. Paris. New York, (1987).

[111] I. Zagorodnov, M. Dohlus, and S. Tomin, "Accelerator beam dynamics at the European X-ray Free Electron Laser". Phys. Rev. Accel. Beams **22**, 024401, (2019).

[112] F. J. Grüner, C. B. Schroeder, A. R. Maier, S. Becker, and J. M. Mikhailova. "Space-charge effects in ultrahigh current electron bunches generated by laser-plasma accelerators". Phys. Rev. ST Accel. Beams **12**, 020701, (2009).

[113] L. Giannessi, C. Ronsivalle, "Sparc Undulator Layout, Undulator Parameters, Start to End Simulation and Tolerances", ENEA C.R. Frascati, via E. Fermi 45, 00044 Frascati (ROMA) (2006)

[114] T, Liu, Shanghai Institute of Applied Physics, Chinese Academy of Sciences, Shanghai, private communication. (2020).

[115] S. K. Barber, et al. "A compact, high resolution energy, and emittance diagnostic for electron beams using active plasma lenses". Appl. Phys. Lett. 116, 234108. (2020).

Eidesstattliche Versicherung / Declaration on oath

Hiermit versichere ich an Eides statt, die vorliegende Dissertationsschrift selbst verfasst und

keine anderen als die angegebenen Hilfsmittel und Quellen benutzt zu haben.

Hamburg, den ___24/10/2021___  Unterschrift _____